Fall 2016

Digital topologic and geometric approaches for CT-based multi-generation characterization of airway and pulmonary vascular tree morphology and their association

Dakai Jin
University of Iowa

DIGITAL TOPOLOGIC AND GEOMETRIC APPROACHES FOR CT-BASED MULTI-GENERATION CHARACTERIZATION OF AIRWAY AND PULMONARY VASCULAR TREE MORPHOLOGY AND THEIR ASSOCIATION

by
Dakai Jin

A thesis submitted in partial fulfillment
of the requirements for the Doctor of Philosophy
degree in Electrical and Computer Engineering in the
Graduate College of
The University of Iowa

December 2016

Thesis Supervisor: Professor Punam K. Saha

Graduate College
The University of Iowa
Iowa City, Iowa

CERTIFICATE OF APPROVAL

_____

PH.D. THESIS

_____

This is to certify that the Ph.D. thesis of

Dakai Jin

has been approved by the Examining Committee
for the thesis requirement for the Doctor of Philosophy degree
in Electrical and Computer Engineering at the December 2016 graduation.

Thesis Committee: _____
Punam K. Saha, Thesis Supervisor

_____
Eric A. Hoffman

_____
Joseph M. Reinhardt

_____
Xiaodong Wu

_____
Junfeng Guo

To my wife Feiran and my daughter Joanna

ACKNOWLEDGMENTS

It has been an amazing journey for me to come to the University of Iowa for pursing the Ph.D. degree. I meet lots of outstanding and nice people here, and I deeply appreciate all the help, advice and guidance they endowed me.

First of all, I would like to thank my advisor, Dr. Punam K. Saha, for his excellent guidance, encouragement and constant support throughout the six years of my Ph.D. study. The invaluable insights, profound knowledge and excellent mentorship have greatly promoted my study, and will continue inspiring me in my future career. I deeply appreciate all the help and advice he gives to me in both work and life. It is my great honor to have this opportunity working under his instruction.

I would also like to give my hearty gratitude to Dr. Eric A. Hoffman who have always been a significant help for his excellent vision and consistent support, especially at the most critical time when I first entered the pulmonary imaging area. Knowledge and guidance gained from meetings and discussions with him has paved my road over the path of research.

A special thanks also goes to Dr. Junfeng Guo for his great help and valuable suggestions. We discussed and cooperated intensively in the projects after I entered the lab. Whenever I encountered problems, you always encouraged me on my work and give me confidence. I would also like to thank Prof. John D. Newell Jr for his help with explanation of lung physiology and showing me example images of diseased lungs.

I cordially appreciate Dr. Joseph M. Reinhardt and Dr. Xiaodong Wu for serving on my defense committee and providing me valuable suggestions with their insights and visions in image processing and medical imaging areas.

Moreover, I would like to give my thanks to all the faculties in the Department of Electrical and Computer Engineering for their brilliant courses I attended. Special thanks go to Dr. Krishna S. Iyer and Timothy M. Dougherty from Biomedical Engineering Department for their help with preparing the experimental data and discussions. Sincere acknowledgement goes to all my former and current lab members, Dr. Zhiyun Gao, Dr. Ziyue Xu, Dr. Yinxiao Liu, Dr. Ryan Amelon, Dr. Guoyuan Liang, Weichen Gao, Cheng Li, Cheng Chen, Xiaoliu Zhang, Syed Ahmed Nadeem and other colleagues Dr. Kunlin Cao, Dr. Shanhui Sun, Zhi Chen, Dr. Junjie Bai, Dr. Li Zhang, Dr. Jui-kai Wang, Dr. Yichao Wang, Yue Tian, Chen Cui and Dr. Qiao Hu. I cherish the wonderful memory with them during my six years Ph.D. study.

My sincere thanks goes to ECE department secretary Catherine Kern and the administrative assistant Dina Blanc for their patient assistance. I would also like to thank the Radiology department secretary Ann Thompson, who makes my travel much easier. Sincere thanks also go to Melissa A. Shirk, Shayna J. Heap and Chelsea Sloan for their help with phantom studies, and Mark Escher for his help with transferring the datasets.

Most of all thanks are to my wife Feiran Jiao for her enduring love, encouragement and support; and to my parents Ying Liu and Changfeng Jin and my parents-in-law Li Qi and Shitong Jiao, for their selfless love and support, without whom it is impossible for me to go this far. Last but not least, may thanks be given to our Heavenly Father for everything He has granted me in my life.

This work has been supported by the NIH grant R01 AR054439 and R01 HL112986.

ABSTRACT

Chronic obstructive pulmonary disease (COPD) is a type of obstructive lung disease characterized by chronically poor airflow, which is the result of breakdown of lung tissue (known as emphysema) and small airways disease. It typically worsens over time. Most treatments are limited to the management of symptoms, which makes early detection more valuable to treat the disease etiology itself. With the advancement of computed tomography (CT), it is able to provide high resolution structural and functional imaging to distinguish the lung anatomic structures, as well as characterize their changes over time. Previously, the majority of CT-based measures have focused on quantifying the extent of airway and parenchymal damage. Recent studies suggests that pulmonary vascular dysfunction is an early lesion in COPD and associated with an emphysematous phenotype. Few studies attempted to quantify pulmonary vessel morphology and compared those measures across COPD groups. However, the scope of examined vascular structures in these studies was limited, majorly due to the lack of a standardized method to quantify a broad range of vascular structures.

In this thesis, we propose to use anatomically defined airway branches as references to locate and morphologically quantify central pulmonary arteries in different lung regions. Although pulmonary vessel trees have complex topologic and geometric structures, airway tree possesses much simpler and consistent branching patterns and standardized anatomic nomenclatures are available up to sub-segmental levels. It is also well-known that airway and arterial branches have a unique pairing that is established by their spatial proximity and parallel configuration. Therefore, anatomically labeled airway tree provides a robust benchmark to locate consistent arterial segments for both intra- and inter-subjects. New

methods have been developed for quantitative assessment of arterial morphology matched and standardized by associated airways at different anatomic branches. First, the skeletons of airway and vessel trees are generated to provide simple and hierarchical representations. Then, topologic and geometric properties of airways and arteries, such as distance, orientation and anatomic positon information, are explored to locate the target arterial segments. Finally, the morphologic properties, e.g. cross-sectional area, of target arterial segments are robustly computed.

The developed methods in this thesis provides a standardized framework to assess and compare the vascular measurements in intra- and inter- subjects from a broad range of vessel branches in different lung regions. The work also serves as a practical tool for large longitudinal or cross-sectional studies to explore the pulmonary vessel roles played at the early stage of COPD.

The major contribution of this thesis include: (1) developing two novel skeletonization methods that are applicable to airway and pulmonary vessel trees; (2) developing a semi-automatic method to locate and quantify central pulmonary arterial morphology associate to anatomic airway branches; (3) developing a fully automatic method to identify and reconstruct central pulmonary arterial segments associated to anatomic airway branches and quantify their morphology; (4) validating the methods using computerized phantoms, physical phantoms and human subjects; (5) applying the developed methods to two human lung disease studies.

PUBLIC ABSTRACT

Chronic obstructive pulmonary disease (COPD) is a type of obstructive lung disease characterized by chronically poor airflow, which is the result of breakdown of lung tissue (known as emphysema) and small airways disease. COPD symptoms are typical of numerous other ailments making it difficult to diagnose and track, where most treatments are limited to the management of symptoms. Technological advancements in computed tomography (CT) imaging have allowed for detailed assessment of small-scale changes in lung structure and function. The majority of CT-based measures have focused on quantifying the extent of airway and parenchymal damage. Recent studies suggests that pulmonary vascular dysfunction is an early lesion in COPD.

In this work, we establish a standardized framework to assess and compare central pulmonary vascular dimensions in intra- and inter- subjects from a broad range of vessel branches in different lung regions. Based on the well-known fact that airway and arterial branches have a unique pairing that is established by their spatial proximity and parallel configuration, we use anatomically defined airway branches as references to locate and morphologically quantify pulmonary arteries. First, the skeletons of airway and vessel trees are generated to provide simple and compact structural representations. Then, topologic and geometric properties between airways and arteries, such as distance, orientation and anatomic positon information, are explored to locate the target arterial segments. Finally, morphologic properties of target arterial segments, e.g. cross-sectional area, are robustly computed. The developed methods have been applied to several human lung studies, and may serve as a practical tool for large longitudinal or cross-sectional studies to explore the pulmonary vascular roles played at the early stage of COPD.

TABLE OF CONTENTS

LIST OF TABLES

LIST OF FIGURES

CHAPTER 1

INTRODUCTION

1.1 Introduction and Project Definition

Chronic obstructive pulmonary disease (COPD) is a type of obstructive lung disease characterized by chronically poor airflow. The poor airflow is the result of breakdown of lung tissue (known as emphysema) and small airways disease known as obstructive bronchiolitis. The relative contributions of these two factors may vary between people. It typically worsens over time. The main symptoms include shortness of breath, cough, and sputum production [1]. Worldwide, COPD affects 329 million people or nearly 5% of the population. In 2012, it ranked as the third-leading cause of death, killing over 3 million people [2]. The number of deaths is projected to increase due to higher smoking rates and an aging population in many countries [3]. It has resulted in an estimated economic cost of $2.1 trillion in 2010 [4].

Poor lung function has been shown to be a powerful predictor in COPD [5, 6]. Although pulmonary hypertension is a well-known feature of advanced COPD [7], less is known about vascular response in the early disease. With the advantage of multi-row detector computed tomography (MDCT), it is able to provide high resolution structural and functional imaging that can distinguish the anatomic structures in lung, such as airway, pulmonary vessels and parenchyma, as well as characterize their changes over time occurred in COPD [6, 8-11].

Recent studies [6, 12, 13] suggest that pulmonary vascular dysfunction is an early lesion in COPD and associated with an emphysematous phenotype that can be potentially amenable to early treatment. Few studies [14, 15] attempted to quantify the pulmonary

vessel morphology and compared those measures of vascular morphology across COPD groups. However, the scope of vascular structures examined in these studies was limited to either the central pulmonary artery trunk or the very small peripheral vessels. Therefore, it is of great importance to develop a standardized method to assess and compare the vascular measurements in intra- and inter- subjects from a broad range of matching vessel branches.

The overall aim of this Ph.D. research is: **development of new algorithms for quantitative assessment of pulmonary arterial morphology standardized by the associated airways at different anatomic branches and their applications in human studies**. This research holds the promise of providing a standardized regional pulmonary artery metric by utilizing the topologic and geometric properties of airway tree and pulmonary vascular tree. The Ph.D. research project was accomplished by completing the following three specific aims:

Aim 1: Development of an efficient curve skeletonization algorithm using minimum-cost path approach to fully automate the anatomic labeling of human airway tree.

Aim 2: Detection and reconstruction of the volumetric arterial segments associated to a given airway anatomic branch and assessment of artery morphology.

Aim 2a: Improvement of the initial segmentation of pulmonary vascular tree using a topologically constrained dilation.

Aim 2b: Development of a new fuzzy skeletonization algorithm used as the first step to skeletonize the pulmonary vascular tree.

Aim 2c: Development of the methods to detect and reconstruct the matching arterial segments associated to a given airway branch.

Aim 2d: Assessment of the morphologic properties of arterial segments using radial sample-line approach with outlier analysis.

Aim 2e: Evaluation of the accuracy and stability of arterial morphologic measurements using physically made phantoms.

Aim 3: Evaluation and application of the above methods in human studies.

Aim 3a: Assessment of the reproducibility and accuracy of pulmonary artery measures in chest scans from the ongoing Bioengineering Research partnership (BRP) study, and establish measurement distributions in normal subjects.

Aim 3b: Evaluation of the arterial morphometric changes in emphysema susceptible and non-susceptible subjects under the Hypoxic Pulmonary Vasoconstriction (HPV) Pilot study.

Aim 3c: Evaluation of the arterial morphometric changes in a population with early and advanced COPD, as part of an NIH-funded SubPopulations and InteRmediate Outcome Measures (SPIROMICS) study.

To achieve the goal of this Ph.D. research work, topologic and geometric properties of airway and pulmonary vascular trees are explored. Specifically, we have developed a new curve skeletonization algorithm to extracts the centerlines of human airway tree efficiently. Conventional curve skeletonization methods are sensitive to small boundary perturbations and, often, produce many false branches. In contrast, the new curve skeletonization method utilizes the minimum-cost path approach to incorporate global information, therefore, it is able to generate curve skeletons without false branches. We apply the new method to establish an accurate 1-D topologic representation of human airway tree, and fully automate the airway anatomic labeling process. This labeled airway tree are used to define an anatomic spatial reference system to measure and analyze

regional arterial morphology and other lung metrics. This work have been published in [16, 17].

We have also developed a new fuzzy surface skeletonization algorithm to compute surface skeletons of fuzzy segmented objects using a notion of fuzzy grassfire propagation, which minimizes binarization related data loss. Although the new curve skeletonization algorithm works very well for tree-like objects, it cannot handle 3D tunnels, which is often the case for pulmonary vascular trees due to the artery and vein touching at different scales. Therefore, a general topology preserving skeletonization method is needed applying to the pulmonary vascular trees. The new fuzzy surface skeletonization algorithm is suitable in this situation and, and applied as a first step to compute the surface skeleton of vascular trees. . Then, a conventional thinning algorithm is applied to derive the curve skeleton of pulmonary vascular trees. This work have been published in [18-21].

To achieve the goal of detection and reconstruction of pulmonary arterial segments and assessment of arterial metrics, we utilize the well-known fact in lung anatomy thst airway and pulmonary arterial branches has a unique pairing that is established by their spatial proximity and parallel configuration. Using the anatomic labeled airway branches as a spatial reference system, both a semi-automatic and an automatic method have been developed to identify the arterial segments and measure its morphologic metrics. The semi-automatic method starts with user-specified endpoints of a target arterial segment associated to a specific airway anatomic branch through a custom-built graphical user interface (GUI). It then automatically detects the centerline joining the endpoints, determines the local structure orientation and computes the arterial morphologic metrics at different locations on the centerline. The semi-automatic method serves as an efficient tool

for measuring pulmonary arterial morphology at different anatomic locations that is accurate, robust and that requires limited user-interaction and can be translated to large cross-sectional and longitudinal studies. The related work and the applications have been published in [11, 22-25].

The fully automatic method utilizes the spatial proximity and parallel properties between an airway and arterial branch to automatically detect a matching artery skeleton point from a specific labeled airway skeleton point. Specifically, a matching function between airway and artery skeleton points is designed to automatically identify the best matching artery skeleton point by incorporating the spatial and orientation information. The method then reconstructs the matching arterial segment and computes the morphologic metrics. The related work has been published in [26, 27].

To summarize, the proposed Ph.D. research projects involves research works related to the following major areas – (1) digital topology and geometry, (2) skeletonization, (3) anatomic properties of pulmonary vascular and airway tree, (4) tree labeling, (5) region growing and (6) morphologic assessment. Therefore, we briefly describe the basics of digital topology and geometry, and the skeletonization, which serves as the fundamental theories to fulfill this work. Then, the anatomic labeling of airway tree are discussed to help establish a standard anatomic spatial systems for regional artery measurements. Finally, methods of morphologic analysis of pulmonary vascular structures are explained and the challenges are discussed. A brief literature survey on each of the above research topics is presented in the following section with emphasis on the contribution from the current research study.

1.2 Literature Survey

1.2.1 Basics of Digital Topology

In 1979, Rosenfeld [28] introduced basic digital topological concepts, including connectedness, curves, thinning, border-following, and adjacency-tree, and their properties were established for binary images in square grids domain. Earlier results on digital topology include the works by Duda and Munson [29] on perimeter, convex hull, concavities, enclosures, and spurs; Rosenfeld [30] on connectivity; Alexander and Thaler [31] on homology; Mylopoulos and Pavlidis [32] on dimension; and Gray [33] on genus. Rosenfeld's approach to digital topology is to use a pair of binary adjacency relations (κ_1, κ_0) where the first adjacency relation κ_1 is used for object points while the second adjacency relation κ_0 is used for background points [34]. Specifically, in a 2-D square grid, 8-adjacency is used for object pixels and 4-adjacency is used for background pixels, or, vice versa. He demonstrated that use of such an adjacency pair leads to a workable framework for digital topology, which has several important mathematical topological properties, including conforming to the Jordan curve theorem [35]. Although the idea of using two different adjacency relations for object and background points appears to be somewhat paradoxical, it is this form of digital topology that has been most popular in the computer vision and image processing community, including medical imaging applications. Kong and Roscoe [36, 37] refined this approach with arbitrary adjacency relations and introduced the notion of "normal digital picture" satisfying the Jordan curve theorem, which was proved with a graph theoretic approach. Kovalevsky [38] discussed the difficulties that arise when classical topological notions were used in digital image applications and suggested the use of cellular complexes for the purpose. Recently, there

is a trend to define the discrete topological transformations using simplicial or cubical complex [39-42].

In 1989, Kong [43] introduced the notion "digital fundamental group" allowing precise understanding of many important results on digital topology. The fundamental group is the most basic topological invariant that carries much of the topological information about an object. The development of digital fundamental group led to useful and alternative approaches to digital topology, narrowing the gap with classical topology. This notion has drawn significant theoretical research interest in digital topology and has been studied by several other researchers including Boxer and Karaca [44], Malgouyres [45], Han [46], and Ayala et al. [47]. Boxer and his colleagues studied the homology groups of digital images [48]. Šlapal [49] defined closure operations for digital topology.

1.2.2 Basics of Digital Geometry

Over the last decades, several research groups have studied and reported important results on various topics of digital geometry, including convexity [50, 51], straight line [52-55], perimeter, area [56], circularity, [57, 58], compactness, distance functions [59], etc. Minsky and Papert [50] and Sklansky [51] were among the first to characterize digital convexity. Following Minsky and Papert, a binary digital object is convex, if there is no triplet of collinear lattice points a, b, c such that b falls in between a, c and a, c are object points while b falls outside object. Following Sklansky's definition [51], a binary digital object is convex if and only if there exists a convex object in the continuous plane whose digitization leads to the target binary digital object.

A digital straight line is generated by digitization of a ray that is defined by its slope and intercept parameters [53]. Bresenham [52] presented a computer controlled algorithm

for digital straight line plotting and established the uniqueness of the digital representation of a ray with a rational slope. Rosenfeld [53] presented a characterization of digital straight lines using a "chord property" and derived several connectivity and regularity properties of digital straight line segments. Brons [54] showed that digital straight lines with rational slopes are periodic while those with irrational slopes are aperiodic. Dorst and Smeulders [55] proved that every digital straight line can be represented by four integers and derived a mathematical expressing for the set of all continuous line segments which could have generated a given digital line segment.

Kulpa [56] defined area and perimeter for binary digital objects using position-invariant local image processing operations and pixel counting and established the properties of these measures. Windreich *et al.* [60] presented a surface area computation algorithm by dividing local surface voxel patterns into classes that were treated differently and applied the method to brain MRI data. Rosenfeld and Haber [61] defined area and perimeter measures for fuzzy digital objects. Sladoje *et al.* [62] reviewed the performance of different compactness, area, and perimeter measures for 2-D and 3-D fuzzy digital objects. For a given object, the ratio perimeter^2/area (P^2/A) is often referred to as "compactness", "circularity", "dispersion" or "shape factor" of the object. Rosenfeld [63] showed that (P^2/A) of a digital object is not a desired measure of dispersion, an inverse of compactness. Interestingly, the measure (P^2/A) yields the smallest value for digital octagons or diamonds and not for digital circles. Haralick [57] analytically showed that $mean_R/std\_dev_R$, where R is a random variable of the distance from the center of the candidate object to any part on its boundary, is a good choice as a measure for circularity of digital figures. Danielson [64] defined the shape factor using the average distance

transform value at object pixels and object area. Nakamura and Aizawa [58] presented a characterization of digital circles and provided an algorithm to detect those.

1.2.3 Skeletonization

Skeletonization provides a simple yet compact representation of an object and is widely used in computer vision, computer graphics, and medical imaging applications including animation, shape matching, object representation, structural and topological analyses, registration, path-finding etc.

The idea of skeletonization was first initiated by Blum [65] in 1967, where he proposed that medial loci would provide an effective and compact representation of an object in R^n. The medial loci of an object in R^3 form its *medial axis*, or *skeleton*, which consists of the surfaces and curves of symmetry with lower dimensionality while possessing the same topology as the object. In two dimensions (2D), the medial axis or skeleton of a shape is a set of curves defined as the locus of points that have at least two closest points on the boundary of the shape. In three dimensions (3D), the corresponding medial axis is called the *medial surface* because in addition to curves, it can also contain surface patches. Alternative definitions are the *centers of maximally inscribed discs* in 2D and *centers of maximally inscribed balls* in 3D [65]. More formally, let $O \subset R^3$ be a 3D object. An (open) ball of radius r centered at $p \in O$ is defined as $Sr(p) = \{q \in R^3, d(p,q) < r\}$, where $d(p,q)$ is the distance between two points p and q in R^3. A ball $Sr(p) \subset O$ is maximal if it is not completely included in any other ball included in O [66]. A more illustrated definition of skeleton is given by the grassfire analogy [65], where the field resembles an object. The fire is simultaneously set at all boundary points and it propagates inwardly at a uniform speed. The medial axis or skeleton is defined as the set

of quench points where two or more fire fronts meet. The process of obtaining a skeleton is called skeletonization.

Following Blum's principle of skeletonization, the skeleton of an object in R^n consists of $n-1$ or lower dimensional structures. For example, in 2D, it reduces an object to a skeleton consisting of one dimensional (1D) structures, i.e., curves, only. In 3D, it converts an object into a skeleton that consists of surfaces, i.e., 2D structures as well as curves. This skeletonization process in 3D is commonly referred to as *surface skeletonization*, as it allows surface structures to exist in a skeleton. In a different formulation of skeletonization, a 3D object is reduced to a "curve skeleton", where, a skeleton is formed strictly by 1-D elements, i.e., curves, and no surface elements may survive in the skeleton. Such a process is referred to as *curve skeletonization* and the skeleton as *curve skeleton*. A few examples of surface and curve skeletons for 3-D digital objects are illustrated in Figure 1. For an object consisting of tubular structures, both surface and curve skeletons are identical, and they are formed by the principle of Blum's grassfire propagation. However, the same may not be true for other objects. Both surface and skeleton skeletonization are widely used in different applications [67, 68], where the curve skeletonization is extremely popular in applications related to tubular or quasi-tubular objects [69].

The above definitions were formulated in continuous space. However, many of the applications require skeletonization working on discrete 3D data sets, such as those acquired using medical scanners. In discrete space, the definitions are analogous to the continuous case, but problems may occur because of discretization. For example, a maximal ball may touch the discrete boundary of an object in a single point, such as the

case of an object whose width is an even number of voxels. Since the diameter of the ball is always an odd number of voxels, the ball will be maximal when it touches the boundary on only one side. As a result, in order to include all centers of maximal balls, the discrete skeleton may be more than one image pixel/voxel thick. Furthermore, resolution can cause a loss of detail for certain objects, such as merging, or even disappearance, of small features.

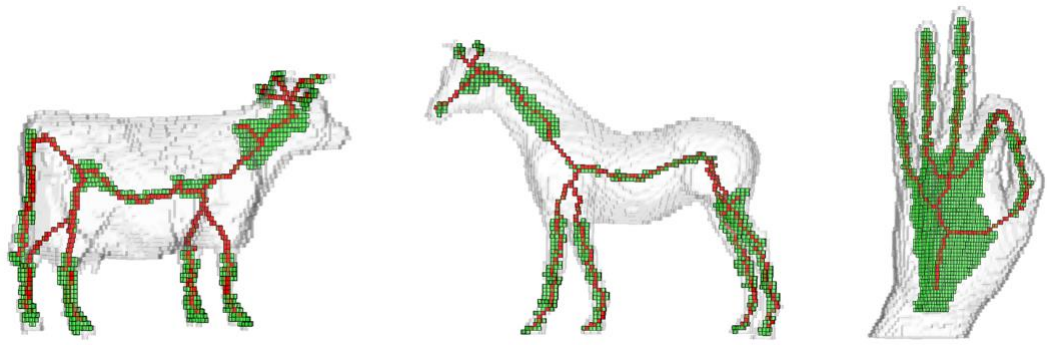

Figure 1 Illustrations of surface and curve skeletons for binary 3-D digital objects in a voxel grid. Voxels representing curve skeletons are shown in red, while those either in red or green constitute surface skeletons.

Therefore, based on the target and applications, some skeletonization algorithms work on continuous geometric data, others deal with discrete objects only. Conversion between these two representations can be performed using well-known algorithms: continuous geometric data can be transformed into a discrete representation by voxelization [70], while voxelized data can be converted into a geometric representation using a surface extraction algorithm [71]. In our work, we only consider the discrete case, since all the target applications are in medical imaging area. In the next few subsections, we describe the desired properties of skeletons and give a brief survey on different classes of voxel-based skeletonization algorithms.

Desired Properties of Skeleton

There is a set of desired properties based on the skeleton definitions and its applications [67-69, 72]. Here, we give a brief description on the most important properties related to our work: homotopy, thinness, centeredness, robustness, smoothness, invariant under isometric transformations and efficiency.

Homotopy (topology preserving): The skeleton should be topologically equivalent to the original object [66, 73, 74]. Preservation of topology can be stated simply as follows: Two objects have the same topology if they have the same number of connected components, tunnels, and cavities. As pointed out in [66], the above formulation applied to an object O_2 derived from an object O_1: "object O_2 preserves the topology of object O_1" is meaningful only if an additional constraint is added: Object O_2 is obtained from O_1 by only removing object voxels (no adding). Otherwise, object O_1 could end up having a completely new configuration, but still have the same topology. With this observation, the above definition of topology preservation is meaningful in the context of skeletonization, where the skeleton is a subset of the original object.

It may be noted that we cannot have cavities in a one-dimensional (1-D) curve, so a curve skeleton cannot preserve the topology of an object having cavities. To accommodate objects with cavities, a relaxed definition of topology preserving may be formulated using the loops of a 1-D curve [75]: The curve skeleton should have at least one loop around each cavity of the original object. However, tunnels in the original object also create loops in the curve skeleton. Therefore, the relaxed definition of topology preserving can be stated as follows: the curve skeleton preserves the topology of the

original object in a relaxed sense if it has the same number of connected components and at least one loop for each tunnel and cavity in the original object.

Thinness: The skeleton should be one voxel thick (no 2×2 foreground-voxel configurations should exist), except at junctions where the skeleton voxels might become thicker for the purpose of preserving the topology.

Robustness: skeletons are very sensitive to small changes in the object boundary. A desirable property for skeleton is to exhibit weak sensitivity to irregularity or noises on the boundary of the object. From another perspective, robustness means to have the skeleton to reflect the original geometry of the object, but to avoid the spurious or false skeletal branches or patches as much as possible. A robust skeleton may not be perfectly centered. Exact centeredness would constrain the skeleton to the medial surface, which is sensitive to boundary perturbations. It should be pointed out that, the robustness is an extremely important requirement in many medical imaging applications, such as the colonoscopy, bronchoscopy, aorta measurement and airway labelling.

Centeredness: For the surface skeletons, centeredness means to keep the skeleton voxels within the center of maximally inscribed ball, which guarantees the skeleton to stay centered in the object. For curve skeletons, no unique centeredness definition exists. Practically, it is often required for the curve skeleton to lie on the medial surface since the medial surface is centered within the object. In addition, some require the curves to be centered within the medial surface patches they belong to [76, 77]. In shape compression and some scientific applications such as vortex core extraction [78], exact centeredness of the curve skeleton may be essential. However, in most cases, exact centeredness of the extracted curve skeleton is not required or desired.

Smoothness: Smoothness is not only a pleasant visual property, but is actually useful in some applications. For example, in virtual navigation, curve skeleton serves as a camera translation path, and the path should be as smooth as possible to avoid abrupt changes in the displayed image. Smoothness can be defined for a curve segment or surface manifold as the variation of the curve tangent or surface norm direction as we move along the curve or surface.

It should be pointed out that smoothness and centeredness are two conflicting properties, especially in digital space. Exact centeredness forces the skeleton voxels to be located within the centers of maximally inscribed ball, hence, would often lead to jagged skeleton, e.g. a tubular object with some random boundary irregularities. On the other hand, smoothness would skip some of the centers of maximally inscribed ball to ensure the smoothness of the curve or surface.

Invariant under isometric transformations: Consider an isometric transformation T, in which the distances between points are preserved. The skeleton of the transformed object $T(O)$, denoted by $Sk(T(O))$, should be the same as the transformed skeleton of the original object O. Formally, the invariance criterion is given by: $T\big(Sk(O)\big) = Sk(T(O))$. This property is important for matching related applications where the skeleton is used as a shape descriptor. In such applications, it is common to have similar objects in different orientations that need to be matched and, for this reason, the shape descriptor must be insensitive to object orientation.

Efficiency: This is the property related to the algorithms that compute the skeleton. It is desired that the skeleton can be computed in real time.

A large number of voxel-based skeletonization algorithms exists in both 2-D and 3-D. Also, different approaches exist to compute surface skeletons [19, 79-84], curve skeletons [76, 77, 85-94], or both [95-101]. Here, we classify the skeletonization algorithms into five categories based on the principles of method design – (1) erosion-based thinning algorithm [80, 95, 96, 102-106]; and (2) distance transform, or DT, based algorithms [97, 100, 107], (3) general field based algorithms [77, 81, 87, 90, 91, 93, 101, 108], (4) minimum-cost path based algorithm [16, 17, 88, 109-112]; (4) fuzzy skeletonization algorithms[19, 113-115].

Erosion Based Thinning

The erosion based thinning algorithms can be further divided into two class: fully predicate-kernel based and structured iterative based thinning.

Fully predicate-kernel based thinning process starts the erosion from the object's boundary and continues inward until no more simple points can be removed. At every iteration, each boundary voxel is tested against a set of predefined topological and geometric preserving conditions and possibly removed. The conditions are usually implemented as templates (or masks) of size 3×3×3 or larger. The center of a mask is placed on the voxel being tested. Each of the voxels in the mask has a value of "0," "1," or "don't care." A value of "0" must match a background voxel, a value of "1" must match an object voxel, while a "don't care" can match either a background or an object voxel. Tsao and Fu [102] proposed the first fully predicate based curve skeletonization algorithm for 3D binary objects in 1981. Then, until 1999, Palágyi and Kuba [104] reported a parallel 12-subiteration 3D thinning for extracting curve skeleton, where it has improved the thinning efficiency and formally proved the topology correctness for their predicate kernels. Later

Palágyi, *et al.* [80, 105, 106] have made several improvement for computing either surface or curve skeletons using this fully predicate based method. One should realize that fully predicate based algorithms implicitly incorporate the topological and geometric conditions into the masks, hence, the key point is to design these masks appropriately and effectively.

Structured iterative based skeletonzation algorithm also utilize the thinning process, but from a different perspective to achieve topology and geometry preservation. Algorithms in this class also starts the erosion from the object's boundary, like thinning, but it explicitly considers the topology and geometry preservation conditions when deleting the boundary voxels. This is completely different from the fully predicate kernel based method. Saha *et al*. [73] and Malainda *et al.* [116] both presented a comprehensive topology preservation condition in 3-D space in early 1990s. See Section 2.2 for a detailed description. The geometry preservation conditions are necessary for both surface and curve structures in the skeleton. For the geometry preservation of curve structures, conditions can be found in [95-97, 103]. Researchers has also put many efforts to study the geometry preservation condition for surface structures. Among them, Lee and Chu [95] proposed a criterion for surface end voxel. Saha *et al.* [96] presented a structured approach by separately modeling conditions for local shape and topology preservation. Borgefors, *et al.* [103] also gave a condition based on DT for surface skeletonization.

Distance Field Based Skeletonization

Distance field based skeletonization algorithms use the DT from boundary to compute the skeleton. The distance transform or *distance field* is defined for each interior point p of a 3D object O as the smallest distance from that point to the boundary $B(O)$ of the object:

$$DT(p)_{p\in O} = \min_{q\in B(O)} \big(d(p,q)\big), \tag{1.1}$$

where d is some distance metric.

Papers falling in this category include [19, 97, 100, 103, 107, 117, 118]. Arcelli and Sannti di Baja [117] introduced the notion of DT-based skeletonization in 2-D and discussed its advantages. Later, they proposed to directly detect the singularity points on DT (call it ridge voxel), and then connect these ridge voxels to form the skeleton. Arcelli *et al.* [107] and Borgefors *et al.* [103, 119] later applied the DT to 3-D skeletonization and gave the formula to compute the CMBs from DT field. Saito and Toriwaki [118] first introduced the idea of using the DT to define the sequence of voxel erosion, which was further studied by other research groups. Pudney [97] and Arcelli *et al*. [82] explored the DT to define both the erosion sequence and the CMBs, generating an effective mixture framework for DT-based skeletonization algorithm. A major advantage of DT based approach is that it avoids repetitive image scans and thus improves computation efficiency. Also, a DT-driven voxel erosion strategy, together with a suitable choice of distance metric [120], makes the skeletons more robust under image rotation. However, an apparently seeming difficulty of this approach is that it may be difficult to parallelize such algorithms, and it often results in spurious skeletal branches due to the nature of the sensitivity of CMBs to small boundary perturbations.

General Field Based Skeletonization

General field based algorithms use fields smoother (with fewer singularities) than DT fields. Such methods are often more robust for noisy shapes than DT based methods, since larger boundary regions have been considered (not just the distance to the closest points on the boundary). Various types of fields can be used. Chuang [87] proposed to use

generalized *potential field* function, where the potential at a point interior to the object is determined as a sum of potentials generated by the boundary points of the object. The curve skeleton is then extracted by detecting the local extremes of the potential field and connecting them. Cornea *et al.* [91] later extended the potential field to the *force vector field* to develop an algorithm that computes a hierarchical curve skeletons.

Siddiqi *et al.* [81] proposed a Hamiltonian formulation of curve evolution and computed the outward flux of the vector field of the underlying system using the *Hamilton-Jacobi equation*. Skeletons are located at the singularity points of this flux field. Additionally, they imposed the topology preservation constraints of digital grids to ensure the robustness of computed skeletons. The idea has been further enhanced with sub-pixel flux calculations [90].

Hassouna and Farag [93] proposed the curve skeletonization algorithm using *gradient vector flow*. The idea comes from the fast marching propagation process for computing the curve skeleton previously studied in [108], where it used the DT to drive a fast marching propagation from a source point with high speed along the center of the structure, and backtracked the centerlines from the detected end points to the source point. Gradient vector field was used as an energy function to control the centerness of the curve skeleton.

Minimum-Cost Path Based Skeletonization

The minimum-cost path is a popular tool, which has been used for computing curve skeletons or tracing centerlines, especially, in those medical imaging applications where the underlying object is quasi-tubular such as colonoscopy [88, 110-112], pulmonary imaging [16, 17], coronary artery tracking [121, 122] etc. Methods of centerline extraction

using minimum-cost path approach can be classified into two major categories --- (1) direct computation of centerlines of tubular objects in raw intensity image without prior object segmentation and (2) centerline computation for pre-segmented binary or fuzzy tubular objects. Often, the methods under the first category use multi-scale Hessian operators on an intensity image for locating potential centerline segments. Finally, these methods apply minimum-cost path techniques to connect such centerline segments [123-127]. A few methods under this category require graphical user input to locate end points of a tubular structure, which are connected to the main centerline tree using minimum-cost paths to interactively grow the target tubular tree object. A thorough survey on related topics available in [128].

Methods under the second category use a prior segmentation of the volumetric tree object as an input and generate its curve skeleton [16, 17, 88, 109-112]. These methods use a local cost function designed to encourage centered paths as compared to paths coming close to object boundaries. Often, distance transform map from the object boundary is used to define centeredness of a given point. A method under this category starts with a root as the initial centerline tree and iteratively augment the tree by adding new centerline branches. First, it identifies a significant extremum point, and then joins it with new centerline branch, which is computed as a centered minimum-cost path. This tree-augmentation process continues until all significant branches are added. A significant difference between a minimum-cost path approach and those discussed in previous subsections is that a minimum-cost path method sequentially adds branches in the order of their significance as compared to other methods, where the entire skeleton is generated at once. This unique property of a minimum-cost path approach offers a natural hierarchical

representation of a centerline tree and provides a robust performance in terms of noisy branch detection.

Fuzzy Skeletonization

Fuzzy skeletonization algorithms directly work on the fuzzy or grey-scale images eliminating the binarization step [129], which may avoid information lost due to the thresholding of original intensity image. This class of algorithms may be a powerful tool in medical imaging process and analysis, where partial volume effect and other imaging artifacts are prevalent.

Compared with the growing results for binary skeletonization, only few works have been proposed for fuzzy skeletonization [19, 113-115]. Pal [113] has proposed an algorithm working on grey image by, first, binarizes a fuzzy object under optimization of fuzzy compactness [130] and then a binary skeletonization algorithm is applied. Yim *et al.* [114] used a significant path selection approach in an ordered region growing (ORG) graph; although, this approach does not use binarization, it is not obvious how to generalize this idea to extract the skeleton of a surface-like object in 3-D. Sanniti di Baja *et al.* [115] used 3-D conversion of a 2-D grey image by uplifting each 2-D voxel with a height equivalent to its grey-value and then followed a 3-D binary skeletonization and finally collapsing from 3-D space to 2-D space. It was until recently that a general framework and a complete algorithm for fuzzy surface skeletonization have been proposed using a new notion of fuzzy grassfire propagation by Jin and Saha [19, 20]. Several new concepts have been introduced in the context of fuzzy skeletonization, namely *collision Impact*, *fuzzy axial voxel* and *global significance factor*. And the *fuzzy distance transform* (FDT) [131] has been used to simulate the process of fuzzy grassfire propagation.

1.2.4 Airway Tree Anatomic Labeling

Airway tree is one of the major organ in lung to achieve the respiration. It is composed of the airway lumen, where is filled by air, and the airway wall. The quantitative assessment of intrathoracic airway trees is of significant importance for the objective evaluation of the bronchial tree structure and function. The first step is the segmentation of airway tress, and a wide variety of methods have been developed to segment the airway lumen [132-140]. It is well known that human airway tree has ten unique anatomic paths, although the geometric branching patterns of airway trees are different inter- and even intra-subject (due to various imaging protocol and airway segmentation results). It is important to have the ability to repeatedly evaluate the same region of the lungs time after time and perform accurate and reliable positional corresponding measurements. Often, after the segmentation of airway lumen the next step is to generate its anatomic model, called airway anatomic labeling. Airway anatomic labeling algorithms have to be operated on the skeleton of the airway tree, because it is much easier to handle and compute structure properties on the dimension reduced skeleton. Therefore, the curve skeleton of airway tree have to be first generated before the anatomic labeling. Many curve skeletonization algorithms [76, 85, 88-90, 92-97, 101, 103, 104] exist in the literature. From the perspective of anatomic labeling, it is desirable to have an airway tree skeleton with as lest false branches as possible in order to get the most accurate labeling. However, none of the curve skeletonization algorithms in the literature fulfilled this purpose. Hence, we have developed a new robust curve skeletonization algorithm using minimum-cost path to ensure lest false skeletal branches in the airway tree curve skeletons. Details of the new curve skeletonization method are described in Section 3.2.

Anatomic labeling of airway tree was originally done by manual labeling. A few works attempted to automatically label airway branches [132, 141-145]. Mori *et al.* [132] presented a knowledge-based labeling algorithm. The proposed algorithm was applied only to incomplete trees, and the built-in knowledge did not incorporate anatomical variations. Additionally, the algorithm is sensitive to the missing or the spurious (false) skeletal branches. Kitaoka *et al.* [141] developed a branch point labeling algorithm that uses a mathematical phantom as reference. Labels are assigned by matching the target tree with this phantom. However, false tree branches have to be pruned first manually in a preprocessing step in order to process the labeling. Tschirren *et al.* [142] presented a complete matching and labeling algorithm for human airway trees, and tested in both normal and diseased subjects. The algorithm was based on the theory of finding the maximum clique in the constructed associate graphs [146, 147]. False branch detection and removal was included in the process of constructing the associate graph, therefore, eliminating the need to prune the skeleton beforehand. Van Ginneken *et al.* [143] and Lo *et al.* [144] used machine learning-based approach to label airway trees by learning the branch geometric features, and the information of tree topology. They utilized branch length, radius, orientation, cross-sectional shape and bifurcation angle as the training features. However, several features are sensitive to the presence of structural noise or diseases, and the assumptions on tree topology make the methods vulnerable to topological differences. Feragen *et al.* [145] presented a supervised algorithm of airway tree labeling based on geodesic distances in a tree-space and evaluated the accuracy, reproducibility and robustness in patients with COPD. In our work, we adopt the algorithm proposed by Tschirren *et al.* [142], since this algorithm delivers the accurate airway tree labeling.

1.2.5 Pulmonary Vessel Segmentation and Quantification

It is of great importance to study the properties of pulmonary vessels because of the roles they played in pulmonary circulation and progression of diseases, such as COPD [6, 14] and pulmonary artery/vein hypertension [7, 148]. Quantitative pulmonary vessel analysis first needs the segmentation of vascular trees. In the late 1990s, several research groups [149-151] proposed the inspiring work on the vessel enhancement using eigenvalue and eigenvector analysis of the Hessian matrix of the image intensity at multiple scales. Following this technique, a large number of the pulmonary vessel segmentation methods has been proposed, where [152, 153] give comprehensive reviews on these methods.

Although pulmonary vascular tree segmentation achieves significant improvement over the past years, segmentation or separation of the pulmonary arteries and veins is still a challenging problem. The difficulties mainly raise from the following factors: (1) arteries and veins are indistinguishable by their intensity values in non-contrast lung CT images; (2) Even in contrast-enhanced CT images, it is difficult to control the timing for image acquisition with sufficient accuracy to distinguish arteries and veins robustly; (3) there is a complex and tight coupling and fusion between artery and vein trees with multi-scale geometry, especially at branching locations, and (4) partial volume effect from limited SNR and relatively low resolution. The anatomic variations of vascular trees between subjects further complicate the task. Separate analysis of the arterial and venous pulmonary trees are of high clinical importance for better understanding pulmonary structures and improving the diagnosis of lung diseases that affect arterial and venous trees differently.

There are few existing artery/vein separation methods for pulmonary CT images in the literature [154-162],which can be divided into three categories: (1) semi-automatic

artery/vein separation[156, 158-160]; (2) automatic artery/vein separation [154, 155, 157, 162]; (3) leaning-based artery/vein separation [161]. In the first category, one of the artery/vein separation methods [160] constructs a minimum-spanning tree with weights derived from local vessel geometric properties, and then applies an edge cutting to separate arteries and veins. The other method [158, 159] utilizes the optimal morphological openings with differently sized kernels to locally split the arteries and veins and the separated regions are independently traced. This method has been applied for morphometric analysis of terminal alveoli and terminal arteries and veins [163]. All these methods involve a significant amount of manual interaction and refinement after the initial separation. In the second category, the automatic artery/vein separation are performed by incorporating different anatomical features like proximity and parallel configuration of arteries and airway branches [154, 155, 162], specific anatomic position between arteries and airways [157] and the uniform distribution of arteries and veins in a given volume [162]. Although arteries and veins were automatically separated, accuracy of methods in this category may not be satisfactory, e.g. the state-of-art method [162] failed to correct separate arteries/veins for some entire lobes in 4 subjects among 25 subjects examined. In the third category, learning-based method is used to formulate an automatic voxel labeling problem based on root detection for both trees [161]. However, it has a training step from contrast-enhancement images, which requires tediously annotated data, and it also has problems near the hilum of the lung, i.e. where arteries and veins are in close proximity.

Most of the existing CT-based pulmonary vessel morphologic quantification involves counting the voxels numbers in the segmented vessel regions to compute vessel

cross-sectional area or volume, or measuring diameters of vessel branch from intensity images using digital caliper.

1.3 Organization of the Thesis

The thesis is organized as follows.

- **Chapter 1** gives an overview of the specific aims and the brief description of the proposed methods. Also, the significance and innovation of the research is discussed and a literature survey of related work is conducted.
- **Chapter 2** provides the basic definitions and notions followed by detailed descriptions of five important theories or concepts in digital topology and geometry, which serves as the fundamental theories to fulfill this Ph.D. work.
- **Chapter 3** presents two new skeletonization algorithms – (1) the curve skeletonization algorithm for robust extraction of the centerlines of airway tree; (2) the fuzzy surface skeletonization algorithm to serve as the first step to skeletonize the pulmonary vascular tree. These two skeletonization algorithms serve as a basic and solid step to achieve the overall aim of this Ph.D. work. Specifically, this chapter describes the research methods, experiments and results related to Aims 1 and 2b.
- **Chapter 4** proposes a semi-automatic framework to quantitatively assess the pulmonary artery morphology associated to specific anatomic airway branches. Experimental plans and results evaluating the accuracy, reproducibility and robustness of the method are presented. Specifically, this chapter describes the research methods, experiments, results, and observations related to Aims 2c, 2d, 2e and 3a.

- **Chapter 5:** presents a fully automatic method to identify and reconstruct the matching arterial segments associated to specific anatomic airway branches. Experimental plans and results evaluating the artery identification accuracy and the measurement reproducibility are presented. Specifically, this chapter describes the research methods, results, and observations related to Aims 2a, 2c, 2d, and 3a.
- **Chapter 6** applies semi-automatic arterial assessment method to examine the central pulmonary artery dimensions in a large population of healthy human non-smokers, which are selected from Bioengineering Research Partnership (BRP) study cohort and SubPopulations and InteRmediate Outcome Measures In COPD Study (SPIROMICS) cohort. The artery dimensions are evaluated in differences genders and their correlation with age is studied. Specially, this chapter describes the research methods, results, and observations related to Aims 3a and 3c.
- **Chapter 7** draws a general conclusion and provides some possible future directions.
- **Appendix A and B** show the application of the semi-automatic method to measure pulmonary arteries dimensions in two human studies – (1) evaluation of the arterial morphometric changes in emphysema susceptible and non-susceptible subjects under the Hypoxic Pulmonary Vasoconstriction (HPV) Pilot study; (2) examination of the arterial morphometric changes in a population with early and advanced COPD, as part of an NIH-funded SubPopulations and InteRmediate Outcome Measures (SPIROMICS) study. Specially, this chapter describes the research methods, results, and observations related to Aims 3b and 3c.

CHAPTER 2

DIGITAL TOPOLOGY AND GEOMETRY

In this chapter, the basic definitions and notions in digital topology and geometry are first given. Then, five important concepts or techniques related to this thesis work are presented, which serve as the fundamental theories to fulfill this research work. Specifically, these five concepts are — (1) digital topology preservation; (2) fuzzy distance transform; (3) fuzzy center of maximal balls; (4) collision impact; (5) minimum-cost path, which are described in detail from the Section 2.2 to Section 2.6.

2.1 Basic Definitions and Notations

In the 3-D discrete image space Z^3, where Z is the set of all integers, each point in Z^3 is referred to as a *voxel*. Two voxels $p, q \in \mathrm{Z}^3$ are referred to as 6-, 18-, or 26-*adjacent* if they share at least a face, an edge, or a vertex, respectively. A κ-*adjacency*, where $\kappa \in \{6,18,26\}$, is defined in a manner such that each voxel is κ-adjacent to exactly κ other voxels. Two κ-adjacent voxels are also referred to as κ-*neighbors* of each other's. The set of 26-neighbors of a voxel p together with the voxel p forms a $3 \times 3 \times 3$ neighborhood and it is denoted by $N_{26}(p)$; $N_{26}^{*}(p)$ denotes the set of all voxels of $N_{26}(p)$ excluding the central voxel p. The other neighborhoods, namely, $N_6(p)$, $N_6^{*}(p)$, $N_{18}(p)$, *and* $N_{18}^{*}(p)$ are defined similarly. For a voxel $p = (p_x, p_y, p_z)$, a middle plane $M_{xy}(p)$ is the set of voxels $\{(p_x + i, p_y + j, p_z) \mid i, j \in \{-1,0,1\}\}$. The other two middle planes, namely, $M_{yz}(p)$ and $M_{zx}(p)$ are defined similarly. These middle planes are used to define two dimensional (2-D) constrains.

A κ-*path* π, where $\kappa \in \{6,18,26\}$, is a nonempty sequence of voxels where every two successive voxels are κ-adjacent. Now, consider a set of voxels $S \subset Z^3$. Two voxels $x, y \in S$ are said to be α-*connected* in S if there exists an α-path from x to y that is contained in S. An α-*component* of S is a maximal subset of S where any two voxels in S are α-connected. S is said to be α-connected if it has just one α-component, or if S is an empty set.. Now, let us consider two subsets $S_1, S_2 \subset Z^3$ where $S_1 \subseteq S_2$. Two voxels $p, q \in S_1$ is said to be κ-*connected* in S_2 if there exists a κ-path from p to q that is contained by S_2. A κ-*component* C of S_1 in S_2 is a maximal subset of S_1 where every two voxels of C is κ-connected in S_2.

A 3D *binary digital image* is described by the quadruple $P = (Z^3, \alpha, \beta, B)$, where $B \subseteq Z^3$ is the set of object voxels representing the object in the image, while $Z^3 \backslash B$ represents the background voxels. The pair (α, β) specifies the object and background connectivity, respectively. In order to avoid topological paradoxes, different values must be chosen for α and β; common choices for 3-D cubic grid are (6,26), (26,6), (6,18) or (18,6). In the same spirit, a fuzzy digital image or a fuzzy object may be defined as $\mathcal{O} = (Z^3, \alpha, \beta, \mu_{\mathcal{O}})$, where $\mu_{\mathcal{O}}: Z^3 \rightarrow [0,1]$ is the membership function of the fuzzy object. In some applications, e.g., image segmentation, the raw image intensity function $F: Z^n \rightarrow R_{\geq 0}$ is used instead of the membership function. The support O of a fuzzy object $\mathcal{O}$ is the set of all voxels with nonzero membership values, i.e., $O = \{p \mid p \in Z^3 \wedge \mu_{\mathcal{O}}(p) > 0\}$. In a fuzzy digital image, the adjacency relation α is used for voxels inside the support of the object while β is used for the voxels inside the background $\bar{O} = Z^3 - O$. The (α, β)-*boundary* ∂S of $S \subset Z^3$is the set of all voxels $p \in S$ such that at least one β-neighbor of p belongs to the background $Z^n - S$, i.e., $\partial S = \{p \mid p \in S \wedge N_\beta^*(p) \cap (Z^n - S) \neq \phi\}$, where

'ϕ' denote an empty set. In our work, 26-adjacency will be used for object voxels while 6-adjacency will be used for background voxels.

2.2 Digital Topology Preservation

In digital topology, we have three types of entities – *objects*, *tunnels* and *cavities*. An *object* is a component of object voxels while a *cavity* is a component of background voxel that is surrounded by object voxels; it may be shown that, in a digital image with a bounded rectangular domain, a cavity is a component of background voxels that does not touch the image boundary. Although tunnels are easily visualized and intuitively described, they are difficult to formally define. However, the number of tunnels in an object can be defined precisely. Intuitively, a tunnel would be the handle of a coffee mug, formed by bending a cylinder to connect the two ends to each other or to a single connected object. There exists a connection between tunnels and handles—when the coffee mug's handle is broken, a tunnel is lost. A ring has one tunnel because the object forms a single solid handle. A hollow torus has two tunnels: the first arises from the cavity inside the ring and the second from the ring itself. More accurately, the *number of tunnels* in an object is the rank of its first homology group [66]. The number of objects, tunnels, and cavities represent the $0th$, $1st$, and $2nd$ Betti numbers, respectively. The numbers of objects, tunnels, and cavities in excluded neighborhood $N^*(p)$ of a voxel p are denoted as $\xi(p)$, $\eta(p)$, and $\delta(p)$, respectively.

For topology preservation in skeletonization, constraints of 3-D simple points are applied while eroding each individual pixel or voxel. A pixel (a voxel in 3-D) is a *simple point*, if and only if, its binary conversion, i.e., conversion from black to white or vice versa, preserves the object components and cavities (and tunnels in 3-D) in the 3×3

neighborhood (3×3×3 neighborhood in 3-D) of the candidate pixel (voxel in 3-D). A concise characterization of 2-D simple points were established in the early 1970s [30, 32, 164, 165]. A characterization of simple points in 3-D is more complex than in 2-D, primarily, due to the presence of tunnels in 3-D. Tourlakis and Mylopoulos [166] presented a generalized characterization of simple points which applies to any dimension. Morgenthaler [167] presented a characterization of 3-D simple points where the preservation of tunnels were imposed by adding a constraint of Euler characteristic preservation before and after the deletion of the candidate voxel. Lobregt *et al.* [168] presented an efficient algorithmic solution for 3-D simple point detection based on the Euler characteristic preservation. However, as described by Saha *et al.* [169], their algorithm fails to detect the violation of topology preservation when the deletion of a point simultaneously splits an object into two and creates a tunnel. Saha *et al.* [73, 169, 170] solved this nontrivial problem of defining the existence or the number of tunnels in the 3×3×3 *excluded neighborhood* of the candidate voxel.

Theorem 1. *If a voxel p has a white 6-neighbor, the number of tunnels $\eta(p)$ in its excluded neighborhood is one less than the number of 6-components of white 18-neighbors of p that contains a 6-neighbor, or, zero otherwise.*

The formulation of the above theorem is based on two observations – (1) Following the Jordon curve property [35], an object $B_R \subset R^3$ entirely contained by a topological sphere S_R forms exactly $n \geq 1$ tunnels if and only if $S_R - B_R$ contains exactly $n+1$ connected components and (2) $N_{26}^*(p)$ forms a digital sphere and the set of corner voxels of $N_{26}^*(p)$, i.e., $N_{26}^*(p) - N_{18}^*(p)$ to avoid a "crossing" between a 26-path in $N_{26}^*(p) \cap B$ and a 6-path in $N_{26}^*(p) \cap \bar{B}$. Saha *et al.* [73, 169, 170] used the above definition of the

number of tunnels to formulate a concise characterization of 3-D simple points in the following four-condition format.

Theorem 2. *A voxel p is a (26,6) simple point in a 3-D binary image if and only if it satisfies the following four conditions.*

Condition 1: p has a white (background) 6-neighbor.

Condition 2: p has a black (object) 26-neighbor.

Condition 3: The set of black 26-neighbors of p is 26-connected.

Condition 4: The set of white 6-neighbors of p is 6-connected in the set of white 18-neighbors.

In the above theorem, Condition 1 ensures that no cavity is created by deletion of a simple point while Condition 2 confirms that no isolated point is deleted. Condition 3 ensures that, after the deletion of the central point p, its neighboring points remains connected. Finally, Condition 4 guarantees that the deletion of a point does not create a tunnel in the neighborhood.

Beside the 3-D simple point constrain necessary to preserve the topology of the binary digital object, it is also recommend by Saha *et al.* [96] that additional constraint of *2-D topology preservation* is applied in all three middle planes of a voxel. This additional constrain of 2-D topology preservation is needed to avoid undesired drilling effects.

2.3 Fuzzy Distance Transform

Distance transform is a local depth measure inside an object and we call it *fuzzy distance transform* when the object representation is fuzzy. Fuzzy distance transform [171] accounts for both partial voxel occupancy and spatial heterogeneity of an object distribution, which is first formulated in continuous space. In digital space, the length of a

link $\langle p, q \rangle$ in a fuzzy object $\mathcal{O}$ is calculated as $\frac{1}{2}(\mu_{\mathcal{O}}(p) + \mu_{\mathcal{O}}(q) \times |p - q|$, where, $|\cdot|$ denotes any valid distance metrics. The *length* $\Pi_{\mathcal{O}}(\pi)$ of a path π in a fuzzy object $\mathcal{O}$, is defined as the sum of lengths of all links along the path, i.e.,

$$\Pi_{\mathcal{O}}(\pi) = \sum_{i=1}^{N-1} \frac{1}{2}\big(\mu_{\mathcal{O}}(p_{i-1}) + \mu_{\mathcal{O}}(p_i)\big) \times |p_{i-1} - p_i|. \tag{2.1}$$

Fuzzy distance between any two voxels p, q, denoted as $\mu_{\mathrm{FD}}(p, q)$, is the length of the shortest path between p, q , i.e.,

$$\mu_{\mathrm{FD}}(p, q) = \min_{\pi \in \Pi_{p,q}} \Pi_{\mathcal{O}}(\pi), \tag{2.2}$$

where $\Pi_{p,q}$ is the set of all possible paths between p, q. It has been shown that fuzzy distance satisfies the metric properties in both continuous as well as discrete spaces in any dimension. For any voxel p inside the support $O = \{q \mid q \in Z^3 \wedge \mu_{\mathcal{O}}(q) > 0\}$ of $\mathcal{O}$, the *fuzzy distance transform* or *FDT* at p, denoted as $FDT_{\mathcal{O}}(p)$, is the fuzzy distance of p from the background $B = Z^3 - O$, i.e.,

$$FDT_{\mathcal{O}}(p) = \min_{q \in Z^3 - O} \mu_{\mathrm{FD}}(p, q). \tag{2.3}$$

2.4 Fuzzy Center of Maximal Balls

Any voxel p in the distance transform can be interpreted as the center of a ball with radius $d(p)$. A *center of maximal ball* (CMB) [172], is any voxel p whose associated ball is included in the object but is not included by any other single ball included in the object. CMB detection can be accomplished by comparing $d(p)$ with the distance values of the neighbors of p, by taking into account the neighboring weights. In detail, p is a center of maximal ball [172] if for every 26-neighbor q of p, the following inequality holds,

$$d(q) - d(p) < |p - q|. \tag{2.4}$$

Similarly, a fuzzy object voxel $p \in O$ is a *fuzzy center of maximal ball* (fCMB) in $\mathcal{O}$ if the following inequality holds for every 26-neighbor q of p

$$FDT_{\mathcal{O}}(q) - FDT_{\mathcal{O}}(p) < \frac{1}{2}\left(\mu_{\mathcal{O}}(p) + \mu_{\mathcal{O}}(q)\right) \times |p - q|. \tag{2.5}$$

Saha and Wehrli [131] introduced the above definition of fCMB which was further studied by Svensson [173]. Also, it may be noted that the definition of quench voxel is equivalent to the seminal notion of CMB for binary digital objects. For a fuzzy digital object, an fCMBs is named as a *fuzzy quench voxel*.

2.5 Minimum-cost Path

Minimum-cost path, or *minimal path*, is formulated in a digital domain using a pre-defined step-cost function $\tau: Z^3 \times Z^3 \rightarrow R^+$, where R^+ is the set of all positive numbers defining the cost of a step between two adjacent voxels. Note that the step-cost is an infinitely large value when the two voxels of a step are non-adjacent. In order to ensure the metric property of minimum cost function, a step-cost function must satisfy the following three properties:

1) $\tau(p, p) = 0$, for any $p \in Z^3$,
2) $\tau(p, q) > 0$, for any $p, q \in Z^3$ and $p \neq 0$, and
3) $\tau(p, q) = \tau(q, p)$, for any $p, q \in Z^3$.

When the second constraint is relaxed, the minimum cost function becomes a pseudo metric. Let path $\pi = \langle p_0, p_1, \cdots, p_{l-1} \rangle$, which is an ordered sequence of voxels where every two successive voxels $p_{i-1}, p_i \in Z^3 | \; i = 1, \cdots, l-1$, are 26-adjacent. Note that $\langle p_{i-1}, p_i \rangle | i = 1, \cdots, l-1$ are the steps on the path π. The cost of a path $\pi =$

$\langle p_0, p_1, \cdots, p_{l-1} \rangle$, denoted as $Cost(\pi)$, is computed as the sum of the costs of all individual steps-along the path, i.e.,

$$Cost(\pi) = \sum_{i=1}^{l-1} \tau(p_{i-1}, p_i). \tag{2.6}$$

In order to define the minimum-cost path between any two voxels $p, q \in Z^3$, not necessarily adjacent, we need to identify the set of all paths between the two voxels. Note that $\Pi_{p,q}$ denote the set of all paths between two voxels p, q. Then, the minimum cost between the two voxel p, q, denoted by $\mathrm{T}(p, q)$, is defined as follows:

$$\mathrm{T}(p, q) = \min_{\pi \in \Pi_{p,q}} Cost(\pi). \tag{2.7}$$

Finally, the minimum-cost path between two voxel p, q, denoted as $\pi^*_{p,q}$, is computed as follows:

$$\pi^*_{p,q} = \arg\min_{\pi \in \Pi_{p,q}} Cost(\pi). \tag{2.8}$$

The minimum-cost path between the starting point p and a given point q is derived from the minimum cost map T using a gradient descent back-propagation starting at q until p is reached. The gradient descent back-propagation always converges to p from q since it has no local minima except at p. The fast marching algorithm [174], which uses a front-propagation approach similar to Dijkstra's algorithm [175] can be used to efficiently compute the minimum cost map. Deschamps and Cohen [124] proposed a simultaneous front propagation approach for minimum-cost path computation. The idea is to simultaneously propagate a front from each of the two voxels p and q and finding the voxel r where the two fronts meet. The minimum-cost path between p and q is computed by separately finding the minimum-cost path from r to each of p and p and then adjoining the

two geodesics. This approach greatly reduces the region covered during front propagation as compared to the Fast Marching algorithms and, also, it allows parallel implementation of the two front propagations.

2.6 Collision Impact

In digital space, the quench voxels, or the CMBs, i.e., the locations of colliding grassfire fronts, have been well-explored in the context of skeletonization, however, the measure of the colliding strength of meeting grassfire fronts at quench voxels has been surprisingly overlooked. The collision impact is defined using the measure of colliding strength of meeting grassfire fronts.

The collision impact is defined using a new notion of fuzzy grassfire propagation, which is discussed in detail in Section 3.3. Here, we give a generalized formulation of collision impact that is applicable to both fuzzy and binary objects in digital space. For fuzzy object $\mathcal{O}$, the *collision impact* at any voxel p, denoted by $\xi_D(p)$, is computed using the following equation:

$$\xi_D(p) = 1 - \max_{q \in N_{26}^*(p)} \frac{f_+\left(FDT_{\mathcal{O}}(q) - FDT_{\mathcal{O}}(p)\right)}{\frac{1}{2}\left(\mu_{\mathcal{O}}(p)+\mu_{\mathcal{O}}(q)\right)\times|p-q|}, \tag{2.9}$$

where the function $f_+(x)$ returns the value of x if $x > 0$ and '0' otherwise. It can be shown that the collision impact value at a quench voxel lies in the interval of (0,1] and it takes the value of '0' value at non-quench voxels. A quench voxel with collision impact value greater than 0.5 will be called a *strong quench voxel*. The intuitive idea behind the formulation of collision impact is explained using Figure 2 in 2D continuous space. It can be seen that the collision impact assigns different values different types of quench voxels, e.g. quench voxels corresponding to a significant and meaningful geometric shapes (quench point **a** in

Figure 2(a), and quench points near θ_{small} Figure 2(b)) have higher collision impact values, while quench voxels associated to nonsignificant geometric shapes or noisy boundary perturbations (quench points near θ_{large} Figure 2(b), or quench points in branch AB in Figure 2(c)) have low collision impact values. This property is very useful to identify meaningful skeletal structures or pruning the false skeletal branches in the skeletonization algorithms. The usage of collision impact in the fuzzy surface skeletonization is described in detail in Section 3.3. In the other hand, the collision impact at non-skeleton voxels has a value of '0'. This additional property makes it suitable in the minimum-cost path based centerline tracing, where the path is encouraged to travel along the voxels with high collision impact values. The usage of the collision impact in the design of cost functions in the minimum-cost path-based curve skeletonization is presented in Section 3.2.

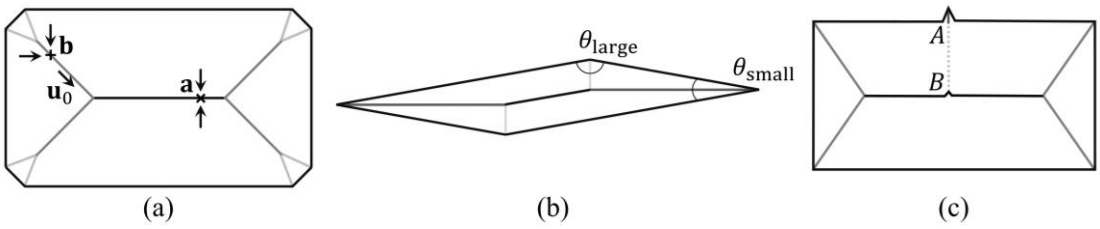

Figure 2 Collision impacts at different skeletal points during grassfire propagation on binary shapes. (a) The fire fronts make head-on collision at the point **a** with the maximum collision impact of '1'. At the point **b**, the fire fronts collide obliquely generating a weaker collision impact. (b) The collision impact along a skeletal branch, originated from a polygonal vertex with a small interior angle, e.g., θ_{small}, is higher than that along a skeletal branch generated from a vertex with a large interior angle, e.g., θ_{large}. (c) The collision impact along the skeletal branch-segment AB connecting a small protruding structure to the central skeleton (dotted line) is low.

2.7 Conclusion

In this chapter, we have presented the basic definitions and notions in digital topology and geometry related to this Ph.D. work. Specifically, five important concepts or approaches related to this thesis work are presented — (1) digital topology preservation; (2) fuzzy distance transform; (3) fuzzy center of maximal balls; (4) collision impact; (5) minimum-cost path. These concepts serve as the fundamental theories to fulfill this research work.

CHAPTER 3

SKELETONIZATION METHODS

3.1 Introduction

In this chapter, we describe two novel skeletonization algorithms – the minimum-cost path based curve skeletonization and the fuzzy surface skeletonization. Skeletonization provides a simple and compact representation of an object. Because of its topologic and geometric simplicity, it has found wide applications in the medical image analysis areas, such as registration, segmentation, path-finding, structural and topological analyses etc. In this Ph.D. work, airway and pulmonary vascular tress are our main focus, which are tubular or quasi-tubular tree-like objects. We explore the topologic and geometric properties of airway and vascular trees to characterize the arterial morphology associated at different airway locations. Skeletons of airway and vascular trees provide simple and natural hierarchical representations, which are suitable to fulfill the purpose of this Ph.D. work.

The new curve skeletonization algorithm is based on the minimum-cost path approach and able to extract the complete curve skeletons of tree-like objects, which are simply-connected objects without tunnels or cavities [73, 176]. We apply the new curve skeletonization algorithm to compute the curve skeleton of an airway tree. Unlike conventional skeletonization methods, the new curve skeletonization algorithm is robust to airway boundary perturbations, imaging noise and other artefacts, producing an accurate 1D topologic representation of an airway tree without generating false skeletal branches. This accurate curve skeleton is used to fully automate the human airway anatomic labeling process, and able to establish an anatomic spatial reference system for further analysis of

regional arterial morphology and other lung metrics. Moreover, an efficient computational framework has been developed, which reduces the computational complexity from $O(N)$ to $O(\sqrt{N})$ (for general tree) or $O(\log N)$ (for balanced tree), where N is the number of terminal branches. Experiments have also been carried out to evaluate the accuracy and robustness of the new curve skeletonization algorithm.

In contrast to the airway tree, which is a simple connected component, the pulmonary vascular trees may have tunnels due to the artery and vein touching at different scales. Therefore, the minimum-cost path based curve skeletonization algorithm may not suitable for applying to pulmonary vascular trees. In this situation, a general topology preserving skeletonization algorithm is required for compute the curve skeleton of vascular trees. In the early stage of my Ph.D. work, I have developed a general-purpose fuzzy surface skeletonization algorithm that minimizes the binarization related data loss, especially suitable in medical image analysis. The new fuzzy skeletonzation algorithm is used as the first step to skeletonize the pulmonary vascular trees. The fuzzy skeletonzation formulation is based on a new notion of fuzzy grassfire propagation, and the algorithm has been examined and validated using both computerized phantoms and real-world examples including medical objects.

The details of these two skeletonization algorithms are described in the following two sections.

3.2 Curve Skeletonization Using Minimum-Cost Path

In the literature, there exist a large number of curve skeletonization methods for elongated 3-D objects [76, 77, 85-96, 100, 102-104, 111, 177], which can be classified into two major categories. Most algorithms under the first category adopted a two-step

approach. First, a surface skeleton is computed from a 3-D object, which is used as an input to compute the curve skeleton. Iterative surface erosion or detection of centers of maximal geodesic balls from the surface geodesic distance transforms are used to compute curve skeletons from surface skeletons [76, 96, 102, 178, 179]. Methods under the second category are designed to directly compute the curve skeleton of an object, which do not require the intermediate step of surface skeletonization. There are various methods under this category which use different mechanisms or functional fields to directly compute the curve skeleton of a 3-D object. These mechanisms or function fields include erosion or peeling [95, 104], distance transform [90, 97, 103, 180], potential field [87, 91], feature distance or medial geodesic transform [77, 92, 101], wave front propagation [93, 108] etc.

The conventional curve skeletonization algorithms using the principle of Blum's transform, often, produce unwanted spurious or false branches due to boundary irregularities, digital effects and other artifacts, even after post-pruning algorithms[181-184]. In contrast, the minimum-cost path approach offers a different skeletonization method, wherein a branch is chosen as a global optimum. The global significance of a branch is naturally utilized to distinguish a noisy branch from a true branch improving its robustness in the presence of noisy perturbations on object boundaries. Therefore, a well-conceived minimum-cost path based curve skeletonization method is superior to conventional methods in terms of noisy branch detection.

Peyré *et al.* [128], presented a thorough survey on minimum-cost path methods and their applications. Minimum-cost path techniques have been extensively used for centerline extraction of tubular or quasi-tubular structures in medical imaging [112, 124, 125, 185-187]. These techniques involve deriving a cost metric [188] from the image in a

way such that minimum-cost path correspond to the centerline of a tubular structure. Such methods connects specified end points to a source point but are not designed for computation of 3D curve skeletons. Sato *et al.* [111] proposed the first algorithm for computing a complete centerline tree of a quasi-tubular tree object. From the same research group, Bitter *et al.* [88] discussed the limitations of their earlier works and presented a framework for computing curve skeletons of quasi-tubular tree structures using minimum-cost path. However, there are several major drawbacks and limitations of their methods, which restrict the use of minimum-cost path as a popular curve skeletonization approach.

In this section, we present a comprehensive and practical solution for direct computation of curve skeletons from 3-D fuzzy digital objects using minimum-cost path. Central challenges for curve skeletonization using a minimum cost-path approach are – (1) assurance of medialness for individual skeletal branches, (2) assessment of branch significance to distinguish a true branch from a noisy one, (3) termination conditions, and (4) computational efficiency. Beside that the new curve skeletonization algorithm is generalized for fuzzy objects, it makes major contributions to overcome each of these challenges. To assure medialness of skeletal branches, we introduce the collision impact [19, 20] to define path cost that is local scale-adaptive and avoids use of parameters. It can be shown that, for a compact object in R^3, a minimum-cost path using the new approach always sticks to the Blum's skeleton. Moreover, in the previous minimum-cost path based approach, a skeletal branch is extended up to an object boundary which contradicts Blum's principle at a rounded surface where the branch of a Blum's skeleton ends to a CMB prior to reaching an object boundary. Our method solves this problem by selecting the farthest CMB instead of object boundary points while adding a new skeletal branch. In regards to

the second and third challenges, a local scale component is introduced while deciding the next most-significant skeletal branch making significant improvements in discriminating among spurious and true branches. And this volume component provides a natural condition for the termination of the algorithm. Finally, a new algorithm is presented that allows simultaneous addition of multiple independent skeletal branches reducing the computational complexity from the order of the number of terminal branches to the worst-case performance of the order of tree-depth.

We evaluated the accuracy of the algorithm using computer-generated phantoms with known skeleton locations. Performance of the method in terms of false and missing skeletal branches, as defined by human experts, has also been examined using *in vivo* CT imaging of human intrathoracic airways. Results from both experiments have established the superiority of the new method as compared to the existing methods in terms of accuracy as well as robustness in detecting true and false skeletal branches. The new algorithm also makes a significant reduction in computational complexity by enabling detection of multiple new skeletal branches in one iteration. Specifically, this method reduces the number of iterations from the number of terminal tree branches to the worst case performance of tree depth. In the next few subsections, we first present the overall workflows and major steps of the new curve skeletonization algorithm, and then, show the experimental results.

3.2.1 Methods and Algorithms

Overall workflows

Conventional curve skeletonization algorithms are designed on the principle of Blum's grassfire transform implemented using voxel erosions, which is subjected to

constraints for preservation of object topology and local "elongatedness". Generally, voxel erosion is controlled by local properties limiting the use of larger contextual information while initiating a skeletal branch during the erosion process. Therefore, such methods often suffer from an intrinsic challenge while handling noisy structures or boundary irregularities, e.g., the small protrusion p_{noise} in Figure 3. The current method works for 2D or 3D tree-like objects (e.g., vascular or airway trees). The method starts with a root voxel, say o, as the initial seed skeleton, which is iteratively grown by finding the farthest CMB and then connecting it to the current skeleton with a new branch. The iterative expansion of the skeleton continues until no new meaningful branch can be found. During the first iteration, the method finds the farthest CMB p_1 from the current skeleton o. Next, the skeletal is expanded by adding a new skeletal branch joining p_1 to the current skeleton. This step is solved by finding a minimum cost-path from o to p_1 (see Figure 3a). Here, it is important that the cost function should be chosen such that the minimum cost-path runs along the centerline of the object and a high cost is applied when it attempts to deviate from the centerline. After the skeletal branch op_1 is found, the representative object volume is computed using a local scale-adaptive dilation along the new branch and marked as shown in Figure 3b. In the next iteration, three skeletal branches are added where each branch connects the farthest CMB in one of the three sub-trees T_1, T_2, and T_3 in the unmarked region. Then the marked object volume is augmented using dilation along the three new skeletal branches. This process continues until no new meaningful branch can be found. Figure 4 presents a color-coded illustration of the marked object volume corresponding to the branches located at different iterations.

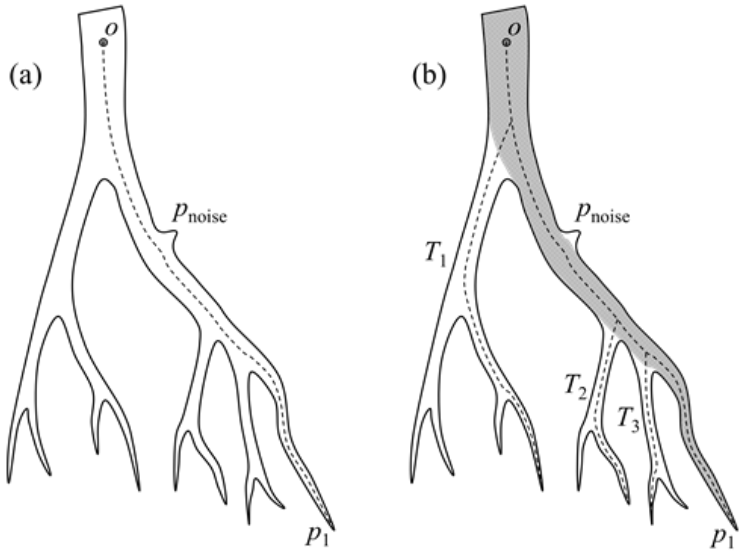

Figure 3 Schematic illustration of the new method. (a) The method starts with the rood point o as the initial skeleton and finds the farthest geodesic point p_1. This farthest point is connected to the skeleton by a new branch op_1 using a minimum-cost geodesic path. (b) The object volume corresponding to the current skeleton is filled and the next farthest geodesic point p_2 is found and another skeletal branch op_2 is added. It may be noted that the noisy protrusion p_{noise} does not create any noisy branch even after all meaningful branches are added to the skeleton.

An important feature of the new method is that the meaningfulness of an individual skeletal branch is determined by its global context. Therefore, the method is superior in arresting noisy branches. Also, the minimum-cost path approach improves the smoothness of skeletal branches. Finally, depending upon the application, the initial root point may be automatically detected, e.g., (1) the point with the largest distance transform value, (2) the deepest points on topmost plane in the airway tree etc. Major steps of the algorithm are outlined in the following.

Begin Algorithm: compute-curve-skeleton

Input: the original object volume O

Output: curve skeleton S

Initialize a root voxel o as the current skeleton S and the current marked object volume O_{marked}

While new branches are found

  Detect disconnected sub-trees $T_1, T_2, T_3, \cdots$ in the unmarked object volume $O - O_{\text{marked}}$

  For each sub-tree T_i

    Find the CMB voxel $v_i \in T_i$ that is farthest from O_{marked}

    If the geodesic distance of v_i from O_{marked} is sufficiently large

      Add a new skeletal branch B_i joining v_i to the current skeleton S using a minimum cost-path

      Augment $S = S \cup B_i$

      Compute local scale-adaptive dilatation D_i along B_i

      Augment $O_{\text{marked}} = O_{\text{marked}} \cup D_i$

End Algorithm: compute-curve-skeleton

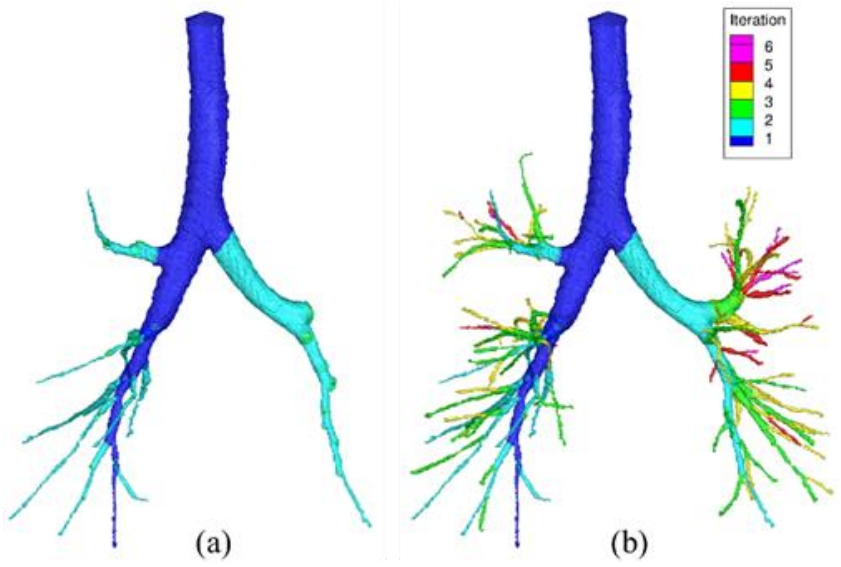

Figure 4 Results at different iteration of the new curve skeletonization algorithm. (a) The marked object volume on a CT-derived human intrathoracic airway tree corresponding to the skeletal branches computed after two iterations. (b) Same as (a) but at the terminal iteration.

In the rest of this section, centered minimum-cost paths are discussed along with detail description of different steps in curve skeletonization.

Centered Minimum-Cost Paths

The general formulation of minimum-cost path approach has been given in section 2.5. The core principle of a minimum-cost path based curve skeletonization algorithm is to iteratively add skeletal branches each connecting the current farthest CMB voxel to the main skeleton using a minimum-cost path. Such a skeletal branch should follow the centerline of the corresponding volumetric brunch structure. To fulfil this objective, an appropriate step-cost function is used that encourages path propagation along the centerline, while heavily penalizing any deviation from it. DT or normalized DT map has been popularly used to impose the centeredness property of minimum-cost paths [88, 110-112, 123, 125, 188]. However, both DT and the normalized DT does not account for local scale dependency.

In this Ph.D. work, we propose to use a local scale independent measure of collision impact in the step cost function to impose centeredness of minimum-cost paths. As introduced in section 2.6, collision impact is always '0' at non-CMB, while it has a positive value at CMB voxels. This property of collision impact ensures that minimum-cost paths are confined to the set of CMBs unless required for topological connectivity. The magnitude of the collision impact capture the strength of impact when Blum's colliding fire fronts meet [20]. As illustrated in Figure 2, the collision impact reflects the angle between the boundary sections from which the colliding fronts had originated. Thus, it generates a high values of collision impact at CMBs located around centerlines of elongated structures, while small values for CMBs produced by small fluctuations at object

boundaries. The definition of collision impact at a voxel p in a fuzzy digital object $\mathcal{O}$, denoted by $\xi_{\mathcal{O}}(p)$, can be found in section 2.6.

Note that the value of collision impact at a voxel lies in the normalized range of [0,1]. A CMB with its collision impact greater than 0.5 may be considered as a *strong CMB* or a *strong quench voxel*. The step cost function τ ensuring centered minimum-cost path is defied using collision impact as follows:

$$\tau_{\mathrm{CI}}(p,q) = \frac{|p-q|}{\epsilon + \left(\frac{\xi_{\mathrm{D}}(p)+\xi_{\mathrm{D}}(q)}{2}\right)^2}, \tag{3.1}$$

where the parameter ϵ is a small number used to overcome problem related to numerical computation of division by zero. A constant value of '0.01' may be used for ϵ. Performance of different step cost functions is illustrated in Figure 5.

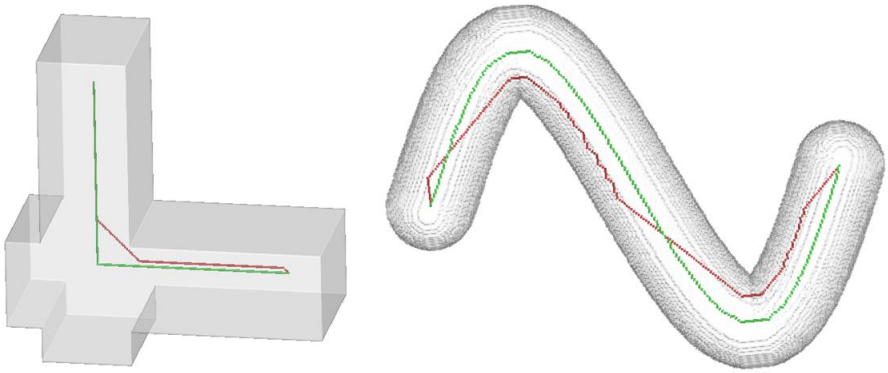

Figure 5 Illustration of geodesics using the new path-cost function. In the left figure, the new geodesic (green) preserves the sharp corner of the shape while the path (red) by Bitter *et al*. fails. In the right example, the new geodesic smoothly follow the centerline of the object while Bitter *et al*.'s path makes several corner cutting.

Skeletal Branch Detection

During an iteration of the new algorithm, multiple meaningful skeletal branches are added to the current skeleton where each branch comes from a connected sub-tree T_i in the unmarked object volume $O - O_{\text{marked}}$. Let $C_O \subset O$ be the set of all strong quench voxels in the fuzzy digital object O. To locate the branch-end voxel in each sub-tree T_i, the geodesic distance (GD) from O_{marked} is computed for each voxel in $C_O \cap T_i$. A path $\pi = \langle p_0, p_1, \cdots, p_{l-1} \rangle$ is an ordered sequence of voxels where every two successive voxels $p_{i-1}, p_i \in Z^3 | \; i = 1, \cdots, l-1$, are 26-adjacent. The length of a path π is defined as

$$length(\pi) = \sum_{i=1}^{l-1} |p_{i-1} - p_i|. \tag{3.2}$$

The geodesic distance or GD of a voxel $p \in C_O \cap T_i$ from O_{marked} is computed as:

$$GD(p) = \min_{\pi \in \Pi_p} length(\pi), \tag{3.3}$$

where Π_p is the set of all geodesic paths from p to O_{marked} confined to O. The branch-end voxel in T_i is selected as farthest (in the geodesic sense) strong quench voxel v_i as follows:

$$v_i = \arg\max_{p \in C_O \cap T_i} GD(p). \tag{3.4}$$

It may be noted that, unlike the algorithm in [88, 110, 111], the above equation ensures that a skeletal branch ends to quench voxel and thus agrees with the Blum's principle of skeletonization. The cost $Cost(\pi)$ of a path π is computed by adding individual step-cost along the path, i.e.,

$$Cost(\pi) = \sum_{i=1}^{l-1} \tau_{\text{CI}}(p_{i-1}, p_i). \tag{3.5}$$

The final task is to connect the selected quench voxel v_i to the current skeleton S using the minimum cost-path. In other words, the path B_i connecting v_i to S is computed as:

$$B_i = \arg\min_{\pi \in \Pi_{v_i,S}} Cost(\pi), \tag{3.6}$$

where $\Pi_{v_i,S}$ is the set of all paths between v_i and S confined to O. It is reemphasized that geodesic distance transform from O_{marked} is used to locate the branch end point v_i, while a collision impact based minimum-cost path from the current skeleton S is used to compute the new skeletal branch B_i.

Object Volume Marking

The final step during an iteration is to mark the object volume represented by a newly added skeletal branch. The purpose of volume marking is to exclude the region already represented by current skeletal branches from subsequent searches for new skeletal branches. This simple idea significantly improves the performance of minimum-cost path based curve skeletonization. First, it drastically reduces repetitious transverse skeletal branches within an object branch, which is a major source of noisy branches, especially, at large scale regions. Also, it improves the ability to distinguish between true and false skeletal branches, because the volume assigned with a spurious branch will be small, although, the length of the branch may be relatively large; for example, consider the possible spurious branch in Figure 3 from the point p_{noise}. Finally, the volume marking step allows a natural termination criterion for the iterative skeletal expansion process. Using volume marking, the iterative process can be terminated when the entire object

region is marked, and it does not require any ad hoc thresholding on branch-length for termination.

The object volume marking step utilizes local scales along a skeletal branch B_i. The local dilation scale $scale(p)$ at a given voxel p on B_i is defined as twice its FDT value (DT value for a binary object). For an object in the continuous domain, the dilation scale at p is exactly the same as its local scale. However, due to various artifacts related to a digital space, we suggest the dilation scale as two times its local scale. Note that a little extra geodesic dilation does not create any risk of missing a true skeletal branch. On the other hand, it reduces false branches, adds stability in the termination criterion by filling small protrusions, and improves computational efficiency. Efficient computation of local scale-adaptive dilation is achieved along the principle of the following algorithm.

Begin Algorithm: compute-local-scale-adaptive-dilation
Input: support O of a fuzzy object; a skeletal branch B_i
local dilation scale map $scale: B_i \rightarrow R^+$
Output: Dilated object volume O_{B_i}
$\forall p \in B_i$, initialize the local dilation scale $DS(p) = scale(p)$
$\forall p \in O - B_i$, initialize dilation scale $DS(p) = -max$
while the dilation scale map DS is changed
$\forall p \in O - B_i$, set $DS(p) = \max_{q \in N^*(p)} DS(q) - |p - q|$
set the output $O_{B_i} = \{p \mid p \in O \wedge DS(p) \geq 0\}$
augment the marked object volume $O_{\text{marked}} = O_{\text{marked}} \cup O_B$
End Algorithm: compute-local-scale-adaptive-dilation

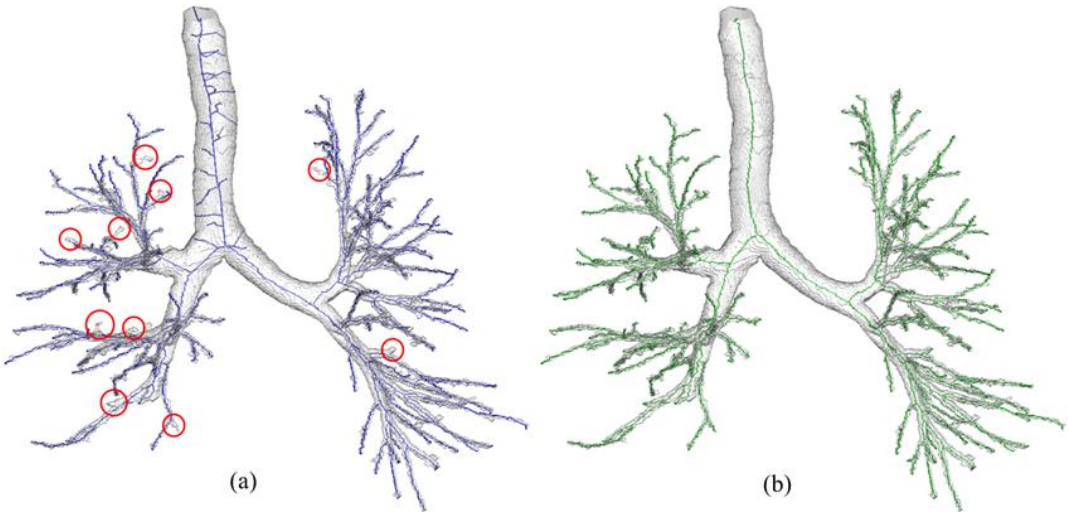

Figure 6 Comparison of skeletal branch performance between Bitter et al.'s algorithm (a) and the new one (b) on a CT-derived human airway tree. The missing branches are marked with red circles. (a) Bitter et al.'s algorithm generates several noisy skeletal while already missing quite a few true branches. (b) Our method neither generates a noisy branch no misses a visually obvious branch.

Termination criterion

As described earlier, the algorithm iteratively adds skeletal branches and it terminates when no more significant skeletal branch can be found. Specifically, the termination is caused by two different situations – (1) the marked volume O_{marked} covers the entire object, or (2) none of the strong quench voxel in the unmarked region $O - O_{\text{marked}}$ generates a significant branch. The first criterion characterize the situation when the entire object is represented with skeleton branches and no further branch is needed. The second situation occur when there are small protrusions left in the unmarked region, however, none of those protrusions warrants a meaningful skeletal branch.

The *significance* of a branch B_i joining a end voxel $v_i \in C_O \cap T_i$ to the skeleton S is computed by adding collision impact values along the skeletal banch, i.e.,

$$significance(B_i) = \sum_{p \in B_i} \xi_D(p). \quad (3.7)$$

A local scale-adaptive significance threshold is used to select a skeletal branch. Let $p_v \in S$ be the voxel where the branch B_i joining an strong quench voxel v meets the current skeleton S. The scale-adaptive significance threshold for the selection of the new branch B_i is set as $\alpha + \beta DT(p_v)$ in the voxel unit. The constant term α plays the major role in determining significance of branches originated from a small scale regions, mostly attributed with branches at a higher generation. The term $\beta DT(p_v)$ becomes the determining factor for branches emanating from large scale regions mostly true for branches at a lower generation. Although, the constant parameters α and β are application dependent, for most applications, the values $\alpha = 3$ and $\beta = 1$ seem to be acceptable.

Three important features of the above termination criterion need to be highlighted. First, the significance of a new branch is computed from the current marked volume instead of the current skeleton. Second, a measure of branch significance is used instead of simple path-length, which elegantly subtracts the portion of a path merely contributing to topological connectivity with little or no significance to object shape. Finally, the new termination criterion uses a scale adaptive threshold for significance. At large-scale object regions, it is possible to visualize a situation where a branch is long enough while failing to become significant under the new criterion. Under such a situation, a large portion of the target branch falls inside the marked object volume resulting in a low significance measure. A scale-adaptive threshold of significance further ensures that such false branch at large scale regions are arrested. Final results of skeletonization for a CT-based human intrathoracic airway tree are shown in Figure 6(b). As it appears visually, the algorithm successfully traces all true branches without creating any false branches as compared to the

results using Bitter *et al.*'s method which creates several false branches while missing several obvious ones (marked with red circles).

Computational Complexity

The computational bottleneck of the minimum-cost path based skeletonization is that it requires re-computation of path-cost map over the entire object volume after each iteration. In previous methods [88], only one branch is added in each iteration. Therefore, the computational complexity is determined by the number of terminal branches N in the skeleton. The new algorithm makes a major improvement in computational complexity. As illustrated in Figure 3, after adding the skeletal branch op_1 and finding the marked object volume along op_1, the unmarked volume generates three disconnected sub-trees T_1, T_2, and T_3 (Figure 3 (b)). These three sub-trees represent the object volume for which skeletal branches are yet to be detected.

An important observation is that, since these sub-trees are disconnected, their representative skeletal branches are independent. Therefore, new skeletal branches can be simultaneously computed in T_1, T_2, and T_3. In other words, in the next iteration, three branches can be simultaneously added where each branch connects to the farthest CMB within each sub-tree. After adding the three branches, the marked volume is augmented using local scale-adaptive dilation along the three new branches. This process continues until dilated skeletal branches fill the entire object volume or all meaningful branches are found. For the example of Figure 3, algorithm terminates in four iteration while it has nine terminal branches.

This simple yet powerful observation reduces the computational complexity of the algorithm from the order of number of terminal branches to worst case performance of the

order of tree-depth. For a tree with N nodes, the average depth of unbalanced bifurcating tree is $O(\sqrt{N})$ [189]. Thus, our average computation complexity is better than $O(\sqrt{N})$ as compared to N using previous algorithms. For a complete bifurcating tree, the number of iteration by our method is $O(\log_2 N)$. For example, the airway tree in Figure 4(b) contains 118 terminal branches and the new algorithm completes the skeletonization process in 6 iterations, only. Note that, as shown in Figure 4a, the method adds twelve skeletal branches after two iterations. See the next subsection for more experimental results demonstrating the improvement of computational efficiency of the new method.

3.2.2 Experimental Results

A few figures have been used to qualitatively demonstrate the performance of the new curve skeletonization method. For example, Figure 4 illustrates the improvement by the method in terms of computation complexity where the skeleton of a tree-like object with a large number of branches is completed in a few iterations. Figure 5 shows the superiority of the new cost function as compared to the one by Bitter *et al*. in tracing the center line of the target object. Figure 6 qualitatively demonstrates the performance of the new method in handling true and noisy branches as compared to Bitter *et al.*'s algorithm using minimum-cost path. Figure 7 shows the robustness of the new algorithm on a variety of shape available online. For all these figures, the method generates a skeletal branch for each visible feature while arresting noisy branches. In the rest of this section, we present quantitative results of three experiments evaluating the method's performance in terms of accuracy, false branch detection, and computational efficiency as compared to two leading methods [95, 190]. The performance of the method was examined on tubular tree phantoms generated from human airway and coronary artery CT images. The method by Palágyi *et*

al. [190] was selected because it was designed for tubular tree objects with an optimized implementation. Another highly cited method by Lee *et al.* [86] available through ITK: The NLM Insight Segmentation and Registration Toolkit, http://www.itk.org was used for comparison. The second method represents a decision-tree based approach for curve skeletonization. The branch performance and computation efficiency of the current method was also compared with Bitter *et al.*'s method.

Data and Phantom Generation

The CT images of human airway and coronary artery were used for quantitative experiments. *In vivo* human airway CT images were acquired from a previous study, whereby subjects were asked to perform volume-controlled breath holds at total lung capacity (TLC). Airway images were acquired on a Siemens Sensation 64 multi-row detector CT scanner using the following parameters: 120 kV, 100 effective mAs, pitch factor: 1.0, nominal collimation: 64×0.6mm, image matrix: 512×512, (0.55 mm) 2 in-plane resolution, and 0.6 mm slice thickness.

Airway phantom images with known skeletons were generated from TLC lung CT images of five subjects. The following steps were applied on each CT image – (1) segmentation of human airway lumen from using a region growing algorithm [138], (2) curve skeletonization [96] and computation of airway lumen local thickness [191], (3) pruning of curve skeleton beyond the 5th anatomic level of branching, (4) up-sampling of the curve skeleton and local thickness map by 2×2×2 voxels, (5) fitting of a B-spline to each individual skeletal branch, (6) smoothing of the thickness values along each skeletal branch, (7) reconstruction of a fuzzy object for the airway tree using local thickness-adaptive dilation along skeletal branches at $5 \times 5 \times 5$ sub-voxel resolution, (8) addition of

granular noisy protrusions and dents on the airway tree boundary, (9) down-sampling of each airway tree object and its skeleton at 3×3×3 voxels, and (10) filling of any small cavities or tunnels [74] artificially created while adding noisy protrusion and dents or down-sampling. For the step of adding noisy protrusions and dents, 1% of the airway boundary voxels are randomly selected as locations for protrusions or dents. The granular protrusion or dent were generated using local-scale adaptive blobs whose radius was randomly chosen from three different ranges depending upon the noise level. Specifically, 30±10%, 50±10% and 70±10% of the local scale were used for the three levels of noise. See Figure 8 for the airway tree phantoms at different levels of noise.

Also, eight online (http://coronary.bigr.nl/) coronary artery datasets with known centerline from the Rotterdam coronary centerline evaluation project [122] were used. Steps 7 to 10, described the previous paragraph, were applied to each coronary dataset to produce four test phantom images at four different noise levels. Besides these phantom data sets ten original human airway tree data-sets derived from in vivo CT imaging were used for evaluating the performance of different algorithms in terms of true/false branch and computational efficiency. Finally, the new algorithm was directly applied on these fuzzy objects while a threshold of 0.5 and filling of small cavities and tunnels were applied prior to applying other methods which are essentially designed for binary objects.

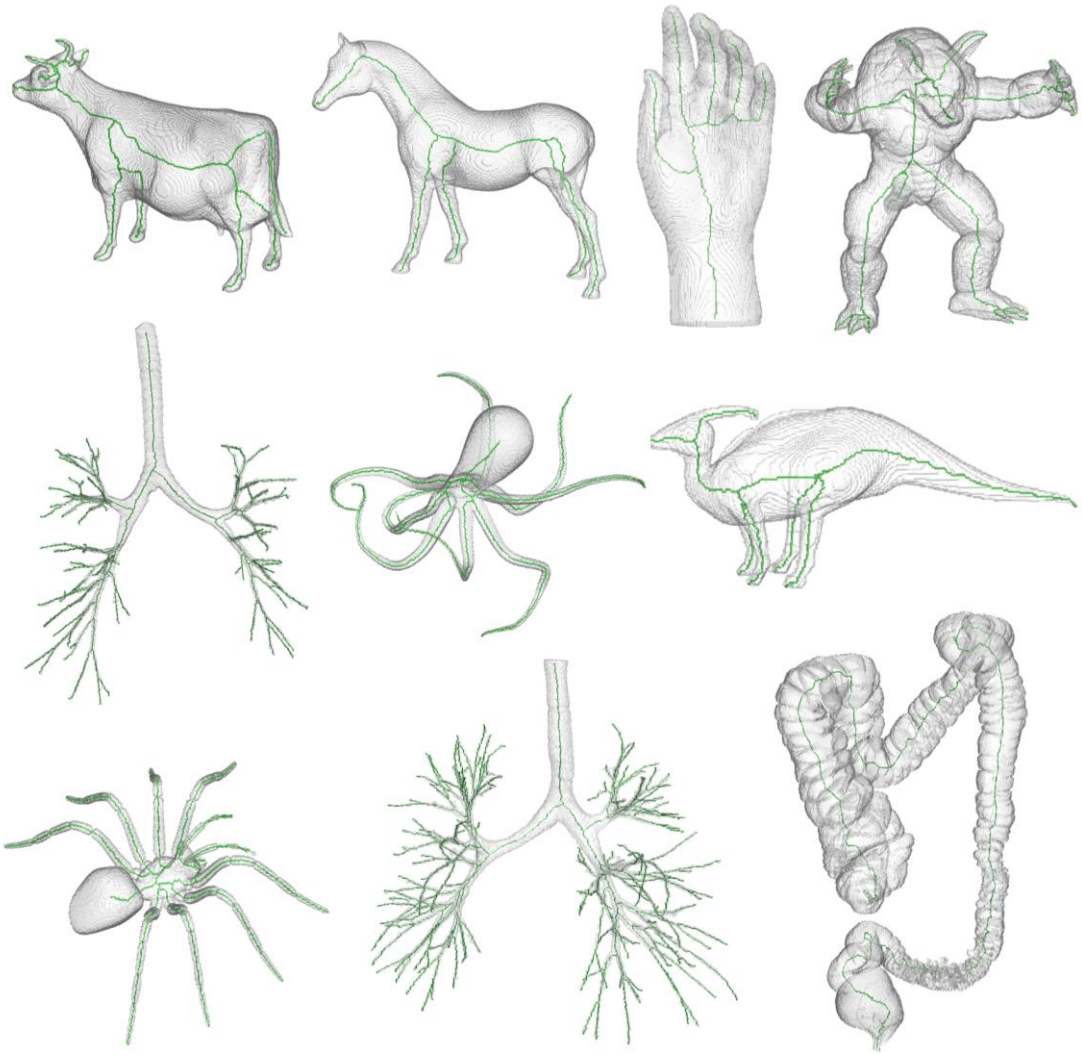

Figure 7 Results of application of the new curve skeletonization algorithm on different 3-D volume objects available online. The object volume is displayed using partial transparency and computed skeletons are shown in green. As observed from these results, the new method does not generate any noisy branch while producing branches for all major geometric features in these objects.

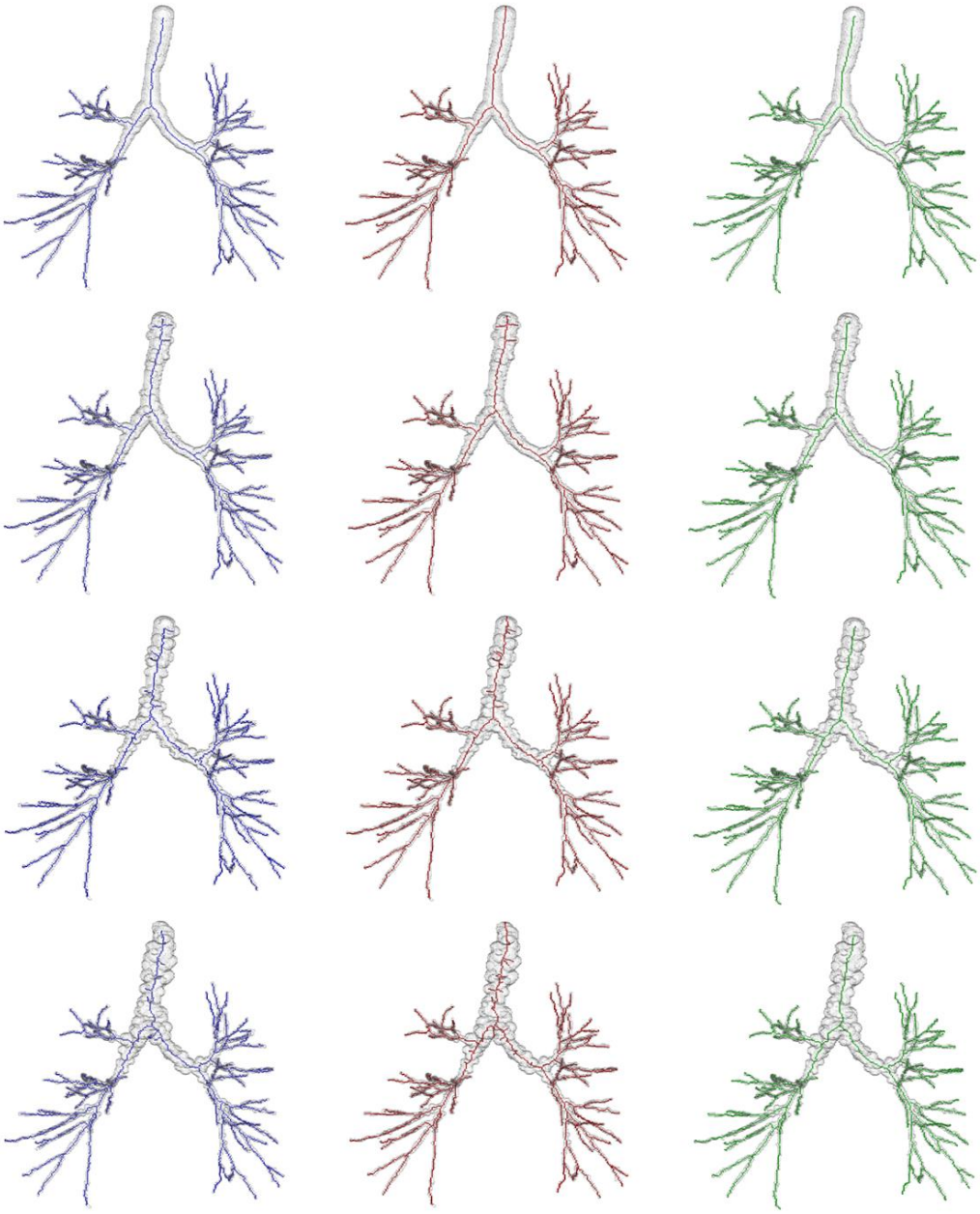

Figure 8 Curve skeletonization results by different methods on airway phantom images at different levels of noise and down sampling. Rows from top to bottom represent phantom images at noise-free, low, medium, and high levels of noise. Left, middle, and right columns present curve skeletonization results using the methods by Lee et al, Palágyi *et al.* and the new method, respectively. It is observed from these figures that both Lee *et al*. and Palágyi *et al.*'s method produce several false branches at low, medium and high noise levels, while the new method produces no visible false branch. All methods have captured all meaningful branches.

Accuracy

Twenty airway (5 images × 4 noise levels) and thirty two coronary artery (8 images × 4 noise levels) phantoms at different levels of noise were used to examine the accuracy of different methods. Results of application of curve skeletonization by different methods on an airway phantom data at different levels of noise are shown in Figure 8. To quantitatively assess the performance of different methods, an error was defined to quantitatively measure the difference between true and computed skeletons. As mentioned earlier, each branch in the true skeleton was represented using a B-spline. The true skeleton was expressed as a set of densely sampled points of the true skeletal branches; let S_T denote the set of N_T number of sample points on a true skeleton. Let S_C denote the set of N_C number voxels in the computed skeleton by a given method. Skeletonization error was computed as follows:

$$error = \frac{1}{2N_T}\sum_{p\in S_T}\min_{q\in S_C}|p-q| \quad + \frac{1}{2N_C}\sum_{p\in S_C}\min_{q\in S_T}|p-q|. \qquad (3.8)$$

Mean and standard deviation of errors by three skeletonization algorithms (Lee *et al.*, Palágyi *et al.* and our method) for airway and coronary phantom images are presented in Figure 9. For both airway and coronary phantoms, the average error and standard deviation using the our algorithm are less than those by Lee *et al.* and Palágyi *et al.* at all noise levels and a paired t-test confirmed that these differences are statistically significant ($p << 0.05$). Also, it is observed from the figure that the average error plus its standard deviation using our method is less than one voxel even at the highest noise level for both airway and coronary phantoms. As discussed in [192], the average digitization error in a skeleton is close to 0.38 voxel. Therefore, after deducting the digitization error, the performance of the new method is highly promising.

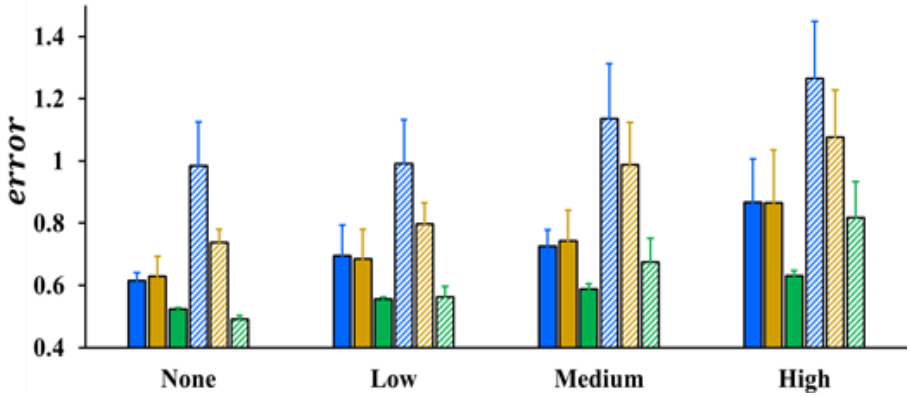

Figure 9 Skeletonization errors by different methods on computerized phantoms at different noise levels – none, low, medium, and high. Blue, gold, and green bars represent skeleton errors by three different methods – Lee et al., Palágyi et al., and the new method. The solid bars represent the errors for airway phantoms which the bars with the slanted pattern show the errors for coronary phantoms.

In general, observed mean skeleton errors for coronary phantoms are higher than airway phantoms. A possible reason behind this observation is that the average thickness of coronary phantoms was greater than airway phantoms in voxel unit. At no noise, neither the algorithm by Lee *et al.* nor by Palágyi *et al.* produced visible false branches (see Figure 8), skeleton errors using those methods are significantly larger than the current method. The most probable explanation behind this observed difference at no noise is that the skeleton produced by the current method is spatially closer to the original centerline as compared to the other two methods.

False and Missing Branches

A qualitative example illustrating the difference among three skeletonization methods at various noise levels has been shown in Figure 8. The new method successfully stopped noisy branches at all noisy granulates on the airway boundary. Although the algorithm by Palágyi *et al.* did not produce any false branch for no noise phantoms, it failed

to do so for noisy phantoms. The algorithm by Lee *et al*. produced false branches even for no noise phantoms.

A quantitative experiment was carried out by two mutually-blinded experts examine the performance of different algorithms in terms of false and missing branches. Each expert independently labelled the false and missing branches in each airway skeleton by visually comparing it with the matching volume tree. The results of this experiment for airway phantoms at different noise levels are summarized in Table 1. It is worth noting that the quantitative results of Table 1 is consistent with the observation of Figure 8. The performance of the new method in terms of false skeletal branches is always superior to the other two methods and the difference is further exacerbated at higher noise levels.

Besides the airway phantoms, ten original segmented human airway trees without down-sampling or addition of external noise were used and analyzed. The labelling of false and missing branches for these original airway trees was confined to the fourth generation of airway branches because the confidence of labelling a false or missing branch beyond the fourth generation was low due to limited resolution even by the experts. The results are summarized in Table 2. Altogether, the new method generated five false branches among which three false branches were generated in one data set. On the other hand, the other two methods generated 65 and 81 false branches. Thus, both qualitative illustrations as well as results from quantitative experiments demonstrate the superiority of the new method in stopping false branches while missing no true branch.

Table 1 Average false branches by three curve skeletonization methods on the five airway phantoms at different levels of noise. None of the three algorithms missed any airway branches up to the 4th anatomic generation of tree.

Noise	Lee *et al.*	Palágyi *et al.*	our method
None	0.8	0	0
Low	4.4	3.8	0
Medium	9.2	14.2	0
High	12.8	17.4	0

Table 2 Comparison of false branch performance on ten original CT-derived human airway tree without down-sampling or addition of external noise.

#false branch	Lee et al.	Palágyi et al.	our method
Average	6.5	8.1	0.5
Std. dev.	4.4	4.7	1.1
Maximum	14	16	3

Computational Efficiency

Computational efficiency of our method was compared with Lee *et al*. and Palágyi *et al*.'s methods and, also, it was examined Bitter *et al.*'s method to assess the improvement by enabling multiple skeletal branch detection in one iteration. For this experiment, ten original CT-derived human airway tree (average image size: 368×236×495 voxels) without down-sampling, smoothing, or external noise were used. First, let us examine the relation between the computation complexity of our method and different tree-properties as discussed earlier. The average number of terminal branches observed in the tem airway trees used for this experiment was 121.7 and the average number of iterations required by

our algorithm was 7.1, which is close to $\log_2 N = \log_2 121.7 = 6.93$ and better than the observed average tree-depth of 11.6 which is close to $\sqrt{N} = \sqrt{121.7} = 11.03$.

The observed average computation time by different methods for these 10 airway trees are reported in Table 3. All the algorithms are implemented in C++ and have run on a PC with a 2.0GHz Intel CPU. Although, our algorithm is slower than Palágyi *et al.*'s, the computation time is comparable on the order of seconds, and it is significantly faster than the other two methods. Especially, the improvement in comparison to Bitter *et al.*'s algorithm, which falls under similar category to the new method, the improvement in computational complexity is very encouraging.

Table 3 Average computational time by different methods on airway trees.

Lee *et al.*	Bitter *et al.*	Palágyi et al.	our method
15.4 mins	21.1 mins	24 secs	82 secs

3.2.3 Discussion

A new robust and efficient curve skeletonization algorithm for 3D elongated fuzzy objects is developed using a minimum cost-path approach, which avoids spurious branches without requiring post-pruning. Results from three experiments have established the superiority of the new method as compared to the existing methods in terms of accuracy as well as robustness in detecting true and false skeletal branches. The new algorithm also makes a major improvement in computational efficiency in reducing the number of iterations from the number of terminal tree branches to the worst case performance of tree

depth. In fact, experimental results suggest that, on an average, the computation complexity is reduced to the logarithm of the number of terminal branches of a tree-like object.

3.3 Fuzzy Surface Skeletonization

In the early stage of my PhD research program, I developed a new fuzzy surface skeletonization algorithm that minimizes the binarization related data loss, especially suitable in medical image analysis. In this section, I will present the theories, major concepts, algorithms and experimental results related to fuzzy skeletonization. The new fuzzy skeletonization algorithm has been applied as the first step to skeletonize pulmonary vascular trees to generate a robust surface skeleton, and then, a conventional thinning algorithm is used to further produce the final curve skeleton of pulmonary vascular trees.

As described in the introduction section 1.2.3, literature of 3D skeletonization is quite rich for binary digital objects. However, the challenges of skeletonization for fuzzy objects are mostly unanswered. In this section, a framework and an algorithm for fuzzy surface skeletonization are presented using a notion of fuzzy grassfire propagation. Several concepts including fuzzy axial voxels, collision impact, and global significance factors are introduced. A skeletal pruning algorithm using global significance factors as significance measures of individual branches is developed. Results of application of the algorithm on several medical anatomy structures, as well as real-world objects have been illustrated. A quantitative comparison with an ideal skeleton has demonstrated that the algorithm can achieve sub-voxel accuracies at various levels of noise and down sampling. Finally, we demonstrate the role of fuzzy skeletonization in thickness and volumetric topological computation of fuzzy objects at relatively low resolution.

3.3.1 Theories and Algorithms

Blum's pioneering work on grassfire transform [65] led to the notion of skeletonization that converts a volumetric object into a union of surfaces and curves. However, the notion of skeletonization for fuzzy objects has not yet been defined. To define a fuzzy skeletonization process, we suggest modifying the Blum's grassfire transform for a fuzzy object where the membership function is interpreted as local material density so that the speed of grassfire at a given point is inversely proportional to its material density. Following this notion, it can be shown that fuzzy distance transform (FDT) [171] value at a point p is proportional to the time when the fire front reaches p. Therefore, during the fuzzy grassfire propagation, the speed of a fire front at a point equates to the inverse of local material density and this equality is violated only at quench points where the propagation process is interrupted. Based on the principle of fuzzy grassfire propagation, a *fuzzy quench voxel*, or fuzzy center of maximal ball in a fuzzy digital object is defined using equation (2.5) in Section 2.4.

During the process of fuzzy skeletonization, voxels are removed in the increasing order of their FDT values. The overall fuzzy skeletonization process is summarized in the following. Here, $O = \{p | \mu_O(p) > 0\}$ denotes the support of the fuzzy object $\mathcal{O}$.

```
Primary skeletonization:
select voxels p ∈ O in the order of FDT values
  if p is not a fuzzy axial voxel and its deletion preserves
  3D topology and 2D topology on mid-planes
     remove p from O, i.e., set μ_O(p) = 0
Final skeletonization:
select voxels p ∈ O in the order of FDT values
  if p is in two-voxel thick structure and its deletion
  preserves 3D topology and 2D topology on mid-planes
```

remove p from O, i.e., set $\mu_O(p) = 0$

select voxels $p \in O$ in the order of FDT values

if topologic and geometric features of p fail to agree and its deletion preserves 3D topology

remove p from O, i.e., set $\mu_O(p) = 0$

Skeleton Pruning:

Remove noisy branches with low global significance values.

This notion of primary and final skeletonization was simultaneously introduced by Saha *et al*. [96] and Sanniti di Baja *et al*. [172]. Saha *et al.* described it in 3D while Sanniti di Baja *et al.* presented the idea in 2D for a DT-based skeletonization algorithm.

Primary Skeletonization

Primary skeletonization is completed in three steps. After locating all fuzzy quench or skeletal voxels using equation (2.5), significant ones are screened and marked based on collision impacts in their neighboring voxels. This initial filtering step is essential in fuzzy skeletonization where a large number of skeletal voxels are generated by small fluctuations in membership values; see Figure 15c. The strategy for screening significant skeletal voxels plays an important role in capturing important geometrical features of a fuzzy object in its skeletal representation while ignoring small dents, protrusions, and fluctuations on membership values. In the last step of primary skeletonization, unmarked voxels are deleted if they preserve the 3D topology of the support of the fuzzy object as well as the continuity of skeletal surfaces.

A well-known challenge with skeletonization is that each small protrusion or dent on an object-boundary creates a noisy skeletal branch. This challenge is further intensified for fuzzy objects where each fluctuation in the membership value creates an extra skeletal branch. Thus, fuzzy skeletonization generates a large set of skeletal structures or quench

points many of which carry little information of object geometry. Therefore, it is imperative to filter out less significant or noisy skeletal points to produce an effective skeleton of a fuzzy object. Here, a new filtering algorithm is presented to remove noisy skeletal voxels using the digital collision impact $\xi_D(p)$ defined in the equation (2.9) in Section 2.6.

In our filtering algorithm, two topologically types of skeletal voxels, namely, *surface-* and *curve-quench voxels*, are identified and different filtering strategies are adopted based on their local properties (Figure 10(a,b)). A surface quench point is formed when two opposite fire fronts meet while a curve quench point is formed when fire fronts meet from all directions on a plane. In a digital space, surface-quench voxel is formed when two opposite fire fronts meet along x-, y- or z-direction and a curve-quench voxel is formed when fire fronts meet from all eight directions in xy-, yz-, or zx-planes. A voxel $p = (p_x, p_y, p_z) \in O$ is an *x-surface-quench voxel* if the following two conditions are satisfied for $p_{x-} = (p_x - 1, p_y, p_z)$, $p_{x+} = (p_x + 1, p_y, p_z)$, and $p_{x++} = (p_x + 2, p_y, p_z)$:

1) $FDT(p) > FDT(p_{x-})$,
2) $FDT(p) > FDT(p_{x+}) \vee \big(FDT(p) = FDT(p_{x+}) \wedge FDT(p) > FDT(p_{x++})\big)$.

The second condition enables the detection of two-voxel thick surface-like skeletal structures. To define a curve-quench voxel, let us first consider the formulation of the situation when fire fronts meet in the xy-plane through the candidate voxel serving as a cutting plane (see Figure 11). Curve quench voxels may form a 2×2 clique on the xy-plane. Let $P_{\text{xy}} = \{(p_x, p_y, p_z), (p_x + 1, p_y, p_z), (p_x, p_y + 1, p_z), (p_x + 1, p_y + 1, p_z)\}$ denote the 2x2 clique. Let $Q(P_{\text{xy}})$ denote the set of voxels within the 2x2 clique P_{xy} with their FDT value identical to that of p, i.e.,

$$Q(P_{xy}) = \{q \mid q \in P_{xy} \wedge FDT(q) = FDT(p)\}.$$

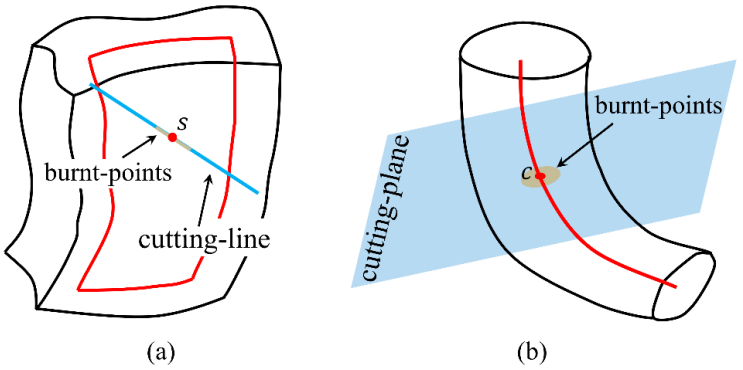

Figure 10 (a,b) Illustration of independent fire fronts meeting at surface-like (a) and curve-like (b) quench points.

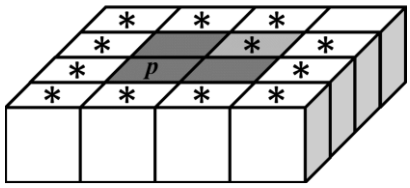

Figure 11 Formation of a curve-skeletal voxel p. The 2×2 clique $P_{xy}(p)$ on the xy-plane through p is shown in grey. The set of possible skeletal voxels $Q_{xy}(p)$ on the clique is shown with a darker gray shading. Fire-fronts simultaneously reach at all voxels in $Q_{xy}(p)$; thus, the FDT value at each voxel in $Q_{xy}(p)$ is equal to $FDT(p)$. Finally, p is a curve-skeletal voxel if and only if each voxel q on the xy-plane marked with a '*' is burnt prior to p, i.e., $FDT(q) < FDT(p)$.

Thus, the fire front reaches simultaneously at every voxel of $Q(P_{\text{xy}})$ from all directions on the xy-plane. Therefore, a voxel $p = (p_x, p_y, p_z) \in O$ is an *xy-curve-quench voxel* if the following condition holds – $\forall\, q \in M_{\text{xy}}(p) - Q(P_{\text{xy}})$, q is 26-adjacent to $Q(P_{\text{xy}})$ implies that $FDT(q) < FDT(p)$, where, $M_{\text{xy}}(p)$ is the set of all voxels constructing the xy-plane through p.

The significance of an x-surface quench voxel $p = (p_x, p_y, p_z)$ is determined as follow. First, for some $i, j \in \{-1,0,1\}$, the projected collision impact $M_p^{\mathrm{x}}(i,j)$ is computed on the xy-plane from the three voxels $q_{i,j}^{+} = (p_x - 1, p_y + i, p_z + j)$, $q_{i,j} = (p_x, p_y + i, p_z + j)$, $q_{i,j}^{-} = (p_x + 1, p_y + i, p_z + j)$ as follow:

$$M_p^{\mathrm{x}}(i,j) = \max\{\xi_D(q_{i,j}^{+}), \xi_D(q_{i,j}), \xi_D(q_{i,j}^{-})\}.$$

These projected collision impacts are averaged over each of the eight kernels $D_i \mid i = 1, \cdots, 8$; see Figure 12. An x-surface-quench voxel p is referred to as *x-significant surface-quench voxel*, if the averaged projected collision impact on any of the eight kernels is greater than a preset threshold. Finally, an object voxel p is referred to as a *significant surface-quench voxel* if it is an x-, y-, or z-significant surface-quench voxel. It may be noted in Figure 12 that an averaging kernel D_i contains exactly six voxels contributing to the average collision-impact and the voxels fall on one side of the central voxel.

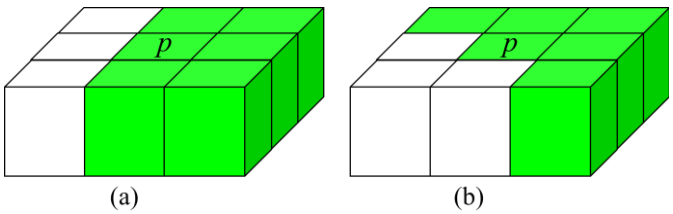

Figure 12 Geometric variations of the kernels used to compute the significance of surface skeletal voxels. The average collision-impact is computed over the green voxels.

An xy-curve-quench voxel $p = (p_x, p_y, p_z)$ is an *xy-significant-curve-quench voxel* if the highest collision impact on either of the two cliques $C_{\mathrm{z}}^{+} = \{(p_x + i, p_y + j, p_z + 1) \mid i, j \in \{-1,0,1\}\}$ and $C_{\mathrm{z}}^{-} = \{(p_x + i, p_y + j, p_z - 1) \mid i, j \in \{-1,0,1\}\}$ is

greater than a preset threshold. An xy-, yz-, or zx-significant curve-quench voxel is referred to as a *significant curve-quench voxel*. A significant surface- or curve-quench voxel is referred to as a *significant quench voxels* during primary skeletonization. For all experiments and results presented in this paper, a constant threshold value of $2/3$ was used to decide the significance of both surface- and curve-skeletal voxels.

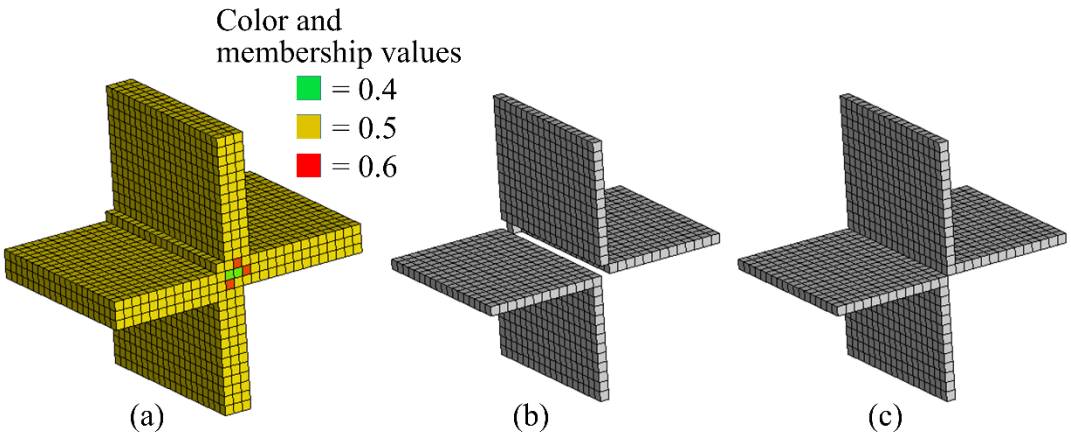

Figure 13 An example demonstrating the need for additional constraints of 2-D topology preservation on each of the three coordinate planes while deletion of individual voxels. (a) An original fuzzy digital object, and (b,c) computed fuzzy skeletons without (b) and with (c) the constraints of 2-D topology preservation.

Removal of a voxel $p \in O$ preserves the topology of O if and only if p is a (26,6) simple voxel [73] in O. Besides the constraints of 3D simple points/voxels, additional constraints of 2D topology preservation on each of the three coordinate digital planes passing through the candidate voxel are used to maintain the continuity of skeletal surface structures. A fuzzy object is illustrated in Fig. 8, where the additional 2D topology preservation is compulsory to stop the undesired drilling effect along the junction. It seems

that such situations may occur only for fuzzy objects and that is why the additional 2D topology preservation has not been investigated in the context of binary skeletonization.

Final Skeletonization

Final skeletonization converts two-voxel thick structures into one-voxel thick structures and it is completed in two steps. Intuitively, a voxel is two-voxel thick if its three non-opposite 6-neighbors are skeletal voxels and forms two-voxel thick surface across x-, y-, and/or z-direction [96]. During the first step, thick voxels are considered for erosion in the order of their FDT values. Specifically, a voxel satisfying two-voxel thickness along all three coordinate directions is deleted if it is a (26,6) simple voxel. A voxel satisfying two-voxel thickness along two directions, say x and y, is deleted if it is a (26,6) simple voxel and it preserves 2D topology in $M_{\mathrm{xy}}(p)$. Finally, a voxel satisfying two-voxel thickness along only one directions, say x, is deleted if it is a (26,6) simple voxel and it preserves 2D topology in both $M_{\mathrm{xy}}(p)$ and $M_{\mathrm{zx}}(p)$.

The second step of final skeletonization brings a new idea of removing voxels with contradicting topological and geometric properties. Specifically, simple voxels must appears at a surface edge or at a curve end. Therefore, a simple voxel is deleted if it fails to satisfy geometric properties of a surface edge or a curve end. For example, for Figure 14(a), the red voxels do not have two opposite 6-neighbors in background to satisfy the geometry of a digital surface. Similarly, for Figure 14 (b,c), the singleton simple voxels (red) are expected to appear at curve end; but, there is no plane where are isolated failing to satisfy the geometric property of a curve end.

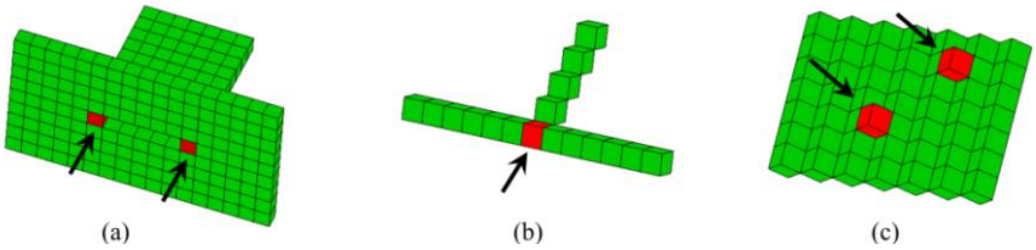

Figure 14 Examples of voxels with contradiction between their topological and geometric properties. Red voxels are simple voxels which may appear at surface edge (a) or at curve end (b,c). However, these voxels fail to satisfy the geometric properties of a surface edge or a curve end.

Skeleton Pruning

The goal of a skeleton pruning algorithm is to discriminate between significant and non-significant branches so that only false branches may be removed. This goal is accomplished by computing LSF-weighted length of an individual branch from its edge to the corresponding junction voxel. This LSF-weighted branch length is used as a global significance factor (GSF) of a specific skeletal branch. This overall process is implemented using the following steps – (1) digital topological analysis (DTA), (2) conversion of two-voxel wide curve-like structures into a true digital curve, (3) computation of GSF for all branches, and (4) removal of non-significant branches.

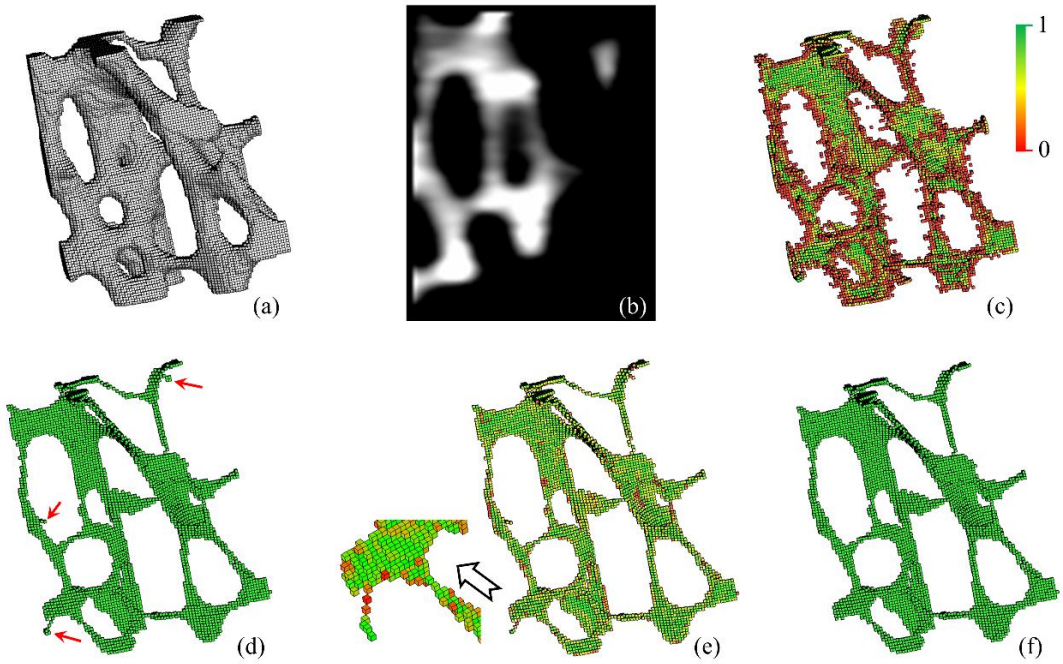

Figure 15 Results of intermediate steps of fuzzy skeletonization. (a) 3D display of trabecular bone region in a micro-CT image of a cadaveric distal tibia specimen. (b) A sagittal image slice displaying the fuzziness in the image. (c) All quench voxels before filtering with local significance measure. (d) Results of final skeleton; noisy branches are indicated by red arrows. (e) Results of local significance computation. (g) Final results after noisy branch pruning.

3.3.2 Experimental Results

Results of intermediate steps of steps of fuzzy skeletonization and pruning on a small region of trabecular bone are illustrated in Figure 15. Results of application of skeletonization and pruning of two other medical anatomic structures and several real-world 3D shapes, available online, are presented in Figure 16 and Figure 17, respectively. To generate fuzzy representations of online 3-D shapes, first, the images were downloaded and reconstructed at $256 \times 256 \times 256$ matrices and then down-sampled at $128 \times 128 \times 128$. For all these examples, the results of skeletonization and pruning are visually encouraging.

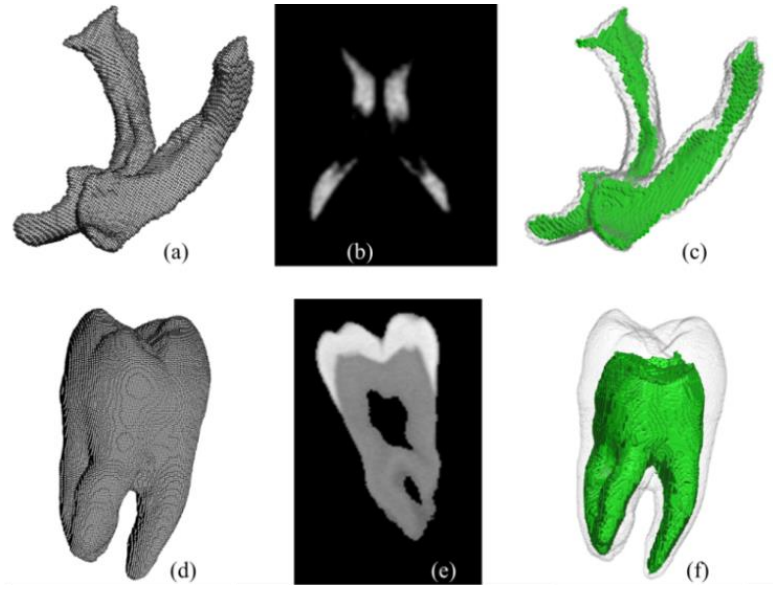

Figure 16 Results of application of fuzzy skeletonization on two anatomic structures fuzzy segmented from acquired images. (a) A part of cerebrospinal fluid segmented from human brain MR imaging. (b) An axial image slice illustrating the fuzziness and noise. (c) Surface rendering of the fuzzy skeleton. (d-f) Same as (a-c) but for micro CT data of a human tooth.

The accuracy of the new fuzzy skeletonization algorithm was examined at different levels of fuzziness and noise using computerized phantoms with known skeletons. We first generated 3D binary objects with their ground truth skeletons at high resolution. Test phantom objects were generated from those high resolution binary objects at different levels of fuzziness and noise using down-sampling and additive random noise. Finally, skeletonization errors were determined by comparing between computed and true skeletons.

Figure 17 Results of application of the new fuzzy skeletonization algorithm on two medical object and several 3-D shapes available online.

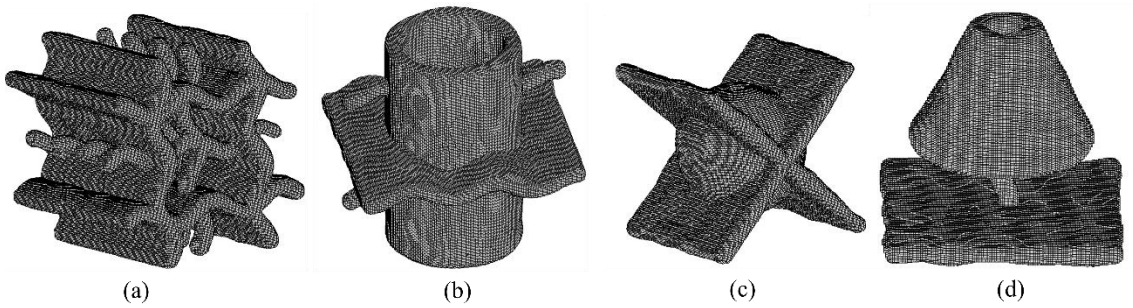

Figure 18 Illustration of computer-generated phantom shapes. Altogether seven phantom shapes were created and used for the accuracy experiment. Specifically, three instances of (a) and two instances (b) were generated by varying the parameters of the sine curves and surfaces.

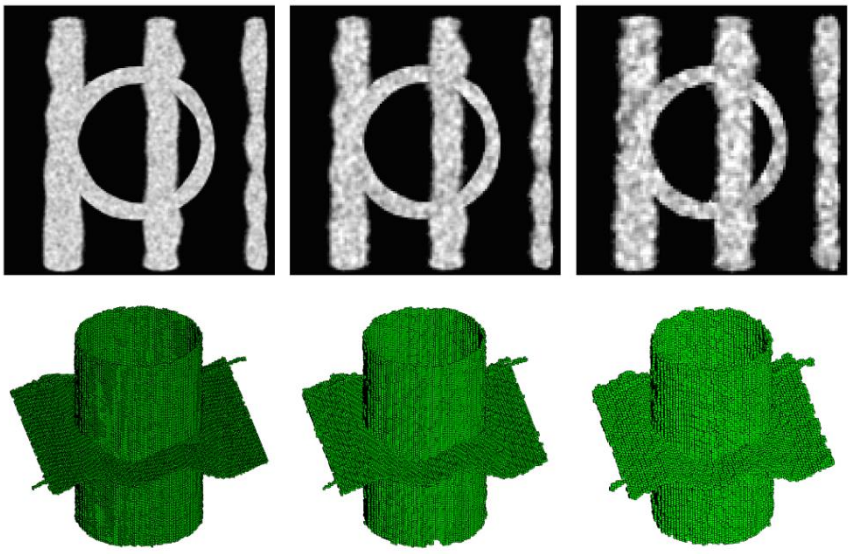

Figure 19 Results of fuzzy skeletonization on the phantom shape of Figure 18(b). Top-row: Axial image slices at the SNR of 24, 12 and 6 and the downsampling by three, four, and five voxels. Bottom-row: Results of fuzzy skeletonization of the phantoms from the top-row.

The high resolution image and true skeleton was generated by sampling an ideal skeleton in the continuous 3-D space R^3. Let S_{T} be the set of N_{T} number of sampled points; S_{T} is considered as the true skeleton. A Euclidean distance transform $DT_{\mathrm{T}}: Z^3 \rightarrow R^+$ is computed from S_{T}. To generate a binary object with non-uniform thickness value, a smooth thickness field $f_{\mathrm{thickness}}: Z^3 \rightarrow R^+$ is computed. Finally, the volumetric object is defined as the set of all voxels with its DT_{T} value less than or equal to the local thickness value$f_{\mathrm{thickness}}$. Seven high resolution binary objects with true skeletons were generated and used for this experiment; see Figure 18. Their original image was generated in a $500 \times 500 \times 500$ array, which were down-sampled by $3 \times 3 \times 3$, $4 \times 4 \times 4$, and $5 \times 5 \times 5$ windows to simulate different levels of fuzziness. Finally, the phantom objects were generated by adding white Gaussian noise at four levels of signal-to-noise ratio (SNR)—

noise-free, 24, 12, 6. See Fig. 12 for phantoms at different levels of down-sampling and noise together with their fuzzy skeletons. To quantitatively assess the accuracy of the algorithm, let $S_C^{l,\rho}$ denote the computed skeleton at the downsampling rate of l and the noise at SNR of ρ and let $N_C^{l,\rho}$ denote the number of voxels in $S_C^{l,\rho}$. The skeletonization error is computed by the following equation:

$$Error_{l,\rho} = \frac{1}{2N_{\mathrm{T}}} \sum_{p \in S_{\mathrm{T}}} \min_{q \in S_C^{l,\rho}} |p - q| + \frac{1}{2N_C^{l,\rho}} \sum_{p \in S_C^{l,\rho}} \min_{q \in S_{\mathrm{T}}} |p - q|. \qquad (3.9)$$

The average error for phantoms at each level of noise and down sampling is presented in Table 4. As shown in the table, the average error is less than a voxel and as shown by Saha *et al*. [192], the error of digitization is close to 0.38 voxel. Therefore, after deducting the digitization error, the performance of the fuzzy skeletonization algorithm even at the highest level of noise and downsampling is encouraging. Further, it is observed that, although, skeletonization errors increase with noise, the increase across a wide range of SNR is small. The primary reason behind this performance is that the new algorithm partially nullifies the effects of noise by integration of fuzzy membership values during path-propagation in fuzzy distance transform analysis. The observed effect of downsampling on skeletonization error is small. It should be noted that skeletonization errors were computed in the voxel unit of down-sampled images.

Table 4 Skeletonization errors at different levels of noise and downsampling.

Different downsampling	Different signal to noise ratio			
	noise free	SNR 24	SNR 12	SNR 6
3×3×3	0.54±0.15	0.57±0.14	0.59±0.15	0.63±0.15
4×4×4	0.56±0.06	0.57±0.07	0.58±0.07	0.60±0.09
5×5×5	0.53±0.10	0.56±0.07	0.57±0.07	0.59±0.08

Skeletonization has be popularly used for effective analysis of morphological features of local object structures including scale, orientation, topology, geometry etc [193-200]. Here, we present two applications of fuzzy skeletonization in thickness and volumetric topologic analysis (VTA) computation, which are demonstrated in Figure 20 and Figure 21. The basic principle of FDT-based thickness computation in [192] is adopted except the fact that fuzzy skeletonization is used instead of binary skeletonization. Here, FDT-based depth values are sampled along the skeleton of the target object; thus providing the regional thickness distribution over the object. Let S_{skeleton} denote the set voxels in the fuzzy skeleton of a fuzzy object $\mathcal{O}$ and let FDT give the fuzzy distance transform map. At each skeletal voxel $p \in S_{\text{skeleton}}$, its thickness value $\tau(p)$ is computed as twice the FDT value $FDT(p)$. Finally, thickness values at non-skeletal voxels are inherited from the nearest skeletal voxel by a feature propagation algorithm. The VTA computation followed the [184], except that the skeletonization step is replaced with the new fuzzy skeletonization. Results of thickness and VTA distribution shown in Figure 20 and Figure 21 are visually satisfactory.

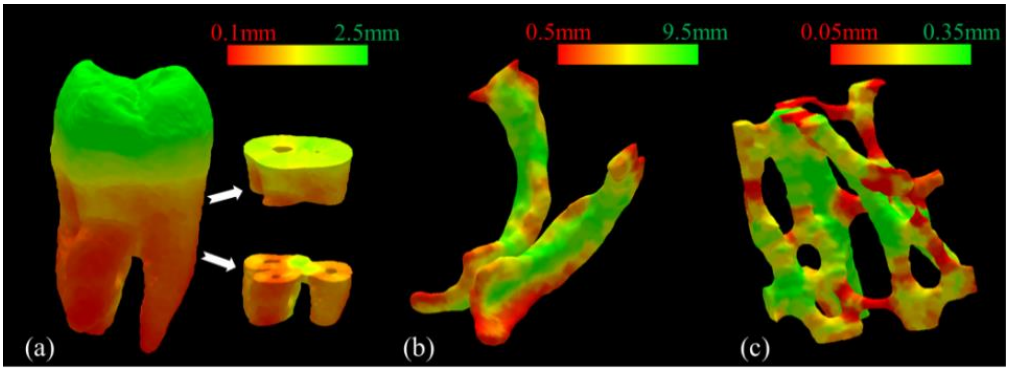

Figure 20 Results of local thickness computation for three anatomic objects using fuzzy skeletonization, FDT, and feature propagation.

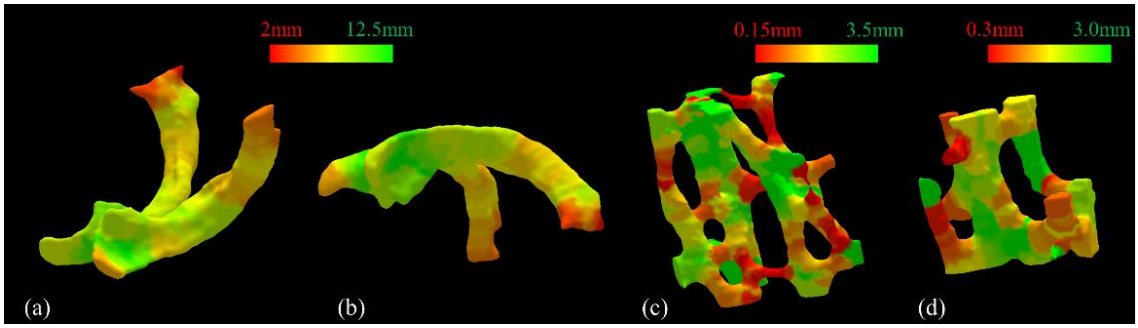

Figure 21 Results of VTA computation for two anatomic objects using fuzzy skeletonization. (a,b) are two different views of the cerebrospinal fluid; (c,d) are two small parts of the trabecular bone.

3.3.3 Discussion

A theoretical framework and a complete algorithm for fuzzy surface skeletonization is developed using a new notion of fuzzy grassfire propagation in this section. The process of fuzzy grassfire propagation is defined. Several new concepts including significant quench voxels, collision impact and global significance factors related to fuzzy skeletonization are introduced and their theoretical formulations are presented. A skeletal noise pruning algorithm using significance measures of individual branches is developed and its performance is demonstrated. From the results of application of the algorithm to several medical anatomic and real-world objects, we see the promising performance of the new algorithm for analyzing fuzzy objects. Therefore, we have applied it as the first step to skeletonize the pulmonary vascular tree, and followed by a conventional thinning algorithm to generate the curve skeletons of pulmonary vascular trees.

3.4 Conclusion

In this chapter, we presented two novel skeletonization methods: a curve skeletonization and a fuzzy surface skeletonization. The new curve skeletonization is

developed based on the minimum-cost path approach, which sequentially adds skeleton branches in the order of their significance as compared to conventional methods, where the entire skeleton is generated at once. This unique property of a minimum-cost path approach offers a natural hierarchical representation of a centerline tree and provides a robust performance in terms of noisy branch detection. Results from the experiments show that the curve skeletonization method generates accuracy curve skeletons for tree-like objects with robust performance in detecting true and false skeletal branches. It also makes a significant reduction in computation complexity by enabling detection of multiple new skeletal branches in one iteration. We will apply the new curve skeletonization to human airway. It generates the airway skeleton without false branches, which will automate the anatomic airway labeling algorithm. The anatomic labeled airway skeleton will also serve as a spatial anatomic system for further analysis of the regional arterial morphology and other lung metrics.

A theoretical framework for fuzzy surface skeletonization is developed using a new notion of fuzzy grassfire propagation. By introducing the concept of collision impact, surface- and curve-like skeletal points and global significance factors, the new method solves several challenges in the skeletonization of fuzzy objects. Experimental results have demonstrated high accuracy of computed fuzzy skeletons in the presence of significant down-sampling and noises. It has also been applied to several medical anatomic and real-world objects, where the new method shows promising performance for analyzing fuzzy objects. Therefore, we will apply it to generate the skeletons of pulmonary vascular trees, which are used in artery identifications and analysis.

CHAPTER 4

A SEMI-AUTOMATIC FRAMEWORK FOR QUANTITATIVE MORPHOLOGIC ASSESSMENT OF PULMONARY ARTERIES

4.1 Introduction

Characterization of arterial morphology are of great importance for early evaluation of the vascular role in pulmonary diseases. Currently, there is a great need for the standardization of a framework for arterial morphological assessment at different lung regions. In this chapter, we present a semi-automatic framework to segment pulmonary arteries at different anatomic airway branches and measure their cross-sectional area (CSA). The arterial CSA measures can be further standardized using the cross-sectional area of its associated airway branch to produce the standardized arterial measure $CSA_{standard}$, which will adjust for size-related variability in arterial morphology.

Pulmonary vascular dysfunction is gaining increased attention in regards to the role played in the development and progression of smoking associated parenchymal destruction (emphysema) [6, 10, 12, 15, 201]. Pulmonary arterial enlargement, measured using multi-row detector CT (MDCT) imaging, has recently been established to be an important predictor of functional lung decline and morbidity in COPD patients [10, 15]. Matsuoka *et al.* [14] reported decreased cross-sectional area of pulmonary peripheral vessels in patients with COPD in relation to increased emphysema and airway flow limitations. Alford *et al.* [201] showed that smokers with normal pulmonary function tests but with CT evidence of early emphysema demonstrate increased heterogeneity of perfusion compared with smokers showing no evidence of emphysema on CT. Using dual energy CT to assess regional perfused blood volume in the lungs, as a surrogate for perfusion, Iyer *et al.* [11]

has demonstrated that the heterogeneity is reversible with sildenafil. Results of these studies suggest that parenchymal heterogeneity may be related to vasoconstriction in regions of inflammation associated with local hypoxia, and upstream arterial enlargement may be related to peripheral vasoconstriction. Therefore, it becomes important to analyze pulmonary arterial morphology for early detection of pulmonary diseases, understanding their etiologies, and evaluating and monitoring treatment effects.

Early attempts of measuring pulmonary arterial morphology date back to the beginning of volumetric CT [202], but lacked a standardized framework for measuring arterial morphological metrics at different lung regions. Standardization of regional arterial metrics requires a robust approach of identifying matching pulmonary arteries in intra- and inter subject scans.

Major challenges toward this goal emerge from complex topology and geometry of pulmonary structures, especially due to the inter-linked presence of arteries, veins and airway with spatial adherence leading to fusion at limited resolution, and the anatomic variations of the airway and vessel, which are further enhanced by artifacts related to heart motion. These challenges limited the previous studies only to aorta or small peripheral vascular regions [10, 14, 15]. Few works have attempted to automatically segment the entire pulmonary arterial trees, but with limited results [154, 155]. Although the automated methods explored the unique pairing relationship between arterial and airway branches that is established by their spatial proximity and parallel configuration [203], they failed to achieve a high accuracy to locate the matching arterial branches due to anatomic complex and variable pairing patterns between airway and arteries [204-208]. Therefore, a method with efficient user interaction is more effective to accurately establish the pairing between

airway and arterial branches, which will be useful for cross-sectional and longitudinal research and clinical studies.

In this chapter, we present a semi-automatic method for segmentation and cross-sectional area (CSA) measurement of the pulmonary arterial branch associated to a specific segmental airway location. The arterial CSA measurement is standardized with the CSA of its associated airway branch to adjust for variabilities in subject size and lung inflations. The accuracy of the method was examined on MDCT scans of physical phantoms consisting of acrylic rods of different diameters placed at different angles. Also, the accuracy study was extended to examine the methods performance at different contrast concentrations. The method was applied to repeat-scan pulmonary MDCT images from 20 healthy subjects at functional residual capacity (FRC) and from another 20 healthy subjects at total lung capacity (TLC). The reproducibility of computed arterial metrics in repeat scans from six segmental airway locations in upper, middle and lower lobes was analyzed, and the results are reported. Also, the inter-user reproducibility of the arterial metrics was studied. Finally, distributions of arterial CSA measurements among normal population in different lung locations are presented.

4.2 Methods and Algorithms

The aim of our method was to develop an efficient semi-automatic tool for measuring pulmonary arterial morphology at different anatomic lung regions defined by the airway anatomic labels. This new tool provides artery measurements which are accurate, robust, and standardized by size-related variables and that will require limited user-interaction and can be translated to large cross-sectional and longitudinal studies. The method is based on the observation that airway and arterial branches has a unique pairing

that is established by their spatial proximity and parallel configuration [203]. Radiologists have long used this pairing as a means of identifying abnormal airway or arterial dimensions such as the "signet" sign, used to identify bronchiectasis [209]. Specifically, the method starts with user-specified end-points of a target arterial segment associated to a specific airway anatomic branch through a custom-built graphical user interface (GUI). Subsequently, the method computes the centerline joining two user-specified end-points of the target arterial segment; determines local structure orientation along the centerline; and computes CSA along the centerline after filtering out adjacent pulmonary structures, such as airway walls or veins. In this context, several new techniques are introduced, including collision-impact based centerline tracing, radial sample-line based CSA computation, and outlier analysis on the radial distance profile subtracting adjacent structures on the arterial boundary.

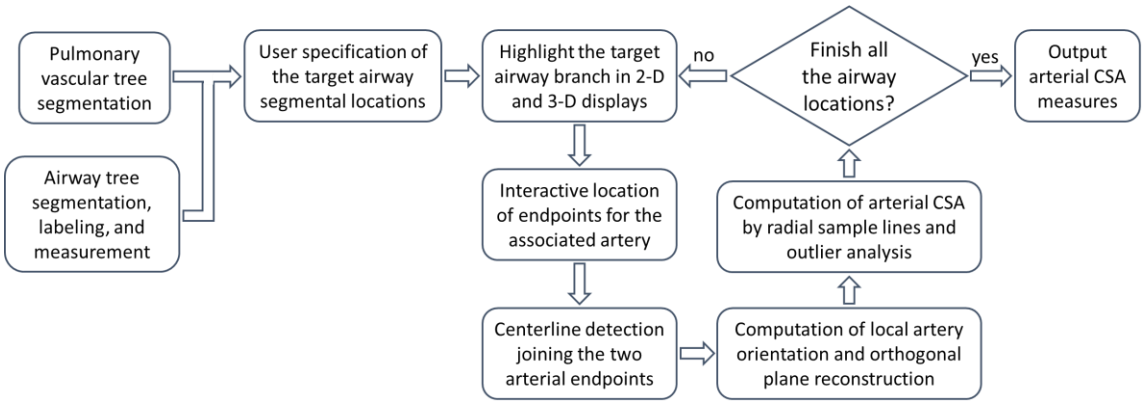

Figure 22 Overall work flow of the new semi-automatic method for computation of arterial CSA and $CSA_{standard}$ at anatomic airway branch locations.

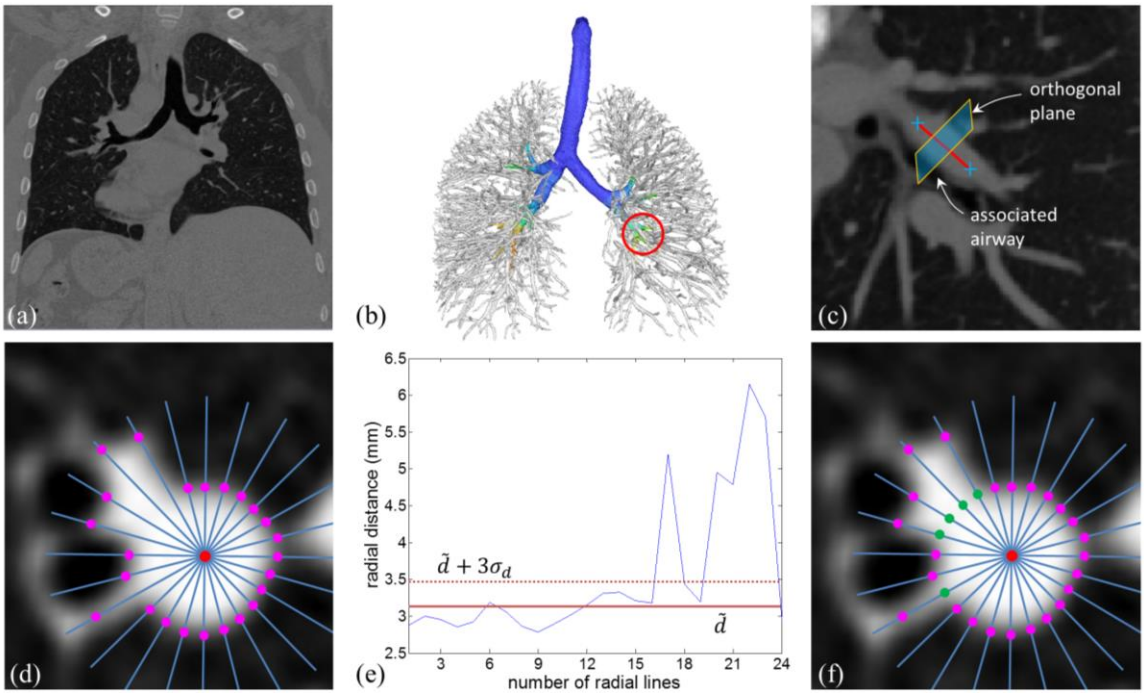

Figure 23 Schematic illustration of the working process of our proposed framework. (a) A coronal view of lung MDCT image, (b) segmented and labeled airway tree overlapped with segmented vascular tree, (c) a zoomed in coronal view of the CT image at the airway branch of LB9 and the user specified two arterial endpoints and the centerline joining them. (d-e) Illustration of the CSA computation with the outlier analysis based on a radial ample line approach on the orthogonal plane cut in (c). (d) 2D orthogonal plane with the initial edge locations determined using half-max criterion. Central point (red), example of 24 sample lines (blue), initial edge locations(pink); (e) outlier analysis of the radial distance distribution, which eliminated incorrect sample lines touching the adjacent structures; (f) new edge locations are marked in green.

4.2.1 Overall Workflows

Overall work flow of our method is illustrated in Figure 22. Theere are six major steps in the entire method—(1) segmentation of vascular structures from CT images [210]; (2) segmentation and labeling of the airway lumen from CT images [138, 142]; (3) GUI-based user-specification of two endpoints of the target arterial branch associated to a specific airway anatomic branch, e.g., RB1 , RB4, RB10, etc., (4) centerline computation

for the target arterial segment, (5) computation of local arterial orientation along the centerline, and (6) computation of arterial mrphological metrics after subtracting adjacent pulmonary structures. Results at interm,ediate steps are shown in Figure 23.

4.2.2 Vessel Segmentation

The method starts with segmenting pulmonary vascular structures from CT images (Figure 23 (b)). The initial segmentation results of pulmonary vascular tree is finished using Pulmonary Workstation 2.0 (VIDA Diagnostics, Iowa City, IA), which is based on vessel enhancement filtering and eigenvalue and eigenvector analysis by Shikata *et al.* [210]. Although, the segmentation method captures most visible vascular structures and preserves their topology, its spatial outlining of vascular volume is not satisfactory. Specifically, segmentation results using this method suffers from two major problems—(1) large portions of the vessel volume are missed; (2) airway walls are included in segmentation results. An example is shown in Figure 24 (a). To overcome this problem, we developed an intensity-constrained geodesic dilation to improve initial vessel segmentation results. The intensity-constraints are performed using a modified fuzzy distance transform analysis.

The geodesic dilation algorithm is designed such that initial vessel segmentation results are allowed to generously dilate inside the vessel region while arresting the dilation process at it attempts to enter inside the parenchymal or airway lumen regions, which have distinctly different intensities than vessels. The following cost function based on original CT values $I: Z^3 \rightarrow [-1000,3000]$ in HU unit.

$$cost(p) = \begin{cases} \epsilon, & \text{if } 0\text{HU} \leq I(p) < 400\text{HU}, \\ \epsilon + (1-\epsilon)\dfrac{|I(p)|}{400}, & \text{if } -400\text{HU} \leq I(p) < 0\text{HU}, \\ 1 & \text{othewise.} \end{cases} \tag{4.1}$$

In the above equation, the term ϵ is used to represent a small number; for our experiments, a value of 0.05 was used for ϵ. The CT range between 0 and 400HU is used for vessel intensity, while the range between -400 and 0HU is used for vessel transition region with airway lumen and parenchyma. At the positive side of the vessel intensity range no transition region is used as the interface tissue must be bone which is anatomically rare. A modified fuzzy distance transform, namely cost-based distance transform, is computed using the following algorithm:

Begin Algorithm: compute-cost-based-distance-transform

Input: support O of a fuzzy object O;

Initial vessel mask V_{orig};

Cost map $cost: \mathrm{Z}^3 \rightarrow R^+$;

A threshold thr_{cost} for the cost-based FDT map $FDT_{\text{cost}}: \mathrm{Z}^3 \rightarrow R^+$

Output: Corrected vessel mask V_{output}

$\forall p \in V_{\text{orig}}$, initialize the FDT value as $FDT_{\text{cost}}(p) = 0$

$\forall p \in O - V_{\text{orig}}$, initialize FDT value as $FDT_{\text{cost}}(p) = \max$

while the cost-based DT map FDT_{cost} is altering

$\forall p \in O - V_{\text{orig}}$, set $FDT_{\text{cost}}(p) = \min_{q \in N^*(p)} (FDT_{\text{cost}}(q) + \frac{1}{2}\big(cost(p) + cost(q)\big) \times |p - q|)$

set the output $V_{\text{output}} = \{p \mid p \in O \wedge FDT_{\text{cost}}(p) \leq thr_{\text{cost}}\}$

End Algorithm: compute-cost-based-distance-transform

The extended vessel mask V_{output} computed using the above algorithm properly fills the vessel volume without leaking into surrounding parenchymal or airway lumen regions, and thus, overcomes the 1st problem of shikata *et al.*'s method. However, V_{output} may still include some airway wall regions. To solve this problem, another constant geodesic dilation of airway lumen mask V_{air} is computed, and the airway walls, wrongly included in vessel segmentation, are excluded. An example of improved vessel segmentation results is shown in Figure 24 (b). It should be clarified that, due to intensity

similarity, it is difficult to automatically separate the arteries and veins in non-contrast CT. Therefore, the whole vascular structure, including both arteries and veins, is used in our algorithm.

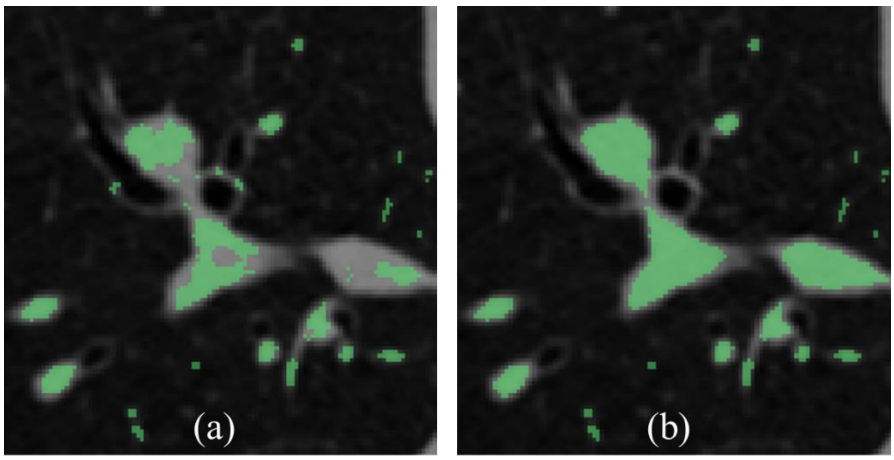

Figure 24 A 2D example of the initial (a) and improved (b) vascular segmentation results.

4.2.3 Airway Segmentation and Labeling

Beside the segmentation of pulmonary vascular structures, the airway tree is also segmented and anatomically labeled from CT images using Pulmonary Workstation 2.0 (VIDA Diagnostics, Iowa City, IA) [138, 142], which is based on the fuzzy connectivity segmentation [211-213] and the theories of finding the maximum clique in the constructed associate graphs [147] (Figure 23 (b)). In contrast to the geometric and topologic complexity of vascular structures, the airway trees possess simpler and more consistent branching patterns and standardized anatomic nomenclatures that are available up to segmental and subsegmental levels [203]. Therefore, segmental and subsegmental airway branches are used to define an anatomic spatial reference system to measure and analyze

regional arterial morphology and other lung metrics. This anatomic reference system benefits the regional analysis of different lung metrics in cross-sectional as well as longitudinal studies.

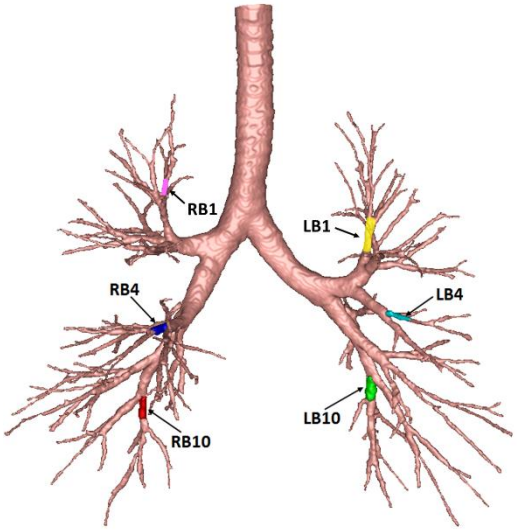

Figure 25 Automated labelling of six airway segmental branches from a lung CT image using Pulmonary Workstation 2.0 (VIDA Diagnostics, Iowa City, IA).

4.2.4 User-specification of Target Arterial Endpoints

The anatomically labeled airway tree, generated during the preprocessing step, serves as a reference for an user to identify the matching arterial segment associated to a specific airway branch. Topology and geometry of pulmoanry vascular trees are non-specific and complex, which are contributed by various factors including artery and verin fusion and their intensity-based non-separability, wide variability in arterial and veinous tree branching patterns as well as heart motion. Although, the spatial pairing between airway and arterial branches are anatomically established facts, variability in arterial branching patterns, complex spatial interaction and intensity based non-separatibility

between arteries and veins adds great challenges to an automatic airway-artery branch pairing algorithm. In general, there is a paired relationship between airway and arterial branches, but varying geometric and topologic patterns of the paired airway-artery relationship also exists [204-208]. Moreover, in several instances, veins come close to an airway branch and may also run parallel for some length. All these factors makes it difficult to fully automatically and accurately identify the matching arterial segment associated to a specific airway branch. For example, the accuracy of an automatic method for the artery identification from the associated airway branches studied in the next 5.3.1 was 83%. These results were observed in TLC scans, but results in FRC scans may be worse.

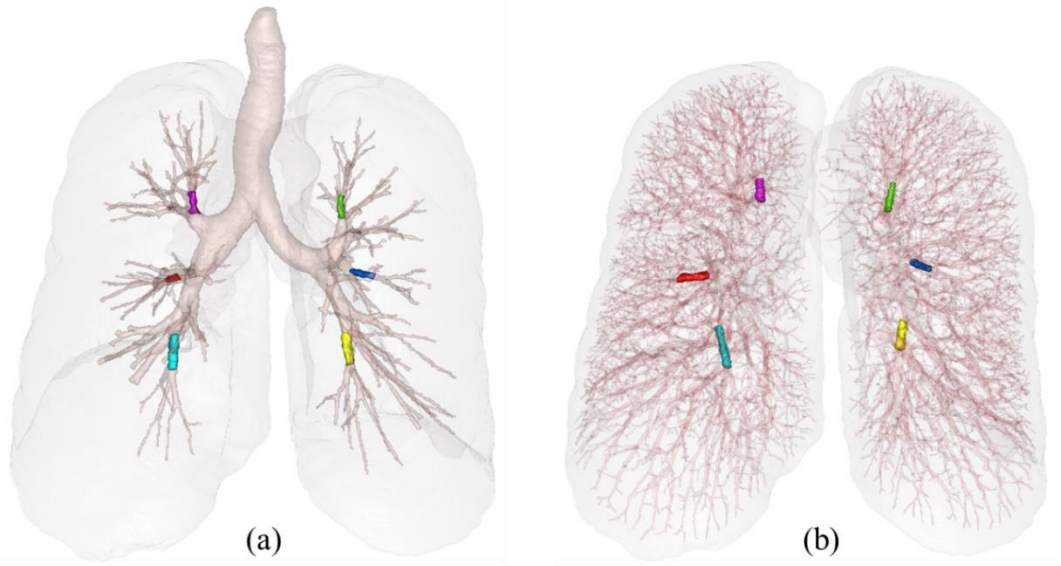

Figure 26 A 3D view example of the matching artery segments (b) with six associated airway segmental branches (a).

To overcome the above difficulties and deliver a method that is accurate and suitable for large studies, we developed an algorithm that uses a limited user interaction

through a custom-designed efficient GUI. Specifically, it works as follows—(a) the user indicates the specific branch label, (2) the algorithm provides a 2-D and 3-D inter-linked smart graphical display of the target airway branch and surrounding structures with navigation facilities, and (3) the user locates and inputs the two endpoints of the associated arterial segment using mouse clicks. The algorithm performs the remaining tasks fully automatically and reports the arterial measures associates to the specific airway branch. For example, if a user specifies RB10 as the target airway branch, the GUI will highlight the specific airway branch in yellow in the 3D display and moves the 2-D navigation cursor to the middle of the branch. Then, an expert user would navigate through the slices to identify the matching arterial segment associated with this specific airway branch. In some cases, the user may need to trace back several generations or even to the main pulmonary artery to locate the true arterial branch near the target airway branch. Next, the user places the two endpoints using mouse clicks indicating the beginning and the end of the associated arterial segment. The algorithm automatically triggers the rest of the steps to finish the computation of arterial morphology at this specific airway location. Figure 29 (c) shows a coronal view of the CT image at the airway branch of LB9 (highlighted by yellow) and the user specified two arterial end-voxels (colored in black). Figure 26 gives a 3D view of the matching artery segments with six associated airway segmental branches.

4.2.5 Tracing of Arterial Centerline

The objective of this step is to compute the centerline of the target arterial segment specified by two user-indicated endpoints. To achieve this goal, a minimum-cost path or minimal path approach [128, 214] was adopted. A conventional minimal path approach may come close to object boundaries or may cut corners at sharp boundaries and junctions.

Therefore, it is necessary to impose local morphological features into the step cost function for path propagation to impose the centeredness constraint in minimal paths. Here, a unique measure of collision impact, introduced in 2.6, was used in the cost function to assure the centeredness feature in minimal paths. Collision impact generates a high value of '1' along the centerline of elongated structures, and small values elsewhere. Based on the gradient map of the fuzzy distance transform [171] of the vascular structures, collision impact at a given object voxel p in CT image, denoted by $\xi_{\mathrm{v}}(p)$, is defined as follow:

$$\xi_{\mathrm{v}}(p) = 1 - \max_{q \in N_{26}^{*}(p)} \frac{f_{+}\left(FDT_V(q) - FDT_V(p)\right)}{\frac{1}{2}\left(f_{\mathrm{ct}}(p) + f_{\mathrm{ct}}(q)\right) \times |p - q|}, \tag{4.2}$$

where $FDT_V(\cdot)$ give the fuzzy distance transform of the vascular structures, $f_{\mathrm{ct}}: Z^3 \rightarrow [0,1]$ is the vessel membership function in the CT image. Collision impact map inside a vascular structure is illustrated in Figure 27(b). As observed in the figures, voxels in the central region of a shape get high values (bright), while other voxels get low values (dark).

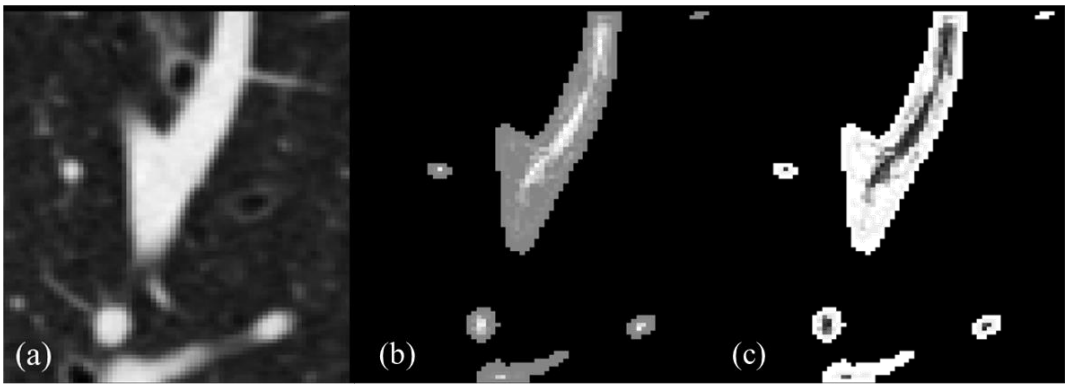

Figure 27 Illustration of the collision impact and step-cost functions on a small region in a 2-D coronal view of a pulmonary CT image. (a) A small region from an original CT image slice. (b) Collision impact values. (c) Path cost functions.

The collision impact measure is used to define the centered path cost as follows. A path π is an ordered sequence of voxels where every two successive voxels are 26-adjacent, i.e., $\pi = \langle p_0, p_1, \cdots, p_{l-1} \rangle$ where $p_{i-1}, p_i \in Z^3$ are 26-adjacent for every $i = 1, \cdots, l-1$. Total path cost is defined by adding the costs of individual discrete steps between every two successive voxels on the path. Finally, the minimal path between any two voxels p, q is computed by identifying the path with minimum path cost among all possible paths between the two voxel p, q. Minimum paths are computed using a dynamic programming or fast marching algorithm [174].

The effectiveness of a minimal path approach depends on the quality of the underlying step-cost function used in defining path cost. The *step-cost function* of a discrete step between two 26-adjacent voxels $p, q \in Z^3$ is defined as follows:

$$cost(p,q) = \frac{|p-q|}{\epsilon + \left(\text{average}\left(\xi_v(p), \xi_v(q)\right)\right)^n}, \tag{4.3}$$

where the parameter ϵ is a small number used to overcome numerical computational difficulties. A constant value of '0.01' is used for ϵ in this thesis. The parameter n determines the trade-off between smoothness and medialness of a path. Often, the value of '2' for n produces good centerline results. Results of the step-cost map are illustrated in Figure 27 (d). See Figure 29(b) for the arterial centerline detection results at the airway branch of RB10 on a CT data.

4.2.6 Computation of Arterial Morphological Measures

After the computation of the arterial centerline, local CSA along the centerline is computed as follows. First, a smooth representation of the arterial centerline is computed using polynomial curve fitting, and the arterial orientation at a specific point on the

centerline curve is computed as its tangent direction. Then, at each centerline point , the cross-section representation of the target vessel together with other adjacent structures is reconstructed using a tri-linear interpolation algorithm [215, 216] (Figure 23 (d)). At a specific location, the arterial CSA is computed from the cross-sectional vessel representation as follows. On the cross-sectional plane, radial sample lines emanating from the centerline point at a uniform angular distribution are used to compute the arterial boundary and CSA. Along a specific sample line, initial vessel boundary is located at the points with the fastest intensity change, i.e., the largest negative first-order derivative on the intensity profiles. Results of edge location along a vessel diameter is shown in Figure 28. Results of initial edge locations on cross-section vessel planes are shown in Figure 23 (d) and Figure 29(c).

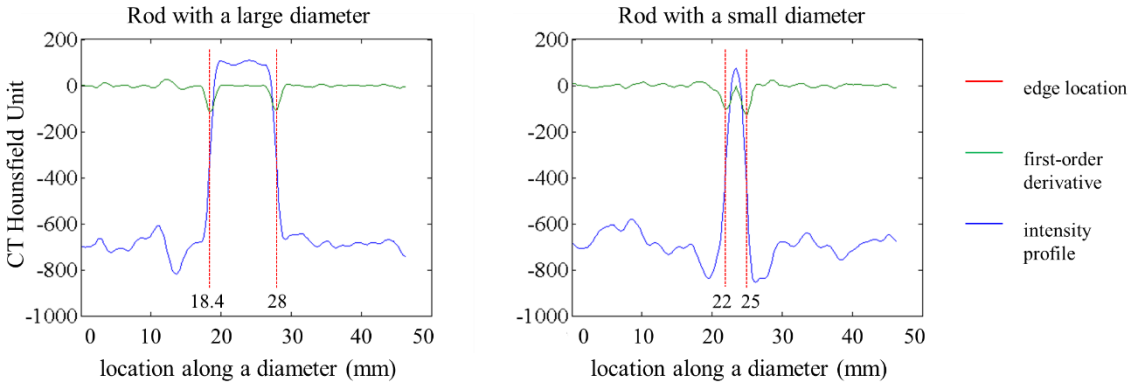

Figure 28 Edge locations along a vessel diameter consisting of two opposite sample lines. The steepest fall on the intensity profile along a sample line is located at the point with the largest negative first-derivative of CT intensity. Results for rods with both large (left) and small (right) diameters are shown.

Initial edge locations computed as above represent the boundary of the targeted vessel along with other neighboring structures, e.g., airway walls and veins. The aim of the next step is to eliminate the influence of adjacent neighboring structures from the initial computed boundary and compute corrected edge location that exclusively represents the vessel boundary, only. This task is accomplished using outlier analysis on radial distance distribution of initial edge locations.

Let, $d_1, d_2, \cdots, d_N$ denote the radial distance of the initial edge locations. It is assumed that at least half the arterial boundary is free from neighboring structures. Thus, the median of the radial distance values is used as the reference radius of the arterial CSA and the standard deviation of arterial radii is computed as follows. Let $\tilde{d}$ denote the median radial distance, and $d_1, d_2, \cdots, d_{n_{\tilde{d}}}$ denote the initial radial distance measures which are smaller than $\tilde{d}$, i.e., $\forall 1 \leq i \leq n_{\tilde{d}} \;\; d_i \leq \tilde{d}$. The standard deviation σ_d is computed as follows:

$$\sigma_d = \sqrt{\frac{1}{n_{\tilde{d}}} \sum_{i=1}^{n_{\tilde{d}}} \left(d_i - \tilde{d}\right)^2} \,. \tag{4.4}$$

During outlier analysis, an edge point at a radial distance greater than $\tilde{d} + 3\sigma_d$ is considered as a non-vessel or incorrect boundary point; others are considered as correct vessel boundary points. The incorrect vessel boundary point on a sample line is replaced by a new point at a radial distance computed by interpolating the two nearest correct boundary points one from each side of the sample line. Corrected vessel boundary points in Figure 23(f) are shown with green dots. Also, Figure 29(d,e) illustrates the performance of vessel boundary correction on a lung CT data. After outlier correction, the CSA is computed using the polygonal representation of vessel boundary. Finally, the CSA of a

target arterial segment is computed by averaging CSA measures over the middle half of the arterial centerline computed from user-specified endpoints.

In order to reduce the influence of size-related factors in CSA measures, the arterial CSA was standardized by CSA of the matching airway branch. CSA of an airway branch was computed over the region including both airway lumen and airway walls using Apollo pulmonary workstation software (VIDA Diagnostics, Coralville, IA). Standardized arterial CSA will be denoted as $CSA_{standard}$.

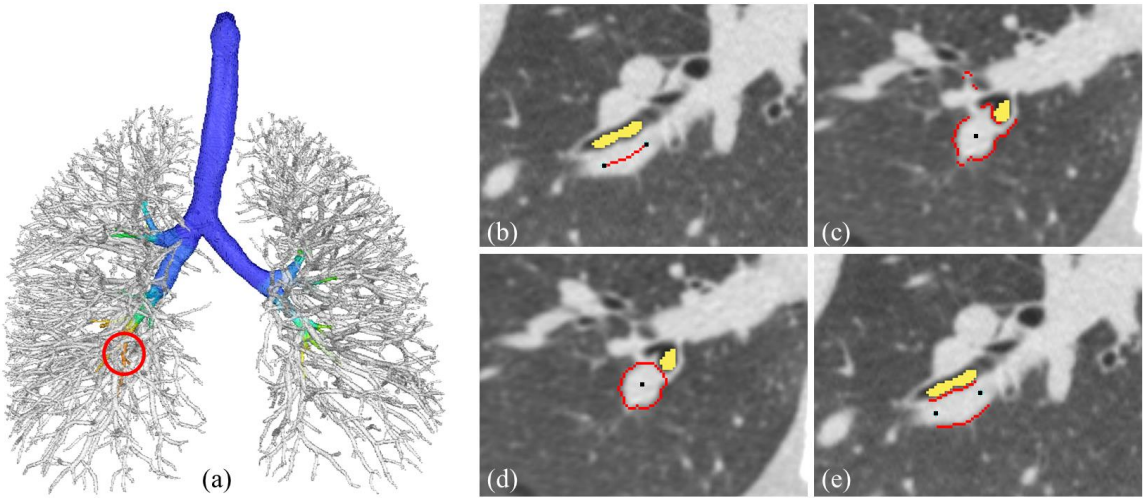

Figure 29 Example of the intermediate results of the arterial centerline tracing and its CSA computation using proposed method at the airway branch of RB10 (a). (b) Coronal plane of the user specified two arterial end-voxels with the minimum-cost path connecting them; (c) the initial edge locations in the transverse plane determined using derivative based criterion; (d,e) the new edge locations after outlier analysis of the radial distance in the transverse (d) and coronal (e) plane.

4.3 Experimental Plans and Methods

To evaluate the effectiveness of the new semi-automatic method, the accuracy and stability of the arterial CSA measure were examined using MDCT imaging of physical

phantoms. Repeat-scan and inter-user reproducibility of arterial CSA and $CSA_{standard}$ measures were tested from *in vivo* MDCT lung images of healthy human subjects. Finally, mean, variation, and range of $CSA_{standard}$ were determined at different lung regions at different stages of a respiratory cycle, e.g., FRC and TLC. Experimental details are described in the following.

4.3.1 Accuracy and Stability using Physical Phantoms

Physical phantoms consisting of acrylic rods were used for this experiment. Acrylic rods were chosen because the HU of acrylic is similar to that of vessel wall or lumen. Three customized phantom plans were designed. Each plan included the same set of five acrylic rods with known diameters (3.11, 4.85, 6.35, 7.96, and 9.55 mm) covering the range of arterial diameters at segmental levels. The rods were buried in dried potato flakes simulating the texture of lung parenchyma in CT imaging. The first plan was designed to test the methods performance at different structure orientation relative to scan direction. In this plan, five acrylic rods were aligned in parallel at a predefined angle with the scan axis. Five scans were acquired with rods positioned at 0, 22.5, 45, 67.5 and 90 degree angles with the scan axis, respectively. A total of 25 CSA measurements were obtained from the five CT scans under the first plan.

The second and the third phantom plans were designed to test the accuracy of CSA computation in the case of airway and vein touching, respectively. In the second plan, tygon tubes and acrylic rods to simulate airways and arteries. Five pairs of rods and tubes of varying sizes were used in a single scan. Specifically, rods with diameters 3.11, 4.85, 6.35, 7.96, and 9.55 mm were paired with tubes of inner and outer diameters (2.38, 3.97), (3.17, 4.76), (4.67, 6.35), (4.67, 7.75), and (6.35, 9.53), respectively, to roughly simulate the

human artery airway pairing size at segmental levels. Three phantom scans were acquired in this plan to simulate different airway touching patterns, namely orthogonal, inclined and parallel. For each scan, five rods (arteries) of different diameters were positioned roughly along the scan axis and a pairing rubber tube was placed on each rod to simulate a specific airway touching pattern. See Figure 30 for CT scans of three different airway touching pattern for one pair of rod and tube. The third phantom plan was similar to the second plan except that two acrylic rods of similar size were used to simulate a touching vein on an artery. CT scans of three different airway touching pattern for one pair of rods is shown in Figure 30. A total of 15 CSA measurements were collected under each of the second and third phantom plans. True CSA of an individual rod was determined by measuring its diameter using a digital caliper. Average of the readings at three locations inside the central 1 cm region of a rod was used as the measure of its diameter.

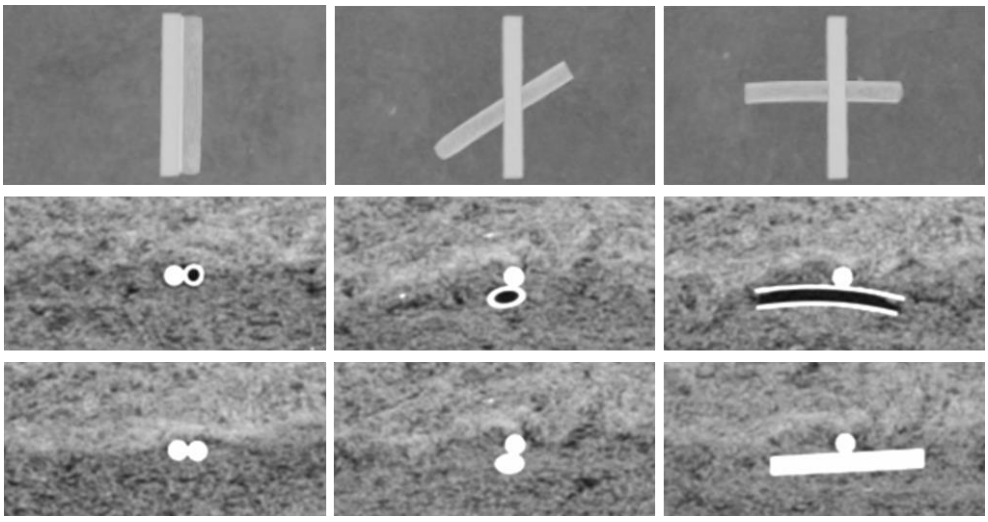

Figure 30 Illustration of the touching conditions in physical phantoms of a middle sized acrylic rod simulating artery and airway wall or vein touching in practice. Top row: MIP images from the coronal view; middle row: airway wall touching condition from a transverse view; bottom row: vein touching condition from a transverse view.

Physical phantoms in these three phantom plans were imaged on a third-generation, dual-source, dual-energy 192-slice MDCT scanner (SOMATOM Force CT scanner, Siemens, Forscheim, Germany) at the University of Iowa Comprehensive Lung Imaging Center. Scan protocol: single source, spiral non-contrast scan at 120 kVp, 100 effective mAs, 1 sec rotation speed, 1.0 pitch factor. Images were reconstructed at a voxel size of $0.5 \times 0.5 \times 0.6$ mm^3 with a non-iterative reconstruction algorithm using Qr40 kernel. The central 1 cm region of each acrylic rod was used for CSA computation.

Another physical phantoms experiment was designed to examine the stability of CSA computation under different CT contrast densities. For this purpose, bendable straws were filled with the iodine contrast agent (ISOVUE-370) at a known density to simulate pulmonary vessels. CSA was computed from virtual non-contrast (VNC) images obtained from dual-energy CT (DECT) decomposition, where iodine is virtually subtracted from the original contrast-enhanced DECT image creating an unenhanced image. Straws of two different diameters were used for this experiment, and two straws were used for each diameter size. The long end of each bendable straw was sealed with hard glue, and the contrast agent was injected from the other end. The straw was bent and placed in a bed of dried potato flakes with the long end horizontal and parallel to scan axis, while the short end faced upward to hold the liquid. Five scans were acquired using different contrast densities attained by mixing iodine agents with water at 0HU, 150HU, 250HU, 400HU and 800HU. A total of 20 CSA measurements were collected in this experiment.

The same CT scanner was used for the stability experiment. Scan protocol: dual-source, dual-energy DECT scans at 150 Sn-kVp and 80 kVp, 110 mAs include both X-ray tube current. Images were reconstructed at a voxel size of $0.5 \times 0.5 \times 0.6$ mm^3 with a non-

iterative reconstruction algorithm using Qr40 kernel. Virtual non-contrast (VNC) images were generated with three material decomposition software from Siemens (Syngo.Via) which estimates and subtracts the iodine content from the mixed CT image. The central 1 cm region of each straw was used for CSA measurement.

4.3.2 Repeat-scan Reproducibility

Reproducibility of the arterial CSA and $CSA_{standard}$ measures at FRC and TLC status was examined using repeat MDCT scans of normal non-smoker human subjects. Forty healthy non-smokers (age: 20-64 Yrs, mean: 28.9 Yrs; 22 female) were recruited from a previous repeatability study, which was approved by the University of Iowa Institutional Review Board and all participants provided written informed consent. Among them, 20 subjects (age: 20-54 Yrs, mean: 28.4 Yrs; 12 female) were scanned repeatedly at FRC status with a time gap of 3–5 mins. The other 20 subjects (age: 21-64 Yrs, mean: 29.5 Yrs; 10 female) were scanned repeatedly at TLC status with a similar time gap.

The scans were acquired on a second-generation, dual-source, dual-energy 128-slice MDCT scanner (SOMATOM Definition Flash CT scanner, Siemens, Forscheim, Germany) at the University of Iowa Comprehensive Lung Imaging Center. Scan protocol: single source, spiral non-contrast scan at 120 kVp, 200 effective mAs, 1 sec rotation speed, 1.0 pitch factor. Images were reconstructed with 0.5–0.6 mm in-plane, 0.5/0.75-mm slice thickness/interval using B35f medium-soft kernel for image reconstruction; (2) a single-source spiral non-contrast volumetric CT scan at FRC with 0.5–0.6 mm in-plane, 0.5-mm slice thickness using B35f medium-soft kernel for image reconstruction. A total of 40 FRC and 40 TLC lung CT images were used to determine repeat-scan reproducibility of the method. For each lung CT image, artery CSA and $CSA_{standard}$ measures were computed at

six segmental airway branches—RB1, RB4, RB10, LB1, LB4 and LB10. The intra-class correlation coefficient (ICC) was reported as the measure of the reproducibility.

4.3.3 Inter-user Reproducibility

The inter-user reproducibility of the arterial CSA measurement method was examined by comparing the arterial CSA results from two mutually-blinded trained users. Each of the 40 subjects mentioned in Section 4.3.2, went through three chest CT scans including one TLC and one FRC; 20 of them had repeat TLC and others had repeat FRC scans. The 40 FRC and 40 TLC non-repeat chest CT scans were used to determine inter-user reproducibility. For each CT image, the arterial CSA measures were also computed at six segmental airway branches—RB1, RB4, RB10, LB1, LB4 and LB10 using interactive inputs from two users, and the ICC of the measurements was computed.

4.4 Results

4.4.1 Accuracy and Stability

Results of the accuracy experiment are presented in Table 5 to Table 7. In these tables, errors are expressed in terms of diameter length instead of CSA for better appreciation of the error range. Table 5 summarizes the accuracy of CSA computation under varying scan angles. The average error was estimated as the root-mean-square-error (RMSE). The error bias and the average error values are given for all scanning angles at a given rod size (bottom row), as well as for all rod sizes at a given scanning angle (right-most column). Table 6 summarizes the results of CSA computation accuracy under different conditions of simulated airway touching, while Table 7 presents the results under

different touching conditions of veins. Results of stability of CSA computation under different contrast densities are shown in Figure 31.

Table 5 Computed CSA errors (mm) in terms of diameter at different scan angle.

True diameter	Scan angle					RMSE
	0°	22. 5°	45°	67.5°	90°	
9.55 mm	0.045	0.051	0.043	0.049	0.023	0.043
7.96 mm	0.032	0.043	0.044	0.059	0.020	0.042
6.35 mm	0.009	0.004	0.021	0.016	0.050	0.026
4.85 mm	0.011	0.026	0.022	0.011	0.028	0.021
3.11 mm	0.107	0.063	0.038	0.108	0.116	0.092
RMSE	0.054	0.043	0.035	0.060	0.059	0.051

Table 6 Computed CSA errors (mm) in terms of diameter error at different simulated conditions of airway touching.

True diameter	Airway touching conditions			RMSE
	Parallel	Inclined	Orthogonal	
9.55 mm	0.003	0.089	0.079	0.053
7.96 mm	0.004	0.082	0.082	0.052
6.35 mm	0.044	0.070	0.019	0.038
4.85 mm	0.044	0.059	0.039	0.037
3.11 mm	0.057	0.091	0.089	0.062
RMSE	0.038	0.079	0.067	0.064

Table 7 Computed CSA error (mm) in terms of diameter error at different simulated conditions of vein touching.

True diameter	Vein touching conditions			RMSE
	Parallel	Inclined	Orthogonal	
9.55 mm	0.014	0.083	0.042	0.042
7.96 mm	0.008	0.014	0.034	0.017
6.35 mm	0.011	0.008	0.011	0.008
4.85 mm	0.075	0.057	0.030	0.044
3.11 mm	0.012	0.101	0.112	0.068
RMSE	0.035	0.064	0.057	0.054

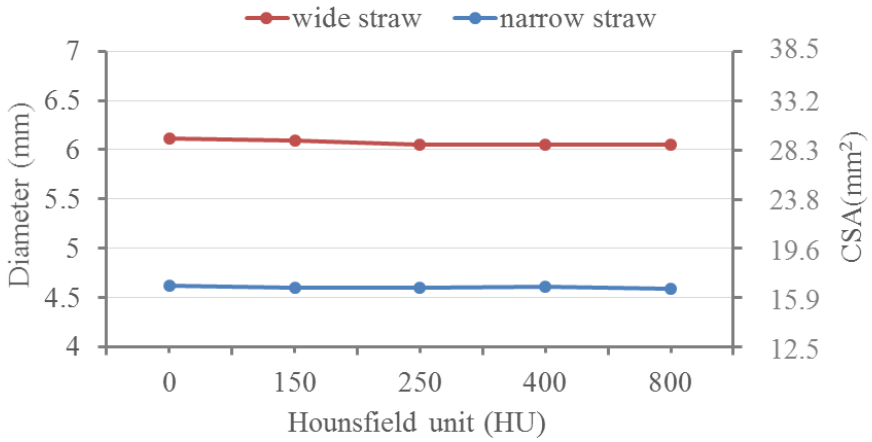

Figure 31 The stability of computed CSA values under different contrast densities. Computed CSA values at different values of iodine contrast density are shown for a narrow (blue) and a wide (red) straws. The maximum change in CSA computation in terms of the diameter over the entire range of contrast density is 0.07 mm and 0.03 mm for large (red) and narrow (blue) straws, respectively.

4.4.2 Repeat-scan Reproducibility

CT data of twenty subjects with repeated FRC scans and twenty subjects with repeated TLC scans were used for reproducibility analysis. As discussed in Section 4.2.4, among the twenty subjects, some of the arterial CSA measurement may not be computed

due to inconsistent anatomic pairing patterns, extremely short segments or the non-contrast CT imaging natures, such as image noise, heart motion, etc. The number of subjects used in the repeat scan reproducibility studies was shown in Table 8. For reproducibility analysis, three measurements: arterial CSA, airway CSA and arterial $CSA_{standard}$, were examined, and their ICC values at different lung regions are summarized in Table 9 and Table 10.

Table 8 Subject number in repeat-scan reproducibility analysis at FRC and TLC.

	Valid subject numbers (N=20) (percentage number)					
	RB1	RB4	RB10	LB1	LB4	LB10
FRC scans	13 (65%)	12 (60%)	17 (85%)	9 (45%)	14 (70%)	19 (95%)
TLC scans	12 (60%)	12 (60%)	19 (95%)	14 (70%)	16 (80%)	15 (75%)

Table 9 ICC values of computed CSA measures from repeat FRC CT scans.

	Airway segmental locations					
Measurements	RB1	RB4	RB10	LB1	LB4	LB10
Arterial CSA	0.94	0.98	0.98	0.95	0.81	0.95
Airway CSA	0.95	0.98	0.99	0.90	0.94	0.96
Arterial $CSA_{standard}$	0.90	0.98	0.93	0.87	0.76	0.91

Table 10 ICC values of computed CSA measures from repeat TLC CT scans.

Measurements	Airway segmental locations					
	RB1	RB4	RB10	LB1	LB4	LB10
Arterial CSA	0.97	0.95	0.97	0.98	0.93	0.94
Airway CSA	0.98	0.97	0.97	0.98	0.95	0.96
Arterial $CSA_{standard}$	0.92	0.86	0.93	0.95	0.89	0.90

4.4.3 Inter-user Reproducibility

Computed CSA values on 40 FRC and 40 TLC datasets by two mutually-blinded trained users. Due to the same reasons described in Section 4.3.2, arterial CSA could not be computed at every segmental airway branch locations for all subjects. Numbers of valid subjects at different segmental locations are summarized in Table 11. Results of the inter-user reproducibility are summarized in the Table 12.

Table 11 Subject number used in the inter-user reproducibility analysis at FRC and TLC scans.

	Valid subject numbers (N=40) (percentage number)					
	RB1	RB4	RB10	LB1	LB4	LB10
FRC scans	23 (57.5%)	24 (60.0%)	36 (90.0%)	23 (57.5%)	30 (75.0%)	34 (85.0%)
TLC scans	25 (62.5%)	24 (60.0%)	36 (90.0%)	24 (60.0%)	30 (75.0%)	34 (85.0%)

Table 12 ICC values for arterial CSA measures between two users in FRC and TLC scans.

Measurements	Airway segmental locations					
	RB1	RB4	RB10	LB1	LB4	LB10
Arterial CSA at FRC	0.93	0.98	0.96	0.94	0.97	0.95
Arterial CSA at TLC	0.97	0.97	0.98	0.96	0.98	0.96

4.5 Discussion

Accuracy results was presented in Table 5 to Table 7. As observed in Table 5, CSA computation errors with respect to rod size are low with the except of the thinnest rod (diameter 3.11 mm). Also, for those rods, there is no specific trend or relation between

CSA error and scan angle. For the thinnest rod size, the error is comparatively high at most of scan angles, except at the angle of 45 degree. These experimental results suggest that there is no clear trend between CSA error and scan angle. By comparing the erros to the voxel size of $0.5 \times 0.5 \times 0.6$ mm^3, it is encouraging to see that our arterial CSA computaion algorithm has produced subvoxel accuracy over all rod sizes and scan angles. The accuracy of CSA computation under different touching conditions with airways and veins were presented in Table 6 and Table 7. As observed in the two tables, the CSA computation errors are similar under different touching conditions of airways and veins. More importantly, the largest CSA computation error observed among all rod sizes and touching conditions with either airways or veins is 0.112 mm. In other words, the CSA computation algorithm always produces a sub-voxel accuracy in the presence of different adhering structures, which in trun validates our method of boundary correction for adhering structures using a new outlier analysis technique.

Results of stability in CSA computation under varying contrast-density was presented in Figure 31. The maximum contrast density tested in this study significantly exceeded the highest contrast density used in regular clinical practice. Computed CSA values for both wide and narrow straws are visually stable across the tested range of contrast densities. For large straws, the maximum difference in computed CSA values in terms of diameter was 0.07 mm, i.e.1.1%, while that for the narrow straw was 0.03 mm, i.e., 0.6%. Results of this study together with accuracy experiments suggest that the CSA computation method is equally applied to non-contrast single-energy CT scans as well as VNC images from contrast enhanced DECT scans.

Results of repeat scan reproducibility were presented in Table 8 to Table 10. As reported in Table 8, matching arterial branch to a given segmental airway branch may not always be found in non-contrast CT imaging. Due to cardiac motion, it is often difficult to visually define arterial boundaries in non-contrast CT imaging around the heart. The influence of this artifact is more prominent at RB1 and LB1, which are in close proximity to the right main pulmonary artery (RPA) and left main pulmonary artery (LPA), respectively. Beside the heart motion artifacts, anatomic varitions in branch-level pairing between artery and airway add further difficulties in locating the unique arterial branch linked to a specific airway location. Three common variations of artery-airway pairing patterns are [204-208] — (1) two segmental airway branches shares a common arterial segment; (2) two or three arteries around a segmental bronchus, which are uniquely paired at the subsegmental level; (3) a artery crosses the boundary of its association at segmental level to supply subsegmental bronchi of another segmantal airway branch. Following the observations in Table 8, our ability to locate pairing arteries associated with lower lobe airway segments was close to 90%, but in the middle and upper lobes it was relatively lower, e.g., ~60% at RB1, RB4, and LB1, and ~75% at LB4.

The ICC values of arterial CSA and $CSA_{standard}$ at LB4 are lowest in FRC images, while these values increased considerably for TLC scans. A possible reason for the reduced repeatability of computed CSA at LB4 in FRC is the cardiac motion artifact, and in FRC the lung volume is shrunk bringing LB4 in the close proximity to the heart. The effect of motion artifact is reduced in TLC when airways and vessels stretch away due to lung expansion, improving the repeatability, especially at LB4. In general, the repeatability of arterial measures in lower lobes is high in both FRC and TLC images. Among the two

lower lobes, the repeatability of the measure in the right lobe is higher. The primary justification behind this observation is the reduced influence of cardiac motion in these two lobes due to their spatial distance from the heart as well as main pulmonary arteries.

Results of inter-user repeatability were presented in Table 11 and Table 12. Observed ICC values of inter-user repeatability for arterial CSA measurements is high (≥0.96) at all airway segmental locations in TLC scans. The repeatability of the measure in FRC is only marginally lower than that in TLC. A possible reason behind this small difference in repeatability in TLC and FRC may be that the expanded volume in TLC improves the performance of locating pairing arteries and reduces artifacts of touching airways and veins. In general, the observed values of inter-user reproducibility are higher than those in repeat scan reproducibility. The intra-user repeatability only accounts for sensitivity of our algorithm to interactive user input. On the other hand, repeat scan reproducibility accounts for variability in patient positioning, lung volume, CT scans as well as user inputs (note that a new set of user inputs is needed for a repeat scan).

4.6 Conclusion

In conclusion, a semi-automatic method has been presented in this chapter to identify airway/artery correspondences and use this relationship as a means of characterizing up-stream pulmonary arterial status. The computed arterial CSA measure is standardized with local airway CSA. In an early stage of most pulmonary diseases, such as emphysema and COPD, there is no obvious morphological changes in airways. Therefore, it is suitable to standardize the measurement of specific arterial branch using its associated airway branch to explore the vascular role in early stages of the disease.

Experimental results suggest that semi-automatic method provides an effective framework for quantitative assessment of pulmonary arterial morphology at segmental airway locations with high levels of accuracy, robustness, and repeatability. The entire process including user interaction through GUI and the automated steps requires 30-60 seconds to complete CSA computation at each airway branch and it requires around 5 minutes for one lung dataset. Overall results suggest that arterial measures at lower lobes are more reproducible. The high accuracy, reproducibility, and computational efficiency of the method highlight its application in large cross-sectional and longitudinal studies exploring arterial roles in different lung diseases.

For examples, this method has already been applied to two human disease studies. In the first study, it has been applied to assess the role of hypoxic pulmonary vasoconstriction (HPV) in emphysema susceptible subjects (i.e. HPV pilot) by measuring the arterial CSA associated to lower lobes. The work has been published in [11, 217]. See Appendix I for reference.

Secondly, the method has been applied to a large population of subjects with both early and advanced lung disease (via SubPopulations and InteRmediate Outcome Measures In COPD Study (SPIROMICS) cohort) to examine arterial morphometric changes in COPD populations and correlate arterial measures with the rate of emphysema progression. The work has been published in [218, 219]. See Appendix II for reference.

CHAPTER 5

AUTOMATIC QUANTITATIVE MORPHOLOGIC ASSESSMENT OF PULMONARY ARTERIES

5.1 Introduction

In the previous Chapter 4, we presented a semi-automatic framework for quantitative morphological assessment of pulmonary arteries. Although the semi-automatic framework produces accurate, robust and reproducible artery measurements, it requires manual interactions, which may be time-consuming when handling thousands of subjects. Therefore, it is meaningful to have a fully automatic method for quantitative assessment of pulmonary arteries at different lung regions, which is the main focus of the current chapter. Specifically, we will present an automatic method for the identification of matching pulmonary arterial segments associated to anatomically defined airway branches in lung CT images. The method then generates volumetric reconstruction of such pulmonary arteries and quantifies their morphologic properties, e.g. cross-sectional area (CSA).

Major challenges for automatic identification of matching pulmonary arteries emerge from geometric and topologic complexity of the pulmonary vascular tree, especially in the presence of arteries, veins, and airway wall fusion due to partial volume effects in CT imaging. These challenges may be further enhanced, by non-linear deformation of the vascular tree at different lung volumes as well as anatomic variations of the vascular tree branching pattern between subjects. To overcome these difficulties, we seek to use the airway tree as the reference for locating the matching arterial segments. In contrast to vessel trees, airway tree possess much simpler and more consistent branching

patterns and standardized anatomic nomenclatures are available in the literature [203] up to several generational or segmental levels. It is observed that pulmonary anatomy has unique pairing between arterial and airway branches that is established by their spatial proximity and parallel configuration [203]. Our automatic method of building the correspondence of matching arterial segments, among intra- and inter-subject scans, is primarily developed on this axiom. Meanwhile, the anatomy information of relative positions between arterial segments and their associated airway branches is also considered in the automatic artery identification process.

In the following sections, the overall process of a fully automated method is presented with primary focus on the algorithms of automatic identification of matching arterial segments from their associated airway branches, as well as the morphologic reconstruction and assessment of the matching arterial segments. The accuracy of artery identification algorithm is tested in lung CT images from 40 healthy subjects scanned at FRC and at TLC, and the results are reported at six segmental airway locations from upper, middle and lower lung lobes. Moreover, the accuracy of morphologic assessment, e.g. in terms of arterial CSA, is also examined by comparing to the computed CSA measures by the semi-automatic method in Chapter 4. Finally, the reproducibility of computed CSA measures by the automatic method is evaluated using CT images from 20 healthy subjects repeatedly scanned at FRC and from another 20 healthy subjects repeatedly scanned at TLC.

5.2 Methods and Algorithms

The automatic method starts with segmentation [138, 210] of airway and pulmonary vessel trees from CT images, which are subjected to curve skeletonization. The

initial segmentation of vessel trees are refined using the vessel extension algorithm in Section 4.2.2, and further refined by excluding the regions coming into airway walls. Then, the new curve skeletonization algorithm (developed in Section 3.2) is used to produce the curve skeleton of airway tree without false branches. And the fuzzy surface skeletonization algorithm (developed in Section 3.3) is applied to vascular structures, which may contain loops, followed by a conventional curve thinning algorithm [96]. Anatomic labeling [142] of individual airway branches is computed from the curve skeleton of airway tree. Next, for a given labeled airway branch, the matching arterial segment is automatically identified using their spatial proximity and parallel configuration, as well as the relative anatomic position between airway and artery branches. Finally, a volumetric reconstruction of the identified arterial segment is computed using local scale-based dilation, and the CSA measures are computed for the matching arterial segment. Figure 32 shows the overall process of our method. The automatic identification and morphological assessment of the matching arteries are described in detail in the next two subsections.

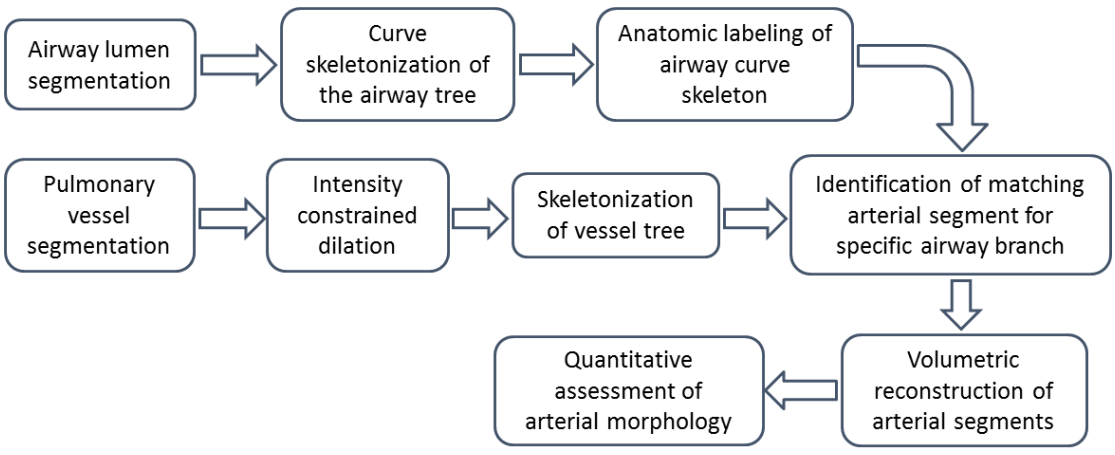

Figure 32 Overall process for the automatic artery identification and measurement method.

5.2.1 Identification of Matching Arterial Segment

We use the curve skeletons of airway and vessel branches to identify the matching artery associated to a specific airway branch, because the curve skeleton has the same topology as the volume object and is much easy to handle. The goal is to explore the information of distance, orientation and anatomy position relationship to build the pairing correspondence between an airway branch and its matching arterial segment.

Specifically, the anatomic labeled airway curve skeleton is used to locate matching arterial segments. Let $\{A_1, A_2, \cdots, A_N\}$ denote the set of uniquely labeled airway skeletal branches. Each A_i is a set of voxels constituting a digital path. Let S_V denote the set of voxels in the curve skeleton of pulmonary vasculature. A smooth representation of each individual arterial or airway curve skeleton is generated using polynomial curve fitting, and the local orientation at a specific skeletal voxel is computed as its tangent direction. Let $\boldsymbol{\tau}(p)$ denote the orientation vector at a skeletal voxel p.

To determine the spatial proximity, fuzzy distance analysis [171] is applied. For each voxel a in a specific airway branch A_i, the best matching vessel skeletal voxel $v \in S_V$ is located as the one that is spatially close to a with similar orientation. Toward this goal, an FDT is computed from a over a sufficiently large neighborhood 51×51×51 voxels that ensures inclusion of relevant vessels. Let $D(a)$ denote the fuzzy distance of a from the nearest vessel skeletal voxel, i.e., $D(a) = \min_{v \in S_V} FD(a, v)$, where, $FD(a, v)$ is the fuzzy distance between two voxels a, v.

Furthermore, observed from the lung anatomy [203, 204], pulmonary arteries and veins often run at different relative positions with respect to their associated airway branches. For example, the segmental artery of RB10 and LB10 runs at dorsal position to

their associated airway segmental branch of RB10 and LB10, while the nearby veins are often grown to the anterior position of the airway branches. Hence, we could restrict our search for the matching arteries from the dorsal direction at the airway branch of RB10 and LB10. For the locations that do not have a prevailing artery-airway position relationship, only orientation and distance information are used to identify the matching arteries. We define a position function $P(a, v)$, which returns value of '0' if the vessel skeletal voxel v is located at the restricted region of the airway skeletal voxel a of RB10 and LB10 locations, otherwise, returns value of '1'.

Finally, by incorporating the orientation, distance and relative anatomy position information, the mismatch function, $M(v, a)$, between a vessel and airway skeletal voxels v and a is defined as,

$$M(v,a) = \frac{1}{(\alpha + D(a)/FD(v,a))(\beta + |\boldsymbol{\tau}(v) \cdot \boldsymbol{\tau}(a)|)} \times P(a,v). \qquad (5.1)$$

In the above equation, the mismatch factor is contributed by both spatial distance as well as by disagreement in local structure orientation. The parameter α and β is for adjusting the weights for the distance and orientation agreement. For all the experiments in this chapter, the values of '1' and '0.25' are used. Finally, the matching vessel skeletal voxel corresponding to the airway skeletal voxel a is defined by the following equation,

$$\arg\min_{v \in S_V} M(v,a). \qquad (5.2)$$

We will refer to those matched voxels as arterial skeletal voxels in the next.

5.2.2 Morphological Assessment of Matching Arteries

Matching arterial segments are reconstructed using dilation of arterial skeletal voxels and the connectivity analysis. Let $V_i = \{v_1, v_2, \cdots, v_{N_i}\}$ denote the set of vessel

skeletal voxels each matching to some skeletal voxel in the airway branch A_i. Based on the voxels in V_i that are matched to the voxels in A_i, V_i may not form a contiguous digital line, even when the voxels in V_i come from single skeletal branch. To solve this problem, a local scale-based dilation is applied, where each voxel in V_i is dilated at a scale that equates to its distance transform value [59]. Let X denote that dilated set of voxels and let $C_1, C_2, \cdots, C_L$ denote its 26-components [74]. Finally, the component C_j with the maximum count of matching arterial skeletal voxels is used to define the matching arterial segment for airway branch A_i. Le S_i be the volumetric representation of the matching arterial segment and T_i denote the set of skeletal voxels within S_i.

To assess the morphology of an arterial segment S_i, central half voxels of S_i are determined. The longest 26-path π in T_i is detected and the central half voxels p_{central} on π are selected. Same as the morphological computation method in semi-automatic Section 4.2.6, the arterial CSA is computed at a skeletal voxel p_i by first interpolating the object representation on an orthogonal plane through p_i, where the normal direction of the plane is determined by the tangent direction in the fitted curve. Then, the arterial CSA is computed using the radial sample-line approach with the novel outlier analysis. And the average of CSA measures at the central half voxels on π is used as the morphological measure for a matching arterial segment.

5.3 Experimental Methods and Results

Three experiments were carried out to evaluate the effectiveness of the automatic method. The first experiment was designed to examine the accuracy of the hypothesis that the vascular segments matched by the automatic algorithm to individual airway branches by their spatial proximity and parallel orientations are pulmonary arteries. We examined

the artery matching accuracy from the whole airway tree, as well as the from six specific airway segmental branches in different lung regions, namely RB1, RB4, RB10, LB1, LB4 and LB10. The second experiment was to test the accuracy of computed arterial CSA by the automatic method compared to CSA computed by semi-automatic method proposed in Chapter 4. The third experiment was aimed to examine the reproducibility of computed arterial CSA measures associated with individual anatomic airway branches.

Same as the human subjects studied in Chapter 4, 40 healthy non-smoker subjects were used to evaluate the performance of the automatic method. Each subject were scanned at both FRC and TLC status. These 40 FRC and 40 TLC images were used in the two accuracy experiments. Meanwhile, among these 40 subjects, 20 subjects were scanned repeatedly at FRC status with a time gap of 3–5 mins, while the other 20 subjects were scanned repeatedly at TLC status with a similar time gap. These 20 repeated FRC and 20 repeated TLC images were used in the repeatability study.

The scanning protocols for these 40 healthy non-smoking subjects have been described in Chapter 4. For the completeness, we also put the CT scanning protocols here. CT images were acquired on a Siemens Sensation 64 or Siemens Definition Flash 128 (at 120kV with effective mAs of 200), and reconstructed with 0.5–0.6 mm in-plane, 0.5/0.75-mm slice thickness/interval using B35f medium-soft kernel for image reconstruction.

5.3.1 Accuracy of Artery Identification

We examined two types of artery identification accuracy: (1) volumetric agreement of all reconstructed arterial segments from airway tree with the artery/vein volume obtained by computer-assisted manual labeling [158]; (2) the rate of the number of correctly identified matching arterial segments and the overall number of the subjects, which are

computed at six airway segmental branches using the manual-labeled arterial segments in Chapter 4 as the ground truth.

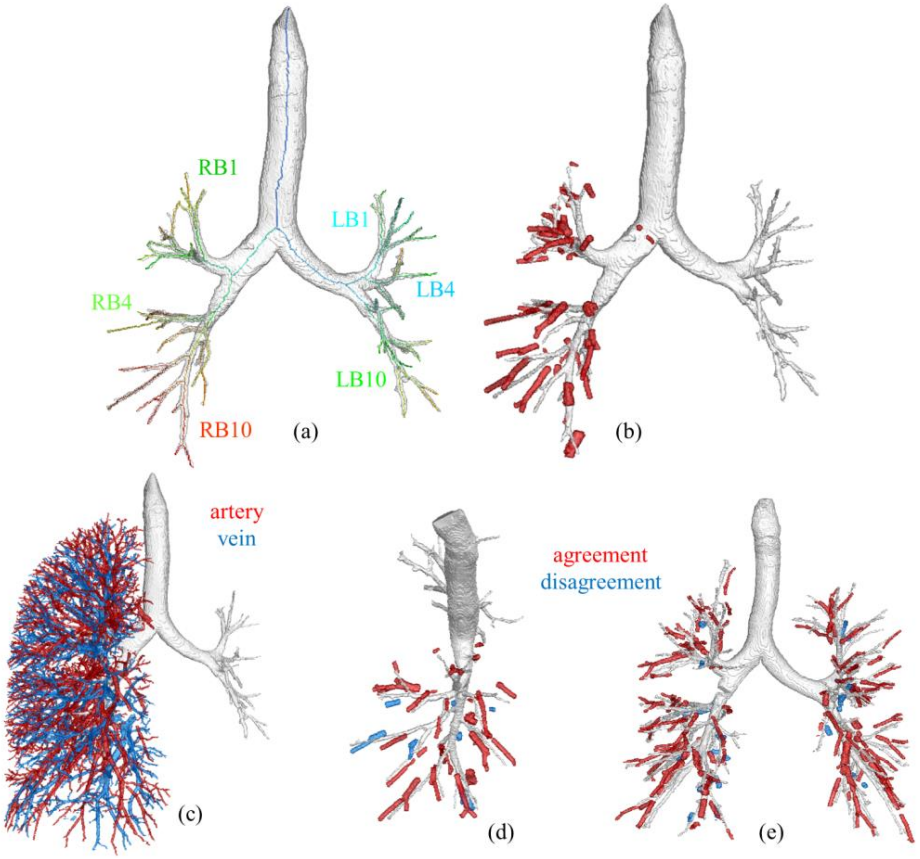

Figure 33 Automated reconstruction of arterial segments matching with individual anatomic airway tree branches. (a) Anatomically labeled branches in an airway tree visualized in the posterior to anterior direction. (b) Reconstructed arterial volume segments matched with airway branches. (c) Manually labeled artery/vein separation. (d) Agreement (red) and disagreement (blue) of reconstructed arterial volume with the manual labeling of arteries. Only the right pulmonary tree are shown in (a-d) for visualization purpose. (e) Another example of reconstructed arterial volume and their agreements with manual labeling.

A. Artery Volumetric Agreement

This experiment was conducted on CT images from a subset of five healthy subjects. Initial results has shown that parallel segments usually occur at or after segmental airway branches (See Figure 33(b, d, e)). *Agreement* was defined as the percent volume overlap of reconstructed arterial volume with manually labeled arteries, while *disagreement* was defined as the percent volume overlap with manually labeled veins. Color-coded display of agreement and disagreement of reconstructed arterial volumes in CT images of two healthy subjects are illustrated in Figure 33(d, e). It was observed in the quantitative analysis that the current method produces 83% overall agreement of arterial volume at the cost of 17% disagreement.

It may be noted that the disagreement errors are contributed by various factors, including anatomic variability among airway, artery and vein trees, and incomplete vessel segmentation, etc. From our observation, almost half (44%) of the disagreement errors occurred along the specific airway branch paths from the middle third of lung, where cardiac motion is large. This region may represent high intrinsic anatomic variability. After excluding those branch paths, the overall disagreement rate dropped to 11%.

B. Number of Matching Arterial Segment Agreement

In this experiment, we test the matching accuracy of identified arterial segments from six airway segmental branches using the manual-labeled arterial segments derived in Chapter 4 as ground truth. Specifically, the identified arterial segments at RB1, RB4, RB10, LB1, LB4 and LB10 airway branches are examined. At each airway location, two matching accuracies are reported: (1) the rate of the number of subjects whose identified arterial segment at a specific airway branch belongs to arteries instead of the veins and the total

number of subjects, namely *artery accuracy*; (2) the rate of the number of subjects whose identified arterial segment at a specific airway branch is exactly the matching arterial segment (identified by the expert) and the total number of subjects, namely *branch-level accuracy*. 40 FRC and 40 TLC lung CT images were analyzed. Among these subjects, some of the arterial segments cannot be identified due to their inconsistent anatomic pairing patterns or the non-contrast CT imaging natures, such as image noises, heart motion, etc. See Section 4.5 for detailed discussions. The total number of subjects used in this experiment has been reported in Table 10 of Chapter 4. The results of artery identification accuracy are summarized in Table 13 and Table 14 for FRC and TLC scans, respectively.

Table 13 Artery identification accuracy of reconstructed arterial segments at different airway segmental locations in FRC scans.

	Airway segmental locations					
	RB1	RB4	RB10	LB1	LB4	LB10
# of Subject	23	24	37	23	30	34
Artery accuracy	52.2%	37.5%	100%	60.9%	50.0%	100%
Branch-level accuracy	30.4%	29.2%	86.5%	52.2%	33.3%	85.3%

Table 14 Artery identification accuracy of reconstructed arterial segments at different airway segmental locations in TLC scans.

	Airway segmental locations					
	RB1	RB4	RB10	LB1	LB4	LB10
# of Subject	25	24	37	24	30	34
Artery accuracy	72.0%	54.2%	100%	70.8%	56.7%	100%
Branch-level accuracy	56.0%	37.5%	83.8%	62.5%	36.7%	85.3%

Table 13 and Table 14 show that the artery accuracy at RB10 and LB10 airway branches are 100% in both FRC and TLC scans., which means the automatic artery identification algorithm will always find the associated arterial branches (instead of veins) at RB10 and LB10 airway locations. The branch-level artery accuracy are also reasonable at RB10 and LB10 airway locations with errors coming from the detection of parent or child arterial segments instead of the exactly matching arterial segment at an airway branch. For example, among 37 subjects, 3 of them found the parent of the matching arterial segment at RB10 airway branch in FRC scans, while 2 of them found one of the children of the matching arterial segment.

It should be noted that it seems easier to identify the exactly matching arterial segments at RB10 and LB10 locations in FRC images than in TLC images. A possible reason may be arterial branches have a better matching relationship with their associated airway branches at FRC status than at TLC status, where the vessel and airway branches are stretched out with inconsistent degrees at TLC status.

In contrast to the results found at lower lobes, both the artery accuracy and the branch-level artery accuracy are not satisfactory at middle and upper lobes, especially at middle lobes. The low accuracy may be caused by the anatomic variability of the airway and vessel branches at middle and upper lobes, especially at middle lobes, e.g. veins often come close to airway with similar orientation. In comparison, the airway and vessel branches at lower lobes have relative prevailing pairing patterns and also have reduced influence of cardiac motion due to their spatial distance from the heart as well as main pulmonary arteries. Based on these results and observations, we focus the next two

experiments on RB10 and LB10 locations, since they are the only potential locations worthwhile in practice.

5.3.2 Accuracy of Arterial Morphologic Assessment

In this experiment, we examine the arterial CSA measure accuracy by the automatic method. Arterial CSA measures derived from the semi-automatic method in Chapter 4 are used as ground truths. We restrict our comparison to those subjects, who find the exact matching arterial segment as compared to the manually identified arterial segment associated to specific airway branch. Arterial CSA measure accuracy at the airway branch of RB10 and LB10 in both FRC and TLC scans are analyzed. The correlations between CSA measures from the automatic method and ground truths are drawn in Figure 34. The Bland-Altman plots of the computed CSA errors are shown in Figure 35.

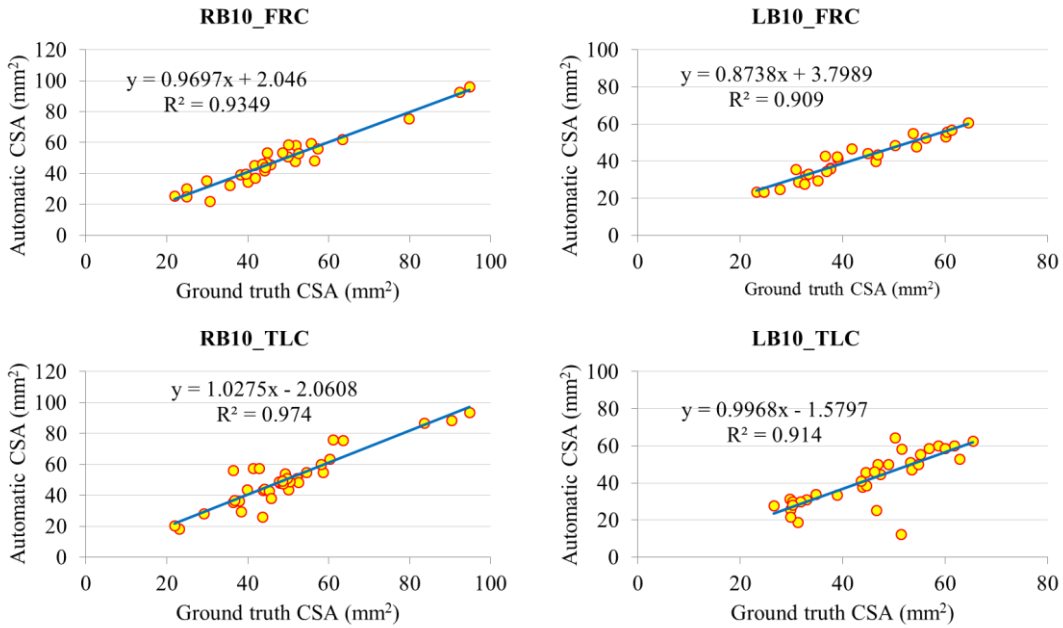

Figure 34 The correlation between CSA measures from automatic method (vertical axis) and the ground truths CSA measures (horizontal axis) at RB10 and LB10 airway location in FRC (top row) and TLC (bottom row) images.

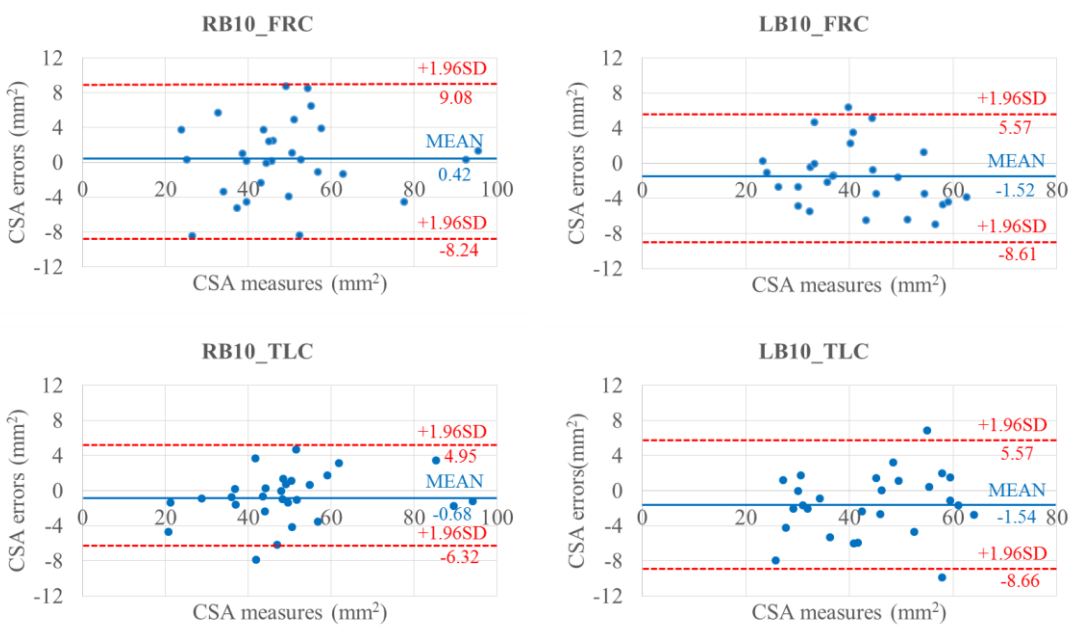

Figure 35 Bland-Altman plots of the computed CSA errors at RB10 and LB10 airway locations between CSA measures from automatic method and the ground truths in FRC (top row) and TLC (bottom row) images.

From Figure 34, we can see that the computed arterial CSA measures by the automatic method correlates well with the ground truth CSA computed by the semi-automatic method at both RB10 and LB10 airway locations ($R > 0.95$). In Figure 35, we see that the mean of computed arterial CSA errors is close to '0' ($\leq 1.0\ \text{mm}^2$) at the location of RB10, while it has a small bias of approximate $-1.5\ \text{mm}^2$ at the location of LB10.

5.3.3 Repeat-scan Reproducibility

In this experiment, the reproducibility of computed arterial CSA measures at by the automatic method is analyzed using the repeat-scan FRC and TLC images. Intra-class correlation (ICC) of the CSA measures are computed in both FRC and TLC repeat scans.

A qualitative illustration of the reproducibility of the method is shown in Figure 36(b, c) in two repeat CT scans of a subject at TLC. CSA was computed at two anatomic airway paths from the lower lobes, RB10 and LB10 for each lung image. 20 repeated FRC and 20 repeated TLC images were used in the repeatability study. The results have included the subjects that found unmatched arterial segment at an airway location between their first and second scans. The results of the ICC and the mean errors of the computed CSA between repeated scans at FRC and TLC are summarized in Table 15.

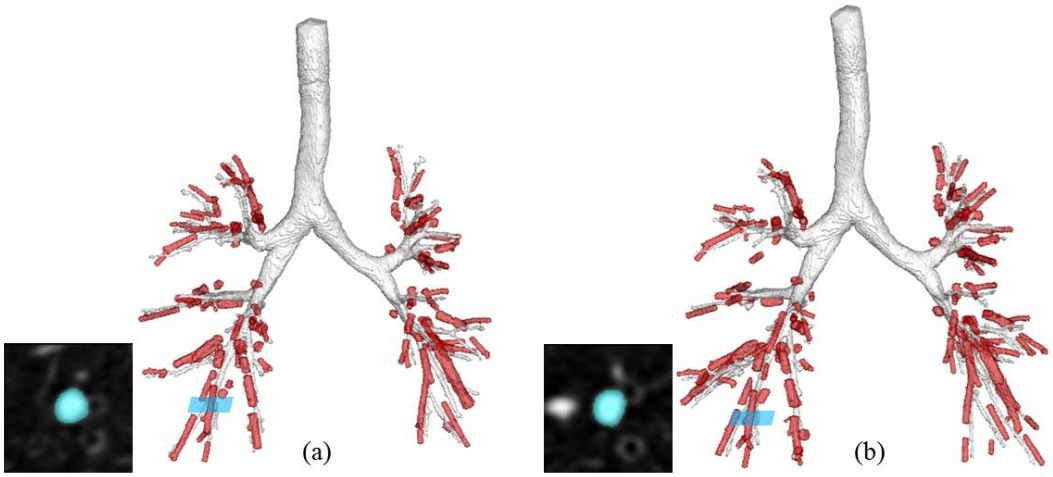

Figure 36 Qualitative illustration of the reproducibility of the automatic method. (a, b) Volumetric arterial reconstruction of matching airways in two repeat MDCT scans at TLC. Arterial morphologies on orthogonal cross-section at a matching location on airway branch RB10 are shown by 2-D zoomed-in panels.

Table 15 Results of ICC and the mean errors of the computed arterial CSA between repeated scans along airway location of RB10 and LB10.

	RB 10		LB10	
	FRC	TLC	FRC	TLC
ICC	95%	91%	92%	89%
Mean error ± S.D. (mm^2)	3.9 ± 3.7	5.7 ± 5.8	3.0 ± 3.3	5.7 ± 4.9

ICC values of computed arterial CSA by the automatic method are higher at RB10 than at LB10 in both TLC and FRC scans with the highest ICC value found at RB10 in FRC scans. Meanwhile, ICC values in FRC scans generally are higher than in TLC scans at both RB10 and LB10 locations, which comes from the fact that the automatic method has high possibility to identify the child or parent arterial segment associated to an airway branch in TLC images than in FRC images (reason has been discussed in Section 5.3.1). Therefore, the errors of repeated scan CSA measures are larger in TLC images than in FRC images from both RB10 and LB10 airway locations.

5.4 Discussion and Conclusion

In this chapter, an automatic method to standardize arterial measurements in relation to anatomic labeled airway branches is presented. This allows us to compute region specific artery measurements automatically. Experimental results have shown that this automatic method achieved an accuracy of 84−87% for identifying the exactly matching arterial segment in lower lobes (RB10 and LB10 airway locations) at different lung respiration status. For those exactly matching arteries, the automatically computed CSA measures correlated very well with the ground truth CSA measures computed by the semi-automatic method ($R > 0.95$). The repeatability study showed that the ICC values of the automatic method are higher in FRC images than in TLC image with the highest ICC value found at airway location of RB10 in FRC (ICC=95%).

It should be noted that artery identification accuracy by the automatic method at upper and middle lobes are not satisfactory, especially at middle lobes. The major reason for low accuracy comes from the anatomic variability of airway and vessel branches at middle and upper lobes, especially at middle lobes, e.g. veins may come close to airway

with similar orientation. Also, airway and vessel branches are more influenced by the cardiac motion effect, which may further increase the challenge of automatic artery identification. In contrast, airway and vessel branches at lower lobes have relative prevailing pairing patterns and also reduced influence of cardiac motion due to their spatial distance from the heart as well as main pulmonary arteries. Therefore, this automatic method for labeling and measuring of pulmonary arterial segments may avoid the upper and middle lung regions.

The automatic method we developed in this chapter offers an alternative and objective method for assessing pulmonary arterial morphometry, and also able to account for differences in lung airway dimensions due to changes in airway resistance from smoking or lung volume changes. Current experiments suggest that the automatic method achieves a reasonable good accuracy to detect the matching arterial segments associated to airway branches from lower lobes. However, the artery identification accuracy may need further improvement to readily apply to large research and clinical studies. Possible directions for the improvement of the artery identification accuracy by the automatic method are discussed in Section 7.2.2.

CHAPTER 6

APPLICATIONS IN NORMAL HUMAN POPULATION

6.1 Introduction

In this chapter, we apply our arterial assessment method to examine the central pulmonary artery dimensions in a large population of normal human subjects. These subjects are healthy non-smokers selected from Bioengineering Research Partnership (BRP) study cohort and SubPopulations and InteRmediate Outcome Measures In COPD Study (SPIROMICS) cohort. The two cohorts were combined to expand the age range evaluated. We computed the arterial cross-sectional area (CSA) associated to lower lobe airway segmental branches, and studied the airway standardized arterial CSA as a function of age and sex.

6.2 Methods and Experiments

In this study, 200 nonsmoking subjects, completing a baseline and one year follow-up (V2) study, were evaluated from the SPIROMICS cohort. Subjects underwent thoracic CT scans performed at both TLC and residual volume (RV, full expiration). Single energy CT scans were performed with guided breath-hold at TLC and RV at 120 kVp in the supine body posture. X-ray tube current was dependent on BMI, scanner model, and TLC/RV scan.

In addition to these 200 nonsmoking subjects from SPIROMICS cohort, 40 normal nonsmoking subjects from BRP study cohort were also added into this evaluation. These 40 subjects underwent thoracic CT scans at both TLC and FRC status. Single energy CT scans were performed in the supine position at 120 kVp and 200 effective mAs using the

MDCT scanner (SOMATOM Definition Flash CT scanner, Siemens, Forscheim, Germany) at the University of Iowa Comprehensive Lung Imaging Center.

Using the semi-automatic method proposed in Chapter 4, arterial segments associated to segmental airway branches were evaluated in TLC CT images for 240 nonsmoking subjects. Arterial segments at upper and middle lobes are not always measurable due to inconsistent anatomic pairing patterns, extremely short segments or the non-contrast CT imaging natures, such as image noise, heart motion, etc. Therefore, we confine our analysis of arterial measurements at airway segmental branches of RB10 and LB10 in lower lobes because of a more prevailing pairing pattern for airway-artery match and the high measurement reproducibility (see in Table 10 Chapter 4). Both arterial CSA and airway- standardized arterial $CSA_{standard}$ were computed. In addition, average $CSA_{standard}$, as well as average arterial CSA, was reported for each subject as the average of two airway-artery pairs in lower lobes per subject.

Subject characteristics and CT measurements from SPIROMICS and BRP baseline visits are reported as mean ± standard deviation. Student t-test was used to determine differences between male and female with a p value ≤ 0.01 considered statistically significant. Multiple linear regression was performed with arterial measurements at different airway locations (e.g. RB10, LB10 or average of RB10 and LB10) as response variable and age, BMI, height and weight as covariates.

6.3 Results

Arterial measurements were evaluated in 240 subjects: 40 from BRP and 200 from SPIROMICS. Among them, there were 97 male subjects and 143 female subjects with similar age (male: 53 ± 14 years, female: 51 ± 14 years). Male subjects had larger values

of weight and height than female subjects. A full summary of subject characteristics can be seen in Table 16.

Table 16 Subject characteristics for male (M) and female (F) non-smokers. Results are expressed as mean ± standard deviation with the exception of number of subject.

Characteristic	**M**	**F**	p value
Number	96	144	
Age (years)	53 ± 14	51 ± 14	0.1
Height (cm.)	176.2 ± 7.8	164.0 ± 6.9	<<0.01
Weight (kg.)	86.3 ± 14.1	74.2 ± 16.0	<<0.01
BMI (kg/m^2)	27.8 ± 4.5	27.5 ± 5.4	0.3

Arterial measurements between male and female non-smokers

The results of CT measurements of airway and arteries in male and female subjects were summarized in Table 17. Airway and Artery CSA in lower lobes were significantly ($p<<0.01$) larger in male subjects than in female subjects. However, the airway standardized artery CSA did not show significant difference between male and female subjects.

Table 17 Airway, artery and standardized CSA measurements in Male (M) and female (F) non-smokers. Results are expressed as mean ± standard deviation.

Airway Branch	CSA Measure	M	F	p-value
RB10	Airway	67.23 ± 13.91	54.00 ± 10.96	<<0.01
	Artery	47.82 ± 14.80	40.31 ± 11.0	<<0.01
	standard	0.721 ± 0.211	0.760 ± 0.202	0.1
LB10	Airway	71.06 ± 14.23	58.32 ± 12.82	<<0.01
	Artery	46.00 ± 11.32	38.11 ± 10.55	<<0.01
	standard	0.667 ± 0.188	0.666 ± 0.172	0.47
Ave of lower lobes	Airway	69.45 ± 12.26	56.47 ± 10.97	<<0.01
	Artery	46.91 ± 11.27	39.36 ± 9.92	<<0.01
	standard	0.697 ± 0.189	0.713 ± 0.176	0.26

Relationship between arterial measurements and age

The regression analysis confirms that average arterial $CSA_{standard}$ measures, as well as arterial $CSA_{standard}$ at specific RB10 and LB10 locations, had significant ($R=[0.49, 0.54]$, $p<4.3e-15$) negative correlations with age (Figure 37 to Figure 39). This negative correlation indicates that, with age, the average arterial $CSA_{standard}$ measures decreases due to an increasing airway size ($R=0.35$, $p=9.7e-8$) and a decreasing artery size ($R=0.2$, $p=0.0029$).

It was also observed that the age effect on artery size was greater in male subjects compared with female subjects, while the age effect on airway size in males and females was similar The average airway size had a significant positive correlation with age in both male (R=0.33, p=0.0018) and female subjects (R=0.37, p=6.9e-6). However, the average artery size had significant (R=0.34, p=0.0014) negative correlation with age in male subjects, and this correlation is not significant (R=0.16, p=0.065) in female subjects.

6.4 Discussion and Conclusion

Cross sectional area of central pulmonary arterial segments associated with airway branches in the lower lobes were examined in healthy nonsmoking subjects. It was observed that both airway and artery sizes were significantly larger in male subjects than in female subjects. However, the airway standardized arterial $CSA_{standard}$ did not show significant difference between male and female subjects. Arterial and airway size changed proportionately between the male and female population.

The multiple linear regression showed that segmental airway CSA, aarterial CSA and airway standardized arterial $CSA_{standard}$ all were significantly associated with age. It was observed that, with age, the segmental airway size (lumen radius + wall thickness) increased, while the segmental artery size decreased. Therefore, the airway standardized artery size $CSA_{standard}$ was a more age-sensitive measurement than airway or artery measurements alone. The age-related change in airway size was similar for male and female subjects while the male subjects had a larger age related decline in artery size compared with females. To our knowledge, these differences within a normal population have not previously been reported. After adjusting for age, other factors, e.g. gender, weight and height, did not have a significant correlation with the arterial $CSA_{standard}$. BMI

demonstrated a weak negative correlation ($p=0.04$) with arterial $CSA_{standard}$ at LB10 location. However, this correlation was not found for RB10 or for combined RB10-LB10 locations.

In summary, we applied our semi-automatic pulmonary arterial assessment method to examine central arterial sizes associated to RB10 and LB10 airway locations in a large population of healthy nonsmoking subjects. We demonstrate significant age and sex related differences with the normal population when evaluating pulmonary arterial size and airway size. These differences in the normal population must be taken into consideration when using airway standardized arterial metrics to evaluate pulmonary pathophysiology.

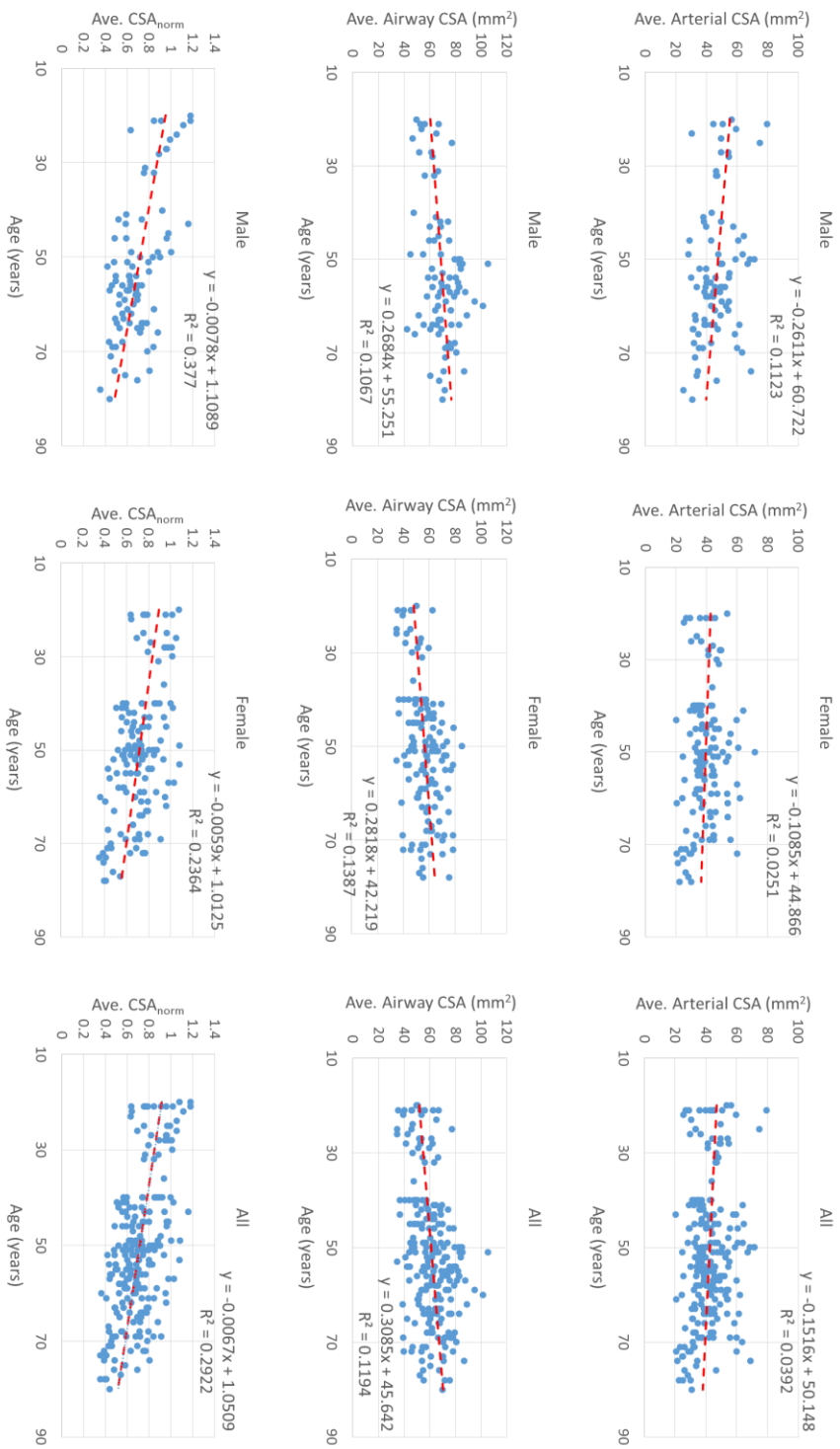

Figure 37 The relationship between age and average artery CSA (top row), average airway CSA (middle row) and average artery $CSA_{standard}$ (bottom row). The relationship in male, female and all subjects are separately illustrated in right, center and left column, respectively. All regressions were statistically significant ($p < 0.002$), except the average artery vs age in female subjects ($p=0.065$).

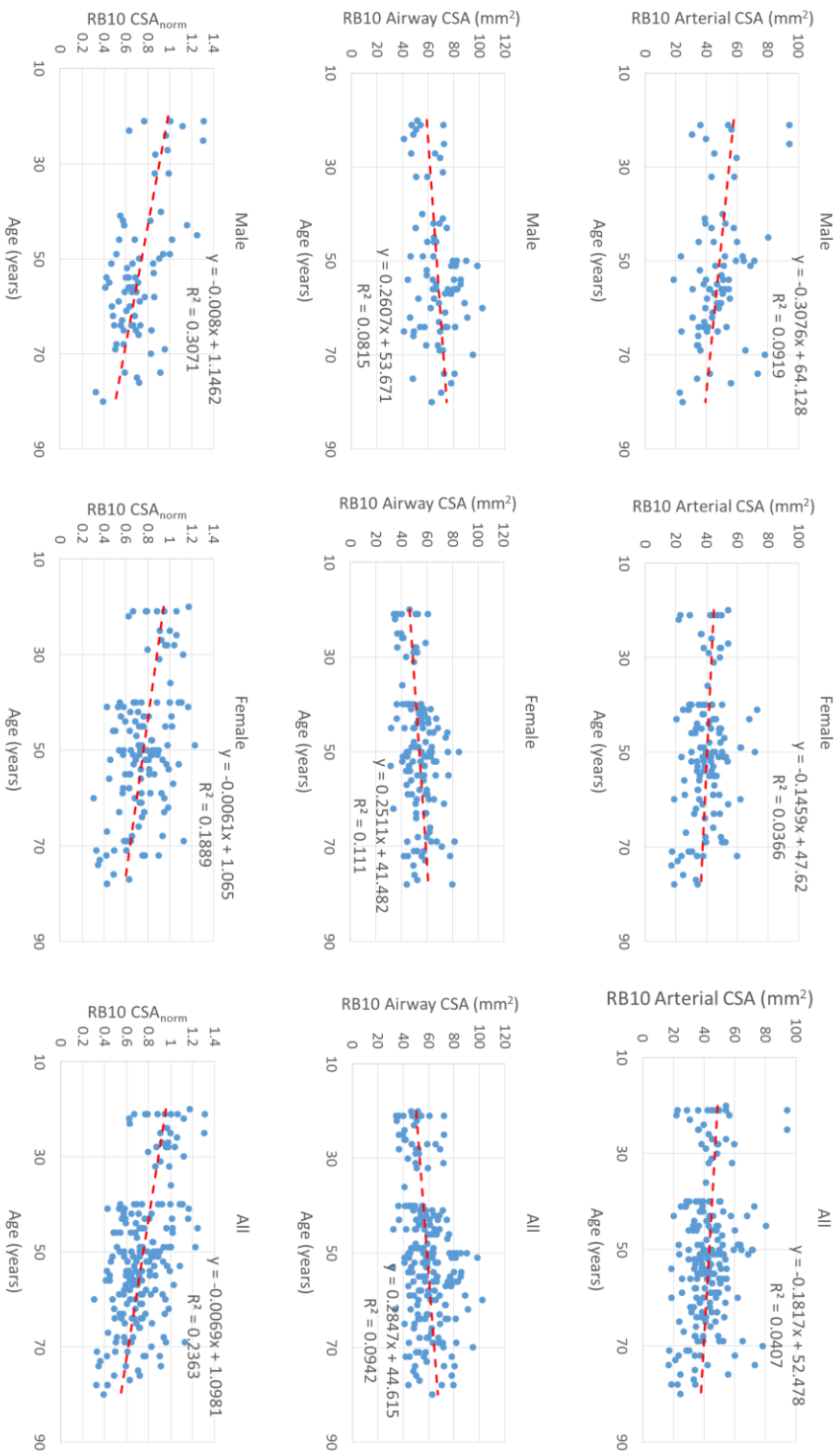

Figure 38 The relationship between age and RB10 artery CSA (top row), RB10 airway CSA (middle row) and RB10 artery $CSA_{standard}$ (bottom row). The relationship in male, female and all subjects are separately illustrated in right, center and left column, respectively. All regressions were statistically significant ($p < 0.008$), except the RB10 artery vs age in female subjects ($p=0.03$).

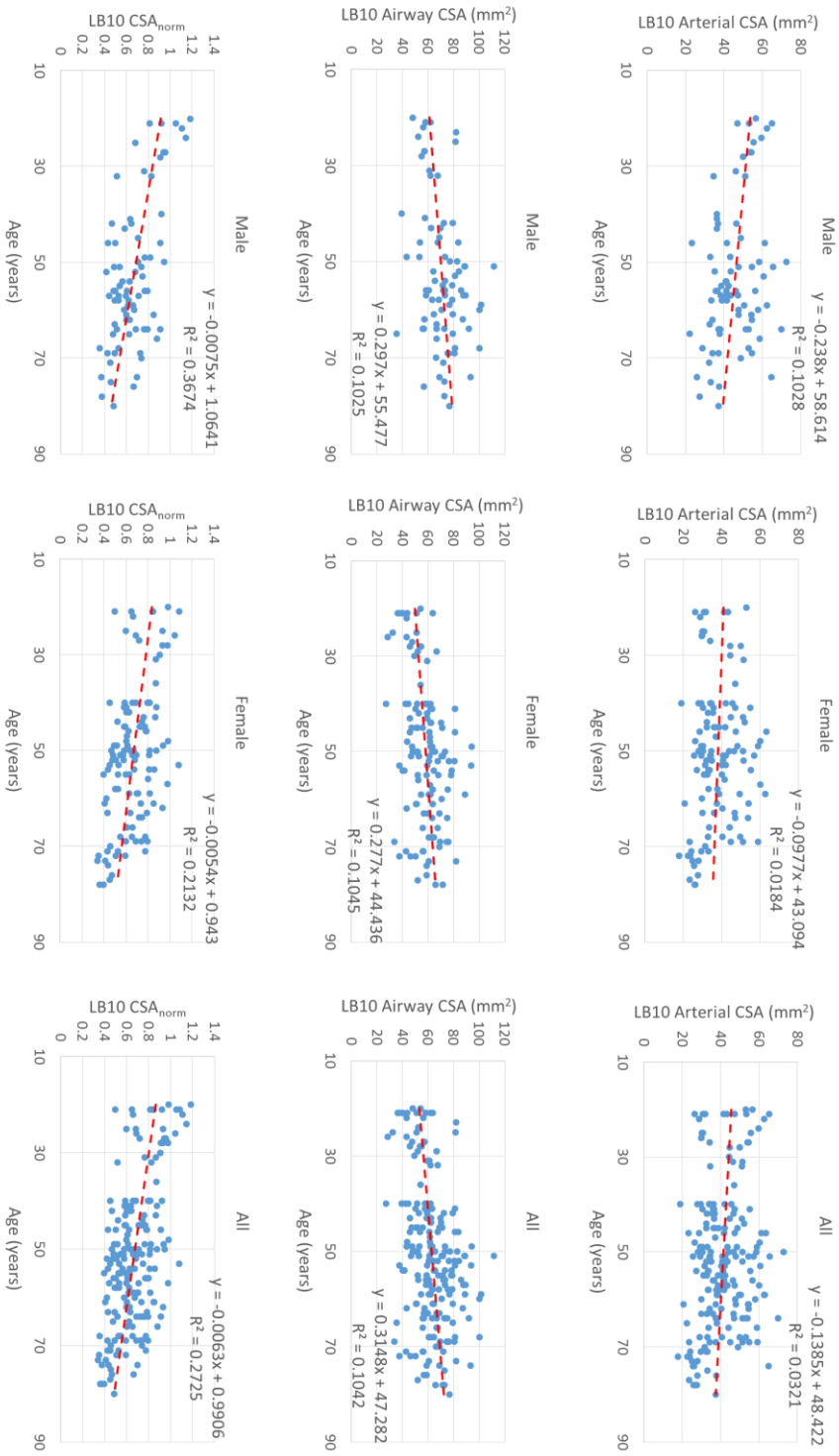

Figure 39 The relationship between age and LB10 artery CSA (top row), LB10 airway CSA (middle row) and LB10 artery $CSA_{standard}$ (bottom row). The relationship in male, female and all subjects are separately illustrated in right, center and left column, respectively. All regressions were statistically significant ($p < 0.01$), except the LB10 artery vs age in female subjects ($p=0.14$).

CHAPTER 7

CONCLUSION AND FUTURE DIRECTIONS

7.1 Conclusion

Recent studies suggest that pulmonary vascular changes may be an early lesion in COPD associated with an emphysematous phenotype that can be potentially amenable to early treatment. In this thesis, we proposed to segment the regional pulmonary arterial branches at their associated anatomic airways branches, and quantify their morphology. This work provides a standardized method to assess and compare pulmonary vascular measurements from a broad range of lung regions in both intra- and inter- subjects. To summarize, we first recall our specific aims:

Aim 1: Development of an efficient curve skeletonization algorithm using minimum-cost path approach to fully automate the anatomic labeling of human airway tree.

Aim 2: Detection and reconstruction of the volumetric arterial segments associated to a given airway anatomic branch and assessment of artery morphology.

Aim 3: Evaluation and application of the above methods in human studies.

Two novel skeletonization algorithms: minimum-cost path based curve skeletonization and fuzzy surface skeletonization are presented in Chapter 3. These two skeletonization methods provides a simple and compact representation of airway and pulmonary vessel trees, respectively (Aim 1 and part of the Aim 2). By using the skeletons of airway and vessel trees, we establish the pairing relations between airway and vessel branches, and characterize the vessel morphology associated at different airway branch locations. The performance of two skeletonization methods have been thoroughly examined by comparing with other state-of-art skeletonization methods using both

computerized phantoms, real-world and medical image examples. Results of new curve skeletonization have established the superiority of the new method as compared to the previous methods in terms of skeleton accuracy as well as robustness in detecting true and false skeletal branches, while results of new fuzzy skeletonization method have shown that the method generates sub-voxel accuracy skeletons and produces nice surface skeleton structures in both real-world shapes as well as medical anatomic structures.

In Chapter 4, we present a semi-automatic framework to segment and measure pulmonary arteries at different lung regions defined by the airway anatomic branches from lung CT images (part of Aim 2 and Aim 3). The method identifies the airway/artery correspondence and use this relationship as a means of characterizing segmental pulmonary arterial dimensions. We have examined the accuracy, stability and reproducibility of the method using healthy human subjects. Experimental results suggest that semi-automatic method provides an effective framework for quantitative assessment of pulmonary arterial morphology at segmental airway locations with high levels of accuracy, robustness, and repeatability, which ensures its application in large cross-sectional and longitudinal studies of exploring arterial roles in different lung diseases.

In Chapter 5, we present an automated method for identifying pulmonary arterial segments from lung CT images using the correspondence with anatomically defined airway branches, and quantifying their morphology (part of Aim 2 and Aim 3). The developed automatic method offers an alternative and objective method for assessing pulmonary arterial morphometry. By combining the orientation, distance and relative anatomy position information of the airway and arterial branches, the automatic method can always find the arterial segments (instead of vein) associated with segmental airway branch at

lower lobes. The experimental results show that the automatic method achieves an accuracy of 84-88% to locate the exactly matching arterial segments (branch level matching accuracy) at lower lobes. Although reasonable good, it may need further improvements to readily apply to large research and clinical studies.

In Chapter 6, we apply our pulmonary arterial assessment method to examine the central pulmonary artery dimensions in a large population of healthy human non-smokers, which were selected from Bioengineering Research Partnership (BRP) study cohort and SubPopulations and InteRmediate Outcome Measures In COPD Study (SPIROMICS) cohort (part of Aim 3). The arterial cross-sectional area (CSA) associated to airway segmental branches of RB10 and LB10 in lower lobes are evaluated, and it is observed that the arterial cross sectional area and airway standardized arterial cross sectional area have a significant negative correlation with age.

In Appendix A and B, the applications of the semi-automatic pulmonary arterial assessment method have been demonstrated in two human disease studies (part of Aim 3): (1) a pilot study for assessing the role of hypoxic pulmonary vasoconstriction (HPV) in emphysema susceptible subjects; (2) part of a SubPopulations and InteRmediate Outcome Measures In COPD Study (SPIROMICS) to evaluate the central pulmonary artery dimensions in subjects with and without emphysema progression. In HPV study, the experimental results show that central pulmonary arterial dimensions associated to segmental airway branches in lower lobes were larger in the emphysema susceptible subjects compared with their emphysema non-susceptible counterparts. In SPIROMICS study, it is shown that emphysema progressors had significantly larger central artery size compared to emphysema nonprogressors and nonsmokers, where the arteries were

measured at segmental airway in middle and lower lobes. Both of these two studies demonstrate the effectiveness of our artery assessment method and indicate the importance of early vascular changes in the early stage of emphysema or COPD.

To summarize, this Ph.D. work holds the promise of providing a standardized and effective regional pulmonary artery metric by exploring the topologic and geometric properties of airway tree and pulmonary vascular tree. It has been successfully applied to large multi-center lung studies, and demonstrates the importance to study the pulmonary vascular changes in the early stage of emphysema or COPD diseases.

7.2 Future Directions

The methods developed in this thesis have a number of potential extensions. Here, we discuss two possible future directions.

7.2.1 Topology Preservation in Curve Skeletonization

Using the minimum-cost path technique, the curve skeletonization method presented in Section 3.2 generates robust and efficient curve skeletons for tree-like objects without noisy skeleton branches. Experiments have shown its superiority in computing airway skeletons. A key difference between a minimum-cost path based skeletonization method and other conventional methods is that a new method sequentially adds branches in the order of their global significance as compared to other methods, where the entire skeleton is generated at once. This unique property of minimum-cost path based method offers a natural hierarchical representation of a centerline tree, and hence, provides a robust performance in terms of noisy branch detection.

However, due to only one skeleton branch being computed (within a subtree) in one iteration, the current method cannot generate a topology-preserved curve skeleton for

objects with tunnels in 3D (loops in 2D). See Figure 40 for a 2D example. Although this limitation does not affect airway skeletonization, it will fail to generate topology-preserved curve skeletons for pulmonary vessel trees, which may have tunnels/loops because of the artery and vein fusion in CT imaging. It would be encouraging if the minimum-cost path based curve skeletonization method can also apply to vessel trees skeletonization.

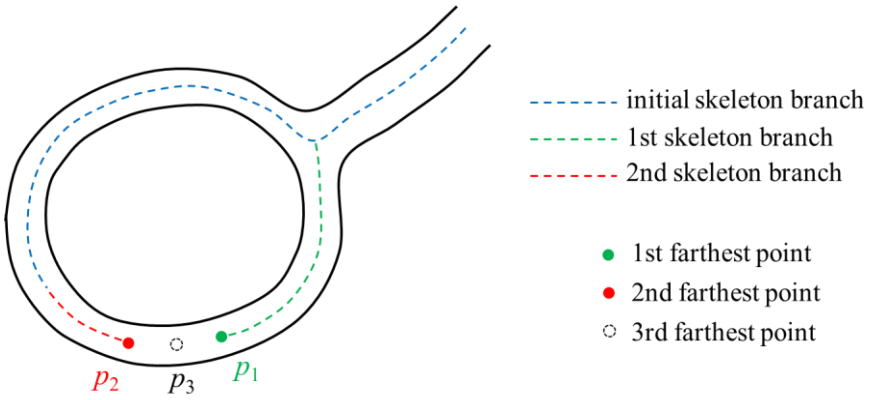

Figure 40 Performance of the new curve skeletonizatoin method in case of a 2D loop structure. The initial skeleton branch is marked by dotted blue line. The method first locates the farthest CMB point p_1 (green), and computes the corresponding skeleton branch (dotted green). After that, the method locates the next farthest point p_2 (red) and generating the corresponding skeleton branch (dotted red). In the next iteration, the farthest point p_3 is found, but it fails to generate a meaningful skeleton branch due to the short distance between p_3 and the nearby skeleton branches.

To solve this problem, it is observed that the detected farthest center of maximal ball (CMB) point and its neighboring points in a subtree in one iteration have different properties in the case of a general branch and tunneled/looped branch. See for Figure 41 the illustration of a 2D case. The observation is also valid in 3D. Recall that the farthest CMB point for a subtree in an iteration is computed by a geodesic distance transform from the current filled object volume to the unmarked object regions, and the CMB point with

largest DT value (in the geodesic sense) in the subtree is detected as the farthest CMB point. For the object without loops, distance values for the CMB point and all of its neighboring points are coming from one distance transform (DT) wave (Figure 41 (a)). In contrast, for a looped object, distance values for certain CMB point and its neighboring points, e.g. n_1, n_2 in Figure 41 (b) are coming from different independent DT waves. Therefore, by checking the sources of DT waves at the farthest CMB point as well as its neighboring points, we can determine if this farthest CMB point is located at a looped branch. If confirmed, then, two skeleton branches can be simultaneously added by computing two minimum-cost paths from this farthest CMB point to two DT sources, respectively.

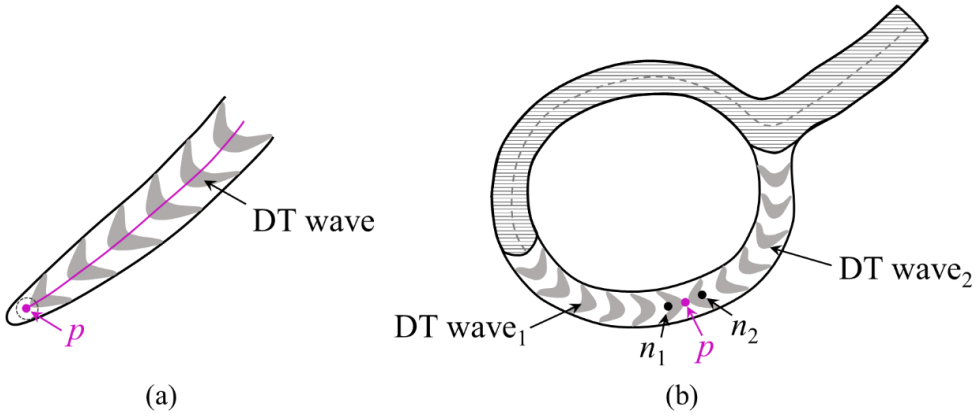

Figure 41 Illustration of the different properties of the farthest CMB point p in a general branch (a) and a looped branch (b). (a) For an object without loops, distance values for the CMB point p and its neighboring points (indicate using dotted circle) are coming from the same distance transform (DT) wave. (b) For a looped object, the shadowed region are current filled object volume. Then, the distance values for the CMB point p and its neighboring points, e.g. n_1, n_2 are coming from different independent DT waves.

7.2.2 Improvements in Automatic Artery Detection

Recall in Chapter 5 that the challenges for the automatic artery identification raise from the topologic and geometric complexity of pulmonary vessel trees, especially in the presence of artery and vein fusions in CT imaging. By utilizing the spatial proximity, parallel orientations and anatomic position information between artery and airway branches, the automatic artery identification method proposed in Chapter 5 can always detect the arterial segments (instead of veins) at the lower lobes of RB10 and LB10 airway branches, with the branch-level artery identification accuracy of 84-88%.

However, for practice use in inter- or intra-subjects analysis, it requires not only to locate arterial segments but also detect the exactly matching arterial segment associated to a specific airway branches (rather than parent or child arterial segments). The current branch-level artery identification accuracy by the automatic method needs to be further improved. The major errors in the current automatic method come from locating either the parent or the child segment of the matching arterial segment associated to an airway branch.

Two directions may be pursued to make the automatic method suitable for practical use. The first direction is to explore larger contextual information when identifying the matching arterial segment, e.g. detection of best matching subtree trees. The current automatic method only found one best matching arterial segment associated to an airway branch, which is vulnerable for small position movement between an airway and artery branch. Instead, a possible improvement is to find a best matching subtree arterial tree from a specific airway segmental plus two sub-segmental branches, which is more stable to locate the exactly matching arterial segment.

The other possible direction is to generate a confidence score for each arterial segment. If the confidence score is low for a detected arterial segment, then, an expert can use the semi-automatic method developed in Chapter 4 to confirm if this is a valid one or not, and re-locate to the true matching arterial segment if needed. Using the confidence score, it may also help to distinguish the different pairing patterns between airway and arterial branches, e.g. if two arterial segments have similar confidence scores at an airway branch, then, it may indicate there are two arterial segments associated to this airway branch. Again, in this case, an expert can use the semi-automatic method to determine the true situation. Possible factors in design of the confidence score include: (1) CSA ratio between airway and artery segments; (2) relative anatomic position between airway and artery segments; (3) overlap rate between airway and artery segments.

REFERENCES

[1] R. A. Pauwels, A. S. Buist, P. M. Calverley, C. R. Jenkins, S. S. Hurd, and G. S. Committee, "Global strategy for the diagnosis, management, and prevention of chronic obstructive pulmonary disease," *American Journal of Respiratory and Critical Care Medicine*, vol. 163 (5), pp. 1256-1276, 2012.

[2] W. H. Organization, "The 10 leading causes of death in the world, 2000 and 2011," *Media center. Updated July*, 2013.

[3] C. D. Mathers and D. Loncar, "Projections of global mortality and burden of disease from 2002 to 2030," *PLoS medicine*, vol. 3 (11), p. e442, 2006.

[4] B. Lomborg, "Global problems, local solutions: Costs and benefits," ed: Cambridge University Press, 2013.

[5] D. D. Sin and S. P. Man, "Chronic obstructive pulmonary disease as a risk factor for cardiovascular morbidity and mortality," *Proceedings of the American Thoracic Society*, vol. 2 (1), pp. 8-11, 2005.

[6] R. G. Barr, D. A. Bluemke, F. S. Ahmed, J. J. Carr, P. L. Enright, E. A. Hoffman, *et al.*, "Percent emphysema, airflow obstruction, and impaired left ventricular filling," *New England Journal of Medicine*, vol. 362 (3), pp. 217-27, Jan 21 2010.

[7] J. A. Barberà, A. Riverola, J. Roca, J. Ramirez, P. D. Wagner, D. Ros, *et al.*, "Pulmonary vascular abnormalities and ventilation-perfusion relationships in mild chronic obstructive pulmonary disease," *American Journal of Respiratory and Critical Care Medicine*, vol. 149 (2), pp. 423-429, 1994.

[8] G. Gould, W. MacNee, A. McLean, P. Warren, A. Redpath, J. Best, *et al.*, "CT measurements of lung density in life can quantitate distal airspace enlargement—an essential defining feature of human emphysema," *American Review of Respiratory Disease*, vol. 137 (2), pp. 380-392, 1988.

[9] W. J. Kim, E. K. Silverman, E. Hoffman, G. J. Criner, Z. Mosenifar, F. C. Sciurba, *et al.*, "CT metrics of airway disease and emphysema in severe COPD," *CHEST Journal*, vol. 136 (2), pp. 396-404, 2009.

[10] J. M. Wells and M. T. Dransfield, "Pathophysiology and clinical implications of pulmonary arterial enlargement in COPD," *International Journal of Chronic Obstructive Pulmonary Disease*, vol. 8 pp. 509-21, 2013.

[11] K. S. Iyer, J. Newell, John D, D. Jin, M. K. Fuld, P. K. Saha, S. Hansdottir, *et al.*, "Quantitative Dual Energy Computed Tomography Supports a Vascular Etiology of Smoking Induced Inflammatory Lung Disease," *American Journal of Respiratory and Critical Care Medicine*, vol. 193 (6), pp. 652-661, 2016.

[12] S. Santos, V. I. Peinado, J. Ramirez, T. Melgosa, J. Roca, R. Rodriguez-Roisin, *et al.*, "Characterization of pulmonary vascular remodelling in smokers and patients with mild COPD," *European Respiratory Journal*, vol. 19 (4), pp. 632-8, Apr 2002.

[13] R. G. Barr, S. Mesia-Vela, J. H. Austin, R. C. Basner, B. M. Keller, A. P. Reeves, *et al.*, "Impaired flow-mediated dilation is associated with low pulmonary function and emphysema in ex-smokers: the Emphysema and Cancer Action Project (EMCAP) Study," *American Journal of Respiratory and Critical Care Medicine*, vol. 176 (12), pp. 1200-1207, 2007.

[14] S. Matsuoka, G. R. Washko, M. T. Dransfield, T. Yamashiro, R. San Jose Estepar, A. Diaz, *et al.*, "Quantitative CT measurement of cross-sectional area of small pulmonary vessel in COPD: correlations with emphysema and airflow limitation," *Academic Radiology*, vol. 17 (1), pp. 93-9, Jan 2010.

[15] J. M. Wells, G. R. Washko, M. K. Han, N. Abbas, H. Nath, A. J. Mamary, *et al.*, "Pulmonary arterial enlargement and acute exacerbations of COPD," *New England Journal of Medicine*, vol. 367 (10), pp. 913-21, Sep 6 2012.

[16] D. Jin, K. S. Iyer, E. A. Hoffman, and P. K. Saha, "A New Approach of Arc Skeletonization for Tree-Like Objects Using Minimum Cost Path," in *International Conference on Pattern Recognition*, Stockholm, Sweden, 2014, pp. 942-947.

[17] D. Jin, K. S. Iyer, C. Chen, E. A. Hoffman, and P. K. Saha, "A robust and efficient curve skeletonization algorithm for tree-like objects using minimum cost paths," *Pattern Recognition Letters*, vol. 76 pp. 32-40, 2016.

[18] D. Jin, Y. Liu, and P. K. Saha, "Application of fuzzy skeletonization to quantitative assess of trabecular bone micro-architecture," presented at the International Conference of the IEEE Engineering in Medicine and Biology Society, Osaka, Japan, 2013.

[19] D. Jin and P. K. Saha, "A new fuzzy skeletonization algorithm and its applications to medical imaging," in *International Conference on Image Analysis and Processing*, Naples, Italy, 2013, pp. 662-671.

[20] D. Jin, C. Chen, and P. K. Saha, "Filtering Non-Significant Quench Points Using Collision Impact in Grassfire Propagation," in *International Conference on Image Analysis and Processing*, 2015, pp. 432-443.

[21] P. K. Saha, D. Jin, Y. Liu, G. E. Christensen, and C. Chen, "Fuzzy Skeletonization: Theories, Algorithms and the Applications," *IEEE Transactions on Visualization and Computer Graphics*, revised.

[22] D. Jin, J. Guo, T. M. Dougherty, K. S. Iyer, E. A. Hoffman, and P. K. Saha, "A semi-automatic framework of measuring pulmonary arterial metrics at anatomic airway locations using CT imaging," in *SPIE Medical Imaging*, 2016, pp. 978816-6.

[23] D. Jin, T. M. Dougherty, J. Guo, E. A. Hoffman, J. Newell, John D, and P. K. Saha, "Exploration of Vascular Role in COPD Etiology: Standardization and Validation of Regional Pulmonary Arterial Cross Sectional Area Measures from CT," *American Journal of Respiratory and Critical Care Medicine*, vol. 193 p. A5821, 2016.

[24] J. Guo, C. Wang, K.-S. Chan, D. Jin, P. K. Saha, J. P. Sieren, *et al.*, "A controlled statistical study to assess measurement variability as a function of test object position and configuration for automated surveillance in a multicenter longitudinal COPD study (SPIROMICS)," *Medical physics*, vol. 43 (5), pp. 2598-2610, 2016.

[25] D. Jin, T. M. Dougherty, J. Guo, K. S. Iyer, J. Newell, John D, E. A. Hoffman, *et al.*, "A CT-based semi-automatic method for quantitative morphometry of pulmonary arteries associated to anatomic airway locations," *Journal of Applied Physiology*, submitted.

[26] D. Jin, K. S. Iyer, E. A. Hoffman, and P. K. Saha, "Automated assessment of pulmonary arterial morphology in multi-row detector CT imaging using correspondence with anatomic airway branches," in *Proceeding of 11th Intern Symp on Visual Computing (ISVC)*, Las Vegas, NV, 2014, pp. 521-530.

[27] D. Jin, K. S. Iyer, E. A. Hoffman, and P. K. Saha, "Reconstruction Of Pulmonary Central Artery Volume In MDCT Imaging Using Airway Correspondence At Different Anatomic Branches," *American Journal of Respiratory and Critical Care Medicine*, vol. 189 p. A4311, 2014.

[28] A. Rosenfeld, "Digital topology," *American Mathematical Monthly*, vol. 86 (8), pp. 621-630, 1979.

[29] R. O. Duda and J. H. Munson, "Graphical-data-processing research study and experimental investigation," Stanford Research Institute, Menlo Park, CA AD657670, 1967.

[30] A. Rosenfeld, "Connectivity in digital pictures," *Journal of Association for Computing Machinery*, vol. 17 pp. 146-160, 1970.

[31] J. C. Alexander and A. Thaler, "The boundary count of digital pictures," *Journal of Association for Computing Machinery*, vol. 18 (1), pp. 105-112, 1971.

[32] J. Mylopoulos and T. Pavlidis, "On the topological properties of quantized spaces II: connectivity and order of connectivity," *Journal of Association for Computing Machinery*, vol. 18 pp. 247-254, 1971.

[33] S. B. Gray, "Local properties of binary images in two dimensions," *IEEE Transactions on Computers*, vol. 100 (5), pp. 551-561, 1971.

[34] A. Rosenfeld, "Adjacency in digital pictures," *Information and Control*, vol. 26 pp. 24-33, 1974.

[35] T. C. Hales, "The Jordan curve theorem, formally and informally," *The American Mathematical Monthly*, pp. 882-894, 2007.

[36] T. Y. Kong and A. W. Roscoe, "A theory of binary digital pictures," *Computer Vision, Graphics, and Image Processing*, vol. 32 (2), pp. 221-243, 1985.

[37] T. Kong and A. Roscoe, "Continuous analogs of axiomatized digital surfaces," *Computer Vision, Graphics, and Image Processing*, vol. 29 (1), pp. 60-86, 1985.

[38] V. A. Kovalevsky, "Finite topology as applied to image processing," *Computer Vision, Graphics and Image Processing*, vol. 46 pp. 141-161, 1989.

[39] T. Y. Kong, "Topology-preserving deletion of 1's from 2-, 3-and 4-dimensional binary images," in *International Workshop on Discrete Geometry for Computer Imagery*, Montpellier, France, 1997, pp. 1-18.

[40] Y. Cointepas, I. Bloch, and L. Garnero, "A cellular model for multi-objects multi-dimensional homotopic deformations," *Pattern Recognition,* vol. 34 (9), pp. 1785-1798, 2001.

[41] G. Bertrand and M. Couprie, "On parallel thinning algorithms: minimal non-simple sets, P-simple points and critical kernels," *Journal of Mathematical Imaging and Vision,* vol. 35 (1), pp. 23-35, 2009.

[42] M. J. Cardoso, M. J. Clarkson, M. Modat, and S. Ourselin, "On the extraction of topologically correct thickness measurements using Khalimsky's cubic complex," in *International Conference on Information Processing in Medical Imaging*, 2011, pp. 159-170.

[43] T. Y. Kong, "A digital fundamental group," *Computers & Graphics,* vol. 13 (2), pp. 159-166, 1989.

[44] L. Boxer and I. Karaca, "Some properties of digital covering spaces," *Journal of Mathematical Imaging and Vision,* vol. 37 (1), pp. 17-26, 2010.

[45] R. Malgouyres, "Homotopy in two-dimensional digital images," *Theoretical Computer Science,* vol. 230 (1), pp. 221-233, 2000.

[46] S.-E. Han, "Digital fundamental group and Euler characteristic of a connected sum of digital closed surfaces," *Information Sciences,* vol. 177 (16), pp. 3314-3326, 2007.

[47] R. Ayala, E. Domınguez, A. R. Francés, and A. Quintero, "Digital homotopy with obstacles," *Discrete Applied Mathematics,* vol. 139 (1), pp. 5-30, 2004.

[48] L. Boxer, I. Karaca, and A. Oztel, "Topological invariants in digital images," *Journal of Mathematical Sciences: Advances and Applications,* vol. 11 (2), 2011.

[49] J. Šlapal, "Closure operations for digital topology," *Theoretical Computer Science*, vol. 305 (1), pp. 457-471, 2003.

[50] M. Minsky and S. Papert, *Perceptrons: An Introduction to Computational Geometry*. Cambridge, MA: MIT Press, 1969.

[51] J. Sklansky, "Recognition of convex blobs," *Pattern Recognition,* vol. 2 (1), pp. 3-10, 1970.

[52] J. E. Bresenham, "Algorithm for computer control of a digital plotter," *IBM Systems Journal,* vol. 4 (1), pp. 25-30, 1965.

[53] A. Rosenfeld, "Digital straight line segments," *IEEE Transactions on Computers,* vol. 100 (12), pp. 1264-1269, 1974.

[54] R. Brons, "Linguistic methods for the description of a straight line on a grid," *Computer Graphics and Image Processing,* vol. 3 (1), pp. 48-62, 1974.

[55] L. Dorst and A. W. Smeulders, "Discrete representation of straight lines," *IEEE Transactions on Pattern Analysis and Machine Intelligence,* (4), pp. 450-463, 1984.

[56] Z. Kulpa, "Area and perimeter measurement of blobs in discrete binary pictures," *Computer Graphics and Image Processing,* vol. 6 (5), pp. 434-451, 1977.

[57] R. M. Haralick, "A measure for circularity of digital figures," *IEEE Transactions on Systems, Man and Cybernetics,* (4), pp. 394-396, 1974.

[58] A. Nakamura and K. Aizawa, "Digital circles," *Computer Vision, Graphics, and Image Processing,* vol. 26 (2), pp. 242-255, 1984.

[59] G. Borgefors, "Distance transformations in digital images," *Computer Vision, Graphics and Image Processing,* vol. 34 pp. 344–371, 1986.

[60] G. Windreich, N. Kiryati, and G. Lohmann, "Voxel-based surface area estimation: from theory to practice," *Pattern Recognition,* vol. 36 (11), pp. 2531-2541, 2003.

[61] A. Rosenfeld and S. Haber, "The perimeter of a fuzzy set," *Pattern Recognition,* vol. 18 (2), pp. 125-130, 1985.

[62] N. Sladoje, I. Nyström, and P. K. Saha, "Measurements of digitized objects with fuzzy borders in 2D and 3D," *Image and Vision Computing,* vol. 23 pp. 123-132, 2005.

[63] A. Rosenfeld, "Compact figures in digital pictures," *IEEE Transactions on Systems, Man and Cybernetics,* (2), pp. 221-223, 1974.

[64] P.-E. Danielson, "A new shape factor," *Computer Graphics and Image Processing,* vol. 7 (2), pp. 292-299, 1978.

[65] H. Blum, "A transformation for extracting new descriptors of shape," *Models for the perception of speech and visual form,* vol. 19 (5), pp. 362-380, 1967.

[66] T. Y. Kong and A. Rosenfeld, "Digital topology: introduction and survey," *Computer Vision, Graphics, and Image Processing,* vol. 48 pp. 357-393, 1989.

[67] K. Siddiqi and S. M. Pizer, *Medial representations: mathematics, algorithms and applications*: Springer, 2008.

[68] P. K. Saha, G. Borgefors, and G. S. di Baja, "A survey on skeletonization algorithms and their applications," *Pattern Recognition Letters,* vol. 76 pp. 3-12, 2016.

[69] N. D. Cornea, D. Silver, and P. Min, "Curve-skeleton properties, applications, and algorithms," *IEEE Transactions on Visualization and Computer Graphics,* vol. 13 (3), pp. 530-548, 2007.

[70] M. Sramek and A. E. Kaufman, "Alias-free voxelization of geometric objects," *IEEE Transactions on Visualization and Computer Graphics,* vol. 5 (3), pp. 251-267, 1999.

[71] W. Lorensen and H. Cline, "Marching Cubes: a high resolution 3D surface construction Algorithm," *Computer Graphics,* vol. 21 pp. 163-169, 1987.

[72] L. Lam, S.-W. Lee, and C. Y. Suen, "Thinning methodologies - a comprehensive survey," *IEEE Transactions on Pattern Analysis and Machine Intelligence,* vol. 14 (9), pp. 869-885, 1992.

[73] P. K. Saha and B. B. Chaudhuri, "Detection of 3-D simple points for topology preserving transformations with application to thinning," *IEEE Transactions on Pattern Analysis and Machine Intelligence*, vol. 16 pp. 1028-1032, 1994.

[74] P. K. Saha and B. B. Chaudhuri, "3D digital topology under binary transformation with applications," *Computer Vision and Image Understanding*, vol. 63 pp. 418-429, 1996.

[75] G. Sanniti di Baja and S. Svensson, "A new shape descriptor for surfaces in 3D images," *Pattern Recognition Letters*, vol. 23 (6), pp. 703-711, 2002.

[76] S. Svensson, I. Nyström, and G. Sanniti di Baja, "Curve skeletonization of surface-like objects in 3d images guided by voxel classification," *Pattern Recognition Letters*, vol. 23 (12), pp. 1419-1426, 2002.

[77] T. K. Dey and J. Sun, "Defining and computing curve-skeletons with medial geodesic function," in *Proceeding of Symposium on Geometry Processing*, 2006, pp. 143-152.

[78] D. C. Banks and B. A. Singer, "Vortex tubes in turbulent flows: identification, representation, reconstruction," in *Proceedings of the conference on Visualization*, 1994, pp. 132-139.

[79] G. Sanniti di Baja and S. Svensson, "Surface skeletons detected on the D6 distance transform," in *Joint IAPR International Workshops on SSPR*, 2000, pp. 387-396.

[80] K. Palágyi, "A 3-subiteration 3D thinning algorithm for extracting medial surfaces," *Pattern Recognition Letters*, vol. 23 (6), pp. 663-675, 2002.

[81] K. Siddiqi, S. Bouix, A. Tannenbaum, and S. W. Zucker, "Hamilton-Jacobi Skeletons," *International Journal of Computer Vision*, vol. 48 (3), pp. 215-231, 2002.

[82] C. Arcelli, G. S. di Baja, and L. Serino, "New removal operators for surface skeletonization," in *International Conference on Discrete Geometry for Computer Imagery*, 2006, pp. 555-566.

[83] M. Couprie, D. Coeurjolly, and R. Zrour, "Discrete bisector function and Euclidean skeleton in 2D and 3D," *Image and Vision Computing*, vol. 25 (10), pp. 1543-1556, 2007.

[84] T. Ju, M. L. Baker, and W. Chiu, "Computing a family of skeletons of volumetric models for shape description," *Computer-Aided Design*, vol. 39 (5), pp. 352-360, 2007.

[85] C. M. Ma and M. Sonka, "A fully parallel 3D thinning algorithm and Its applications," *Computer Vision Image Understanding*, vol. 64 pp. 420-433, 1996.

[86] Y. Zhou, A. Kaufman, and A. W. Toga, "Three-dimensional skeleton and centerline generation based on an approximate minimum distance field," *The Visual Computer*, vol. 14 (7), pp. 303-314, 1998.

[87] J.-H. Chuang, C.-H. Tsai, and M.-C. Ko, "Skeletonization of three-dimensional object using generalized potential field," *IEEE Transactions On Pattern Analysis And Machine Intelligence,* vol. 22 pp. 1241-1251, 2000.

[88] I. Bitter, A. E. Kaufman, and M. Sato, "Penalized-distance volumetric skeleton algorithm," *IEEE Transactions on Visualization and Computer Graphics,* vol. 7 (3), pp. 195-206, 2001.

[89] W. Xie, R. P. Thompson, and R. Perucchio, "A topology-preserving parallel 3D thinning algorithm for extracting the curve skeleton," *Pattern Recognition,* vol. 36 pp. 1529-1544, 2003.

[90] S. Bouix, K. Siddiqi, and A. Tannenbaum, "Flux driven automatic centerline extraction," *Medical Image Analysis,* vol. 9 (3), pp. 209-221, 2005.

[91] N. D. Cornea, D. Silver, X. Yuan, and R. Balasubramanian, "Computing hierarchical curve-skeletons of 3D objects," *The Visual Computer,* vol. 21 (11), pp. 945-955, 2005.

[92] D. Reniers, J. J. Van Wijk, and A. Telea, "Computing multiscale curve and surface skeletons of genus 0 shapes using a global importance measure," *IEEE Transactions on Visualization and Computer Graphics,* vol. 14 (2), pp. 355-368, 2008.

[93] M. S. Hassouna and A. A. Farag, "Variational curve skeletons using gradient vector flow," *IEEE Transactions on Pattern Analysis and Machine Intelligence,* vol. 31 (12), pp. 2257-2274, 2009.

[94] S. Wang, J. Wu, M. W, and X. Ma, "Robust curve skeleton extraction for vascular structures," *Graphical Models,* vol. 74 pp. 109-120, 2012.

[95] T.-C. Lee, R. L. Kashyap, and C.-N. Chu, "Building skeleton models via 3-D medial surface/axis thinning algorithm," *CVGIP: Graphical Models and Image Processing,* vol. 56 (6), pp. 462-478, 1994.

[96] P. K. Saha, B. B. Chaudhuri, and D. D. Majumder, "A new shape preserving parallel thinning algorithm for 3D digital images," *Pattern Recognition,* vol. 30 pp. 1939-1955, 1997.

[97] C. Pudney, "Distance-ordered homotopic thinning: a skeletonization algorithm for 3D digital images," *Computer Vision and Image Understanding,* vol. 72 (2), pp. 404-413, 1998.

[98] C. M. Ma and S. Y. Wan, "Parallel thinning algorithms on 3D (18, 6) binary images," *Computer Vision and Image Understanding,* vol. 80 pp. 364-378, 2000.

[99] C. Lohou and G. Bertrand, "A 3D 6-subiteration curve thinning algorithm based on P-simple points," *Discrete Applied Mathematics,* vol. 151 (1), pp. 198-228, 2005.

[100] C. Arcelli, G. Sanniti di Baja, and L. Serino, "Distance-driven skeletonization in voxel images," *IEEE Transactions on Pattern Analysis and Machine Intelligence,* vol. 33 (4), pp. 709-720, Apr 2011.

[101] A. C. Jalba, A. Sobiecki, and A. C. Telea, "An unified multiscale framework for planar, surface, and curve skeletonization," *IEEE Transactions on Pattern Analysis and Machine Intelligence*, vol. 38 (1), pp. 30-45, 2016.

[102] Y. F. Tsao and K. S. Fu, "A parallel thinning algorithm for 3D pictures," *Computer Graphics and Image Processing*, vol. 17 pp. 315-331, 1981.

[103] G. Borgefors, I. Nyström, and G. Sanniti di Baja, "Computing skeletons in three dimensions," *Pattern Recognition*, vol. 32 (7), pp. 1225-1236, 1999.

[104] K. Palágyi and A. Kuba, "A 3D 6-subiteration thinning algorithm for extracting medial lines," *Pattern Recognition Letters*, vol. 19 (7), pp. 613-627, 1998.

[105] K. Palágyi and A. Kuba, "A parallel 3D 12-subiteration thinning algorithm," *Graphical Models and Image Processing*, vol. 61 pp. 199-221, 1999.

[106] G. Németh, P. Kardos, and K. Palágyi, "Thinning combined with iteration-by-iteration smoothing for 3D binary images," *Graphical Models*, vol. 73 pp. 335–345, 2011.

[107] C. Arcelli and G. Sanniti di Baja, "Finding Local Maxima in a Pseudo- Euclidean Distance Transform," *Computer Vision, Graphics and Image Processing*, vol. 43 pp. 361-367, 1988.

[108] M. S. Hassouna and A. A. Farag, "Robust centerline extraction framework using level sets," in *IEEE Computer Society Conference on Computer Vision and Pattern Recognition*, 2005, pp. 458-465.

[109] D. S. Paik, C. F. Beaulieu, R. B. Jeffrey, G. D. Rubin, and S. Napel, "Automated flight path planning for virtual endoscopy," *Medical Physics*, vol. 25 (5), pp. 629-637, 1998.

[110] I. Bitter, M. Sato, M. Bender, K. T. McDonnell, A. Kaufman, and M. Wan, "CEASAR: a smooth, accurate and robust centerline extraction algorithm," in *Proceedings of the conference on Visualization*, 2000, pp. 45-52.

[111] M. Sato, I. Bitter, M. A. Bender, A. E. Kaufman, and M. Nakajima, "TEASAR: Tree-structure extraction algorithm for accurate and robust skeletons," in *Proceedings of the Eighth Pacific Conference on Computer Graphics and Applications.* , 2000, pp. 281-449.

[112] M. Wan, Z. Liang, Q. Ke, L. Hong, I. Bitter, and A. Kaufman, "Automatic centerline extraction for virtual colonoscopy," *IEEE Transactions on Medical Imaging*, vol. 21 pp. 1450-1460, 2002.

[113] S. K. Pal, "Fuzzy skeletonization of an image," *Pattern Recognition Letters*, vol. 10 pp. 17-23, 1989.

[114] P. J. Yim, P. L. Choyke, and R. M. Summers, "Gray-scale skeletonization of small vessels in magnetic resonance angiography," *IEEE Transactions on Medical Imaging*, vol. 19 (6), pp. 568-76, Jun 2000.

[115] G. Sanniti di Baja, I. Nyström, and G. Borgefors, "Discrete 3D tools applied to 2D grey-level images," presented at the International Conference on Image Analysis and Processing, *LNCS-3617*, 2005.

[116] G. Malandain and G. Bertrand, "Fast characterization of 3-D simple points," in *11th International Conference on Pattern Recognition*, 1992, pp. 232-235.

[117] C. Arcelli and G. Sanniti di Baja, "A width-independent fast thinning algorithm," *IEEE Transactions on Pattern Analysis and Machine Intelligence,* vol. 7 (4), pp. 463-474, Apr 1985.

[118] T. Saito and J.-I. Toriwaki, "A sequential thinning algorithm for three dimensional digital pictures using the Euclidean distance transformation," in *9th Scandinavian Conference on Image Analysis (SCIA'95), IAPR*, Uppsala, Sweden, 1995, pp. 507-516.

[119] G. Borgefors, I. Nyström, G. Sanniti di Baja, and S. Svensson, "Simplification of 3D skeletons using distance information," presented at the SPIE: Vision Geometry, *4117*, San Diego, CA, 2000.

[120] G. Borgefors, "On digital distance transformation in three dimensions," *Computer Vision Graphics Image Processing,* vol. 64 pp. 368-376, 1996.

[121] S. D. Olabarriaga, M. Breeuwer, and W. J. Niessen, "Minimum cost path algorithm for coronary artery central axis tracking in CT images," in *International Conference on Medical Image Computing and Computer-Assisted Intervention*, 2003, pp. 687-694.

[122] M. Schaap, C. T. Metz, T. van Walsum, A. G. van der Giessen, A. C. Weustink, N. R. Mollet, *et al.*, "Standardized evaluation methodology and reference database for evaluating coronary artery centerline extraction algorithms," *Medical Image Analysis,* vol. 13 (5), pp. 701-14, 2009.

[123] S. R. Aylward and E. Bullitt, "Initialization, noise, singularities, and scale in height ridge traversal for tubular object centerline extraction," *IEEE Transaction on Medical Imaging,* vol. 21 pp. 61-75, 2002.

[124] T. Deschamps and L. D. Cohen, "Fast extraction of minimal paths in 3D images and applications to virtual endoscopy," *Medical Image Analysis,* vol. 5 pp. 281-299, 2001.

[125] O. Wink, A. F. Frangi, B. Verdonck, M. A. Viergever, and W. J. Niessen, "3D MRA coronary axis determination using a minimum cost path approach," *Magnetic Resonance in Medicine,* vol. 47 (6), pp. 1169-1175, 2002.

[126] F. Benmansour and L. D. Cohen, "Tubular structure segmentation based on minimal path method and anisotropic enhancement," *International Journal of Computer Vision,* vol. 92 (2), pp. 192-210, 2011.

[127] Y. Rouchdy and L. D. Cohen, "Geodesic voting for the automatic extraction of tree structures. Methods and applications," *Computer Vision and Image Understanding,* vol. 117 (10), pp. 1453-1467, 2013.

[128] G. Peyré, M. Péchaud, R. Keriven, and L. D. Cohen, "Geodesic methods in computer vision and graphics," *Foundations and Trends in Computer Graphics and Vision*, vol. 5 (3–4), pp. 197-397, 2010.

[129] P. K. Saha and J. K. Udupa, "Optimum threshold selection using class uncertainty and region homogeneity," *IEEE Transactions on Pattern Analysis and Machine Intelligence*, vol. 23 pp. 689-706, 2001.

[130] S. K. Pal and A. Rosenfeld, "Image enhancement and thresholding by optimization of fuzzy compactness," *Pattern Recognition Letters*, vol. 7 pp. 77-86, 1988.

[131] P. K. Saha and F. W. Wehrli, "Fuzzy distance transform in general digital grids and its applications," presented at the 7th Joint Conference on Information Sciences, Research Triangular Park, NC, 2003.

[132] K. Mori, J. Hasegawa, Y. Suenaga, and J. Toriwaki, "Automated anatomical labeling of the bronchial branch and its application to the virtual bronchoscopy system," *IEEE Transactions on Medical Imaging*, vol. 19 (2), pp. 103-14, Feb 2000.

[133] R. Swift, A. Kiraly, A. Sherbondy, A. Austin, E. Hoffman, G. McLennan, *et al.*, "Automatic axis generation for virtual bronchoscopic assessment of major airway obstructions," *Computerized Medical Imaging and Graphics*, vol. 26 (2), pp. 103-118, 2002.

[134] T. Schlathoelter, C. Lorenz, I. C. Carlsen, S. Renisch, and T. Deschamps, "Simultaneous segmentation and tree reconstruction of the airways for virtual bronchoscopy," in *SPIE: Medical Imaging*, 2002, pp. 103-113.

[135] A. P. Kiraly, J. P. Helferty, E. A. Hoffman, G. McLennan, and W. E. Higgins, "Three-dimensional path planning for virtual bronchoscopy," *IEEE Transactions on Medical Imaging*, vol. 23 (11), pp. 1365-79, Nov 2004.

[136] T. Bülow, C. Lorenz, and S. Renisch, "A general framework for tree segmentation and reconstruction from medical volume data," in *International Conference on Medical Image Computing and Computer-Assisted Intervention*, 2004, pp. 533-540.

[137] C. I. Fetita, F. Prêteux, C. Beigelman-Aubry, and P. Grenier, "Pulmonary airways: 3-D reconstruction from multislice CT and clinical investigation," *IEEE Transactions on Medical Imaging*, vol. 23 (11), pp. 1353-1364, 2004.

[138] J. Tschirren, E. A. Hoffman, G. McLennan, and M. Sonka, "Intrathoracic airway trees: segmentation and airway morphology analysis from low-dose CT scans," *IEEE Transactions on Medical Imaging*, vol. 24 (12), pp. 1529-1539, 2005.

[139] M. W. Graham, J. D. Gibbs, and W. E. Higgins, "Robust system for human airway-tree segmentation," in *SPIE: Medical Imaging*, 2008, pp. 69141J-69141J-18.

[140] P. Lo and M. de Bruijne, "Voxel classification based airway tree segmentation," in *SPIE: Medical Imaging*, 2008, pp. 69141K-69141K-12.

[141] H. Kitaoka, Y. Park, J. Tschirren, J. Reinhardt, M. Sonka, G. McLennan, *et al.*, "Automated nomenclature labeling of the bronchial tree in 3D-CT lung images," in *International Conference on Medical Image Computing and Computer-Assisted Intervention*, ed: Springer, 2002, pp. 1-11.

[142] J. Tschirren, G. McLennan, K. Palagyi, E. A. Hoffman, and M. Sonka, "Matching and anatomical labeling of human airway tree," *IEEE Transactions on Medical Imaging*, vol. 24 (12), pp. 1540-1547, Dec 2005.

[143] B. van Ginneken, W. Baggerman, and E. M. van Rikxoort, "Robust segmentation and anatomical labeling of the airway tree from thoracic CT scans," in *International Conference on Medical Image Computing and Computer-Assisted Intervention*, ed: Springer, 2008, pp. 219-226.

[144] P. Lo, E. M. van Rikxoort, J. Goldin, F. Abtin, M. de Bruijne, and M. Brown, "A bottom-up approach for labeling of human airway trees," in *International Conference on Medical Image Computing and Computer-Assisted Intervention*, 2011, pp. 23-34.

[145] A. Feragen, J. Petersen, M. Owen, P. Lo, L. H. Thomsen, M. M. Wille, *et al.*, "A hierarchical scheme for geodesic anatomical labeling of airway trees," in *International Conference on Medical Image Computing and Computer-Assisted Intervention*, ed: Springer, 2012, pp. 147-155.

[146] R. Carraghan and P. M. Pardalos, "An exact algorithm for the maximum clique problem," *Operations Research Letters*, vol. 9 (6), pp. 375-382, 1990.

[147] M. Pelillo, K. Siddiqi, and S. W. Zucker, "Matching hierarchical structures using association graphs," *IEEE Transactions on Pattern Analysis and Machine Intelligence*, vol. 21 (11), pp. 1105-1120, 1999.

[148] M. G. Linguraru, J. A. Pura, R. L. Van Uitert, N. Mukherjee, R. M. Summers, C. Min- niti, *et al.*, "Segmentation and quantification of pulmonary artery for noninvasive CT assessment of sickle cell secondary pulmonary hypertension.," *Medical Physics*, vol. 37 (4), pp. 1522-1532, 2010.

[149] Y. Sato, S. Nakajima, N. Shiraga, H. Atsumi, S. Yoshida, T. Koller, *et al.*, "Three-dimensional multi-scale line filter for segmentation and visualization of curvilinear structures in medical images.," *Medical Image Analysis*, vol. 2 (2), pp. 143-168, 1998.

[150] A. F. Frangi, W. J. Niessen, R. M. Hoogeveen, T. van Walsum, and M. A. Viergever, "Model-based quantitation of 3-D magnetic resonance angiographic images.," *IEEE Transactions on Medical Imaging*, vol. 18 (10), pp. 946-956, 1999.

[151] K. Krissian, G. Malandain, N. Ayache, R. Vaillant, and Y. Trousset, "Model Based Detection of Tubular Structures in 3D Images.," *Computer Vision and Image Understanding*, vol. 80 (2), pp. 130-171, 2000.

[152] E. M. van Rikxoort and B. van Ginneken, "Automated segmentation of pulmonary structures in thoracic computed tomography scans: a review.," *Physics in Medicine and Biology*, vol. 58 pp. 187-220, 2013.

[153] R. D. Rudyanto, S. Kerkstra, E. M. van Rikxoort, C. Fetita, P.-Y. Brillet, C. Lefevre, *et al.*, "Comparing algorithms for automated vessel segmentation in computed tomography scans of the lung: the VESSEL12 study.," *Medical Image Analysis*, vol. 18 (7), pp. 1217-1232, 2012.

[154] C. Pisupati, L. Wolff, W. Mitzner, and E. Zerhouni, "Tracking 3-D pulmonary tree structures," in *Proceeding of the Workshop on Mathematical Methods in Biomedical Image Analysis*, 1996, pp. 160-169.

[155] T. Büelow, R. Wiemker, T. Blaffert, C. Lorenz, and S. Renisch, "Automatic extraction of the pulmonary artery tree from multi-slice CT data," in *SPIE: Medical Imaging*, San Diego, CA, 2005, pp. 730-740.

[156] S. Park, C. Bajaj, and G. Gladish, "Artery-vein separation of human vasculature from 3D thoracic CT angio scans.," in *International Symposium CompIMAGE*, 2006, pp. 331-336.

[157] T. Yonekura, M. Matsuhiro, S. Saita, M. Kubo, Y. Kawata, N. Niki, *et al.*, "Classification algorithm of pulmonary vein and artery based on multi-slice CT image," in *SPIE: Medical Imaging*, San Diego, CA, 2007, pp. 65142E1-65142E8.

[158] P. K. Saha, Z. Gao, S. K. Alford, M. Sonka, and E. A. Hoffman, "Topomorphologic separation of fused isointensity objects via multiscale opening: separating arteries and veins in 3-D pulmonary CT," *IEEE Transactions on Medical Imaging*, vol. 29 (3), pp. 840-851, 2010.

[159] Z. Gao, R. Grout, C. Holtze, E. A. Hoffman, and P. K. Saha, "A new paradigm of interactive artery/vein separation in non-contrast pulmonary CT imaging using multi-scale topo-morphologic opening," *IEEE Transactions on Biomedical Engineering*, vol. 59 (11), pp. 3016-3027, 2012.

[160] S. Park, S. M. Lee, N. Kim, J. B. Seo, and H. Shin, "Automatic reconstruction of the arterial and venous trees on volumetric chest CT.," *Medical Physics*, vol. 40 (7), p. 071906, 2013.

[161] Y. Kitamura, Y. Li, W. Ito, and H. Ishikawa, "Data-dependent higher-order clique selection for artery-vein segmentation by energy minimization," *International Journal of Computer Vision*, vol. 117 (2), pp. 142-158, 2016.

[162] C. Payer, M. Pienn, Z. Balint, S. A., T. E., N. E., *et al.*, "Automated integer programming based separation of arteries and veins from thoracic CT images," *Medical Image Analysis*, vol. (in press) 2016.

[163] D. M. Vasilescu, Z. Gao, P. K. Saha, L. Yin, G. Wang, B. Haefeli-Bleuer, *et al.*, "Assessment of morphometry of pulmonary acini in mouse lungs by nondestructive imaging using multiscale microcomputed tomography," *Proceedings of the National Academy of Sciences of the United States of America*, vol. 109 (42), pp. 17105-10, Oct 16 2012.

[164] A. Rosenfeld, "Arcs and curves in digital pictures," *Journal of the Association for Computing Machinery*, vol. 20 pp. 81-87, 1973.

[165] C. J. Hilditch, "Linear skeletons from square cupboards," in *Machine Intelligence*. vol. 4, B. Meltzer and D. Michie, Eds., ed Edinburgh, U.K.: Edinburgh Univ. Press, 1969, pp. 403-420.

[166] G. Tourlakis and J. Mylopoulos, "Some results on computational topology," *Journal of Association for Computing Machinery,* vol. 20 pp. 439-455, 1973.

[167] D. G. Morgenthaler, "Three-dimensional simple points: serial erosion, parallel thinning and skeletonization," Computer Vision Laboratory, University of Maryland, College Park, MD1981.

[168] S. Lobregt, P. W. Verbeek, and F. C. A. Groen, "Three-dimensional skeletonization, principle, and algorithm," *IEEE Transactions on Pattern Analysis and Machine Intelligence,* vol. 2 pp. 75-77, 1980.

[169] P. K. Saha, B. B. Chaudhuri, B. Chanda, and D. D. Majumder, "Topology preservation in 3D digital space," *Pattern Recognition,* vol. 27 pp. 295-300, 1994.

[170] P. K. Saha, B. Chanda, and D. D. Majumder, "Principles and algorithms for 2-D and 3-D shrinking," Indian Statistical Institute, Calcutta, India TR/KBCS/2/91, 1991.

[171] P. K. Saha, F. W. Wehrli, and B. R. Gomberg, "Fuzzy distance transform: theory, algorithms, and applications," *Computer Vision and Image Understanding,* vol. 86 pp. 171-190, 2002.

[172] G. Sanniti di Baja, "Well-shaped, stable, and reversible skeletons from the (3,4)-distance transform," *Journal of Visual Communication and Image Representation,* vol. 5 pp. 107-115, 1994.

[173] S. Svensson, "Aspects on the reverse fuzzy distance transform," *Pattern Recognition Letters,* vol. 29 pp. 888-896, 2008.

[174] J. A. Sethian, *Level Set Methods and Fast Marching Methods*: Cambridge University Press, 1996.

[175] E. Dijkstra, "A note on two problems in connection with graphs " *Numeric Mathematics,* vol. 1 pp. 269-271, 1959.

[176] P. K. Saha, R. Strand, and G. Borgefors, "Digital topology and geometry in medical imaging: a survey," *IEEE Transactions on Medical Imaging,* 2015.

[177] L. Serino, C. Arcelli, and G. Sanniti di Baja, "On the computation of the <3,4,5> curve skeleton of 3D objects," *Pattern Recognition Letters,* vol. 32 pp. 1406-1414, 2010.

[178] G. Borgefors, I. Nyström, and G. S. di Baja, "Skeletonizing volume objects part II: From surface to curve skeleton," in *Joint IAPR International Workshops* 1998, pp. 220-229.

[179] C. Arcelli, G. Sanniti Di Baja, and L. Serino, "From 3D discrete surface skeletons to curve skeletons," in *International Conference on Image Analysis and Recognition,* 2008, pp. 507-516.

[180] A. Telea and A. Vilanova, "A robust level-set algorithm for centerline extraction," in *Proceedings of the symposium on Data visualisation 2003*, 2003, pp. 185-194.

[181] D. Attali, G. Sanniti di Baja, and E. Thiel, "Pruning discrete and semicontinuous skeletons," in *Internaltional Conference on Image Analysis and Processing*, 1995, pp. 488-493.

[182] D. Attali, G. Sanniti di Baja, and E. Thiel, "Skeleton simplification through non significant branch removal," *Image Processing and Communications,* vol. 3 (3-4), pp. 63-72, 1997.

[183] X. Bai, L. J. Latecki, and W.-Y. Liu, "Skeleton pruning by contour partitioning with discrete curve evolution," *Pattern Analysis and Machine Intelligence, IEEE Transactions on,* vol. 29 (3), pp. 449-462, 2007.

[184] P. K. Saha, Y. Xu, H. Duan, A. Heiner, and G. Liang, "Volumetric topological analysis: a novel approach for trabecular bone classification on the continuum between plates and rods," *IEEE Transactions on Medical Imaging,* vol. 29 (11), pp. 1821-1838, Nov 2010.

[185] J. Staal, M. D. Abramoff, M. Niemeijer, M. A. Viergever, and B. van Ginneken, "Ridge-based vessel segmentation in color images of the retina," *IEEE Transactions on Medical Imaging,* vol. 23 (4), pp. 501-9, Apr 2004.

[186] L. D. Cohen, "Multiple contour finding and perceptual grouping using minimal paths," *Journal of Mathematical Imaging and Vision,* vol. 14 (3), pp. 225-236, 2001.

[187] L. D. Cohen and T. Deschamps, "Segmentation of 3D tubular objects with adaptive front propagation and minimal tree extraction for 3D medical imaging," *Computer Methods in Biomechanics and Biomedical Engineering,* vol. 10 (4), pp. 289-305, 2007.

[188] L. D. Cohen and R. Kimmel, "Global minimum for active contour models: A minimal path approach," *International Journal of Computer Vision,* vol. 24 (1), pp. 57-78, 1997.

[189] P. Flajolet and A. Odlyzko, "The average height of binary trees and other simple trees," *Journal of Computer and System Sciences,* vol. 25 (2), pp. 171-213, 1982.

[190] K. Palágyi, J. Tschirren, E. A. Hoffman, and M. Sonka, "Quantitative analysis of pulmonary airway tree structures," *Computers in Biology and Medicine,* vol. 36 (9), pp. 974-996, 2006.

[191] Y. Liu, D. Jin, C. Li, K. F. Janz, T. L. Burns, J. C. Torner, *et al.*, "A robust algorithm for thickness computation at low resolution and its application to in vivo trabecular bone CT imaging," *IEEE Transactions on Biomedical Engineering,* vol. 61 (7), pp. 2057-2069, 2014.

[192] P. K. Saha and F. W. Wehrli, "Measurement of trabecular bone thickness in the limited resolution regime of in vivo MRI by fuzzy distance transform," *IEEE Transactions on Medical Imaging,* vol. 23 pp. 53-62, 2004.

[193] H. Kobatake and Y. Yoshinaga, "Detection of spicules on mammogram based on skeleton analysis," *IEEE Transactions on Medical Imaging,* vol. 15 (3), pp. 235-45, 1996.

[194] M. Näf, G. Székely, R. Kikinis, M. E. Shenton, and O. Kübler, "3D Voronoi skeletons and their usage for the characterization and recognition of 3D organ shape," *Computer Vision and Image Understanding,* vol. 66 (2), pp. 147-161, 1997.

[195] P. K. Saha, B. R. Gomberg, and F. W. Wehrli, "Three-dimensional digital topological characterization of cancellous bone architecture," *International Journal of Imaging Systems and Technology,* vol. 11 pp. 81-90, 2000.

[196] R. Zwiggelaar, S. M. Astley, C. R. Boggis, and C. J. Taylor, "Linear structures in mammographic images: detection and classification," *IEEE Transactions on Medical Imaging,* vol. 23 (9), pp. 1077-1086, Sep 2004.

[197] X. S. Liu, P. Sajda, P. K. Saha, F. W. Wehrli, G. Bevill, T. M. Keaveny, *et al.*, "Complete volumetric decomposition of individual trabecular plates and rods and its morphological correlations with anisotropic elastic moduli in human trabecular bone," *Journal of Bone and Mineral Research,* vol. 23 (2), pp. 223-35, Feb 2008.

[198] S. Dudley-Javoroski, P. K. Saha, G. Liang, C. Li, Z. Gao, and R. K. Shields, "High dose compressive loads attenuate bone mineral loss in humans with spinal cord injury," *Osteoporosis International,* vol. 23 (9), pp. 2335-46, Sep 2012.

[199] P. K. Saha, Y. Liu, C. Chen, D. Jin, E. M. Letuchy, Z. Xu, *et al.*, "Characterization of trabecular bone plate-rod microarchitecture using multirow detector CT and the tensor scale: Algorithms, validation, and applications to pilot human studies," *Medical physics,* vol. 42 (9), pp. 5410-5425, 2015.

[200] C. Chen, D. Jin, Y. Liu, F. W. Wehrli, G. Chang, P. J. Snyder, *et al.*, "Trabecular bone characterization on the continuum of plates and rods using in vivo MR imaging and volumetric topological analysis," *Physics in Medicine and Biology,* vol. 61 (18), pp. 478-496, 2016.

[201] S. K. Alford, E. J. van Beek, G. McLennan, and E. A. Hoffman, "Heterogeneity of pulmonary perfusion as a mechanistic image-based phenotype in emphysema susceptible smokers," *Proceedings of the National Academy of Sciences,* vol. 107 (16), pp. 7485-7490, 2010.

[202] Y. H. Liu, E. A. Hoffman, and E. L. Ritman, "Measurement of three-dimensional anatomy and function of pulmonary arteries with high-speed x-ray computed tomography," *investigative Radiology,* vol. 22 (1), pp. 28-36, Jan 1987.

[203] S. Singhal, R. Henderson, K. Horsfield, K. Harding, and G. Cumming, "Morphometry of the human pulmonary arterial tree," *Circulation Research,* vol. 33 (2), pp. 190-7, Aug 1973.

[204] E. A. Boyden, *Segmental anatomy of the lungs: a study of the patterns of the segmental bronchi and related pulmonary vessels*. New York: McGraw-Hill, 1955.

[205] H. Yamashita, *Roentgenologic anatomy of the lung*. Tokyo: Igaku-Shoin, 1978.

[206] S. Kadir, *Atlas of normal and variant angiographic anatomy*. Philadelphia: Pa: Saunders, 1991.

[207] K. Lee, W. Bae, B. Lee, I. Kim, E. Choi, and B. Lee, "Bronchovascular anatomy of the upper lobes: evaluation with thin-section CT," *Radiology,* vol. 181 (3), pp. 765-772, 1991.

[208] M. Jardin and J. Remy, "Segmental bronchovascular anatomy of the lower lobes: CT analysis," *American Journal of Roentgenology,* vol. 147 (3), pp. 457-468, 1986.

[209] G. B. Marshall, B. A. Farnquist, J. H. MacGregor, and P. W. Burrowes, "Signs in thoracic imaging," *Journal of Thoracic Imaging,* vol. 21 (1), pp. 76-90, Mar 2006.

[210] H. Shikata, G. McLennan, E. A. Hoffman, and M. Sonka, "Segmentation of pulmonary vascular trees from thoracic 3D CT images," *Journal of Biomedical Imaging,* vol. 2009 p. 24, 2009.

[211] J. K. Udupa and P. K. Saha, "Fuzzy connectedness and image segmentation," *Proceedings of the IEEE,* vol. 91 pp. 1649-1669, 2003.

[212] P. K. Saha, J. K. Udupa, and D. Odhner, "Scale-based fuzzy connected image segmentation: theory, algorithms, and validation," *Computer Vision and Image Understanding,* vol. 77 pp. 145-174, 2000.

[213] P. K. Saha and J. K. Udupa, "Relative fuzzy connectedness among multiple objects: theory, algorithms, and applications in image segmentation," *Computer Vision and Image Understanding,* vol. 82 pp. 42-56, 2001.

[214] P. Saha, R. Strand, and G. Borgefors, "Digital topology and geometry in medical imaging: a survey," *IEEE Transactions on Medical Imaging,* vol. 34 (9), pp. 1940-1964, 2015.

[215] T. M. Lehmann, C. Gonner, and K. Spitzer, "Survey: Interpolation methods in medical image processing," *IEEE Transactions on Medical Imaging,* vol. 18 (11), pp. 1049-1075, 1999.

[216] E. H. Meijering, W. J. Niessen, and M. A. Viergever, "Quantitative evaluation of convolution-based methods for medical image interpolation," *Medical Image Analysis,* vol. 5 (2), pp. 111-126, 2001.

[217] K. S. Iyer, "Dual energy CT based approach to assessing early pulmonary vascular dysfunction in smoking-associated inflammatory lung disease," Ph.D., Department of Biomedical Engineering and Radiology, University of Iowa, Iowa City, 2015.

[218] T. M. Dougherty, "Quantitative computer tomography based measures of vascular dysfunction for identifying COPD phenotypes and subphenotypes," M.S., Department of Biomedical Engineering, University of Iowa, Iowa City, 2016.

[219] T. M. Dougherty, D. Jin, M. K. Han, J. J. D. Newell, P. K. Saha, R. G. Barr, *et al.*, "Enlarged Segmental Pulmonary Arteries Differentiate Rapid Emphysema Progressors from Non Progressors in the SPIROMICS Cohort," *American Journal of Respiratory and Critical Care Medicine,* submitted.

APPENDIX

A. HYPOXIC PULMONARY VASOCONSTRICTION PILOT STUDY

This paper has been published in American journal of respiratory and critical care medicine. 193 (6), 652-661.

Note: in this paper, we used the term "airway normalized arterial cross sectional area CSA_{norm}" to refer to the "airway standardized arterial cross sectional area $CSA_{standard}$".

Quantitative Dual Energy Computed Tomography Supports a Vascular Etiology of Smoking Induced Inflammatory Lung Disease

Running Title: DECT Vascular Metrics In Inflammatory Lung Disease

Krishna S. Iyer, PhD[1]
John D. Newell, Jr, MD[1,3]
Dakai Jin, MS[2]
Matthew K. Fuld, PhD[4]
Punam K. Saha, PhD[2]
Sif Hansdottir, MD, PhD[5]
Eric A. Hoffman, PhD[1,3,5]

[1]Department of Biomedical Engineering, University of Iowa, Iowa City, IA, 52242
[2]Department of Electrical Engineering, University of Iowa, Iowa City, IA 52242
[3]Department of Radiology, University of Iowa, Iowa City, IA, 52242
[4]Siemens Medical Solutions Inc., Malvern, PA 19355
[5]Division of Pulmonary Medicine, Department of Internal Medicine, University of Iowa, Iowa City, 52242

Correspondence to:
Eric A. Hoffman, Ph.D.
Professor of Radiology, Medicine and Biomedical Engineering
Department of Radiology
University of Iowa Carver College of Medicine
200 Hawkins Drive
Iowa City, Iowa 52242

Phone: 319-356-1381
Fax: 319-356-1503
e-mail: eric-hoffman@uiowa.edu

Disclosures:
EAH is a founder and shareholder of VIDA Diagnostics, a member of the Siemens CT advisory board and a consultant to Glaxo-Smith Kline. JDN Jr. is a consultant for and

holds stock options in VIDA Diagnostics and is a consultant to Glaxo-Smith Kline. MKF is a collaborations engineer for Siemens Medical Solutions, Inc.

Key Words: Quantitative Computed Tomography, Emphysema, COPD, Vascular Dysfunction, Endothelial Dysfunction, Pulmonary Blood Flow, Sildenafil

Author Contributions:

Study design: KSI, EAH, JDN, MKF, SH

Statistical analyses: KSI, JDN

Data interpretation: KSI, EAH, JDN, SH, DJ, PKS

Manuscript writing: KSI, EAH, JDN

Critical review of the manuscript for important intellectual content: KSI, JDN, DJ, MKF, PKS, SH, EAH

Abstract

Rationale: Endothelial dysfunction is of interest in relation to smoking-associated emphysema, a component of chronic obstructive pulmonary disease (COPD). We previously demonstrated that computed tomography (CT)-derived pulmonary blood flow (PBF) heterogeneity is greater in smokers with normal pulmonary function tests (PFTs) but with visual evidence of centriacinar emphysema (CAE) on CT.

Objectives: We introduce dual energy CT (DECT) perfused blood volume (PBV) as a PBF surrogate to evaluate whether the CAE-associated increased PBF heterogeneity is reversible with sildenafil.

Methods: Seventeen PFT-normal current smokers were divided into CAE-susceptible (SS, n=10), and non-susceptible (NS, n=7) smokers, based on the presence or absence of CT detected CAE. DECT-PBV images were acquired before and 1-hour after administration of 20mg oral sildenafil. Regional PBV and PBV coefficient of variation (CV), a measure of the spatial blood flow heterogeneity, were determined, followed by quantitative assessment of the central arterial tree.

Measurements and Main Results: Post sildenafil, regional PBV-CV decreased in SS subjects but not NS subjects ($p<0.05$), after adjusting for age and pack-years. Quantitative evaluation of the central pulmonary arteries revealed higher arterial volume and greater cross-sectional area (CSA) in the lower lobes of SS smokers, suggestive of arterial enlargement in response to increased peripheral resistance. Post sildenafil, arterial CSA decreased in SS but not NS smokers ($p<0.01$).

Conclusions: These results demonstrate that sildenafil restores peripheral perfusion and reduces central arterial enlargement in normal SS subjects with little effect in NS subjects, highlighting DECT-PBV as a biomarker of reversible, endothelial dysfunction in smokers with CAE.

Introduction

X-ray computed tomography (CT) is providing quantitative maps of lung destruction and airway remodeling (1) in large multi-center studies (COPDGene (2), MESALung (3), SPIROMICS (4), etc.) seeking to assess sub-phenotypes of chronic obstructive lung disease (COPD). However, a better understanding of these anatomic alterations is insufficient to identify causal factors of emphysema, critical to the development of new therapeutic interventions. We present a multi-spectral computed tomographic method (Dual Energy Computed Tomography: DECT) for the assessment of regional pulmonary perfused blood volume (PBV), a surrogate for pulmonary blood flow (PBF) (5), with the goal of establishing a novel phenotype based upon a difference in the peripheral pulmonary vascular response to sildenafil. Sildenafil inhibits phosphodiesterase-5 (PDE-5), the enzyme responsible for hydrolyzing cGMP, and enhances the vasodilator effects of endogenous nitric oxide blocking hypoxic pulmonary vasoconstriction (HPV) (6).

In approximately 50% of smokers, regional lung injury resolves with maintenance of normal parenchyma, but in the remaining smokers, response to injury is faulty and COPD ensues (7). Pulmonary vascular changes have been characterized as an early event in COPD (8, 9). More recently, enhanced delivery of progenitor cells to sites of lung injury has been demonstrated (10, 11). Thus, it is clear that the normal pulmonary response to constrict local vasculature in poorly ventilated regions (i.e. injured), shunting blood to better-ventilated regions, would be counterproductive to the smoking-associated immune response and repair process.

Evidence suggests that, in humans, HPV is normally blocked in the presence of inflammation (12, 13) thus allowing for maintenance of perfusion to inflamed regions. In animals exposed to tobacco smoke, pulmonary vascular abnormality precedes emphysema (14-16). Using dynamic, contrast-enhanced CT to assess regional PBF, we have demonstrated that smokers with normal pulmonary function tests, but small visually detectible signs of centriacinar emphysema (CAE) have an increase in coefficient of variation (CV) of CT-based regional PBF and mean transit time, two measures of spatial PBF heterogeneity (17). We have hypothesized that this is due to the inability of CAE susceptible smokers to maintain perfusion to inflamed lung due to a failure to block HPV (17). If increased vascular tone in an inflamed region is a critical event in the etiology of

emphysema, this would have greater consequences in the lung apices where PBF is further compromised due to gravitational effects, explaining the predominance of apical pathology of smoking-associated CAE. In support of these observations, Hueper et al. (18) have recently demonstrated, via magnetic resonance imaging, that microvascular perfusion is reduced in normal appearing lung parenchyma of subjects with mild to moderate COPD.

In this study, we have sought to demonstrate that the increased heterogeneity of PBV (a surrogate for PBF) in CAE susceptible normal smokers (17) *is reversible and not simply an index of early destruction. A subset of results presented here have been preliminarily reported in abstract form (19, 20).*

Methods:

Subject characteristics: The institutional review board and the radiation safety committee approved the study and written consent was obtained from all subjects prior to entering the study. Current smokers with normal pulmonary function tests (see on-line supplement) were evaluated, by CT, for the presence or absence of centriacinar emphysema. Emphysema susceptible smoker (SS) were defined as presenting with visually detected centriacinar emphysema (CAE), ground glass nodules and ground glass opacities on inspiratory CT scans, and NS did not have any of these CT-based findings. All subjects were recruited based upon prior CT scanning within the Iowa cohort of COPDGene (2) or SPIROMICS (4). These scans were evaluated by an experienced CardioThoracic Radiologist (see Online Supplement).

CT scanning: Subjects were imaged in the supine posture at pre-defined lung volumes, using a computer-controlled lung volume controller (see Fuld et al. (21) for details and Iyer et al. (22) for validation). Lung volumes, measured as a percent of vital capacity (19) were standardized to subjects' individual lung mechanics: Non-contrast scans obtained at 90% VC (approximating total lung capacity (TLC)) were acquired for emphysema assessment, and DECT scans at 20% VC (approximating functional residual capacity (FRC)) were acquired for PBV assessment.

Subjects were imaged supine on a second-generation dual-source dual-energy 128-slice multi-detector row CT (MDCT) scanner (Siemens SOMATOM Definition Flash, Forscheim, Germany). Details of the scan protocol are in supplemental **Table E1**. The CT scanning protocol consisted of: 1) A spiral non-contrast volumetric CT scan at TLC to assess lung parenchymal structure (0.5-0.6 mm in-plane, 0.5mm slice thickness); 2) a 30 ml iodinated contrast test bolus (Isovue 370, Bracco Diagnostics) delivered at 4 ml/sec was used with a breath hold at 20% VC to measure the scan delay required for stead-state contrast equilibration within the pulmonary circulation (determined as the time to reach a contrast enhancement of 100 Hounsfield Units (HU) within the left atrium); 3) two contrast-enhanced DECT-PBV scans, before and after sildenafil, were performed with the subject holding their breath at 20% VC with 4ml/sec contrast delivery commencing at the pre-determined time prior to onset of scanning and continuing throughout the scanning period. Subject's vital signs, including heart rate, ECG, arterial blood pressure, and oxygen saturation (SpO_2) were monitored (Philips IntelliVue) during and for 1 hr after the end of imaging. No contrast or sildenafil associated adverse events (or any other adverse events) were reported in any of the subjects.

DECT Image Analysis: Whole lung (right and left), individual lung lobe masks and pulmonary vascular tree masks were segmented from CT images (Apollo pulmonary workstation software, VIDA Diagnostics, Iowa City, IA) from the non-contrast TLC and contrast-enhanced PBV scans (using the Sn140 kVp image). The lung masks for the TLC images were used to define the voxels from which measures of mean lung density, tissue fraction (%), air fraction (%), and an emphysema index (% voxels below -950HU (EI_{-950})) were obtained. The 80 kVp and 140 kVp DECT images were combined to generate an image of contrast distribution in the lung (i.e perfused blood volume, PBV). (5)

Briefly, lung segmentations were used to extract PBV signals from the lung parenchyma, removing signal from large central pulmonary vessels. The PBV signals were then normalized to the iodine concentration of blood in the main pulmonary artery (PA). This normalization was performed to account for any contrast enhancement differences in the pre- vs. post-sildenafil studies as well as any variations between subjects. For each subject, post-sildenafil lungs were warped into the shape of the pre-sildenafil lung using in-house

image matching software (23, 24) which has been shown to have an accuracy on the order of 1 mm when matching full inspiration to functional residual volume. Here we were matching closely related lung volumes. Each un-warped lung was divided into 30x30x40 voxel regions (~0.3-0.5ml) and PBV heterogeneity for each region was assessed and then the regional PBV-CV's for the post-sildenafil image sets were mapped into its pre-sildenafil shape. (see Online Supplement for details) **Figure 1** provides a flow diagram of the process of image acquisition and analysis of PBV images.

Central Pulmonary Artery analysis: CT-derived central pulmonary vessel trees were separated into arteries and veins using custom in-house segmentation software and manually placed seed points were placed in branches of the main pulmonary artery and veins to initialize the algorithm (25). Total pulmonary arterial tree volumes (TPAV) for the right lungs were analyzed. We excluded the left lungs due to cardiac motion interference with measurement stability. Total pulmonary vascular volumes (TPVV: arteries and veins) and TPAV were measured pre- and post-sildenafil. The right lung vessels were further divided into upper, middle, and lower lobe vessels, using the lobe masks generated from the 20% VC images. The right upper lobe was subject to artifacts related to the high iodine concentration in the subclavian artery so we further limited analysis to the right lower lobe (RLL). TPVV and TPAV were both normalized to the right lower lobe volume (denoted herein as $TPVV_{norm}$ for total vascular and $TPAV_{norm}$ for total arterial volume percent).

Arterial cross-sectional area: Cross-sectional area (CSA) of selected arterial branches in the lower lobes of the right and left lung (RB10 and LB10) were measured from reconstructed CT images. The branches were chosen according to their association with anatomically defined airway segments and arterial CSA was computed semi-automatically at a specific branch. Arterial centerlines (26) were connected by a centerline-detection algorithm (27). The CT image was reconstructed in the plane orthogonal to the center line and the arterial CSA was measured using a radial sample-line approach (28). Airway CSA (using the outer boarder of the airway to minimize the effects of any early smoking-associated changes in luminal area or wall thickness) were measured from segmented airway trees (Apollo, VIDA Diagnostics) and the airway-normalized arterial (CSA_{norm})

cross sectional areas were reported to account for inter-subject differences in inherent airway and arterial sizes. *We have shown, in a small cohort (N=10) of normal smokers with repeat scans, the intra class correlation (ICC) for RB10 and LB10 artery/airway metrics were 92 and 98% respectively (29).* Algorithm and sampling details are provided in the Online Supplement.

Statistical Analysis: Data for PBV and PBV-CV difference pre- and post-sildenafil was represented as a mean ± SD for the whole lung and lung regions. A one-way ANOVA (R v. 3.1.1 statistical toolbox) followed by post-hoc analysis using Bonferroni method was used to determine statistical differences between NS and SS subjects with a p value ≤ 0.05 considered significant. The right lower lobe volumes and corresponding lobar vascular volumes ($TPAV_{norm}$), and airway normalized arterial areas (CSA_{norm}) were compared between NS and SS subjects using one-way ANOVA. Subjects served as their own controls when comparing pre vs. post differences in PBV, CV, and $TPAV_{norm,}$ and CSA_{norm}. Subject's age and pack years were adjusted in multi-variate analyses to assess between group baseline CVs and sildenafil-based CV changes between groups. Paired t tests assessed differences in the dependent vs. nondependent regions.

Results:

Subject characteristics: Twenty-two subjects were enrolled in this study, three were excluded prior to scanning because they were on blood pressure or asthma medications. The remaining 19 smokers were characterized as either NS (8) or SS (11).

Quantitative assessments of CT lung volumes, calculated via Apollo workstation for both the pre- and post-DECT scans, were performed on all nineteen subjects and in seventeen subjects there was no significant difference in the lung volumes before and after administration of sildenafil. One NS and one SS subject had more than 500 ml difference in their lung volumes and were excluded from study based upon the previously reported influence of lung volume levels on DECT measures of regional PBV (5). NS and SS demographics and physiologic findings for the seventeen remaining subjects are provided (**Table 1).**

SS subjects were slightly older (mean 9 years) and had a greater number of pack years smoking history. Both groups, on average, started smoking at similar ages. Thus, the greater pack years in the SS group were likely age-related. Spirometric measurements, including VC and FEV_1/FVC, did not differ between groups. The lung diffusing capacities (DLCO, %predicted), although normal, were significantly lower in SS compared to NS subjects. Urine cotinine level and C-reactive protein (CRP), an index of inflammation, did not differ between groups and was suggestive of active smoking The CRP level in one NS subject was considerably higher (6.4 mg/L) than the other subjects. Except for this one subject, all others had a value <1.0mg/L. If the one subject with a value of 6.4 mg/L was eliminated from statistical analysis, the CRP was borderline greater ($p<0.06$) in the SS subjects.

Non-contrast CT performed at full inspiration pre-sildenafil: The CT-based EI_{-950} was not significantly different between groups despite the presence of visually detected CAE in SS subjects (**Table 1**). EI_{-950} for each group was within the range of what has been previously described as normal (30). Mean lung densities were higher in both groups, as expected, when compared to normal non-smokers (22) but did not differ between groups. This is consistent with the presence of smoking-associated inflammation in both groups.

Sildenafil decreases PBV heterogeneity in SS subjects without affecting whole lung PBV: The spatial heterogeneity of PBV was measured by whole lung and regional CV's. As demonstrated, we divided the lung (ignoring apical regions that contain CT beam hardening artifacts from dense subclavian contrast) into thirds by vertical height (ventral-to-dorsal in supine position) and compared the PBV-CV's for each region between SS and NS subjects (**Fig. 2*a***). Baseline CVs were similar to those measured by Alford et al. (17) averaging 0.42 ± 0.09 and 0.37 ± 0.03 for SS and NS subjects, respectively. The gravitationally non-dependent lung (compared with the dependent lung) had the greatest ($p<0.01$) heterogeneity pre-sildenafil for both the SS and NS subjects. Region-for-region, PBV-CV's were greater in the SS vs. NS subjects with borderline significance. (p-values ranging from 0.6-0.9). Mid-coronal sections from representative SS and NS subjects: (SS-1, top

row, and NS-1, bottom row) are depicted with pre-sildenafil images in the left column and registered post-sildenafil images in the right column (**Fig. 2b**). The regional CVs were higher in the pre-sildenafil SS subjects. Post-sildenafil there was little change in the CV of the NS subjects while the color distribution of the SS subject depicted here shifts (decreases) to closely match the NS subject. Note the significant left shift (0.10) in the mode of the SS histogram pre- vs. post-sildenafil, with the post-sildenafil CV mode coming into alignment with the NS histograms (**Fig. 2*c***). This CV mode shift was significant for the cohort of SS subjects compared with the NS subjects ($p<0.05$).

Following sildenafil, the whole lung PBV-CVs significantly ($p<0.05$) decreased in SS subjects by 0.03 (-5%) and did not significantly change in NS subjects. The decrease in CV occured in all lung regions (dependent, middle and non-dependent) of SS subjects (**Fig. 3**). Despite shifts in CV with sildenafil in SS subjects, mean PBV (normalized to iodine content in the pulmonary artery) did not differ between groups either pre (0.16 ± 0.05 and 0.17 ± 0.04 in NS and SS, respectively) or post (0.17 ± 0.05 and 0.17 ± 0.03 in NS and SS,respectively). . Thus, shifts in CV were not likely due to shifts in cardiac ouput or perfusion pressures and decreased CV in the SS subjects represents a homogenization of perfusion with shifts in flow from high to low flow regions.

The central arterial volume response to sildenafil also differentiates NS and SS smokers:
With the notion that downstream vascular resistance would reflect in up-stream changes of vascular volume, we examined the acute arterial response in NS and SS subjects to sildenafil using right lower lobe CT-based total pulmonary arterial volume (TPAV: central volume detectable anatomically by CT) normalized to the lobar volume ($TPAV_{norm}$). The right lower lobe $TPAV_{norm}$ in SS subjects was significantly greater ($p<0.05$) compared to NS subjects. Administering sildenafil increased the $TPAV_{norm}$ in both NS and SS subjects and differences between the groups were eliminated. **Figure 4** shows the change in $TPAV_{norm}$ vs. the change in PBV pre- vs. post-sildenafil. PBV and $TPAV_{norm}$ changes with sildenafil were inversely correlated in SS subjects ($R^2 = 0.62$; $p<0.01$) while in NS subjects there was little change in PBV in response to sildenafil and no significant relationship ($R^2 = 0.13$; $p > .05$) between PBV and $TPAV_{norm}$ changes.

The arterial CSA, an algorithmically independent measure from that of $TPAV_{norm}$, was compared between SS and NS subjects pre- and post-sildenafil. The RB10 and LB10 associated arterial segments are highlighted in red (**Fig. 5*a*),** and the arterial and airway CSA's are in blue and green overlays, respectively (**Fig. 5*b*).** The SS smoker CSA_{norm}'s were significantly ($p<0.01$) larger than the NS subjects' CSA_{norm} pre-sildenafil values. (**Fig. 5*c***) These SS vs. NS differences were eliminated with sildenafil. Sildenafil increased the CSA_{norm} in NS and decreased the CSA_{norm} in the SS subjects with a change that was significantly different between the two groups ($p<0.01$) (**Fig. 5*d***).

At higher lung volumes there is compression of the micro-vascular bed and/or stiffening of the more central vasculature and parenchyma at higher lung volumes. Because of this we used the 20% VC DECT image data in the $TPAV_{norm}$ and the CSA_{norm} analyses to maximize the sensitivity of central vascular measures to differences in peripheral vasoconstriction. To test this, we performed the same CSA_{norm} analysis as described above using the non-contrast 90% VC scans. As expected, the between group differences and sildenafil effects observed using the 20% VC scans were not found at this higher lung volume.

Discussion:

In this study, we introduce the use of multi-spectral CT (DECT) to provide quantitative, functional and structural measures of the central and peripheral pulmonary vasculature by demonstrating the presence of a unique phenotype associated with SS vs. NS subjects. We show that the previously established (17) elevated PBF heterogeneity in SS subjects is reversible with sildenafil and thus not simply a result of early lung destruction but rather evidence of a peripheral vasoconstriction unique to CAE susceptible subjects. In both the SS and NS subjects the PBV-CV was significantly greater in the non-dependent lung regions consistent with prior observations of Alford et al. (17) using dynamic perfusion CT. In addition, the PBV-CV trended higher in the SS subjects vs. the NS subjects ($p=0.06$ and $p=0.08$ for dependent vs. non-dependent lung regions, respectively), suggesting greater vasoconstriction in the non-dependent lung of SS subjects. It is important to note that the

sildenafil induced reduction in CV was not merely an artifact of altered cardiac output since mean PBV did not differ between groups before or after sildenafil.

While PBV has been shown to be a strong surrogate for true parenchymal perfusion (5), the measurement method implemented in this study (Siemens SOMATOM Definition Flash without iterative reconstruction, relatively low dose imaging, coupled with a relatively small sample size) likely explain this level of statistical strength. The noise in the PBV measurement is expected to diminish with newer generation scanners and improved iterative reconstruction software for DECT (31). The noise effects on the PBV response to sildenafil was less of a concern since we carefully controlled lung volumes and matched PBV image pairs before and after sildenafil.

It is important to recognize that, while our SS population is selected based upon visual evidence of CAE; the NS cohort is selected based upon an absence of CT evidence for CAE. It is possible for NS subjects to be incorrectly classified simply because they were studied earlier in the pathologic process (the SS subjects were older by an average of 9 years). A larger population study would be useful and could provide the ability to age match the two groups. However, age was accounted for in the multi-variate analysis model and did not contribute to group differences.

Central pulmonary vascular dimensions ($TPAV_{norm}$ and CSA_{norm}) was larger in the SS population, consistent with the notion of peripheral vasoconstriction and increased central pulmonary arterial volume (32). The increased CSA_{norm} in the SS subjects was eliminated with sildenafil, and the change in arterial volume inversely correlated with PBV change. These observations support the hypothesis that CAE-susceptibility is associated with alterations in peripheral vascular physiology. This also supports the previously reported relationship between increased CT percent emphysema, reduced venous return, and reduced left ventricular filling (33), suggesting a link between pulmonary vascular dysfunction and emphysema. While dilation of central arteries, due to distal vessel pruning, is associated with advanced COPD (8, 9, 34), we observed dilation of central arteries in our SS cohort with limited parenchymal destruction. Restoration of a more uniform PBV distribution may represent restoration of PBF to inflamed lung regions. Perfusion to injured lung regions is important to the inflammatory response cascade, including delivery of progenitor cells promoting parenchymal repair (10, 35).

The signaling pathway(s) that subsequently mediate pulmonary arteriolar vasoconstriction is controversial, but a strong contender is the attenuation of the nitric oxide–cyclic GMP pathway (36, 37). (**Fig. 1)** Decreased expression of endothelial NO has been found in primary pulmonary arterial hypertension and pulmonary hypertension associated with diseases, such as COPD (38-40). It was recently demonstrated that increasing nitric oxide production, such as by stimulating guanylate cyclase, blocked the development of pulmonary hypertension and emphysema in cigarette smoke-exposed animal models and human lung tissue (41). Sildenafil has been shown to inhibit hypoxic vasoconstriction in healthy subjects (42, 43).

A recent study by Blanco et al. (44) demonstrated that, in patients with pulmonary hypertension associated with COPD, sildenafil (20 mg and 40 mg) improved hemodynamics at rest and exercise. This effect was accompanied by the inhibition of HPV that impaired arterial oxygenation at rest (but not exercise). An important result of the current study is that in SS subjects, sildenafil improved pulmonary blood flow without impairing a pulse oximeter-derived measure of oxygenation. While the de-oxygenation associated with restoration of flow to poorly ventilated lung regions has been interpreted as a negative outcome of Blanco et al. (44), it is possible that such flow restoration, if tolerated, could have longer-term benefits including improved repair mechanism and restoration of parenchymal architecture.

The decrease in PBV heterogeneity with sildenafil was not accompanied by an increase in mean PBV, suggesting a redistribution of parenchymal blood flow from areas with low CV's to areas with high CV's, presumably representing restoration of perfusion to regions of lung injury experiencing smoking-associated pulmonary vasoconstriction. Alford et al. (17), using a more difficult-to-implement method of dynamic perfusion CT, similarly observed an increased PBF heterogeneity in SS subjects not associated with a difference in mean PBF between SS, NS and non-smokers.

The technical challenges of this study were largely associated with the attainment of similar lung volumes pre and post sildenafil during scanning.. Large volume differences are known to cause changes in regional perfusion whereby stretch of the parenchyma increases peripheral vascular/capillary level resistance. We accomplished lung volume control via the use of a turbine volume-controller, (21, 22). We acknowledge that attaining

rigorous volume control may be difficult in large clinical studies, for which the effects of coaching and spirometric methods on quantitative PBV and PBV-CV need to be further evaluated. However, an approximate lung volume (FRC) can be achieve with appropriate coaching and is adequate when on simply wishes to perform a single scan for the assessment of perfusion heterogeneity.

In summary, the key finding of this study is that increased perfusion heterogeneity (assessed via DECT-based PBV), in subjects with early mild emphysema and associated pulmonary arterial enlargement are reversible, suggesting an early functional mechanism promoting parenchymal destruction and serving as a target for early intervention. The image-based biomarkers we described may be useful for exploring other inflammatory lung diseases beyond COPD.

Acknowledgements:

The authors thank Melissa Shirk, RTR, BS, Jered Sieren, RTR, BS and Chelsea Sloan, BA for their help with both scanning and subject lung volume control. Additionally, we thank Deb O'Connell-Moore, BS and Kaylene Crawford, BA who served as the human studies coordinators for this project. This work was supported, in part, by an NIH Bioengineering Research Partnership Grant, R01HL-112986 and an NIH MSTP training grant, 5T32-GM007337.

Table

Table 1: Subject characteristics. The Institutional Review Board and Radiation Safety Committee approved this study. Written consent was obtained from all subjects. Results are expressed as mean ± SD unless noted. Spirometry and DLCO is reported as percent predicted. BDI, baseline dyspnea index; BMI, body mass index; CRP, c-reactive protein; DLCO, diffusing capacity of the lung for carbon monoxide; EI, emphysema index; FEV1, forced expiratory volume in 1 second; FVC, forced vital capacity; MLD, mean lung density; no., number of subjects; NS, non-susceptible smokers; SS, emphysema-susceptible smokers; SpO_2, oxygen saturation; *****$p<0.05$ vs. NS subjects.

Characteristic	NS	SS
N	7	10
Gender (% male)	14	10
Age (years)	41 ± 10	50 ± 6*****
BMI (kg/m^2)	26.2 ± 3.7	25 ± 4.5
Heart rate: pre-sildenafil (bpm)	74.8 ± 6.3	70.4 ± 9.9
Heart rate: post-sildenafil (bpm)	73.8 ± 10.4	71.7 ± 12.9
Blood pressure (mm Hg)		
Systolic BP (mmHg): pre-sildenafil	120 ± 15.5	113 ± 13.6
Diastolic BP (mmHg):pre-sildenafil	69.9 ± 9.9	68.8 ± 6.0
Systolic BP (mmHg): post-sildenafil	116 ± 15	114 ± 14
Diastolic BP (mmHg):post-sildenafil	67.3 ± 8.7	68.5 ± 8.6
SpO_2: Pre-sildenafil	99 ± 1.0	99 ± 0.92
SpO_2: Post-sildenafil	99.1 ± 0.69	99 ± 1.1
CRP (mg/L)	1.4 ± 2.21	2.23 ± 2.61
Pack-years	20 ± 13	32 ± 9*****
Age started smoking (years)	16 ± 4	16 ± 3
BDI	11.9 ± 0.38	10.1 ± 2.0
FEV_1 (%)	120 ± 16	115 ± 18
FVC (%)	116 ± 10	118 ± 28
FEV_1/FVC (%)	80 ± 4.8	78 ± 6.9
DLCO pre-Sildenafil (%)	113 ± 22	85 ± 14*****
TLC air volume (L) (CT)	4.96 ± 0.40	4.81 ± 0.71
Tissue volume (L) (CT)	0.97 ± 0.15	0.97 ± 0.081
EI_{-950} (%)	0.36 ± 0.25	0.43 ± 0.31
MLD (HU)	-830.7 ± 17.3	-820 ± 19.5

Figure Legends

Figure 1: Illustration of the process of PBV imaging from acquisition, data collection, processing, and comparison of regional PBV measures. (a) DECT PBV imaging is performed using 80 kVp and Sn140 kVp energies, detectors 95º apart, acquiring low and high energy contrast-enhanced CT images. (b) Axial CT images obtained after the test bolus injection were used to determine where to draw a region of interest (ROI) in the left atrium to compute a time versus contrast density curve. This curve was used to establish the delay time in seconds necessary between the start of contrast injection and the start of the DECT acquisition. The delay time was determined by computing the interval in seconds between the start of contrast injection and the contrast density reaching 100 HU in the left atrium, white vertical line. (c) 80 kVp and Sn140 kVp images used to calculate PBV images (d) Regional PBV analysis, showing lung mask outlining only the lung parenchyma. Large vessels and airways are excluded. e) Image registration: images are warped from Sn140 kVp images (post is moving, pre is target). The displacement for this registration is used to warp the post PBV image to the pre PBV image. This is done to ensure accurate comparison of the CVs for the same regions pre and post sildenafil.

Figure 2: Example of PBV-CV measures derived from DECT images for NS and SS subjects. a) The whole lung was divided into dependent, middle and non-dependent thirds by vertical height and the PBV-CV's were calculated for each of these regions. **b-c)** A representative SS and NS subject (SS-1 and NS-1) pre and post sildenafil using image matching. PBV images divided into 30x30x40 regions of interest to compute PBV CV for each region. Mid-coronal sections from subject SS-1 (top row) and NS-1 (bottom row) are depicted in **(b)** with pre sildenafil images on the left and post-sildenafil images on the right. CVs for each region are scaled as per color bars shown in the middle of each image pair. **c)** A representative CV histogram for SS-1/NS-1 subjects pre and post sildenafil.

Figure 3: Regional and whole lung PBV CV changes pre and post sildenafil. The PBV images for NS (open bars, ± standard error) and SS (shaded bars, ± standard error) subjects were divided by vertical height into the non-dependent (ventral), middle and dependent (dorsal) regions, depicted in the lower left sagittal PBV image. The relative % change (i.e

(post-pre)/pre) in CV in response to sildenafil for the SS subjects significantly decreased for each lung region while there were no significant changes in CV in any of the lung regions for the NS subjects.

Figure 4: Volumetric CT evaluation of total pulmonary arterial volume pre and post-sildenafil. The right lower lobe (RLL) $TPAV_{norm}$ was identified as largest in SS subjects' pre-sildenafil (upper left insert). The relative change in $TPAV_{norm}$ pre to post sildenafil inversely correlated with the RLL-PBV change in SS subjects ($R^2 = 0.62$) but not in NS subjects ($R^2 = 0.13$).

Figure 5: Volumetric CT evaluation of arterial cross-sectional area pre and post sildenafil. (**Left Column**) Segmental branches of the arterial tree (associated with the RB10 and LB10 bronchial segments) were sampled in the right and left lower lobes. **a)** RB10 (left side) and LB10 (right side) airway-associated arterial segments are in red; **b)** RB10 cross sectional area (green) and associated arterial segment (blue) are shown with their superposition in top left for an SS and NS subject. **c)** Arterial CSA normalized to the airway CSA area (CSA_{norm}) was significantly larger in SS subjects pre-sildenafil and this relationship was eliminated post-sildenafil. **d)** Pre to post sildenafil change in CSA_{norm} in SS and NS subjects.

References

1. Hoffman EA, Simon BA, McLennan G. State of the Art. A structural and functional assessment of the lung via multidetector-row computed tomography: phenotyping chronic obstructive pulmonary disease. *Proc Am Thorac Soc* 2006; 3: 519-532.
2. Regan EA, Hokanson JE, Murphy JR, Make B, Lynch DA, Beaty TH, Curran-Everett D, Silverman EK, Crapo JD. Genetic Epidemiology of COPD (COPDGene) Study Design. *COPD* 2010; 7: 32-43.
3. Hoffman EA, Jiang R, Baumhauer H, Brooks MA, Carr JJ, Detrano R, Reinhardt J, Rodriguez J, Stukovsky K, Wong ND, Barr RG. Reproducibility and validity of lung density measures from cardiac CT Scans--The Multi-Ethnic Study of Atherosclerosis (MESA) Lung Study. *Acad Radiol* 2009; 16: 689-699.
4. Couper D, LaVange LM, Han M, Barr RG, Bleecker E, Hoffman EA, Kanner R, Kleerup E, Martinez FJ, Woodruff PG, Rennard S. Design of the Subpopulations and Intermediate Outcomes in COPD Study (SPIROMICS). *Thorax* 2014; 69: 491-494.
5. Fuld MK, Halaweish AF, Haynes SE, Divekar AA, Guo J, Hoffman EA. Pulmonary perfused blood volume with dual-energy CT as surrogate for pulmonary perfusion assessed with dynamic multidetector CT. *Radiology* 2013; 267: 747-756.
6. Galie N, Ghofrani HA, Torbicki A, Barst RJ, Rubin LJ, Badesch D, Fleming T, Parpia T, Burgess G, Branzi A, Grimminger F, Kurzyna M, Simonneau G. Sildenafil citrate therapy for pulmonary arterial hypertension. *N Engl J Med* 2005; 353: 2148-2157.
7. Lundback B, Lindberg A, Lindstrom M, Ronmark E, Jonsson AC, Jonsson E, Larsson LG, Andersson S, Sandstrom T, Larsson K. Not 15 but 50% of smokers develop COPD?--Report from the Obstructive Lung Disease in Northern Sweden Studies. *Respir Med* 2003; 97: 115-122.
8. Pauwels RA, Buist AS, Calverley PM, Jenkins CR, Hurd SS. Global strategy for the diagnosis, management, and prevention of chronic obstructive pulmonary disease. NHLBI/WHO Global Initiative for Chronic Obstructive Lung Disease (GOLD) Workshop summary. *Am J Respir Crit Care Med* 2001; 163: 1256-1276.
9. Wright JL, Churg A. Advances in the pathology of COPD. *Histopathology* 2006; 49: 1-9.
10. Peinado VI, Ramirez J, Roca J, Rodriguez-Roisin R, Barbera JA. Identification of vascular progenitor cells in pulmonary arteries of patients with chronic obstructive pulmonary disease. *Am J Respir Cell Mol Biol* 2006; 34: 257-263.
11. Ishizawa K, Kubo H, Yamada M, Kobayashi S, Numasaki M, Ueda S, Suzuki T, Sasaki H. Bone marrow-derived cells contribute to lung regeneration after elastase-induced pulmonary emphysema. *FEBS letters* 2004; 556: 249-252.
12. Schuster DP, Marklin GF. The effect of regional lung injury or alveolar hypoxia on pulmonary blood flow and lung water measured by positron emission tomography. *Am Rev Respir Dis* 1986; 133: 1037-1042.

13. Gust R, Kozlowski J, Stephenson AH, Schuster DP. Synergistic hemodynamic effects of low-dose endotoxin and acute lung injury. *Am J Respir Crit Care Med* 1998; 157: 1919-1926.

14. Wright JL, Churg A. Effect of long-term cigarette smoke exposure on pulmonary vascular structure and function in the guinea pig. *Exp Lung Res* 1991; 17: 997-1009.

15. Seimetz M, Parajuli N, Pichl A, Veit F, Kwapiszewska G, Weisel FC, Milger K, Egemnazarov B, Turowska A, Fuchs B, Nikam S, Roth M, Sydykov A, Medebach T, Klepetko W, Jaksch P, Dumitrascu R, Garn H, Voswinckel R, Kostin S, Seeger W, Schermuly RT, Grimminger F, Ghofrani HA, Weissmann N. Inducible NOS inhibition reverses tobacco-smoke-induced emphysema and pulmonary hypertension in mice. *Cell* 2011; 147: 293-305.

16. Ferrer E, Peinado VI, Castaneda J, Prieto-Lloret J, Olea E, Gonzalez-Martin MC, Vega-Agapito MV, Diez M, Dominguez-Fandos D, Obeso A, Gonzalez C, Barbera JA. Effects of cigarette smoke and hypoxia on pulmonary circulation in the guinea pig. *Eur Respir J* 2011; 38: 617-627.

17. Alford SK, van Beek EJ, McLennan G, Hoffman EA. Heterogeneity of pulmonary perfusion as a mechanistic image-based phenotype in emphysema susceptible smokers. *Proc Natl Acad Sci U S A* 2010; 107: 7485-7490.

18. Hueper K, Vogel-Claussen J, Parikh MA, Austin JH, Bluemke DA, Carr J, Choi J, Goldstein TA, Gomes AS, Hoffman EA, Kawut SM, Lima J, Michos ED, Post WS, Po MJ, Prince MA, Liu K, Rabinowitz D, Skrok J, Smith BM, Watson K, Yin Y, Zambeli-Ljepovic AM, Barr RG. Pulmonary Microvascular Blood Flow in Mild Chronic Obstructive Pulmonary Disease and Emphysema. The MESA COPD Study. *Am J Respir Crit Care Med* 2015.

19. Iyer KS, Fuld MK, Kravchuk OA, Sieren JP, Hansdottir S, Newell JD, Hoffman EA. Sildenafil Reduces Dual-Energy Computed Tomography Determined Pulmonary Perfusion Heterogeneity In Normal Smokers That Are Susceptible To Emphysema. Am J Respir Crit Care Med; 2013. p. A2369-A2369.

20. Iyer KS, Fuld MK, Sieren JP, Hansdottir S, Newell JJ, Hoffman EA. Pulmonary Vascular Volume Changes Following Sildenafil In Emphysema-Susceptible Smokers As A Measure Of Early Pulmonary Vascular Dysfunction. Am J Respir Crit Care Med; 2014. p. A4345-A4345.

21. Fuld MK, Grout RW, Guo J, Morgan JH, Hoffman EA. Systems for lung volume standardization during static and dynamic MDCT-based quantitative assessment of pulmonary structure and function. *Acad Radiol* 2012; 19: 930-940.

22. Iyer KS, Grout RW, Zamba GK, Hoffman EA. Repeatability and Sample Size Assessment Associated with Computed Tomography-Based Lung Density Metrics. *Chronic Obst Pulm Dis (Miami, Fla)* 2014; 1: 97-104.

23. Yin Y, Choi J, Hoffman EA, Tawhai MH, Lin C-L. A multiscale MDCT image-based breathing lung model with time-varying regional ventilation. *J Comput Phys*; 2013. p. 168-192.

24. Jahani N, Yin Y, Hoffman EA, Lin C-L. Assessment of regional non-linear tissue deformation and air volume change of human lungs via image registration. *J Biomech*; 2014. p. 1626-1633.

25. Saha PK, Gao Z, Alford SK, Sonka M, Hoffman EA. Topomorphologic Separation of Fused Isointensity Objects via Multiscale Opening: Separating Arteries and Veins in 3-D Pulmonary CT. *IEEE Trans Med Imaging*; 2010. p. 840-851.

26. Cohen L. Minimal Paths and Fast Marching Methods for Image Analysis. In: Paragios N, Chen Y, Faugeras O, editors. Handbook of Mathematical Models in Computer Vision: Springer US; 2006. p. 97-111.

27. Jin D, Iyer KS, Chen C, Hoffman EA, Saha PK. A robust and efficient curve skeletonization algorithm for tree-like objects using minimum cost paths. *Patt Recog Lett* in press.

28. Saha PK. Tensor scale: A local morphometric parameter with applications to computer vision and image processing. *Comp Vision Imag Understand* 2005; 99: 384-413.

29. Jin D, Guo J, Dougherty TM, Iyer KS, Hoffman EA, Saha PK. A semi-automatic framework of measuring pulmonary arterial metrics at anatomic airway locations using ct imaging. SPIE Medical Imaging 2016 (in press);San Diego, CA.

30. Hoffman EA, Ahmed FS, Baumhauer H, Budoff M, Carr JJ, Kronmal R, Reddy S, Barr RG. Variation in the percent of emphysema-like lung in a healthy, nonsmoking multiethnic sample. The MESA lung study. Ann Am Thorac Soc 2014;11:898-907.

31. Newell JD, Jr., Fuld MK, Allmendinger T, Sieren JP, Chan KS, Guo J, Hoffman EA. Very low-dose (0.15 mgy) chest ct protocols using the COPDgene 2 test object and a third-generation dual-source ct scanner with corresponding third-generation iterative reconstruction software. Invest Radiol 2015;50:40-45.

32. Santos S, Peinado VI, Ramirez J, Melgosa T, Roca J, Rodriguez-Roisin R, Barbera JA. Characterization of pulmonary vascular remodelling in smokers and patients with mild COPD. Eur Respir J 2002;19:632-638.

33. Barr RG, Bluemke DA, Ahmed FS, Carr JJ, Enright PL, Hoffman EA, Jiang R, Kawut SM, Kronmal RA, Lima JA, Shahar E, Smith LJ, Watson KE. Percent emphysema, airflow obstruction, and impaired left ventricular filling. N Engl J Med 2010;362:217-227.

34. Wells JM, Washko GR, Han MK, Abbas N, Nath H, Mamary AJ, Regan E, Bailey WC, Martinez FJ, Westfall E, Beaty TH, Curran-Everett D, Curtis JL, Hokanson JE, Lynch DA, Make BJ, Crapo JD, Silverman EK, Bowler RP, Dransfield MT. Pulmonary arterial enlargement and acute exacerbations of copd. N Engl J Med 2012;367:913-921.

35. Pizarro S, Garcia-Lucio J, Peinado VI, Tura-Ceide O, Diez M, Blanco I, Sitges M, Petriz J, Torralba Y, Marin P, Roca J, Barbera JA. Circulating progenitor cells and vascular dysfunction in chronic obstructive pulmonary disease. PLoS One 2014;9:e106163.

36. Moudgil R, Michelakis ED, Archer SL. Hypoxic pulmonary vasoconstriction. J Appl Physiol (1985) 2005;98:390-403.

37. Barbera JA, Peinado VI, Santos S, Ramirez J, Roca J, Rodriguez-Roisin R. Reduced expression of endothelial nitric oxide synthase in pulmonary arteries of smokers. Am J Respir Crit Care Med 2001;164:709-713.

38. Dinh-Xuan AT, Higenbottam TW, Clelland CA, Pepke-Zaba J, Cremona G, Butt AY, Large SR, Wells FC, Wallwork J. Impairment of endothelium-dependent pulmonary-artery relaxation in chronic obstructive lung disease. N Engl J Med 1991;324:1539-1547.

39. Giaid A, Saleh D. Reduced expression of endothelial nitric oxide synthase in the lungs of patients with pulmonary hypertension. N Engl J Med 1995;333:214-221.

40. Peinado VI, Barbera JA, Ramirez J, Gomez FP, Roca J, Jover L, Gimferrer JM, Rodriguez-Roisin R. Endothelial dysfunction in pulmonary arteries of patients with mild COPD. Am J Physiol 1998;274:L908-913.

41. Weissmann N, Lobo B, Pichl A, Parajuli N, Seimetz M, Puig-Pey R, Ferrer E, Peinado VI, Dominguez-Fandos D, Fysikopoulos A, Stasch JP, Ghofrani HA, Coll-Bonfill N, Frey R, Schermuly RT, Garcia-Lucio J, Blanco I, Bednorz M, Tura-Ceide O, Tadele E, Brandes RP, Grimminger J, Klepetko W, Jaksch P, Rodriguez-Roisin R, Seeger W, Grimminger F, Barbera JA. Stimulation of soluble guanylate cyclase prevents cigarette smoke-induced pulmonary hypertension and emphysema. Am J Respir Crit Care Med 2014;189:1359-1373.

42. Ghofrani HA, Pepke-Zaba J, Barbera JA, Channick R, Keogh AM, Gomez-Sanchez MA, Kneussl M, Grimminger F. Nitric oxide pathway and phosphodiesterase inhibitors in pulmonary arterial hypertension. J Am Coll Cardiol 2004;43:68S-72S.

43. Zhao L, Mason NA, Morrell NW, Kojonazarov B, Sadykov A, Maripov A, Mirrakhimov MM, Aldashev A, Wilkins MR. Sildenafil inhibits hypoxia-induced pulmonary hypertension. Circulation 2001;104:424-428.

44. Blanco I, Gimeno E, Munoz PA, Pizarro S, Gistau C, Rodriguez-Roisin R, Roca J, Barbera JA. Hemodynamic and gas exchange effects of sildenafil in patients with chronic obstructive pulmonary disease and pulmonary hypertension. Am J Respir Crit Care Med 2010;181:270-278.

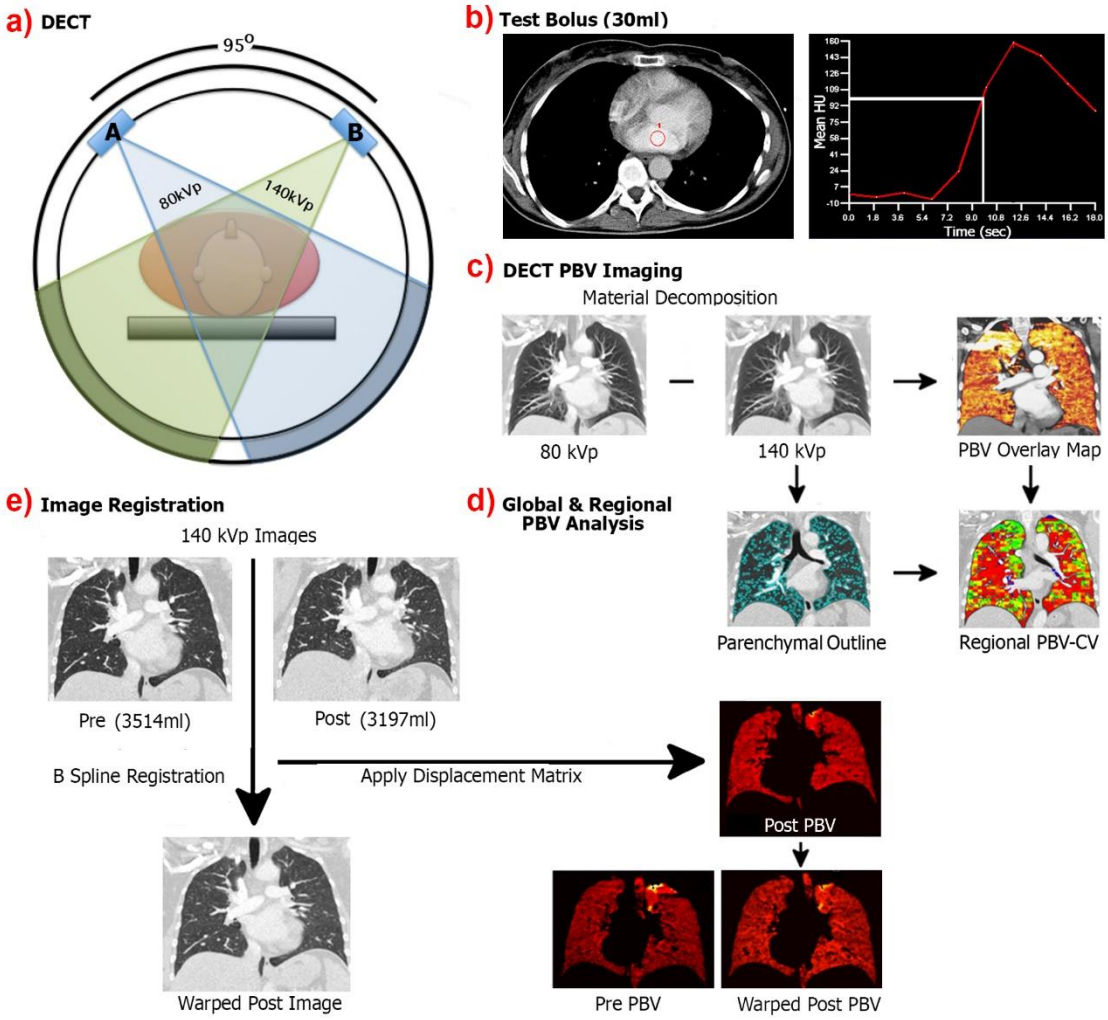

Figure 1

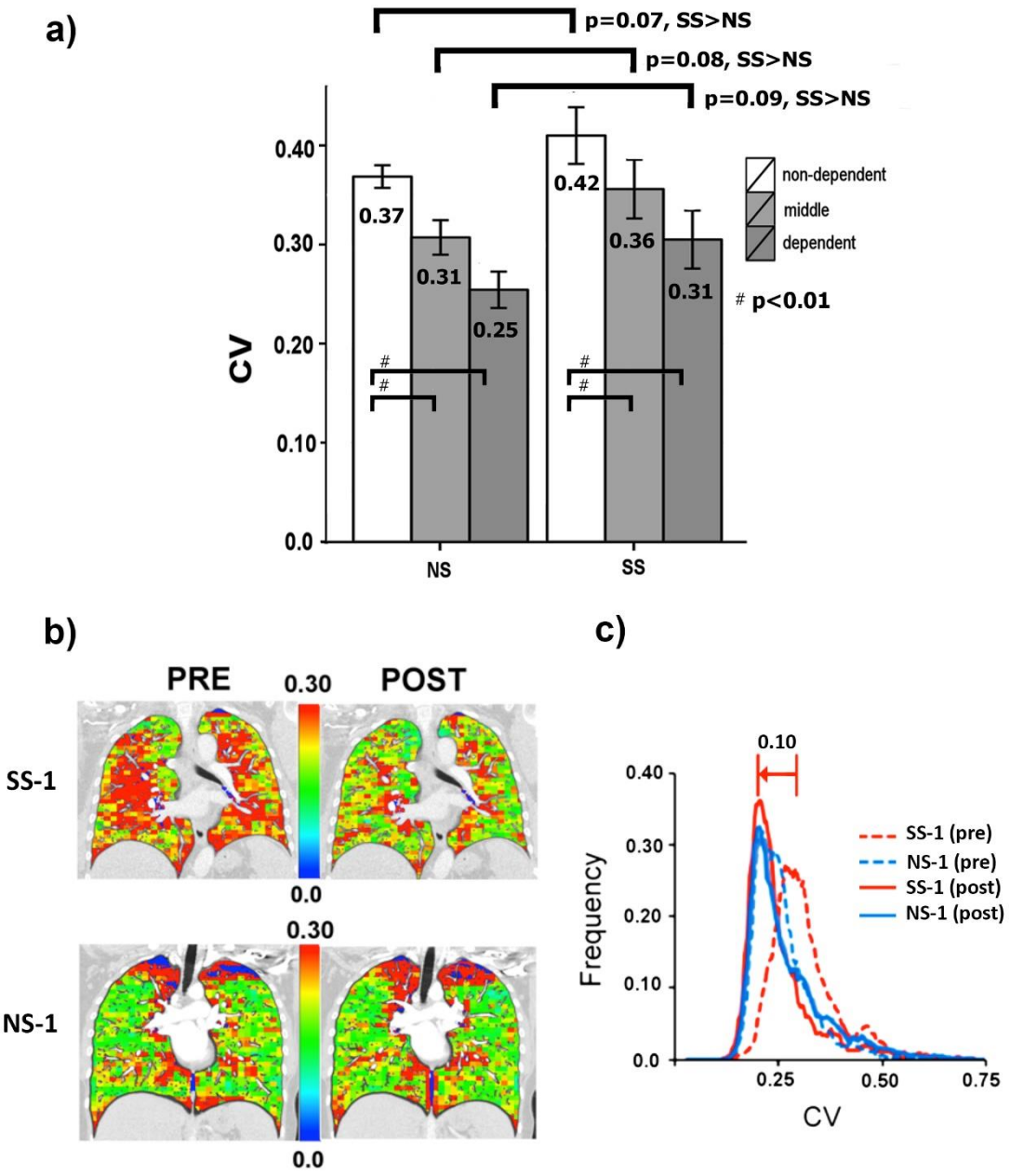

Figure 2

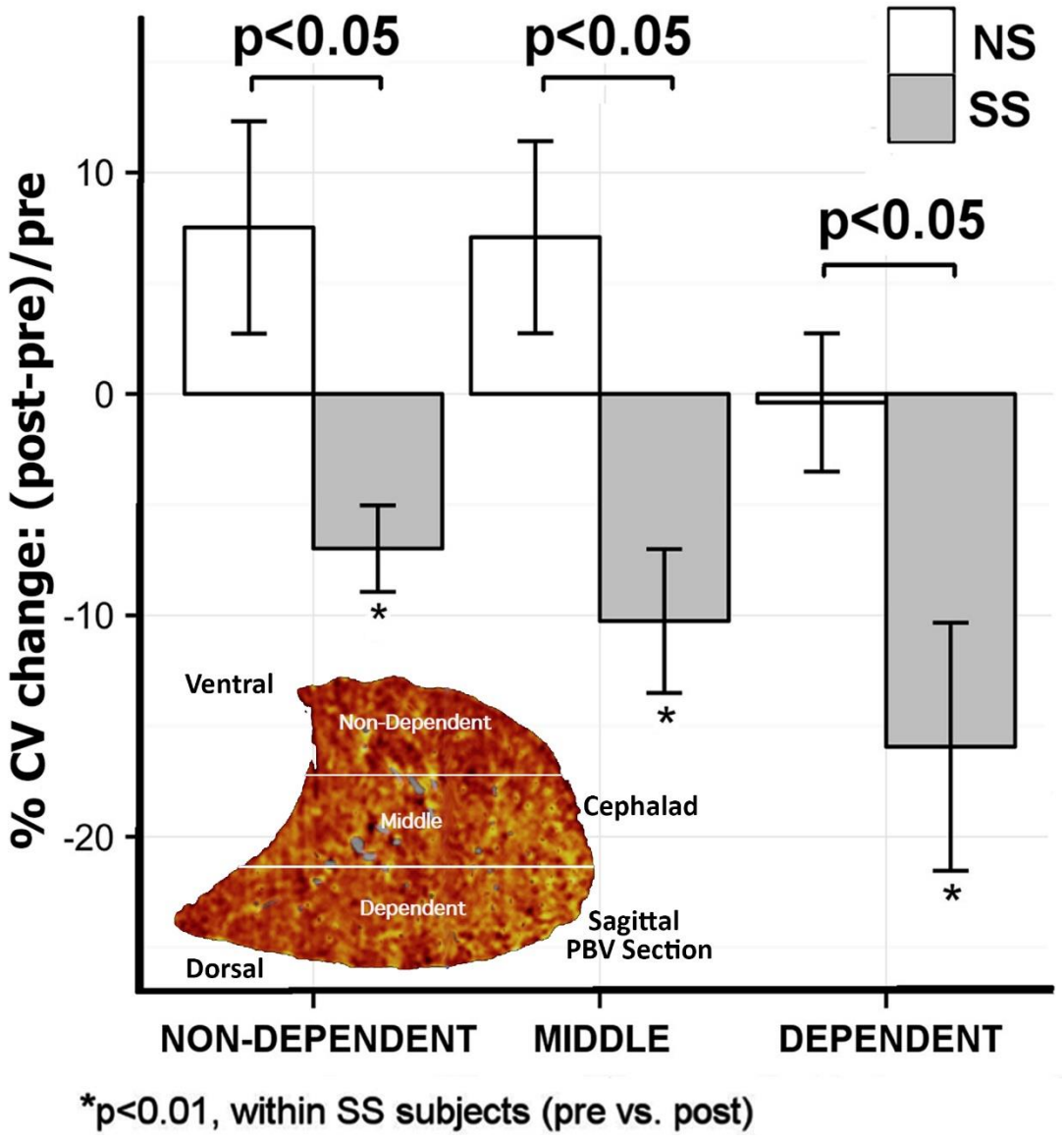

Figure 3

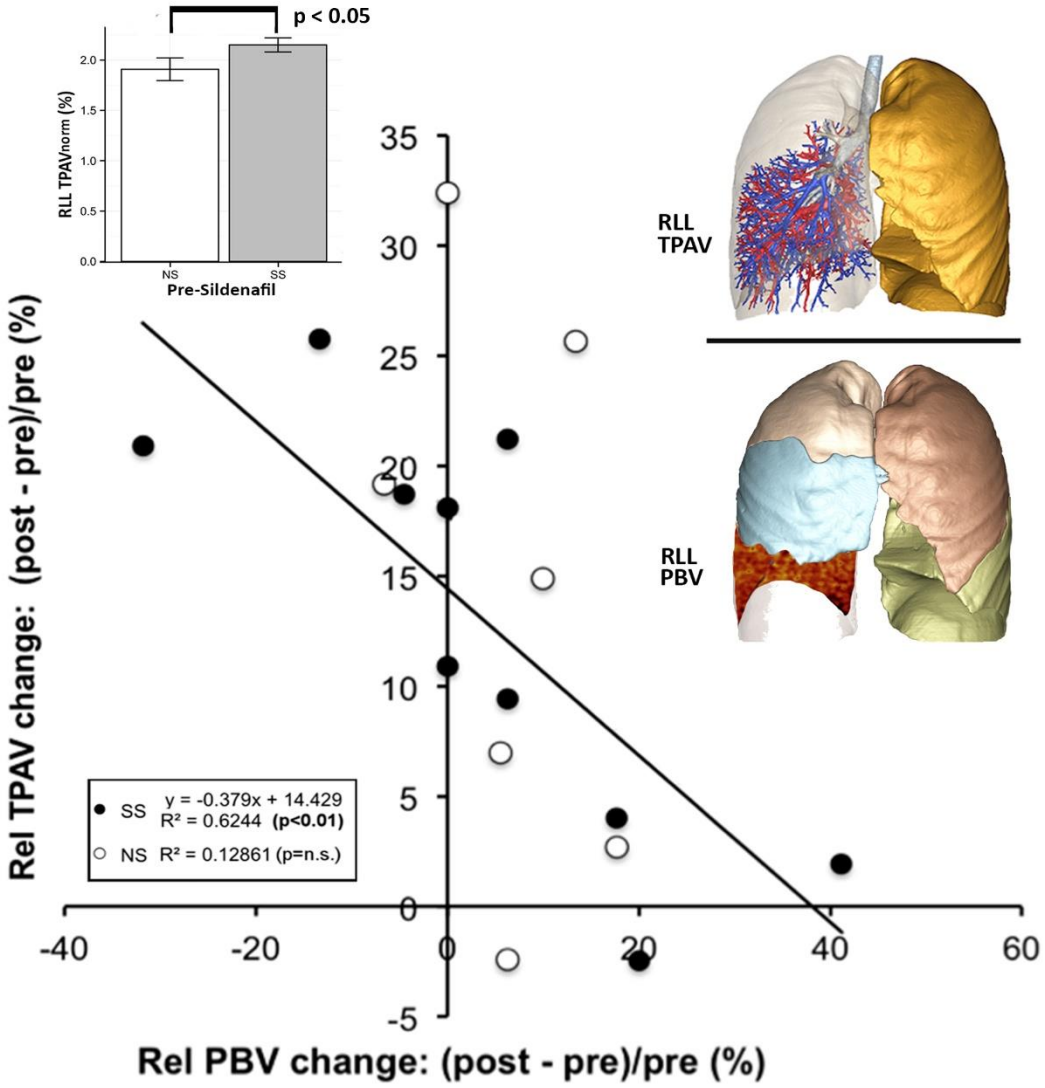

Figure 4

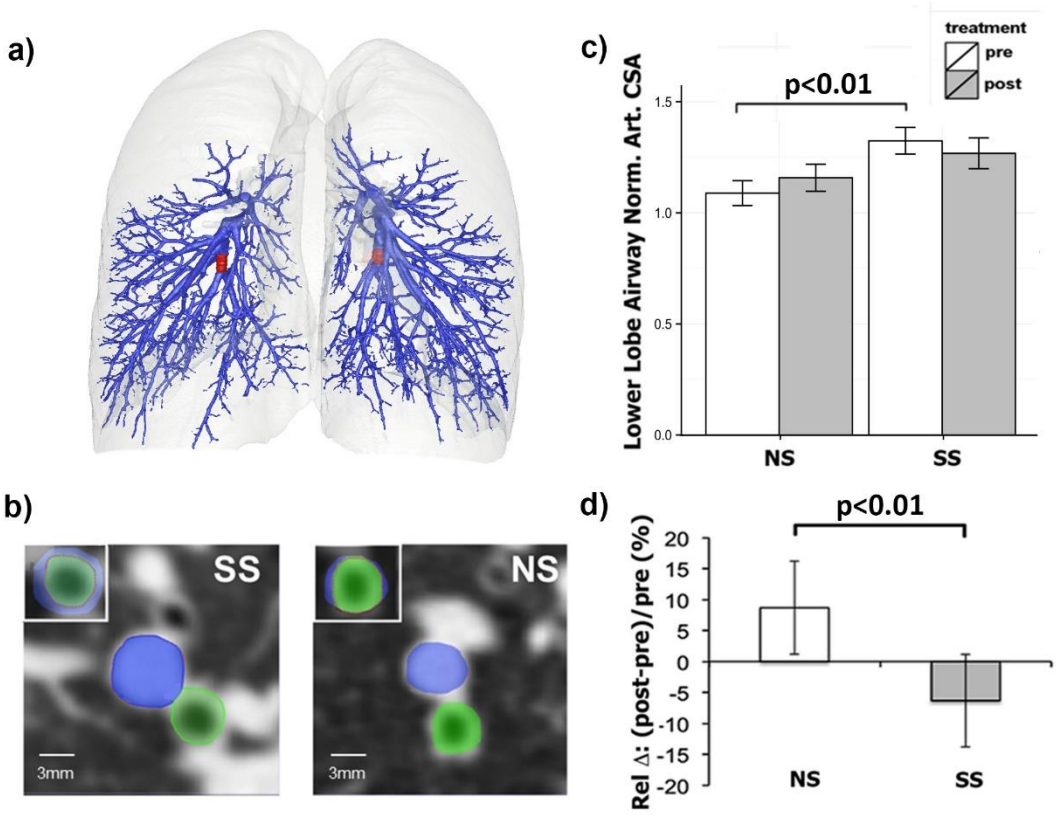

Figure 5

B. SUBPOPULATIONS AND INTERMEDIATE OUTCOME MEASURES IN COPD STUDY (SPIROMICS)

This paper has been submitted to American journal of respiratory and critical care medicine.

Enlarged Segmental Pulmonary Arteries Differentiate Rapid Emphysema Progressors from Non Progressors in the SPIROMICS Cohort

Dougherty TM[1], Jin D[2], Han MK[3], Newell Jr JD[1,5], Saha PK[2,5], Barr RG[6], Bleecker ER[7], Carretta EE[8], Comellas AP[4], Cooper CB[9], Couper D[8], Guo J[1,5], Hansel NN[10], Kanner RE[11], Kazeroni EA[12], Kleerup EC[9], Martinez FJ[13], Rennard S[14], Woodruff PG[15] & Hoffman EA[1,4,5] for the SPIROMICS Research Group

[1]Department of Biomedical Engineering, University of Iowa, Iowa City, IA

[2]Department of Computer and Electrical Engineering, University of Iowa, Iowa City, IA

[3]Department of Internal Medicine, University of Michigan Medical School, Ann Arbor, MI

[4]Department of Medicine, University of Iowa Carver College of Medicine, Iowa City, IA

[5]Department of Radiology, University of Iowa Carver College of Medicine, Iowa City, IA

[6]Department of Medicine and Department of Epidemiology, Columbia University College of Medicine, New York, NY

[7]Center for Human Genomics and Personalized Medicine, Wake Forest University health Sciences, Winston-Salem, North Carolina

[8]Department of Biostatistics, University of North Carolina, Chapel Hill, NC

[9]Department of Medicine, University of California Los Angeles, Los Angeles, CA

[10]Department of Medicine, The Johns Hopkins University, Baltimore, MD

[11]Department of Internal Medicine, University of Utah, Salt Lake City, UT

[12]Department of Radiology, University of Michigan Medical School, Ann Arbor, MI

[13]Department of Medicine, Weill Cornell Medical College, New York, NY

[14]Department of Internal Medicine, University of Nebraska, Omaha, NE

[15]Department of Medicine, University of California San Francisco, San Francisco, CA

Running Head: Standardized Cross-Platform Lung CT Protocol

Keywords: Lung Imaging, COPD, Asthma, Pulmonary Parenchyma, Pulmonary Airways, Multicenter Trials

Contact Information:

Eric A. Hoffman, PhD
Department of Radiology
University of Iowa Carver College of Medicine
200 Hawkins Drive
CC 701 GH
Iowa City, IA 52242
eric-hoffman@uiowa.edu

"The authors thank the SPIROMICS participants and participating physicians, investigators and staff for making this research possible. More information about the study and how to access SPIROMICS data is at www.spiromics.org. We would like to acknowledge the following current and former investigators of the SPIROMICS sites and reading centers: Neil E Alexis, PhD; Wayne H Anderson, PhD; R Graham Barr, MD, DrPH; Eugene R Bleecker, MD; Richard C Boucher, MD; Russell P Bowler, MD, PhD; Elizabeth E Carretta, MPH; Stephanie A Christenson, MD; Alejandro P Comellas, MD; Christopher B Cooper, MD, PhD; David J Couper, PhD; Gerard J Criner, MD; Ronald G Crystal, MD; Jeffrey L Curtis, MD; Claire M Doerschuk, MD; Mark T Dransfield, MD; Christine M Freeman, PhD; MeiLan K Han, MD, MS; Nadia N Hansel, MD, MPH; Annette T Hastie, PhD; Eric A Hoffman, PhD; Robert J Kaner, MD; Richard E Kanner, MD; Eric C Kleerup, MD; Jerry A Krishnan, MD, PhD; Lisa M LaVange, PhD; Stephen C Lazarus, MD; Fernando J Martinez, MD, MS; Deborah A Meyers, PhD; John D Newell Jr, MD; Elizabeth C Oelsner, MD, MPH; Wanda K O'Neal, PhD; Robert Paine, III, MD; Nirupama Putcha, MD, MHS; Stephen I. Rennard, MD; Donald P Tashkin, MD; Mary Beth Scholand, MD; J Michael Wells, MD; Robert A Wise, MD; and Prescott G Woodruff, MD, MPH. The project officers from the Lung Division of the National Heart, Lung, and Blood Institute were Lisa Postow, PhD, and Thomas Croxton, PhD, MD. SPIROMICS was supported by contracts from the NIH/NHLBI (HHSN268200900013C, HHSN268200900014C, HHSN268200900015C, HHSN268200900016C, HHSN268200900017C, HHSN268200900018C, HHSN268200900019C, HHSN268200900020C), which were supplemented by contributions made through the Foundation for the NIH from AstraZeneca; Bellerophon Therapeutics; Boehringer-Ingelheim Pharmaceuticals, Inc; Chiesi Farmaceutici SpA; Forest Research Institute, Inc; GSK; Grifols Therapeutics, Inc; Ikaria, Inc; Nycomed GmbH; Takeda Pharmaceutical Company; Novartis Pharmaceuticals Corporation; Regeneron Pharmaceuticals, Inc; and Sanofi."

Author Contributions:
Conception and Design
TMD, DJ, MKH, JDN, PKS, RGB, ERB, EEC, APC, CBC, DC, JG, NNH, REK, EAK, ECK, FJM, SR, PGW, EAH
Analysis and interpretation
TMD, DJ, MKH, JDN, PKS, RGB, EEC, DC, JG, AM, EAH
Drafting the manuscript
TMD, DJ, JDN, PKS, MKH, EAH
Intellectual content
TMD, DJ, MKH, JDN, PKS, RGB, ERB, EEC, APC, CBC, DC, JG, NNH, REK, EAK, ECK, FJM, SR, PGW, EAH
Final approval
TMD, DJ, MKH, JDN, PKS, RGB, ERB, EEC, APC, CBC, DC, JG, NNH, REK, EAK, ECK, FJM, SR, PGW, EAH

Conflict of Interest: EAH is a founder and shareholder of VIDA Diagnostics, a company commercializing lung image analysis software developed, in part, at the University of Iowa; JDN is a consultant to VIDA Diagnostics; JPS is currently an employee of VIDA Diagnostics and JG is a shareholder in VIDA Diagnostics.

Abstract

Rationale: In previous studies, we have shown that emphysema susceptible smokers with normal lung function have increased perfusion heterogeneity and pulmonary arterial dilation; both reversible with sildenafil. In this study, we seek to determine if pulmonary arterial dilation, reflective of downstream constriction, is associated with 1-year progression of emphysema assessed via quantitative computed tomography (QCT). **Methods:** From an initial 1855 subjects studied in the SubPopulations and InterMediate Outcome Measures in COPD Study (SPIROMICS), 599 former smokers were selected based upon a matching total lung volume (±10% on full inspiration QCT scans) between baseline and 1 year Subjects were divided into three groups based on rate of emphysema index (EI; % voxels < -950HU) progression: rapid progressors (RP; N = 188; ΔEI>1%), non progressors (NP; N = 301; ΔEI±0.5%) and never smokers (NS; N = 110). Airway standardized pulmonary cross sectional area ($CSA_{standard}$) associated with segmental level airways was assessed for RB4, RB10, LB4, LB10. Total pulmonary vascular volume (TPVV) was assessed for the whole lung, peel and core. **Results:** Average $CSA_{standard}$ for RP (0.73 ± 0.22) was significantly higher (p = 0.0074) compared with NP (0.68 ± 0.18) and a significant (p = 3.6E-09) decrease in %TPVV for the RP (2.71% ± 0.4%) subjects suggest a reduced venous volume compared to NP (2.94% ± 0.4%) despite similar age and smoking history. RP subjects were found to have an increased EI at baseline and $CSA_{standard}$ was inversely proportional to FEV_1/FVC. **Conclusion:** These data demonstrate that rapid one year progression of emphysema is associated with increased pulmonary $CSA_{standard}$ and a decreased %TPVV suggestive of a decreased pulmonary venous volume. These data support the hypothesis that emphysema progression is associated with a peripheral arterial dysfunction associated with enhanced pulmonary vascular resistance.

Introduction

Recent studies have brought focus onto a link between vascular dysfunction and COPD (1-9). The cause of vascular alterations is unclear, but it seems to occur before emphysematous changes in the lung (1, 5, 8, 10, 11). Alford et al. (1) demonstrated that smokers with normal pulmonary function tests could be divided into empnysema suceptible and emphysema resistant based upon the visual identification of localized centri-acinar emphysema. The emphysema susceptible subjects, on dynamic CT, had twice the heterogeneity of pulmonary parenchymal perfusion compared with the emphysema resistant subjects. This observation supported the notion that emphysema susceptibility was related to a subjects inability to over-ride hypoxic pulmonary vasoconstriction (HPV) in regionally inflamed lung parenchyma, and the inability to block HPV in inflamed lung regions leads to emphysematous parenchymal destruction due to the persistence of the inflammation and the inability to deliver progenitor cells to the region, required for initiation of repair (1). The normal response of the lung, endowing the subject with resistance to emphysema, is the ability to over-ride HPV in the presence of inflammation (12). Hoffman et al. (13) demonstrated, in a sheep model, the ability to regionally maintain HPV in a normal lung region while blocking HPV in a region of inflammation. Iyer et al. (5), using dual energy computed tomography to assess perfused pulmonary blood volume, recently demonstrated that indeed the increased heterogeneity of perfusion in emphysema susceptible subjects is not just a function of parenchymal destruction but is rather a reversible property of the pulmonary vascular bed. A single oral dose of sildenafil reduced perfusion heterogeneity to the level found in emphysema resistant subjects. In this same study it was shown that central pulmonary arterial dimensions were increased in the emphysema susceptible subjects and this too was reversible with sildenafil.

In this study, we seek to expand these observations by hypothesizing that pulmonary arterial dimensions will be increased, due to downstream arterial constriction, in subjects susceptible to a more rapid progression of emphysema. To study this we evaluated the pulmonary vascular tree of subjects studied within the SubPopulations and InteRmediate Outcome Measures In COPD Study (SPIROMICS) (14) which included full inspiration, non-contrast CT scan at baseline and at the one year follow-up visit (15).

Methods

Study Cohort: Participants in this study were enrolled in the SubPopulations and InteRmediate Outcome Measures In COPD Study (SPIROMICS) (14). SPIROMICS is a prospective study of over 3000 subjects classified into four strata: smokers without COPD, mild/moderate COPD, severe COPD and non-smoking controls. Participants were eligible to enroll in SPIROMICS if they were between the ages of 40 and 80 at baseline. Smoking history was limited to ≤ 1 pack-year for non-smokers (Stratum 1) and ≥ 20 pack-years for current and former smokers (Strata 2 – 4). Participants underwent baseline tests including physical examination, spirometry performed pre- and post-bronchodilator, 6-minute walk test, questionnaires, and thoracic CT scans performed at total lung capacity (TLC, full inspiration) and residual volume (RV, full expiration).

CT Imaging Protocol: Single energy thoracic CT scans were performed with coached breath-hold at TLC and RV without administration of contrast agents at 120 kVp in the supine body posture. X-ray tube current was dependent on BMI, scanner model, and TLC/RV scan (14). CT scans were conducted within 2 hours post bronchodilator associated with spirometry. Calibration was performed on CT scanners at each site using the COPDGene Lung Phantom (16) prior to subject enrollment and monthly through the duration of the study.

Criteria for Emphysema Progression Groups: Our study evaluated the first 1,855 SPIROMICS participants who completed baseline and one year follow-up (V2) visits. Three groups of subjects were identified from these first 1,855 SPIROMICS subjects based upon their emphysema progression determined from the TLC CT scan pairs (baseline and V2). Emphysema index (EI), calculated as the percent of voxels within the lung with a Hounsfield Unit (HU) less than -950, was used to identify our groups. Rapid progressors (RP) were defined as having a one-year increase in EI greater than 1%. Non progressors (NP) were defined as having a one-year change in EI between -0.5% and +0.5%. The final group contained non-smoking (NS) controls.

We excluded participants with a lung volume difference between baseline and V2 of greater than ±10%. It was assumed that one-year changes in disease status would not

cause substantial changes in a participant's TLC. Large changes in lung volume between visits would change regional lung density and interfere with the assessment of actual changes in EI. We also excluded GOLD 4 (110 subjects) and current smoking participants (500 subjects). The decision to include only current non smokers was based upon the observation that a change in smoking status (cessation) alters lung density due to change in the inflammatory response (17, 18), and it was felt that this would reduce our sensitivity to one year changes in the EI. If an individual was smoking at baseline and then stopped, the smoking cessation could serve to reduce lung density and incorrectly cause a mis-classification into the RP group. If the subject was a former smoker and, after the baseline study, began smoking again, this could cause an increase in lung density and cause a mis-classification into the NP group. By choosing to study only subjects who were classified as former smokers at baseline, we minimized the likelihood of misclassifying individuals into the RP group if their smoking status changed. The decision to exclude GOLD 4 subjects was based upon the observations of Suki and colleagues (19) that once the emphysematous process is initiated, mechanical forces take over, serving to strongly influence the progression of parenchymal failure, likely masking influences such as perfusion of inflamed lung regions we have sought to elucidate here. **Figure 1** provides a flow chart of the subject inclusion process.

Pulmonary Vascular Dimensions: Vessel, lung and lung lobe segmentations were acquired from the Apollo 2.0 workstation (VIDA Diagnostics, Coralville, IA). Peel-core (outer 1.5 cm and remaining core of whole lung) segmentations were processed using the in-house Pulmonary Analysis Software Suite (PASS). The Apollo vessel segmentations (20), including arteries and veins, were refined to fill in holes and gaps in the central pulmonary vessels and used to measure total (CT-detectable arteries + veins) pulmonary vascular volume (TPVV). Whole lung, lobar, core and peel TPVV and %TPVV, TPVV measures in relation to the lung volume for which TPVV was being calculated, were computed. In addition, peel to core TPVV ratio ($\%TPVV_{PC}$) was calculated as the $\%TPVV_{Peel}$ divided by the $\%TPVV_{Core}$.

Labeled airway segmentations (21) and associated airway CSA measurements were acquired from Apollo 2.0. A custom-built graphical user was developed within PASS

which displayed sagittal, coronal, and transverse views of the CT image along with sequential presentations of an overlay mask of the target airway segment (RB4, Rb10, LB4 and LB10). These arterial segments (depicted in **Figure 2**) were evaluated in TLC CT scans for 599 subjects falling into one of the three groups previously discussed: NS, NP and RP.

An experienced user was stepped through a series of displays highlighting airway segments of interest, and the user placed starting and ending points to identify proximal and distal portions of the target artery segment (22) associated with the corresponding locations on the airway segment. The panels of this user interface are displayed within **Figure 3**. The arterial segment centerline was automatically identified and the vessel's edges were identified at locations free of juxtaposed airway walls and neighboring arteries and veins. Measurement of the arterial cross sectional geometry was assessed in an orientation perpendicular to the centerline. The average cross-sectional area (CSA_{Artery}) and standard deviation of the artery segment are computed and displayed to the user. Inappropriate evaluation of oblique segments can arise from too few slices and can yield an over-estimate of CSA_{Artery}. In order to avoid this, availability of at least eight slices per segment was required. Because of this requirement we assessed less than 100% of the targeted airway-artery segment pairs, as reported in the results section. CSA_{Artery} measurements were standardized (22) ($CSA_{standard}$) by the associated airway CSA (CSA_{Airway}) where CSA_{Airway} was defined as the lumen area + outer wall area (obtained from Apollo). Defining CSA_{Airway} in this way eliminated biasing the standardization of artery measures by thickened airway walls or mucus lined airway segments, common symptoms in COPD subjects.

Using a cohort of 40 normal non-smokers with same day repeat scans at TLC, Jin et al. (22, 23) have reported the CSA measurement reproducibility. The observed intraclass correlation coefficient (ICC) for absolute arterial cross-sectional area at RB4, RB10, LB4 and LB10 were 95, 97, 93 and 94%, respectively, and the ICC values of standardized arterial cross-sectional area at those airway branch locations were 86, 93, 89, and 90%, respectively.

Statistical Analysis: To avoid multiple measures from the same subject, for the purpose of statistical analysis, $CSA_{standard}$ was calculated as the average of the per-subject airway-

artery pairs. Participant characteristics and CT measurements from SPIROMICS baseline visits are reported as mean ± standard deviation. One-way analysis of variance (ANOVA) with post-hoc analysis for multiple tests was performed to compare subject characteristics and CT, CSA and TPVV data between NS-NP, NP-RP and RP-NS. Linear regression was performed between average $CSA_{standard}$ and EI, one-year change in EI, FEV_1/FVC and % predicted FEV_1 among RP participants. EI and one-year change in EI were also regressed in RP participants.

Results:

Participant Characteristics: Vessel dimensions were evaluated in 599 participants: 188 RP, 301 NP and 110 NS. A full summary of participant characteristics can be seen in **Table 1**. RP and NP participants were approximately the same age (RP: 68 years, NP: 67 years, p = 0.1) and had similar history of smoking (RP: 53.8 pack-years, NP: 51.3 pack-years, p = 0.32). Despite these similarities, RP had a significantly higher emphysema index, a lower mean lung density, a larger TLC volume, a larger % air volumes, more males, lower BMI, and more severe GOLD status, a lower FEV_1% predicted and a lower FEV_1/FVC percent predicted.. NS were younger, had smaller TLC volume and had a larger female group membership.

TPVV and CSA Measurements: CSA_{Artery} measurements were obtained in 93% of RB10, 90% of LB10, 48% of RB4 and 73% of LB4 associated arteries. CSA_{Airway} was similar among all groups for all target airways, but CSA_{Artery} and $CSA_{standard}$ varied by group (**Table 2**). CSA_{Artery} and $CSA_{standard}$ was significantly larger in RP for arteries associated with RB10 and LB4 airway segments (**Table 2**) and trended larger in the other two artery-airway pairs. As shown in **Figure 4**, the group average of the per-subject average $CSA_{standard}$ was significantly larger in the RP than either the NP or NS groups while this metric was also larger in the NP compared with the NS group. The %TPVV in the whole lung (RP: 2.71% ± 0.4%, NP: 2.94% ± 0.4%; p = 3.6E-09), peel (RP: 1.94 % ± 0.4%, NP: 2.05% ± 0.3%; p = 0.002) and core (RP: 3.59% ± 0.6%, NP: 4.03% ± 0.7%; p = 1.7E-14) were all significantly smaller in RP, but similar in NP and NS groups (**Figure 5**). The $\%TPVV_{PC}$ ratio was significantly (RP vs NP: p = 1.4E-05; RP vs NS: p = 1.2E-06) larger

in RP (54.5% ± 8.4%) than NP (51.3% ± 7.1%) and NS (50.2% ± 6.6%) (**Figure 5**) due to the fact that the %TPVV is more reduced in the core than the peel for the RP group These data, combined with the observations that the pulmonary arteries in the RP group are larger suggest that the smaller %TPVV in the RP group is due to a smaller venous volume, consistent with the notion that there is peripheral arterial constriction.

Association between Vessel Dimensions and Disease Severity/Progression: Average $CSA_{standard}$ significantly correlated with baseline EI (R = 0.29, p = 7.27e-05) (**middle left panel of Figure 6**) as well as for each of the individual lobes as shown in the remaining panels of **Figure 6**. In a multivariable logistic regression comparing rapid progressors to non-progressors, $CSA_{Standard}$ remained strongly associated with progression when adjusted for age, gender and scanner manufacturer (p=0.01). Average $CSA_{Standard}$ is also significantly inversly correlated with FEV1/FVC (R2 = 0.2, p = 6e-09) (**Figure 7**) and % predicted FEV1 in RP (R2 = 0.2, p = 5.17e-10).

A positive correlation between baseline EI and one-year change in EI was observed in the RP group (R2 = 0.03, p = 0.028) (**middle right, Figure 8**). This relationship was also significant when evaluated within the left and right lower lobe, and was strongest in the left lower lobe but was not significant in the remaining lobes.

Discussion:

By dividing SPIROMICS subjects into RP and NP groups solely on the basis of a one year change of a CT-based imaging metric (EI), we identified two groups of individuals. As seen in table 2, these 2 groups demonstrate distinctly different lung volumes, tissue volumes, BMIs, and PFT's with no differentiation in age or pack year history but with a greater number of males in the RP group. We believe that this serves as testimony to the strength of the imaging protocol and careful quality control (15) combined with inclusion criteria outlined in **Figure 1** serving to eliminate some of the know confounders which, if present, would add ambiguity to the imaging-based metrics. Having divided the subjects into the RP and NP groups, we have demonstrated that subjects defined as having rapidly progressing emphysema over a one-year period have larger $CSA_{Standard}$ than subjects with non-progressing emphysema. We further demonstrate that the RP group has a significant

decrease in TPVV which, when combined with larger pulmonary arteries, translates to a reduction in central pulmonary venous volume. Together, these findings are consistent with the RP group having an unopposed peripheral hypoxic pulmonary vascular constriction in regions of inflammation as hypothesized and supported by the studies of Alford et al. (1) and Iyer et al. (5). Emphysema susceptible smokers with normal pulmonary function tests, have been demonstrated to have an increased $CSA_{Standard}$ that is reversible with sildenafil. (5) This again suggests that a peripheral pulmonary vascular constriction is an active process rather than a result of fixed remodeling, at least in the early stages. These data are in harmony with the observation of Barr et al. (3) whereby it was found that, down to low amounts of emphysema, there was a direct relationship between the emphysema index from CT and left ventricular filling derived from magnetic resonance imaging. The data presented here are also consistent with the study of Wells et al. (9) in which they demonstrated an increased pulmonary artery to aorta diameter ratio (PA:A) in subjects with COPD and a relationship between a PA:A ratio greater than 1 with an increased prevalence of COPD associated severe exacerbations. Matsuoka et al. (6), assessing the number of small pulmonary vessels in COPD subjects, found a negative correlation between the total area of these small pulmonary vessels and the extent of emphysema. While the findings of Matsuoka et al. could be interpreted as reflecting peripheral parenchymal destruction, we believe that our measurements showing a greater TPVV decrease in the lung core reflects the paired loss of central pulmonary venous volume associated with an increase in central pulmonary arterial volume. These observations, when combined, further strengthen our hypothesis that emphysema progression is related to vascular dysfunction. The observations, in **Figure 6**, showing a correlation, in the RP group, between the emphysema index at baseline and the $CSA_{Standard}$, supports the fact that these subjects already, at baseline, were differentiating themselves as rapid vs. slow progressors. It is of particular note that this cohort of individuals continued to be rapid progressors of emphysema despite their "former smoker" baseline status, demonstrating the perpetuation of disease despite smoking cessation. As might be expected, PFT results reflect CT findings. In **Figure 7**, subjects with larger $CSA_{Standard}$ have a lower FEV1/FVC ratio.

In **Figure 8** it is observed that individuals with a higher emphysema index at baseline will be the individuals with a more rapid one year emphysema index increase.

While our observations provide a strong link between rapid progression and pulmonary vascular dysfunction, at some point in the process it is likely that, as Suki and colleagues have discussed (19), once emphysema is present, at some point, mechanical factors serve to trigger further structural deterioration independent other driving forces.

Conclusion

In this study, we identified subjects from the SPIROMICS cohort as rapid and non-emphysema progressors. CSA of airway-standardized arterial segments associated with RB10, LB10, RB4 and LB4 bronchial segments along with a measure of total pulmonary vascular volume demonstrated a relationship between the rate of emphysema progression and arterial enlargement as well as central pulmonary venous volume reduction. These data are in support of a growing body of evidence suggesting a direct causal relationship between pulmonary arterial dysfunction and emphysema development and progression.

Table Legends

Table 1: Subject characteristics for rapid progressors (RP), non progressors (NP) and non-smoking controls (NS). Results are expressed as mean ± standard deviation with the exception of sex (% male) and GOLD status. N, number of subject; TLC, total lung capacity; EI, emphysema index; MLD, mean lung density; BMI, body mass index; FEV_1, forced expiratory volume in 1 second; FVC, forced vital capacity; GOLD, Global initiative for chronic Obstructive Lung Disease. * $p<0.05$ RP vs. NP, $^{\#}$ $p<0.05$ NP vs. NS, $^{\$}$ $p<0.05$ NS vs. RP

Table 2: Airway, artery and standardized CSA measurements by group. Results are expressed as mean ± standard deviation. Results that significantly differ ($p < 0.05$) from one another are marked as follows: *RP-NP, $^{\#}$NP-NS and $^{\$}$NS-RP.

Figure Legends

Figure 1: Flow chart of methods for defining the three groups of subjects used in this analysis: rapid progressors (RP), non-progressors (NP), and non-smokers (NS).

Figure 2: Shown here is a CT-derived image of the human airway tree labeled with the target airway segments serving to direct the identification of the target arterial segments used for our standardized arterial cross sectional area metric ($CSA_{standard}$): RB4 (blue), LB4 (cyan), RB10 (red) and LB10 (green).

Figure 3: This sequence of images demonstrate the interactive image processing steps taken to standardize arterial cross sectional area by use of the cross sectional area of the adjacent airway segment. The location of an arterial segment associated with a given airway segment is accomplished by the user visually identifying the segment and placing a starting (A) and ending (B) point location marker. Sagittal (C) and 3D rendered (D) views of the labeled airway (green) and artery (red outline in C, blue in D) pair are displayed so as to aid in the determination of the correct artery has been identified. In most cases, the airway and artery segments are in close proximity and reasonably parallel to one another. (note, these images provide the user with guidance for locating the corresponding airway-artery locations: they do not represent the exact edge locations used for calculating cross sectional areas). Once the user has identified the starting and ending location of the arterial segment associated with an airway segment of interest, computation of the airway and artery cross sectional areas and the $CSA_{Artery}/CSA_{Airway}$ ratio to generate $CSA_{Standard}$ is performed automatically by the software. The artery centerline is automatically computed guided by the identification of the segment based upon the user defined end points (A and B). The arterial cross section perpendicular to the centerline is calculated and rays are cast to find the edges of the vessel. Details are provided in the on-line supplement to Iyer et al. (5) and in Jin et al. (22). The airway cross sectional area utilizes the outer wall boarder. Neighboring airways and abutting veins and arteries are identified and removed from the CSA_{Artery} calculation.

Figure 4: Box plot distribution of the per-subject average $CSA_{standard}$ in RP, NP, and NS. Solid black lines indicate group medians, white triangles indicate group means, and white circles indicate group outliers.

Figure 5: Mean total pulmonary vascular volume relative to associated lung volume (%TPVV) (top) and $\%TPVV_{Peel}/\%TPVV_{Core}$ (bottom) in RP, NP and NS groups. Significance is indicated by "*" (Whole: RP vs NP – p = 3.6E-09, RP vs NS – p = 1.9E-05; Peel: RP vs NP – p = 0.001, RP vs NS – p = 0.03; Core: RP vs NP – p = 1.7E-14, RP vs NS – p = 3.5E-11; Peel/Core Ratio: RP vs NP – p = 1.4E-05, RP vs NS – p = 1.2E-06)

Figure 6: The baseline emphysema index significantly correlated with the individual average $CSA_{Standard}$ for the whole lung (middle left panel) as well as for each of the individual lobe.

Figure 7*:* Baseline FEV_1/FVC significantly correlated with the average $CSA_{standard}$ assessed for each member of the RP group.

Figure 8*:* A statistically significant (p = 0.028) relationship was observed between baseline EI and one year change in EI for the whole lung (left middle panel), which suggests that past rate of emphysema progression is a predictor of future rate of progression. This same relationship was highly significant when evaluated for the left and right lower lobes, but not for the other lobes.

References

1. Alford SK, van Beek EJ, McLennan G, Hoffman EA. Heterogeneity of pulmonary perfusion as a mechanistic image-based phenotype in emphysema susceptible smokers. *Proc Natl Acad Sci U S A* 2010; 107: 7485-7490.

2. Barr RG. The epidemiology of vascular dysfunction relating to chronic obstructive pulmonary disease and emphysema. *Proc Am Thorac Soc* 2011; 8: 522-527.

3. Barr RG, Bluemke DA, Ahmed FS, Carr JJ, Enright PL, Hoffman EA, Jiang R, Kawut SM, Kronmal RA, Lima JA, Shahar E, Smith LJ, Watson KE. Percent emphysema, airflow obstruction, and impaired left ventricular filling. *N Engl J Med* 2010; 362: 217-227.

4. Barr RG, Mesia-Vela S, Austin JH, Basner RC, Keller BM, Reeves AP, Shimbo D, Stevenson L. Impaired flow-mediated dilation is associated with low pulmonary function and emphysema in ex-smokers: the Emphysema and Cancer Action Project (EMCAP) Study. *Am J Respir Crit Care Med* 2007; 176: 1200-1207.

5. Iyer KS, Newell JD, Jr., Jin D, Fuld MK, Saha PK, Hansdottir S, Hoffman EA. Quantitative Dual-Energy Computed Tomography Supports a Vascular Etiology of Smoking-induced Inflammatory Lung Disease. *Am J Respir Crit Care Med* 2016; 193: 652-661.

6. Matsuoka S, Washko GR, Dransfield MT, Yamashiro T, San Jose Estepar R, Diaz A, Silverman EK, Patz S, Hatabu H. Quantitative CT measurement of cross-sectional area of small pulmonary vessel in COPD: correlations with emphysema and airflow limitation. *Acad Radiol* 2010; 17: 93-99.

7. Peinado VI, Gomez FP, Barbera JA, Roman A, Angels Montero M, Ramirez J, Roca J, Rodriguez-Roisin R. Pulmonary vascular abnormalities in chronic obstructive pulmonary disease undergoing lung transplant. *The Journal of heart and lung transplantation : the official publication of the International Society for Heart Transplantation* 2013; 32: 1262-1269.

8. Peinado VI, Pizarro S, Barbera JA. Pulmonary vascular involvement in COPD. *Chest* 2008; 134: 808-814.

9. Wells JM, Washko GR, Han MK, Abbas N, Nath H, Mamary AJ, Regan E, Bailey WC, Martinez FJ, Westfall E, Beaty TH, Curran-Everett D, Curtis JL, Hokanson JE, Lynch DA, Make BJ, Crapo JD, Silverman EK, Bowler RP, Dransfield MT, Investigators CO, Investigators ES. Pulmonary arterial enlargement and acute exacerbations of COPD. *N Engl J Med* 2012; 367: 913-921.

10. Peinado VI, Barbera JA, Abate P, Ramirez J, Roca J, Santos S, Rodriguez-Roisin R. Inflammatory reaction in pulmonary muscular arteries of patients with mild chronic obstructive pulmonary disease. *Am J Respir Crit Care Med* 1999; 159: 1605-1611.

11. Santos S, Peinado VI, Ramirez J, Melgosa T, Roca J, Rodriguez-Roisin R, Barbera JA. Characterization of pulmonary vascular remodelling in smokers and patients with mild COPD. *Eur Respir J* 2002; 19: 632-638.

12. Schuster DP, Marklin GF. Effect of changes in inflation and blood volume on regional lung density--a PET study: 2. *J Comput Assist Tomogr* 1986; 10: 730-735.

13. Hoffman EA, Simon BA, McLennan G. State of the Art. A structural and functional assessment of the lung via multidetector-row computed tomography: phenotyping chronic obstructive pulmonary disease. *Proc Am Thorac Soc* 2006; 3: 519-532.

14. Couper D, LaVange LM, Han M, Barr RG, Bleecker E, Hoffman EA, Kanner R, Kleerup E, Martinez FJ, Woodruff PG, Rennard S. Design of the Subpopulations and Intermediate Outcomes in COPD Study (SPIROMICS). *Thorax* 2014; 69: 491-494.

15. Sieren JP NJJ, Barr RG, Bleecker ER, Burnette N, Caretta EE, Couper D, Goldin J, Guo J, Han MK, Hansell NN, Kanner RE, Kazeroni EA, Martinez FJ, Rennard S, Woodruff PG, Hoffman EA. SPIROMICS Protocol for Multicenter Quantitative CT to Phenotype the Lungs. *American Journal of Critical Care Medicine* In Press, 2016.

16. Regan EA, Hokanson JE, Murphy JR, Make B, Lynch DA, Beaty TH, Curran-Everett D, Silverman EK, Crapo JD. Genetic epidemiology of COPD (COPDGene) study design. *COPD* 2010; 7: 32-43.

17. Shaker SB, Stavngaard T, Laursen LC, Stoel BC, Dirksen A. Rapid Fall in Lung Density Following Smoking Cessation in COPD. *COPD: Journal of Chronic Obstructive Pulmonary Disease* 2011; 8: 2-7.

18. Zach JA, Williams A, Jou S-S, Yagihashi K, Everett D, Hokanson JE, Stinson D, Lynch DA. Current Smoking Status Is Associated With Lower Quantitative CT Measures of Emphysema and Gas Trapping. *Journal of Thoracic Imaging* 2016; 31: 29-36.

19. Suki B, Jesudason R, Sato S, Parameswaran H, Araujo AD, Majumdar A, Allen PG, Bartolak-Suki E. Mechanical failure, stress redistribution, elastase activity and binding site availability on elastin during the progression of emphysema. Pulmonary pharmacology & therapeutics 2012; 25: 268-275.

20. Shikata H, McLennan G, Hoffman EA, Sonka M. Segmentation of Pulmonary Vascular Trees from Thoracic 3D CT Images. *Int J Biomed Imaging*, 2009, 636240.

21. Tschirren J, McLennan G, Palagyi K, Hoffman EA, Sonka M. Matching and anatomical labeling of human airway tree. *IEEE Trans Med Imaging* 2005; 24: 1540-1547.

22. Jin D, Guo J, Dougherty TM, Iyer KS, Hoffman EA, Saha PK. A semi-automatic framework of measuring pulmonary arterial metrics at anatomic airway locations using CT imaging. SPIE: Medical Imaging, 2016. 978816.

23. Jin D. Digital topologic and geometric approaches for CT-based multi-generation characterization of airway and pulmonary vascular tree morphology and their association. PhD Thesis, Electrical and Computer Engineering, University of Iowa, Iowa City, Iowa, USA, 2016.

Table 1

Characteristic	RP	NP	NS
N	188	301	110
Δ TLC Volume (%) *$	1.69 ± 4.0	-0.66 ± 4.2	-0.34 ± 4.7
Δ EI (%) *#$	2.45 ± 1.6	0.02 ± 0.3	-0.14 ± 0.5
EI (%) *#$	13.33 ± 10.1	3.86 ± 6.3	1.60 ± 1.7
MLD (HU) *$	-858 ± 19	-829 ± 27	-833 ± 25
Air Volume (L) *#$	5.58 ± 1.2	4.73 ± 1.2	4.47 ± 1.1
Tissue Volume (L) *#$	0.85 ± 0.17	0.88 ± 0.17	0.81 ± 0.14
TLC Volume (L) *#$	6.43 ± 1.4	5.61 ± 1.3	5.28 ± 1.2
Age (years) #$	68 ± 6	67 ± 8	56 ± 10
Sex (male %) *#$	58.5	45.5	35.5
Height (in.) $	67.2 ± 3.8	66.8 ± 4.0	66.2 ± 3.6
Weight (lbs.) *#	174 ± 35.8	189 ± 38.5	176 ± 37.6
BMI (kg/m^2) *#	27.0 ± 4.6	29.7 ± 4.8	28.2 ± 5.0
Smoking Pack Years	53.8 ± 24.7	51.3 ± 28.5	N/A
FEV_1 % Predicted *#$	64.9 ± 24.3	82.2 ± 21.3	103.6 ± 12.2
FVC (L) #$	3.19 ± 1.0	3.19 ± 1.0	3.63 ± 0.9
FEV_1/FVC (%)*#$	48.7 ± 13.5	64.6 ± 13.1	78.9 ± 4.7
GOLD Status:			
GOLD 0	17	146	0
GOLD 1	31	50	0
GOLD 2	78	75	0
GOLD 3	62	30	0

Table 2

		Group		
Airway Branch	CSA Measure	NS	NP	RP
RB10	Airway	60.45 ± 14.1	59.33 ± 14.7	58.51 ± 14.0
	Artery ***$**	41.19 ± 14.5	42.52 ± 14.8	46.80 ± 20.4
	Stand. ***$**	0.693 ± 0.22	0.730 ± 0.22	0.812 ± 0.32
LB10	Airway	66.13 ± 14.8	66.00 ± 17.5	65.33 ± 16.3
	Artery #$	39.21 ± 12.7	45.43 ± 17.0	47.11 ± 19.1
	Stand. #$	0.614 ± 0.18	0.702 ± 0.23	0.743 ± 0.30
RB4	Airway	43.40 ± 11.0	41.71 ± 11.0	41.57 ± 10.1
	Artery $	22.26 ± 8.1	24.27 ± 7.7	26.13 ± 9.6
	Stand.#$	0.524 ± 0.17	0.603 ± 0.21	0.640 ± 0.21
LB4	Airway	39.67 ± 10.0	41.20 ± 12.1	40.23 ± 13.3
	Artery *#$	20.50 ± 7.8	24.02 ± 10.5	26.75 ± 11.9
	Stand.*$	0.523 ± 0.17	0.590 ± 0.22	0.684 ± 0.26

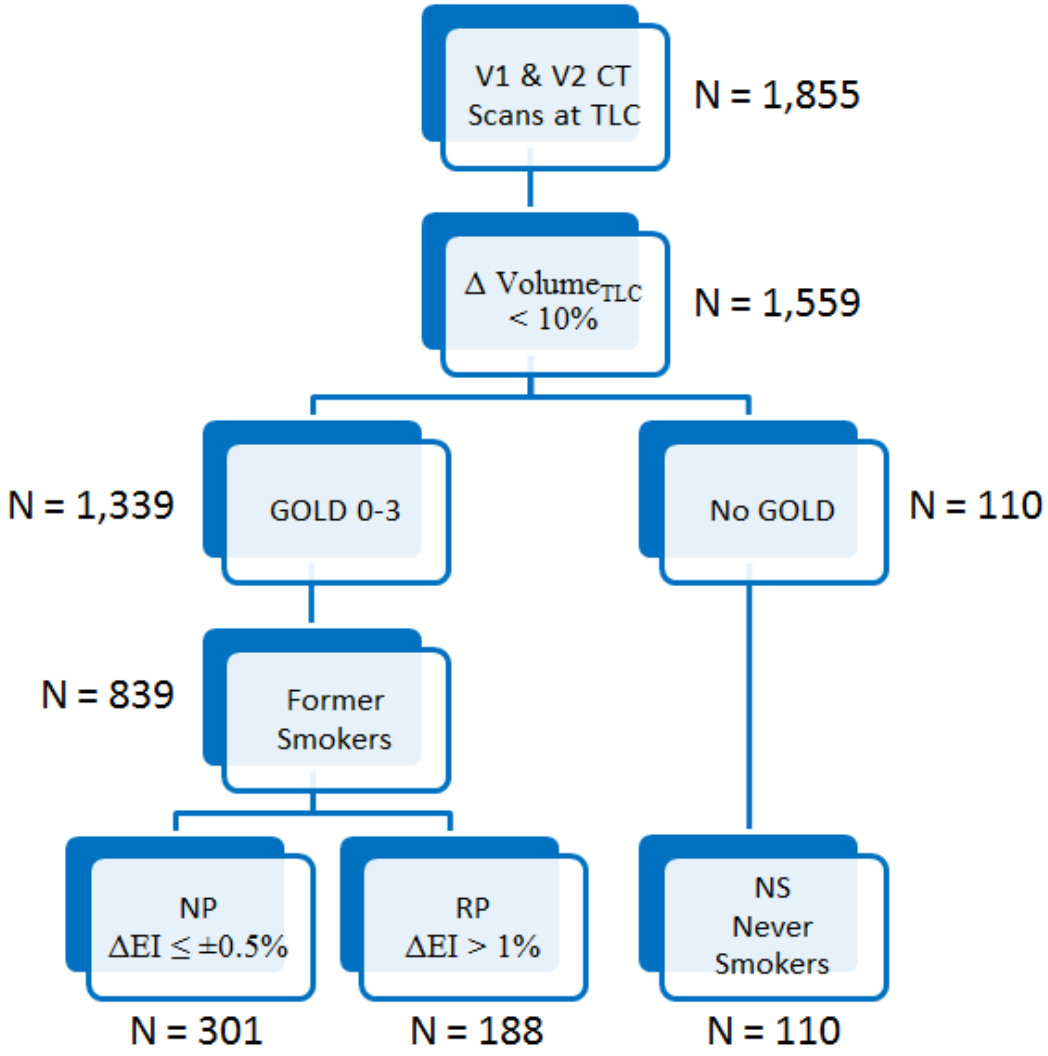

Figure 1

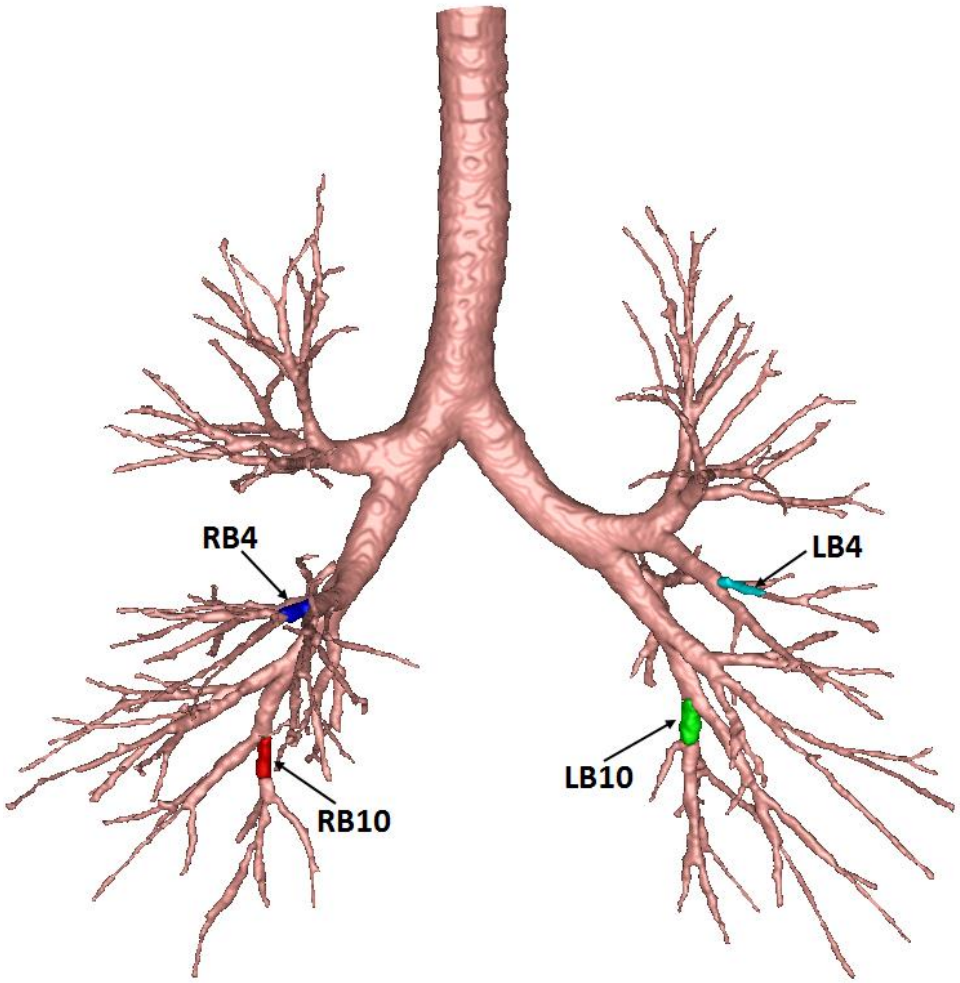

Figure 2

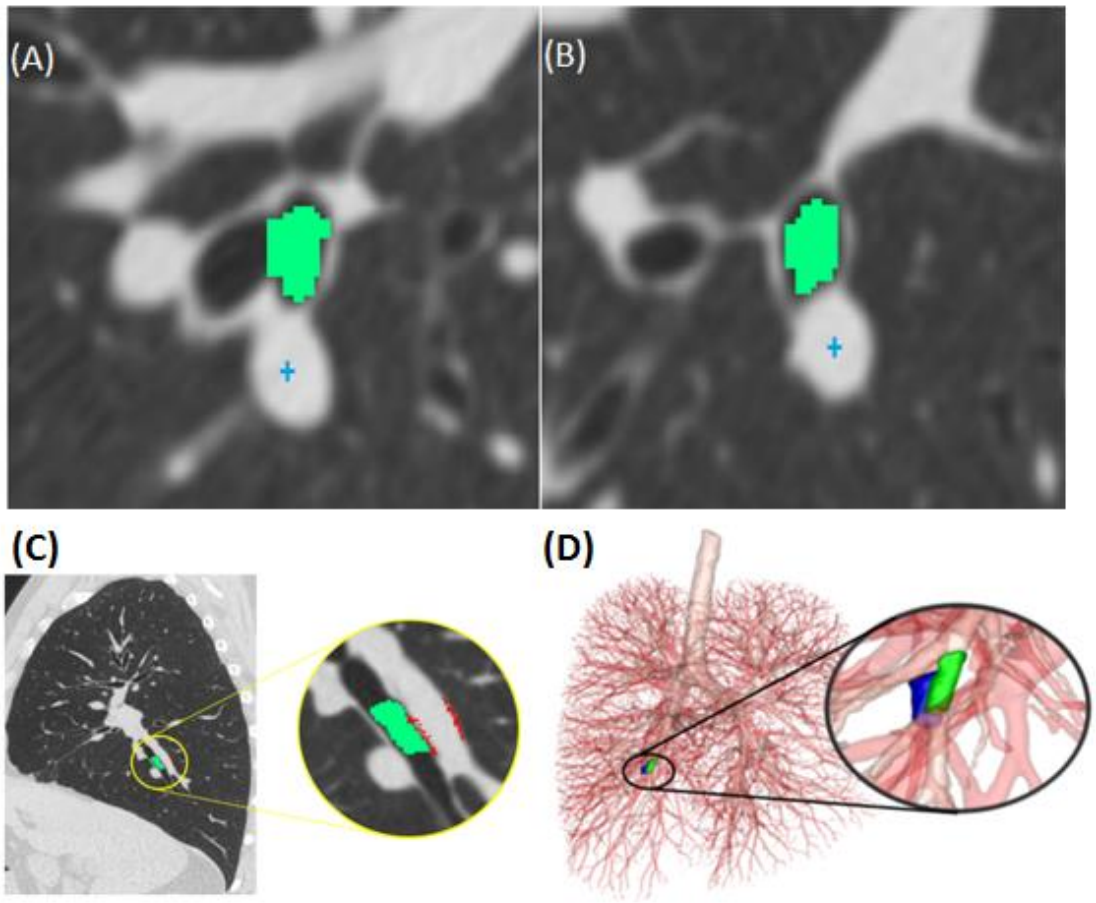

Figure 3

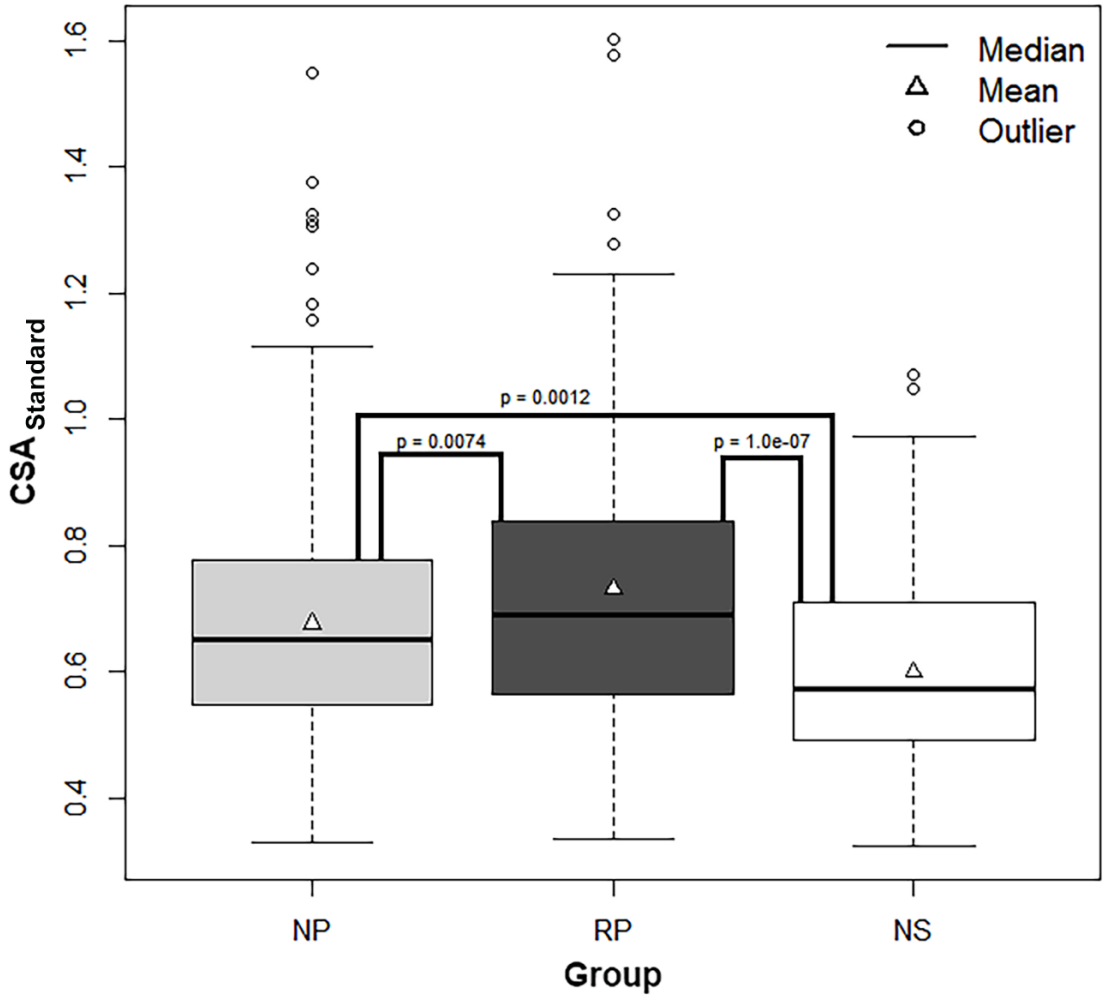

Figure 4

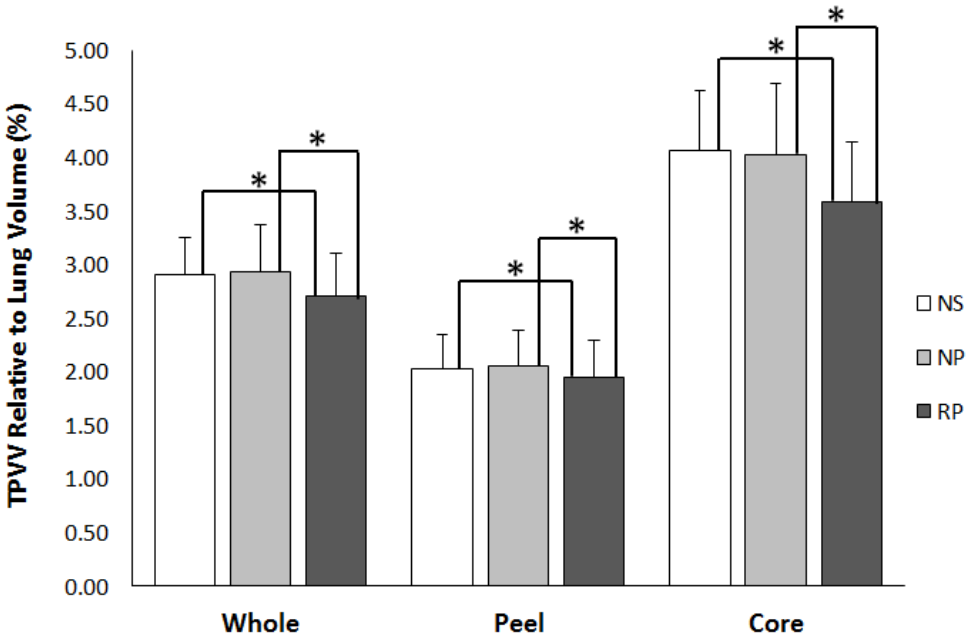

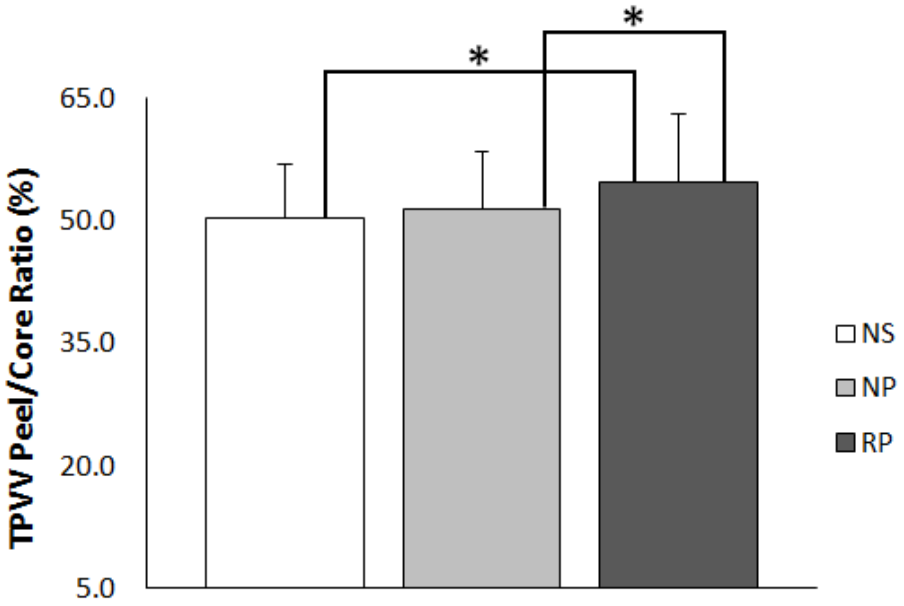

Figure 5

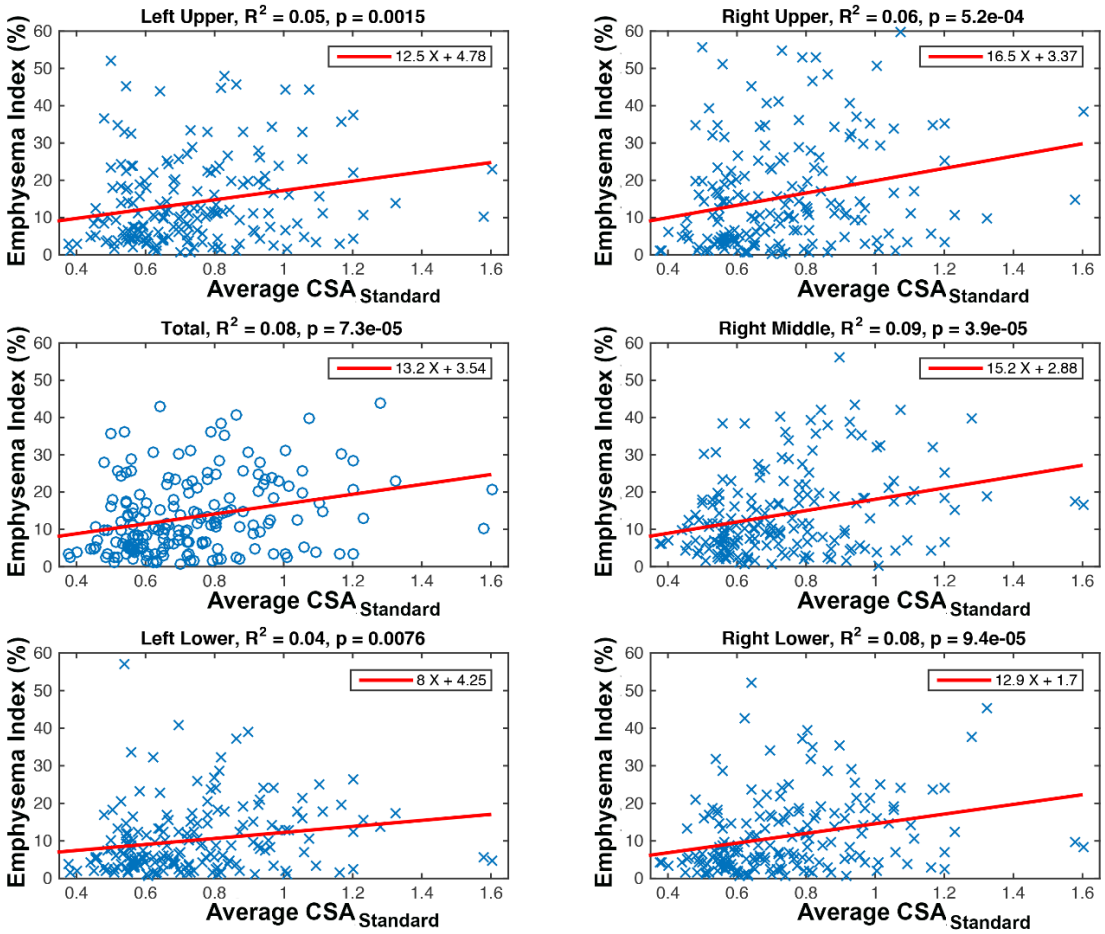

Figure 6

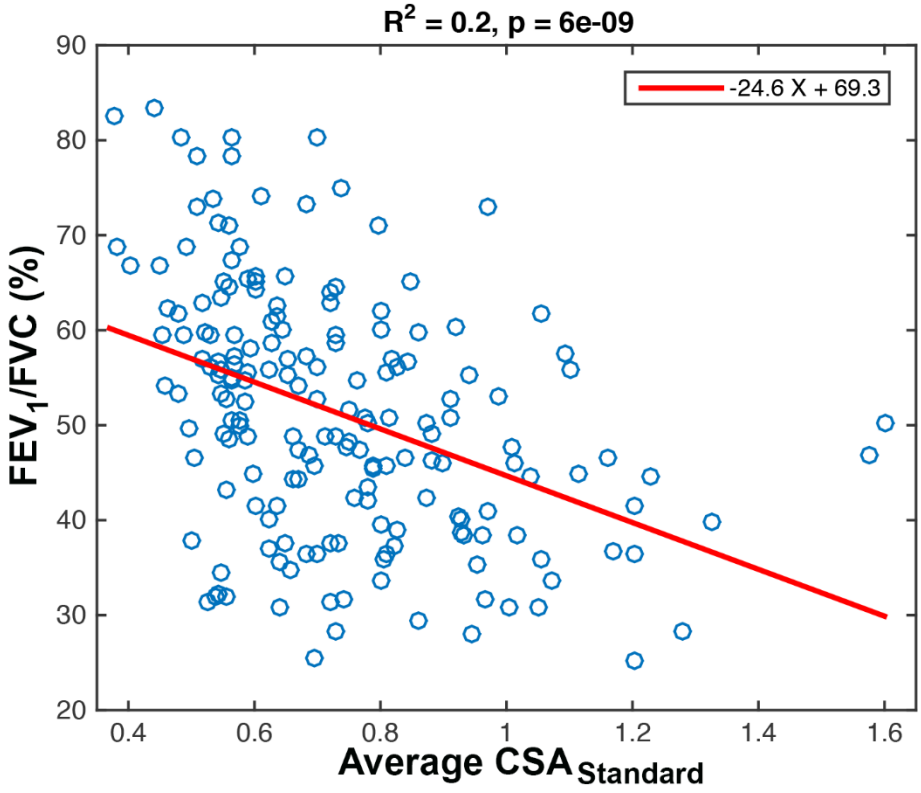

Figure 7

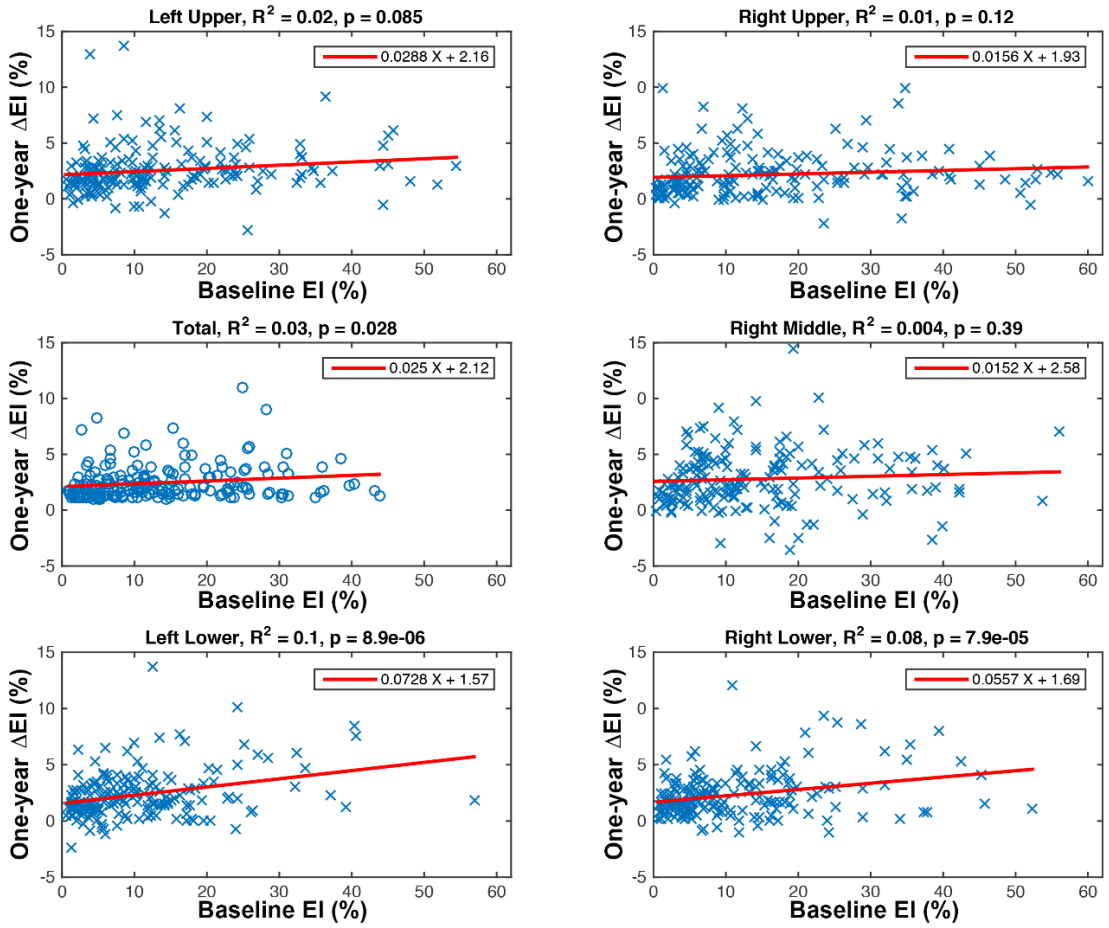

Figure 8